



**HAL**  
open science

# Modeling Study of Pyrolysis of Composite Materials: Application to Wood and Carbon/Epoxy Composite

Xiaowen Qin

► **To cite this version:**

Xiaowen Qin. Modeling Study of Pyrolysis of Composite Materials: Application to Wood and Carbon/Epoxy Composite. Other. ISAE-ENSMA Ecole Nationale Supérieure de Mécanique et d'Aérotechnique - Poitiers, 2021. English. NNT : 2021ESMA0006 . tel-03167564

**HAL Id: tel-03167564**

**<https://theses.hal.science/tel-03167564>**

Submitted on 12 Mar 2021

**HAL** is a multi-disciplinary open access archive for the deposit and dissemination of scientific research documents, whether they are published or not. The documents may come from teaching and research institutions in France or abroad, or from public or private research centers.

L'archive ouverte pluridisciplinaire **HAL**, est destinée au dépôt et à la diffusion de documents scientifiques de niveau recherche, publiés ou non, émanant des établissements d'enseignement et de recherche français ou étrangers, des laboratoires publics ou privés.

# THESE

Pour l'obtention du Grade de  
**DOCTEUR DE L'ECOLE NATIONALE SUPERIEURE DE MECANIQUE ET  
D'AEROTECHNIQUE**

(Diplôme National – Arrêté du 25 mai 2016)

Ecole Doctorale :  
Sciences et Ingénierie en Matériaux, Mécanique, Energétique et Aéronautique

Secteur de Recherche : Fluide, Thermique et Combustion

Présentée par:

**Xiaowen QIN**

\*\*\*\*\*

**Modeling study of pyrolysis of composite materials-Application to wood and  
carbon/epoxy composite**

\*\*\*\*\*

Directeur de thèse: Pr. Thomas Rogaume

Co-encadrant: Dr. Franck Richard

Co-encadrant: Dr. Benjamin Batiot

## JURY

### Rapporteurs:

Pr. Alexis Coppalle  
Pr. Bernard Porterie

Professeur - INSA Rouen (France)  
Professeur - Université d'Aix-Marseille (France)

### Membres du jury:

Pr. Pascal Boulet  
Dr. Jean Lachaud  
Dr. Virginie Dréan  
Pr. Thomas Rogaume  
Dr. Franck Richard  
Dr. Benjamin Batiot

Professeur - Université de Lorraine (France)  
Maitre de Conférences - Université de Bordeaux (France)  
Chef de projet - Efectis France (France)  
Professeur - Université de Poitiers (France)  
Maitre de Conférences - Université de Poitiers (France)  
Maitre de Conférences - Université de Poitiers (France)



## Acknowledgements

This thesis would be not completed without the guidance of my supervisors. First and foremost, I would like to thank Prof. Thomas Rogaume for giving me the chance and providing a good working environment for pursuing a Ph.D. degree in France, also the other two supervisors helping me a lot: Franck Richard and Benjamin Batiot. Among them, I appreciate sincerely and deeply the caring in every aspect from Franck Richard who is in charge of my work. He spent valuable time concerning experiments, numerical simulations, and the corresponding discussions. His kindness, knowledge, and encouragement make me feel inspiring when experiencing the dilemma.

I would like to thank Marc for helping me finish the Cone Calorimeter tests concerning Carbon/Epoxy composite pyrolysis. I would like to thank Dr. Jean Lachaud who gave me some useful suggestions when using PATO. I would like to thank Prof. Bernard Porterie, Prof. Alexis Coppalle, Prof. Pascal Boulet, Dr. Jean Lachaud, and Dr. Virginie Dréan for being the jury members of my Ph.D. defense. Their questions and suggestions helped me to improve my knowledge of fire safety topics. I acknowledge the financial support from the Chinese Scholarship Council (CSC) for 48 months.

I am thankful to all team members for sharing goodness and enjoyment during the last four years, including Fabien, Simon, Pierre, Julien, Minh, Jérémy, Tarik, Safae, etc. Also Chinese friends making my life warm, including Wei He, Xinwen Xie, Mengmeng Wang, Weiping Zou, etc. Lastly, I am deeply grateful to all my family members, I always recall my life in Zichang, Shaanxi. I feel quite regretful for my maternal grandmother who passed away two years ago, her love will bear in my heart forever.



# Abstract

Composite materials occupy a critical position in industrial applications or more broadly in our daily life. Synthetic composites substitute metallic materials due to their lightweight properties to achieve identical mechanical performance. They are widely used in the fields of energy transportation and storage. Natural composites (wood) are also widely used, especially in the construction industry. The disadvantage of these materials involves the disability in maintaining their mechanical characteristics in a fire scenario, and the study of their fire resistance is therefore a major issue. This thesis aims to develop a mathematical model of the thermal decomposition of composite materials subjected to different heating conditions. The simulations of different cases of thermal decomposition make it possible to study the interactions among the processes of heat and mass transfer as well as chemical reactions within the solid. The developed 3D model describes the gas transport within the pores of materials at the Darcy scale. Thermal conductivity is formulated in a tensor form allowing the definition of heat transfer in three directions of the domain. For the two types of materials, a multi-step reaction scheme is defined to describe the pyrolysis process. The cone calorimeter tests used to validate the model were carried out under an inert atmosphere (Nitrogen) which makes it possible to eliminate the presence of flame on the material surface as well as the heterogeneous reactions which can occur in the presence of oxygen. Therefore, the defined boundary conditions are quite simple and well-controlled to characterize without considering the unsteady flame. Pyrolysis gasses are assembled into an inert gas, therefore, the gas reactions in the pore are neglected and the local thermal equilibrium between the solid and gas phase is assumed. The implementation

of this pyrolysis model follows a scale separation process with two types of materials. The different heat and mass transfer processes, as well as chemical reactions, are studied separately to avoid the interactions, then the model is reconstructed to take these interactions into account. The pyrolysis behavior is firstly studied at a "0D" scale to develop the part of chemical reactions. The thermogravimetric analysis (TGA) is used at this scale and related experiments are conducted at different heating rates under an inert atmosphere. At this scale, only the chemical reactions are involved with known kinetics, and the heat and mass transport within the solid can be neglected with homogeneous temperature distribution. The different chemical reactions are described with the Arrhenius-type equation. The kinetic parameters are calculated by the inverse modeling method. The influence of the heating rate on the pyrolysis process is analyzed and 2D simulations are conducted at two heating rates to analyze the evolution of thermal and pressure gradients within the solid. The phenomena of heat and mass transport are considered and studied by bench-scale experiments which are conducted in the cone calorimeter. The corresponding simulations are implemented under two heat flux. The interactions among the heat and mass transport as well as chemical reaction processes are studied by analyzing the local time and length scales to identify what are the dominant phenomena through the whole pyrolysis process.

**Keywords:** wood combustion, calorimeters, composite materials, fire prevention, pyrolysis, simulation methods, heat transfer, mass transfer

# Table of contents

List of figures	xi
List of tables	xxiii
Nomenclature	xxv
<b>1 Introduction</b>	<b>1</b>
1.1 Background and motivation . . . . .	1
1.2 Research aim . . . . .	6
1.3 Research methodology . . . . .	7
1.4 Thesis outline . . . . .	9
<b>2 Literature review</b>	<b>13</b>
2.1 Composite materials: general background . . . . .	13
2.2 Pyrolysis phenomenon in the fire scenario . . . . .	18
2.2.1 Pyrolysis process description . . . . .	18
2.2.1.1 Macroscopic observation of pyrolysis of composite materials . . . . .	19
2.2.1.2 Heat and mass transfer aspect . . . . .	21
2.2.1.3 Chemical reaction aspect . . . . .	23
2.2.1.4 Physical structure change . . . . .	24
2.2.2 Pyrolysis process modeling . . . . .	29
2.2.2.1 Chemical reaction model . . . . .	34

---

2.2.2.2	Heat and mass transfer model . . . . .	39
2.2.2.3	Physical structure change model . . . . .	41
2.2.2.4	Boundary conditions . . . . .	42
2.2.2.5	Pyrolysis model evaluation . . . . .	43
2.3	Multi-scale experiment and parameters estimation . . . . .	47
2.3.1	Milligram-scale TGA and kinetics . . . . .	48
2.3.2	Bench-scale cone calorimeter . . . . .	50
2.3.3	Parameters estimation . . . . .	54
2.4	Conclusion . . . . .	57
<b>3</b>	<b>Description of the PATO solver</b>	<b>59</b>
3.1	The theory of volume averaging . . . . .	60
3.2	Pyrolysis kinetics . . . . .	63
3.3	Conservation equations . . . . .	67
3.3.1	Solid mass conservation equations . . . . .	67
3.3.2	Gas mass conservation equations . . . . .	67
3.3.3	Gas momentum conservation equations . . . . .	67
3.3.4	Energy conservation equation . . . . .	68
3.4	Boundary conditions . . . . .	72
3.5	Modeling work protocol . . . . .	73
3.6	Modeling assumption and simulation options . . . . .	74
3.7	Conclusion . . . . .	76
<b>4</b>	<b>Particle scale modeling of the wood pyrolysis</b>	<b>77</b>
4.1	TGA experimental procedure . . . . .	78
4.2	TGA Experimental results . . . . .	80
4.3	TGA Pyrolysis modeling study . . . . .	86
4.3.1	Numerical comparison under different heating rates . . . . .	93
4.3.2	Analysis of the influence of the kinetic parameters . . . . .	96
4.3.3	Analysis of the 0D and 2D modeling influence . . . . .	101

---

4.4	Conclusion . . . . .	110
<b>5</b>	<b>Cone calorimeter experiments and model validation for wood pyrolysis</b>	<b>113</b>
5.1	CACC experiment description and temperature measurement . . . . .	114
5.2	Inverse analysis to obtain heat convection coefficient . . . . .	123
5.3	Inverse analysis to obtain wood thermophysical parameters . . . . .	127
5.4	Inverse analysis to obtain char thermophysical parameters . . . . .	132
5.5	Model validation for moisture evaporation . . . . .	137
5.6	Model validation for wood pyrolysis under different scenarios . . . . .	147
5.6.1	Model validation for temperature and mass loss profiles . . . . .	148
5.6.2	Model validation for char front evolution . . . . .	164
5.6.3	Numerical analysis with global and single scalars . . . . .	169
5.7	Conclusion . . . . .	182
<b>6</b>	<b>Multi-scale application of the model to carbon/epoxy composite pyrolysis</b>	<b>185</b>
6.1	TGA experiments and model validation . . . . .	186
6.2	Cone calorimeter experiments and model validation . . . . .	192
6.2.1	Experimental protocol . . . . .	192
6.2.2	Determination of the thermophysical parameters . . . . .	193
6.2.3	Experimental and numerical prediction analysis . . . . .	197
6.3	Conclusion . . . . .	207
<b>7</b>	<b>Sensitivity analysis</b>	<b>209</b>
7.1	Kinetic and thermodynamic parameters influence . . . . .	212
7.1.1	Activation energy influence . . . . .	213
7.1.2	Pre-exponential factor influence . . . . .	215
7.1.3	Reaction order influence . . . . .	217
7.1.4	The heat of thermal decomposition influence . . . . .	219

7.2	Thermal and physical parameters influence . . . . .	221
7.2.1	Virgin thermal conductivity influence . . . . .	223
7.2.2	Char thermal conductivity influence . . . . .	225
7.2.3	Virgin and char specific heat capacity influence . . . . .	227
7.2.4	Virgin and char permeability influence . . . . .	230
7.2.5	Char emissivity influence . . . . .	234
7.3	Boundary parameters influence . . . . .	235
7.4	Water content influence . . . . .	237
7.5	Conclusion . . . . .	239
<b>8</b>	<b>Conclusion and perspective</b>	<b>241</b>
8.1	Conclusion . . . . .	241
8.2	Perspective . . . . .	247
	<b>References</b>	<b>251</b>
	<b>Appendix A Summary in French for each chapter/Résumé en français</b>	
	<b>pour chaque chapitre</b>	<b>267</b>
A.1	Chapitre 1: Introduction . . . . .	267
A.2	Chapitre 2: Revue de la littérature . . . . .	271
A.3	Chapitre 3: Description du solveur PATO . . . . .	273
A.4	Chapitre 4: Modélisation à l'échelle des particules de la pyrolyse du bois	275
A.5	Chapitre 5: Expériences au cône calorimètre et validation du modèle de pyrolyse du bois . . . . .	279
A.6	Chapitre 6: Modélisation de multi-échelle à la pyrolyse du composite carbone/époxy . . . . .	281
A.7	Chapitre 7: Analyse de sensibilité . . . . .	283
A.8	Chapitre 8: Conclusion et perspective . . . . .	285

# List of figures

1.1	Fire hazard of timber structures and airplane carbon fiber composite . . . . .	3
2.1	Wood composite consisting of hemicellulose, cellulose, and lignin structure	15
2.2	Molecular linkage for thermoplastic and thermoset . . . . .	16
2.3	The pyrolysis process schematic in case of charring materials (wood) in fire conditions under bench-scale tests . . . . .	18
2.4	Schematic illustration of different zones for charring solid pyrolysis under 1D . . . . .	20
2.5	Porous char residue under heat flux condition for carbon/epoxy composite	22
2.6	Thermal delamination process of carbon fiber reinforced polymer (CFRP) composite during pyrolysis . . . . .	26
2.7	Macroscopic observation of thermal delamination of fiber laminated composite at different fire heat fluxes . . . . .	27
2.8	Microscopic observation of fire-damaged composite . . . . .	28
2.9	One-step global reaction scheme of wood thermal decomposition . . . . .	36
2.10	Multi-step reaction schemes of wood thermal decomposition . . . . .	36
2.11	Parallel reaction schemes of wood thermal decomposition . . . . .	37
2.12	One-step global reaction schemes of epoxy resin decomposition . . . . .	38
2.13	A multiple parallel reaction schemes of epoxy resin (polymer) thermal decomposition . . . . .	38
2.14	A two-step reaction scheme of epoxy resin thermal decomposition . . . . .	38
2.15	Chemical reaction/heat transfer map for biomass pyrolysis . . . . .	48

---

2.16	Experimental and model prediction of mass loss profile of three pseudo-components of wood pyrolysis . . . . .	50
2.17	Cone Calorimeter setups . . . . .	52
2.18	Heat transfer of the thermocouple junction in solid materials . . . . .	54
3.1	Principle of the averaging volume containing multiple solid phases and single gas phase . . . . .	61
3.2	Pyrolysis process assumptions with considered and neglected phenomena in this study . . . . .	75
4.1	TGA apparatus of Mettler-Toledo type . . . . .	79
4.2	Average experimental NML at 10 K/min of TGA experiment . . . . .	80
4.3	Average experimental NML at 50 K/min of TGA experiment . . . . .	81
4.4	Comparison of experimental NML under 10 K/min and 50 K/min . . . . .	81
4.5	Experimental MLR under 10 K/min and 50 K/min . . . . .	82
4.6	Experimental MLR under 10 K/min and 50 K/min . . . . .	82
4.7	Deviation of NML and NMLR between 10 K/min and 50 K/min . . . . .	84
4.8	Deconvolution of experimental NMLR at 10 K/min and 50 K/min (the solid line is 10 K/min, the dashed line is 50 K/min) . . . . .	85
4.9	One-step global reaction scheme of wood pyrolysis . . . . .	88
4.10	Four independent parallel reactions scheme of wood pyrolysis . . . . .	88
4.11	Experimental and optimized NML under different reaction schemes for 10 K/min . . . . .	89
4.12	Experimental and optimized MLR under different reaction schemes for 10 K/min . . . . .	90
4.13	Experimental and optimized NML under different reaction schemes for 50 K/min . . . . .	90
4.14	Experimental and optimized MLR under different reaction schemes for 50 K/min . . . . .	91

---

4.15	NML profile for wood components for 10 K/min (solid lines) and 50 K/min (dashed lines) . . . . .	93
4.16	MLR profile of wood components for 10 K/min (solid lines) and 50 K/min (dashed lines) . . . . .	94
4.17	NMLR profile of wood components for 10 K/min (solid lines) and 50 K/min (dashed lines) . . . . .	95
4.18	Optimized NMLR at 10 K/min (black solid line) and simulated at 10 K/min (black dashed line) with kinetic parameters optimized at 50 K/min (correspondingly for other two curves at 50 K/min) . . . . .	97
4.19	NMLR difference between optimization and simulation at 10 K/min (correspondingly at 50 K/min) . . . . .	98
4.20	Reaction rates of wood components at 10 K/min (optimized and simulated)	98
4.21	Reaction rates of wood components at 50 K/min (optimized and simulated)	99
4.22	The difference of each wood component reaction rate between optimized and simulated at 10 K/min . . . . .	99
4.23	The difference of each wood component reaction rate between optimized and simulated at 50 K/min . . . . .	100
4.24	Mass evolution for different mesh sizes and time steps . . . . .	102
4.25	MLR for 0D and 2D mesh at 10 K/min . . . . .	103
4.26	MLR for 0D and 2D mesh at 50 K/min . . . . .	103
4.27	Three characteristic time points for hemicellulose reaction rate . . . . .	104
4.28	Three characteristic time points for cellulose reaction rate . . . . .	105
4.29	Three characteristic time points for lignin reaction rate . . . . .	105
4.30	Reaction advancement of hemicellulose, cellulose, and lignin through the sample thickness at the different given characteristic time . . . . .	106
4.31	Normalized reactions rates of hemicellulose, cellulose, lignin through the sample thickness at the different given characteristic time . . . . .	107
4.32	Temperature difference for each reaction of hemicellulose, cellulose, lignin through the sample thickness at the different given characteristic time . . . . .	108

---

4.33	Heating rate for each reaction of hemicellulose, cellulose, lignin through the sample thickness at the different characteristic time . . . . .	109
5.1	CACC apparatus . . . . .	115
5.2	Monte-Carlo heat flux distribution at the top surface of axis-symmetry under 20 kW/m <sup>2</sup> . . . . .	116
5.3	Experimental sample holder of cylindrical silicate . . . . .	118
5.4	Thermal conductivity of porous silicate . . . . .	119
5.5	Specific heat capacity of porous silicate . . . . .	120
5.6	Schematic illustration of temperature measurement for wood pyrolysis .	121
5.7	Schematic of modeling configuration for wood under 1D and 2D axis-symmetry . . . . .	122
5.8	Schematic illustration of temperature measurement for the Al block sample . . . . .	124
5.9	Schematic of modeling configuration for Aluminum under 1D and 2D axis symmetry . . . . .	125
5.10	Temperature evolution between measured and model-predicted for Al heat conduction under 1D and 2D subjected to incident irradiance of heat flux of 20 kW/m <sup>2</sup> . . . . .	126
5.11	Experimental and predicted temperature evolution of wood pure heat conduction at different locations . . . . .	129
5.12	Comparison of wood thermal conductivity of reported and predicted values in this study . . . . .	131
5.13	Comparison of wood specific heat capacity of reported and predicted values in this study . . . . .	131
5.14	Temperature evolution of char pure conduction at different locations at the heat flux of 20 kW/m <sup>2</sup> . . . . .	133
5.15	Temperature evolution of char pure conduction at different locations at the heat flux of 50 kW/m <sup>2</sup> . . . . .	133
5.16	Comparison between predicted and reported char thermal conductivity	136

---

5.17	Comparison between predicted and reported char specific heat capacity	137
5.18	Mass loss for water evaporation of wet wood under 5 kW/m <sup>2</sup>	138
5.19	Mass loss rate for water evaporation of wet wood under 5 kW/m <sup>2</sup>	139
5.20	Temperature evolution at different locations for water evaporation of wet wood under 5 kW/m <sup>2</sup>	139
5.21	Water reaction rate with velocity arrows colored by pressure at three characteristic time points:500 s (a)	141
5.22	Water reaction rate with velocity arrows colored by pressure at three characteristic time points:1700 s (b)	141
5.23	Water reaction rate with velocity arrows colored by pressure at three characteristic time points:3500 s (c)	142
5.24	Experimental temperatures evolution for dry wood and wet wood at three locations	143
5.25	Experimental temperature differences between dry wood and wet wood at three locations	144
5.26	Predicted reaction rate of wet wood evaporation through the thickness	145
5.27	Predicted temperature evolution through the sample thickness for dry wood (dashed lines) and wet wood (solid lines) at three characteristic time points	145
5.28	Predicted temperature differences between dry wood and wet wood through the sample thickness at three characteristic time points	146
5.29	Heating rate profiles across the sample thickness for dry wood (dashed lines) and wet wood (solid lines) at three characteristic time points	146
5.30	Experimental heating rates for 20 kW/m <sup>2</sup> at three locations	149
5.31	Experimental heating rates for 50 kW/m <sup>2</sup> at three locations	149
5.32	Experimental and modeled total mass evolution for dry wood pyrolysis under 20 kW/m <sup>2</sup>	151
5.33	Influence of mesh size and time steps during simulation for 2D model at 20 kW/m <sup>2</sup>	152

---

5.34	Influence of mesh size and time steps during simulation for 2D model at 50 kW/m <sup>2</sup> . . . . .	152
5.35	Influence of mesh size and time steps during simulation for 1D model at 20 kW/m <sup>2</sup> . . . . .	153
5.36	Experimental and predicted mass loss profile for wet wood pyrolysis at the irradiant heat flux of 20 kW/m <sup>2</sup> . . . . .	154
5.37	Experimental and predicted mass loss rate for wet wood pyrolysis at the irradiant heat flux of 20 kW/m <sup>2</sup> . . . . .	155
5.38	Experimental and predicted temperature evolution for wet wood pyrolysis at the irradiant heat flux of 20 kW/m <sup>2</sup> . . . . .	155
5.39	Experimental and predicted mass loss profile for dry wood at the irradiant heat flux of 20 kW/m <sup>2</sup> . . . . .	156
5.40	Experimental and predicted mass loss rate for dry wood pyrolysis at the irradiant heat flux of 20 kW/m <sup>2</sup> . . . . .	156
5.41	Experimental and predicted temperature evolution for dry wood pyrolysis at the irradiant heat flux of 20 kW/m <sup>2</sup> . . . . .	157
5.42	Experimental and predicted mass loss for wet wood pyrolysis at the irradiant heat flux of 50 kW/m <sup>2</sup> . . . . .	160
5.43	Experimental and predicted mass loss rate for wet wood pyrolysis at the irradiant heat flux of 50 kW/m <sup>2</sup> . . . . .	160
5.44	Experimental and predicted temperature evolution for wet wood pyrolysis at the irradiant heat flux of 50 kW/m <sup>2</sup> . . . . .	161
5.45	Experimental and predicted mass loss rate for dry wood pyrolysis at the irradiant heat flux of 50 kW/m <sup>2</sup> . . . . .	161
5.46	Experimental and predicted mass loss rate for dry wood pyrolysis at the irradiant heat flux of 50 kW/m <sup>2</sup> . . . . .	162
5.47	Experimental and simulated temperature evolution for dry wood pyrolysis at the irradiant heat flux of 50 kW/m <sup>2</sup> . . . . .	162

---

5.48	Charring front propagation at different time (205 s, 605 s, 1005 s, 1805 s, and 2405 s) for wet wood pyrolysis under 20 kW/m <sup>2</sup> . . . . .	166
5.49	Comparison of measured and predicted char depth at different times for wet wood pyrolysis under 20 kW/m <sup>2</sup> . . . . .	167
5.50	Charring front propagation at different time (105 s, 405 s, 805 s, 1205 s, and 1405 s) for wet wood pyrolysis under 50 kW/m <sup>2</sup> . . . . .	168
5.51	Comparison of measured and predicted char depth at different times for wet wood pyrolysis under 50 kW/m <sup>2</sup> . . . . .	169
5.52	Total mass evolution for dry and wet wood pyrolysis cases at 20 kW/m <sup>2</sup> and 50 kW/m <sup>2</sup> . . . . .	170
5.53	Total Mass loss rate evolution for wet and dry wood pyrolysis cases at 20 kW/m <sup>2</sup> . . . . .	171
5.54	Total Mass loss rate evolution for wet and dry wood pyrolysis cases at 50 kW/m <sup>2</sup> . . . . .	172
5.55	Total reaction rates evolution for wet (dashed lines) and dry (solid lines) wood pyrolysis cases at 20 kW/m <sup>2</sup> . . . . .	172
5.56	Total reaction rates evolution for wet (dashed lines) and dry (solid lines) wood pyrolysis cases at 50 kW/m <sup>2</sup> . . . . .	173
5.57	Temperature evolution for dry (solid line) and wet (dashed lines) cases at 20 kW/m <sup>2</sup> . . . . .	174
5.58	Temperature evolution for dry (solid line) and wet (dashed lines) cases at 50 kW/m <sup>2</sup> . . . . .	175
5.59	Temperature difference between dry and wet cases for 20 kW/m <sup>2</sup> (solid line) and 50 kW/m <sup>2</sup> (dashed lines) . . . . .	175
5.60	Total pressure evolution for wet (dashed lines) and dry (solid lines) cases at 20 kW/m <sup>2</sup> and 50 kW/m <sup>2</sup> . . . . .	177
5.61	Pyrolysis and water evaporation front for dry (top slices) and wet case (bottom slices) at 20 kW/m <sup>2</sup> . . . . .	179

---

5.62	Pyrolysis and water evaporation front for dry (top slices) and wet case (bottom slices) at 50 kW/m <sup>2</sup> . . . . .	179
5.63	Reaction rates evolution across the sample thickness for three pyrolysis front locations for dry (solid lines) and wet (dashed lines) cases at 20 kW/m <sup>2</sup> (left plot) and 50 kW/m <sup>2</sup> (right plot) . . . . .	181
5.64	Heating rate evolution across the sample thickness for three pyrolysis front locations for dry (solid lines) and wet (dashed lines) cases at 20 kW/m <sup>2</sup> (left plot) and 50 kW/m <sup>2</sup> (right plot) . . . . .	181
5.65	Temperature evolution across the sample thickness for three pyrolysis front locations at 20 kW/m <sup>2</sup> (left plot) and 50 kW/m <sup>2</sup> (right plot) for dry (solid lines) and wet (dashed lines) cases . . . . .	182
6.1	Experimental heating rate evolution at middle locations during cone calorimeter tests under 20 kW/m <sup>2</sup> . . . . .	187
6.2	Experimental heating rate evolution at middle locations during cone calorimeter tests under 50 kW/m <sup>2</sup> . . . . .	187
6.3	Two parallel reactions scheme of epoxy resin thermal decomposition . .	188
6.4	Comparison for the measured and simulated mass loss under an inert atmosphere at 20 K/min in TGA . . . . .	189
6.5	Comparison for the measured and simulated mass loss under an inert atmosphere at 50 K/min in TGA . . . . .	189
6.6	Comparison for measured and simulated mass loss rate under an inert atmosphere at 50 K/min in TGA . . . . .	190
6.7	Schematic of experimental preparation of carbon/epoxy composite pyrolysis in cone calorimeter apparatus . . . . .	193
6.8	Specific heat capacity of carbon/epoxy composite from literature and in this study . . . . .	195
6.9	Specific heat capacity of carbon/epoxy composite char from literature and in this study . . . . .	195

---

6.10	Thermal conductivity at the in-plane direction of carbon/epoxy composite from literature and in this study . . . . .	196
6.11	Thermal conductivity at the through-thickness direction of carbon/epoxy composite from literature and in this study . . . . .	196
6.12	Thermal conductivity of carbon/epoxy composite char from literature and in this study . . . . .	197
6.13	Experimental and prediction of mass loss of carbon/epoxy composite pyrolysis at 20 kW/m <sup>2</sup> with 1D and 3D model . . . . .	198
6.14	Experimental and prediction of mass loss rate of carbon/epoxy composite pyrolysis at 20 kW/m <sup>2</sup> with 1D and 3D model . . . . .	198
6.15	Experimental and prediction of temperature evolutions of carbon/epoxy composite pyrolysis at 20 kW/m <sup>2</sup> with 1D and 3D model (Top location)	201
6.16	Experimental and prediction of temperature evolutions of carbon/epoxy composite pyrolysis at 20 kW/m <sup>2</sup> with 1D and 3D model (Middle location)	201
6.17	Experimental and prediction of temperature evolutions of carbon/epoxy composite pyrolysis at 20 kW/m <sup>2</sup> with 1D and 3D model (Bottom location)	202
6.18	Experimental and prediction of mass loss of carbon/epoxy composite pyrolysis at 50 kW/m <sup>2</sup> with 1D and 3D model . . . . .	203
6.19	Experimental and prediction of mass loss rate of carbon/epoxy composite pyrolysis at 50 kW/m <sup>2</sup> with 1D and 3D model . . . . .	203
6.20	Experimental and prediction of temperature evolution of carbon/epoxy composite pyrolysis at 50 kW/m <sup>2</sup> with 1D and 3D model (Middle location)	204
6.21	Experimental and prediction of temperature evolution of carbon/epoxy composite pyrolysis at 50 kW/m <sup>2</sup> with 1D and 3D model (Bottom location)	205
7.1	Influence of activation energy on the mass loss rate and temperature evolution at heat flux of 20 kW/m <sup>2</sup> . . . . .	213
7.2	Influence of activation energy on the mass loss rate and temperature evolution at heat flux of 50 kW/m <sup>2</sup> . . . . .	214

---

7.3	Influence of pre-exponential factor on the mass loss rate and temperature evolution at heat flux of 20 kW/m <sup>2</sup> . . . . .	215
7.4	Influence of pre-exponential factor on the mass loss rate and temperature evolution at heat flux of 50 kW/m <sup>2</sup> . . . . .	216
7.5	Influence of reaction order on the mass loss rate and temperature evolution at heat flux of 20 kW/m <sup>2</sup> . . . . .	217
7.6	Influence of reaction order on the mass loss rate and temperature evolution at heat flux of 50 kW/m <sup>2</sup> . . . . .	217
7.7	Influence of decomposition heat factor on the mass loss rate and temperature evolution at heat flux of 20 kW/m <sup>2</sup> . . . . .	219
7.8	Influence of decomposition heat factor on the mass loss rate and temperature evolution at heat flux of 50 kW/m <sup>2</sup> . . . . .	219
7.9	Influence of virgin thermal conductivity on the mass loss rate and temperature evolution at heat flux of 20 kW/m <sup>2</sup> . . . . .	223
7.10	Influence of virgin thermal conductivity on the mass loss rate and temperature evolution at heat flux of 50 kW/m <sup>2</sup> . . . . .	224
7.11	Influence of char thermal conductivity on the mass loss rate and temperature evolution at heat flux of 20 kW/m <sup>2</sup> . . . . .	225
7.12	Influence of char thermal conductivity on the mass loss rate and temperature evolution at heat flux of 50 kW/m <sup>2</sup> . . . . .	226
7.13	Influence of virgin specific heat capacity on the mass loss rate and temperature evolution at heat flux of 20 kW/m <sup>2</sup> . . . . .	227
7.14	Influence of virgin specific heat capacity on the mass loss rate and temperature evolution at heat flux of 50 kW/m <sup>2</sup> . . . . .	228
7.15	Influence of char specific heat capacity on the mass loss rate and temperature evolution at heat flux of 20 kW/m <sup>2</sup> . . . . .	228
7.16	Influence of char specific heat capacity on the mass loss rate and temperature evolution at heat flux of 50 kW/m <sup>2</sup> . . . . .	229

---

7.17 Influence of virgin permeability on the mass loss rate and temperature evolution at heat flux of 20 kW/m <sup>2</sup> . . . . .	231
7.18 Influence of virgin permeability on the mass loss rate and temperature evolution at heat flux of 50 kW/m <sup>2</sup> . . . . .	231
7.19 Influence of char permeability on the mass loss rate and temperature evolution at heat flux of 20 kW/m <sup>2</sup> . . . . .	232
7.20 Influence of char permeability on the mass loss rate and temperature evolution at heat flux of 50 kW/m <sup>2</sup> . . . . .	232
7.21 Influence of char emissivity on the mass loss rate and temperature evolution at heat flux of 20 kW/m <sup>2</sup> . . . . .	234
7.22 Influence of char emissivity on the mass loss rate and temperature evolution at heat flux of 50 kW/m <sup>2</sup> . . . . .	234
7.23 Influence of heat convection on the mass loss rate and temperature evolution at heat flux of 20 kW/m <sup>2</sup> . . . . .	236
7.24 Influence of heat convection on the mass loss rate and temperature evolution at heat flux of 50 kW/m <sup>2</sup> . . . . .	236
7.25 Influence of water content on the mass loss rate and temperature evolution at heat flux of 20 kW/m <sup>2</sup> . . . . .	238
7.26 Influence of water content on the mass loss rate and temperature evolution at heat flux of 50 kW/m <sup>2</sup> . . . . .	238



# List of tables

2.1	Different mass fraction of wood components . . . . .	14
2.2	The carbon/epoxy composite element analysis (dry basis) . . . . .	17
3.1	The description for the sub-components of wood . . . . .	62
3.2	The description for the sub-components of carbon/epoxy composite . . . . .	62
3.3	Pyrolysis parameters for each component in wood (estimated in this study) . . . . .	64
3.4	Pyrolysis parameters for each component in carbon/epoxy composite . . . . .	65
3.5	Pyrolysis reaction parameters for each component in wood . . . . .	66
3.6	Pyrolysis reaction parameters for each component in carbon/epoxy composite . . . . .	66
3.7	Simulation options involved in this study . . . . .	76
4.1	Optimized kinetic parameters with the one-step global reaction scheme . . . . .	88
4.2	Optimized kinetic parameters under independent parallel reaction scheme . . . . .	89
5.1	Thermal parameters of Aluminum block sample . . . . .	124
5.2	Pyrolysis front locations with different characteristic time for the 4 cases . . . . .	178
7.1	The variation range of kinetic and thermodynamic parameters for the sensitivity analysis . . . . .	213
7.2	The variation range of thermal and physical parameters for the sensitivity analysis . . . . .	223



# Nomenclature

## Roman Symbols

$\mathbf{K}$	permeability tensor
$\mathbf{k}$	thermal conductivity tensor
$\mathbf{V}$	gas velocity
$\mathbf{X}$	space variable
$\dot{m}_{pg}$	pyrolysis gas production rate
$\phi$	porosity
$\underline{\underline{\beta}}$	Klinkengerg tensor
$\zeta_{i,j,k}$	stoichiometric coefficient of gas element
$A$	Arrhenius pre-exponential factor
$A_k$	specific gas element
$c_p$	specific heat capacity
$E$	Arrhenius apparent activation energy
$e_t$	specific energy
$F_{i,j}$	mass fraction of subphase $j$ in solid phase $i$

$h$  specific enthalpy/heat convection coefficient

$M$  gas molecular weight

$m$  mass

$m_{i,j}$  Arrhenius reaction order

$n$  reaction order/variation order

$N_e$  number of gas element

$n_{i,j}$  Arrhenius temperature coefficient

$N_p$  number of solid phases

$p_g$  pressure

$P_{i,j}$  pyrolysis reaction of  $j$  in solid phase  $i$

$P_i$  number of subphase in solid phase  $i$

$R$  perfect gas constant number

$T$  temperature

$t$  time

$Y_i$  mass fraction of solid phase  $i$

### **Greek Symbols**

$\alpha$  conversion extent/absorptivity

$\chi_{i,j}$  pyrolysis reaction advancement of reaction  $j$  in solid phase  $i$

$\epsilon$  emissivity

$\epsilon_g$  volume fraction

---

$\mu$	dynamic gas viscosity
$\nu$	stoichiometric coefficients
$\pi_k$	pyrolysis production of gas element/species
$\psi$	genetic variable
$\rho$	density
$\sigma$	Stefan-Boltzmann constant
$\tau$	total advancement of pyrolysis
$\zeta$	mass stoichiometric coefficient
$p_i$	pyrolysis gas production rate

**Subscripts**

0	initial value
$\infty$	ambient
<i>bottom</i>	bottom surface
<i>c</i>	char/cellulose
<i>g</i>	gas phase
<i>h</i>	hemicellulose
<i>i</i>	solid phase <i>i</i>
<i>j</i>	subphase <i>j</i> in solid phase <i>i</i>
<i>l</i>	lignin
<i>middle</i>	middle surface

$pg$  pyrolysis gas

$s$  solid

$side$  side surface

$t$  solid and gas phase

$top$  top surface

$v$  virgin

### Other Symbols

$\dot{m}_g$  gas mass flux

$\phi(0)$  values at reference temperature

$\phi(T)$  values as function of temperature

$f(\alpha)$  conversion function

$k(T)$  reactionrate dependent on temperature

$k_c$  reaction rates of char

$k_g$  reaction rates of gas

$k_t$  reaction rates of tar

$Q_p$  endothermic heat of reaction

$T_r$  reference temperature

$\dot{q}_e''$  irradiant heat flux

### Acronyms / Abbreviations

0D Zero-dimensional

1D One-dimensional

2D Two-dimensional

3D Three-dimension

CACC Controlled Atmosphere Cone Calorimeter

CFD Computational Fluid Dynamics

CFRP Carbon Fiber Reinforced Polymer

DSC Differential scanning calorimetry

FDS Fire Dynamic Simulator

FPA Fire Propagation Apparatus

GA Genetic Algorithm

Gpyro General Pyrolysis Model

ML Mass Loss

MLR Mass Loss Rate

NML Normalized Mass Loss

NMLR Normalized Mass Loss Rate

PAN polyacrylonitrile

PATO Porous material Analysis Toolbox based on OpenFOAM

PICA Phenolic Impregnated Carbon Ablator

REV Representative Equivalent Volume

SCE Shuffled Complex Evolution

SHC Stochastic Hill Climbing

TGA Thermogravimetric Analysis

ThermaKin Thermal Kinetic Model of Burning

wt% mass fraction

# Chapter 1

## Introduction

### 1.1 Background and motivation

There are two major sets of fiber-reinforced composite materials, i.e. natural fiber and synthetic fiber ones [1]. Wood, which is a kind of biomass material, stands for the most commonly employed natural fiber composites which mainly comprise hemicellulose, cellulose, and lignin [2]. Wood is one of the most potential sustainable energy for heat or power through thermal conversion [3] as well as one of the commonly utilized building structure materials which are environmentally friendly and cost-effective [4].

Synthetic composite materials, which are a combination of some sub-components in different handling processes, have the potential to be one kind of the most influential materials used due to their large-scale different application field in the industry. For example, vehicles and the aerospace industry are employing many composite materials for their efficiency of lightweight accompanying advanced mechanical properties which involve the chief consideration [5–10]. Some applications also in fields such as high-pressure storage containers which care about the thermal resistance performance [11], while some others regard it as important for the cost-effective advantage when utilizing these composite materials [12].

Carbon fiber composites represent one of the widely employed synthetic fiber composites [13]. They tend to be the most successfully applied carbon fiber composites

that impregnate the carbon fiber with matrix epoxy resin polymers [7]. Carbon/epoxy composites belong to the thermal set polymer matrix materials and it behaves perfectly as a type of thermally insulating material due to its thermal and mechanical performance [14–19] as well as the light-weight capacity [20]. In addition to the excellent performance for thermal and mechanical properties, carbon fiber composites can be repaired quickly and efficiently in the aerospace industry [21].

However, both natural composite and synthetic materials possess a relatively high potential to induce fire which could produce a large amount of toxic gas and smoke [22]. In the high-pressure industry, the carbon/epoxy composites are employed largely for hydrogen storage tanks and it could have catastrophic fire and explosion events when the carbon/epoxy composite is damaged under external heat or mechanical source [23]. Also, the fire disaster ought to be taken into account seriously such as in the airplane industry which involves a large amount of carbon fiber composite utilization [21]. Wood pyrolysis and fire safety studies should also be continuously conducted in wildland fire as well as related fields such as wood thermal treatment and timber building fire [24]. Briefly, all these composite materials have high fire risk which can be seen in Figure 1.1, and fundamental thermophysical as well as chemical processes need to be studied largely and correspondingly [12, 25].

There are two main research fields concerning composite fire, one involves some fundamental experimental or theoretical study for the prediction and prevention of material flammability tendencies such as the fire-retardant research [28]. This concerns the reaction to fire. The other one is concentrated on fire resistance and concerns fire structure integrity study such as in infrastructure or transportation industry. Indeed, due to the fire influence on the composite structure as well as leading to serious casualties [29], the fire structure studies are partly conducted concerning the material response from fire heating and exposure time [30]. To conclude, many catastrophic fire events and risk tendencies involve carbon/epoxy composite and wood in our daily life or related industrial fields [31].



Fig. 1.1 Fire hazard of timber structures [26] and airplane carbon fiber composite [27]

These composite materials involve a similarity under fire conditions, remaining some amount of char residue, although this char could change differently when considering chemical or thermophysical structure. Due to this similarity of char residue formation, they are classified as charring materials. Indeed, unlike thermoplastic materials, charring materials could exhibit different layers including char and virgin layer separated by a chemical reaction layer [32]. This chemical reaction layer refers to the pyrolysis process leading to the gaseous volatiles release, and after the char formation, it can undergo oxidation [24].

Pyrolysis is the representation of molecular bond breakage while solid materials absorb thermal energy. During the pyrolysis process, some volatile gases produced migrate to the surface and could react with the atmospheric oxygen. If the conditions are adequate, this process gives rise to the material ignition. Thanks to the influence of the char layer on the thermal decomposition and the ignition processes, many studies have tried to modify the chemical structure to yield a larger fraction of char especially for fire-retardant research [33].

The fundamental phenomenon of the fire is the pyrolysis, then its modeling is an efficient way to assess the behaviors [29]. The pyrolysis modeling study is one important part as the supplementary approach to experimental work and detailed pyrolysis phenomenon implementation to predict the fire growth. The pyrolysis model has been widely utilized to obtain and to optimize the materials fire behavior, especially for the novel materials which are quite complicated and advanced [33, 34]. Besides, for the complex and expensive test to manipulate the pyrolysis process, pyrolysis modeling study has been widely performed to predict the thermal and chemical response of materials such as the mass loss profile and temperature evolution to gradually predict the ignition process [4, 35]. The pyrolysis model is then necessary and can be applied to better estimate the heat release rate, time to ignition, and flame spreading in a fire scenario [36]. Many numerical studies have been conducted for charring materials pyrolysis in addition to fire scenarios [37–44]. When developing pyrolysis models, it is reasonably efficient to integrate the chemical, heat, and mass transfer process into a robust model while having the capability to choose the corresponding boundary conditions, and it could promote the trend for interdisciplinary research.

For many pyrolysis models, the composite material is considered generally as a novel homogeneous structure [10] that involves individual thermal and physical properties consisting of different components. The thermal conductivity of substrate and char, which are crucial properties during the pyrolysis process, are normally treated as constant values across different directions although it behaves much differently in reality. Indeed, the carbon/epoxy composite accounts for the thermal conductivity variation of approximately 5-15 times the difference between in-plane and through-thickness direction [21, 45, 46]. To capture correctly the pyrolysis behavior of materials when under different heating scenarios, the numerical models employed need to describe in detail all physicochemical processes at all time and length scales. Indeed, heat and mass transfer processes should be described in the porous media. Some physical parameters such as thermal conductivity could be non-isotropic and have different values in the case of multiple condensed phases material type. In such a case, most of

the actual pyrolysis models such as those developed by [42, 43] solve one global energy conservation equation by dealing with average parameters estimated with all intrinsic ones for all condensed phases. This treatment of the material properties should be taken carefully because of the average estimation among quite different components which behave differently both in the chemical and physical aspect.

The matrix structure change during the pyrolysis process is still a challenge in modeling. Indeed, it could affect significantly the apparent parameters calculated. The porous media is also treated most of the time at the “Darcy scale” by using the concept of “Representative Equivalent Volume” (REV) [47–50] to define apparent properties from local ones by using upscaling techniques. But, when the structure of the porous media changes in time and space during the pyrolysis process, the upscaling techniques could be hard to derive. The homogeneous and heterogeneous reactions within pores or between gas and solid surface could affect the pyrolysis process.

In addition to the thermophysical parameters, the kinetic parameters are generally treated as generalized values under different TGA heating rates [51], which is acceptable due to the relatively small range of heating rates, considering thermal lag influence under high heating rates. However, it could behave differently under different heating rates due to the complexity of multiple and overlap kinetics of different components. For example, the difference of final char yield and porosity under different heating rates display that quite different kinetic processes take place. Thus, much attention should be taken when analyzing milligram-scale TGA tests and the bench-scale experiment such as cone calorimeter for its heating rate difference at different locations. Indeed, at the initial stage of the pyrolysis process in the cone calorimeter, the experiments conducted in our team show that the sample top surface heating rate could be much higher than that at the middle or bottom surface locations.

Many studies have been performed to explore the composite material pyrolysis behavior, such as TGA experiments for searching kinetics mechanisms, and the cone calorimeter employed to capture the 1D heat and mass transfer process [52]. However, many cone calorimeter experiments are conducted under ambient atmosphere to study

the combustion behavior and limited studies are found under anaerobic conditions. This is often the right choice when considering the practical fire scenario, but it could cause much uncertainty when performing pyrolysis model validation due to the perturbation of flame and char oxidation. Indeed, under an ambient atmosphere, the flame is controlled by the gas volatiles transportation generated by pyrolysis and the interaction with oxygen. However, the variation of gas volatile release rate and intensity is predominant during different stages of pyrolysis. Thus, it is crucial to eliminate these related uncertainties to maximize the prediction accuracy for pyrolysis model validation.

When modeling the pyrolysis process concerning some experiments such as cone calorimeter, it is usually assumed to have an empirical value of heat convection coefficient [53] which has a substantial effect on the pyrolysis rate and temperature evolution. Moreover, very few modeling studies consider the side and bottom surface boundary condition, an assumption of adiabatic or impenetrable is usually performed. This assumption could give us relatively agreeable results when compared with experimental data as cone calorimeter can be treated approximately as one-dimensional simulation cases [43] and the thermal insulation material at the bottom surface involves good quality [54, 55]. However, it could give us many errors during the model validation process especially under low heat flux where the corresponding results are seriously sensitive to the heat convection loss from side and bottom surface.

## 1.2 Research aim

The research aim of the present work is to develop a comprehensive pyrolysis model dealing with heat and mass transfers into porous media as well as chemical reactions involved at the same time.

Wood and carbon/epoxy composite material are chosen to develop a 3D model including non-isotropic physical parameters. The most important fire prediction parameters are concentrated including pyrolysis front, mass loss profile, and temperature

distribution at different in-depth locations. The three processes including heat, mass transfer, and chemical reactions involved are implemented over different time and length scales which mainly include milligram-scale TGA and bench-scale controlled atmosphere cone calorimeter tests. The different heating rates employed in the TGA test are extracted from corresponding cone calorimeter experiments to approach the real heating behavior. Thermal and boundary parameters are quite uncertain concerning different test configurations. Therefore, concentration is made to obtain the material properties exactly employed in this study. Under different fire scenarios, these processes could interact more or less strongly together. A focus is made on that to point out the different key parameters involved and investigate their role in these interactions.

### 1.3 Research methodology

This work focuses on the pyrolysis model validation and related work such as properties and parameters estimation. A new comprehensive pyrolysis model dealing with heat and mass transfer through porous media as well as chemical reactions is developed and proposed. As mentioned above, the process of heat transfer, mass transfer, and chemical thermal decomposition could interact through many time and length scales.

The solid combustion process is very complicated because it involves the initial pyrolysis of the condensed phase, the gas phase combustion, and the interaction between each one of those 2 phases. In consequence, since a comprehensive numerical model is usually impractical to characterize the combustion behavior for all phases, classically the gas and condensed phase are considered separately. Thus, the pyrolysis modeling in this study does not involve the combustion in the gas phase and char oxidation which contains much perturbation in the boundary. The thermophysical and chemical processes are focused in the condensed phase.

To characterize correctly each process and to validate them carefully, they are investigated one by one at separate scales in time and space. After capturing correctly

each one by the numerical model, the work is focused on interactions between them. Some regimes are identified when one of the processes governs the whole pyrolysis part. In such a case, the key parameters governing the overall pyrolysis are identified and analyzed by sensitivity analysis.

With respect to the thermally thin theory [38], the milligram-scale TGA experiment and model fitting method [56] are employed to obtain the exact kinetic parameters (i.e. activation energy, pre-exponential factor, reaction order) and the final char yield mass fraction under different heating rates. Two different sets of kinetic parameters are explored based on different reaction schemes of pyrolysis kinetics. Then, the exact kinetic parameters and final char yield mass fraction are regarded as input parameters when analyzing the heat and mass transfer process in bench-scale experiments. At this “TGA scale”, the physical space is ignored because of the study of a very thin sample. The assumption of a 0D thermal decomposition is made even though in reality, some scalar gradients remain, this point is discussed. Thus, only the chemistry part is investigated through different time scales. The heating rates in TGA involve the specimen heating rate at the middle location in bench-scale cone calorimeter experiment under different heat fluxes.

Controlled Atmosphere Cone Calorimeter (CACC) experiments are conducted to obtain the mass loss rate and the temperature gradient evolution at different locations. Mass loss rate, temperature evolution, and pyrolysis front are employed to validate the model and to gain the knowledge of pyrolysis development in detail. Two different charring materials under different heat flux are considered to study the generality application of the model: Fir wood and carbon fiber/epoxy composite. The unknown thermophysical properties such as the specific heat capacity, thermal conductivity, and the boundary heat convection coefficients are predicted using the inverse modeling method. Lastly, the different sensitivity analyses of parameters are performed to characterize the model uncertainty. At the “cone calorimeter scale”, the heat transfer, mass transfer, and chemical reactions evolve simultaneously. Different conditions of heating are investigated to vary the intensity and interactions between those processes

to investigate the role of each process. Modeling have been conducted on the two materials in 1D and 2D. Firstly, a specific effort has been kept on the description of the wood pyrolysis at TGA and cone calorimeter scale. Specific attention has been focused on the humidity influence and on the heat and mass transfer into the wood sample during its thermal decomposition. Secondly, the model approach developed has been applied to the carbon fiber/epoxy resin composite.

## 1.4 Thesis outline

Chapter 2 is dedicated to the literature review in the context of the subject of the thesis. Detailed materials information is introduced concerning wood and carbon fiber/epoxy composite in order to have a broad knowledge about their chemical and physical properties. The pyrolysis process specifically involved in the fire scenario is discussed including chemical kinetics, heat transfer, and gas transportation, as well as related boundary conditions and structure change induced. Lastly, the mostly employed pyrolysis models in the fire community are introduced. The simple and comprehensive pyrolysis models are compared. Different assumptions during pyrolysis processes including chemical, heat transfer, and mass transfer process are discussed and the evaluation for different pyrolysis models are given. The process of input parameters for model implementation is introduced and some evaluations are made.

Chapter 3 permits to present PATO pyrolysis model. Based on OpenFOAM, it incorporates complete chemical and thermophysical mechanisms in the condensed phase. The model assumption concerning volume averaging theory is introduced. Mass, momentum, and energy conservation equations are presented and the parameters involved to describe the pyrolysis kinetics concerning wood and carbon/epoxy composite are illustrated. The model assumptions and simulation options to perform the corresponding equations employed in this study are given.

Chapter 4 concerns the particle scale modeling work for wood pyrolysis. The kinetics analysis based on the TGA experiment is presented coupling with the op-

timization method to obtain corresponding parameters. Different heating rates are involved which are linked to the cone calorimeter experiments at different heat fluxes presented in Chapter 5. Their corresponding parameters obtained by one-step global and independent parallel reaction schemes are evaluated. The verification process is conducted employing kinetic parameters to predict the pyrolysis behavior under the other heating rate. The influence of heating rates on the reaction of each component is studied. The TGA simulations concerning the 2D model are made and the influence of thermal gradients is analyzed.

Chapter 5 focuses on the cone calorimeter experimentation and its modeling study concerning wood pyrolysis. Different input parameters are estimated firstly by the inverse analysis which includes heat convection coefficient, specific heat capacity and thermal conductivity of wood, specific heat capacity and thermal conductivity of char. The dried wood sample based on cone heating is obtained and the model predicted water evaporation process is validated against the experimental data. The evaporation process at different time and length scales is analyzed. Then, the pyrolysis cases concerning the wet wood and dry wood are studied at different heat fluxes. The experimental data concerning the mass, temperature, and char front are analyzed against the predicted data. The water influence and the reaction interaction during the pyrolysis process at different heat fluxes are discussed.

The multi-scale model validation work for carbon /epoxy composite pyrolysis is addressed in Chapter 6. Similar to the wood kinetic analysis, different heating rates are estimated which are linked to the cone calorimeter test. The kinetic parameters are extracted to predict the experimental curve and some discussions are made. The bench-scale test in cone calorimeter is made and the model prediction process is performed. The anisotropic properties concerning thermal conductivity under 3D are checked and the interaction within the pyrolysis process is compared with 1D. The model validation process under different heat fluxes is conducted and the corresponding analysis is performed.

Chapter 7 permits the sensitivity analysis of the wood pyrolysis process at a bench scale. The sensitivity of mass loss rate and temperature evolutions at different in-depth locations and different heat fluxes are analyzed concerning different uncertain parameters. These uncertain parameters involve chemical, heat of decomposition, thermal, and physical properties. The sensitivity analysis is conducted at different time and length scales. Some suggestions concerning the parameters preparation are made for modeling work in the future.

Lastly, the main conclusions extracted from this work are presented and some suggestions for modeling work based on this study are given to supplement and achieve in the future.



# Chapter 2

## Literature review

### 2.1 Composite materials: general background

This part presents a broad range of knowledge related to the two charring composite materials studied, i.e. wood and carbon/epoxy composite, in particular their different characteristics of components. Then the pyrolysis phenomenon is introduced in the fire scenario, and the pyrolysis modeling studies are reviewed.

Many charring composite materials could be viewed of interest. The motivation to select wood and carbon/epoxy composite as our objective is that their differences during the pyrolysis process tend to stand for two important categories: materials of surface shrinkage or swelling, and also homogeneous or heterogeneous assumption. Despite the presence of cracks at surface or interior sites, the thermal delamination of carbon/epoxy composite could take place in the virgin layer during the pyrolysis process due to the gas pressure and the bond interaction between carbon fiber and epoxy matrix. Moreover, the thermal conductivity of wood is treated as homogeneous for most studies due to the relatively minor difference of longitudinal and radial direction [57–59]. While for carbon/epoxy composite, the thermal conductivities could exhibit much differently under in-plane and through-thickness direction [45, 46]. For pyrolysis modeling work, these involved differences should be put much emphasis to validate the model. Another consideration is that the post-fire structure difference, the char structures of wood and

Table 2.1 Different mass fraction of wood components [62, 63]

Wood type	Lignin	Cellulose	Hemicellulose	Extractives	Ref.
Silver birch	0.22	0.41	0.30	0.032	[62]
American beech	0.22	0.48	0.28	0.02	[62]
Average Hardwood	0.20-0.22	0.40-0.42	0.33-0.35	0.02-0.03	[63]
Scandinavian spruce	0.29	0.43	0.27	0.018	[62]
Scandinavian pine	0.29	0.44	0.26	0.053	[62]
Douglas fir	0.29	0.39	0.23	0.053	[62]
Scots pine	0.28	0.40	0.25	0.035	[62]
Average Softwood	0.27-0.28	0.40-0.43	0.21-0.23	0.03-0.05	[63]

carbon/epoxy composite have their intrinsic behavior and should be studied differently despite its irrelevance to this study.

Wood, which is one type of lignocellulosic biomass, is treated as a polymer-based composite formed naturally and its main components are hemicellulose, cellulose, and lignin [2]. Hemicellulose and cellulose are chemically treated as carbohydrate macromolecules while lignin is treated as a cross-linked phenolic polymer [58]. It should be highlighted that there still exist some amounts of extractives and inorganic ashes, which are usually negligible due to their low content (approximately 10% by mass fraction [2]). However, these extractives may impose a catalytic effect during the pyrolysis process, and commonly, this mass fraction is added to hemicellulose [60]. The “pseudo-components” are often employed when predicting the components pyrolysis for hemicellulose, cellulose, and lignin [61].

Wood is classified into softwood and hardwood for the chemical composition difference, for example, softwood comprises much more mass fraction of cellulose and lignin than that of hardwood, and their hemicellulose chemical compound types are also different [60]. As shown in table 2.1 with the different mass fractions of these correspondent components for softwood and hardwood [58].

Figure 2.1 shows the three components distribution inside the lignocellulose plant cells structure [2]. In this porous structure, the cellulose can be assumed as the main fiber perform which is surrounded by matrix hemicellulose and lignin.

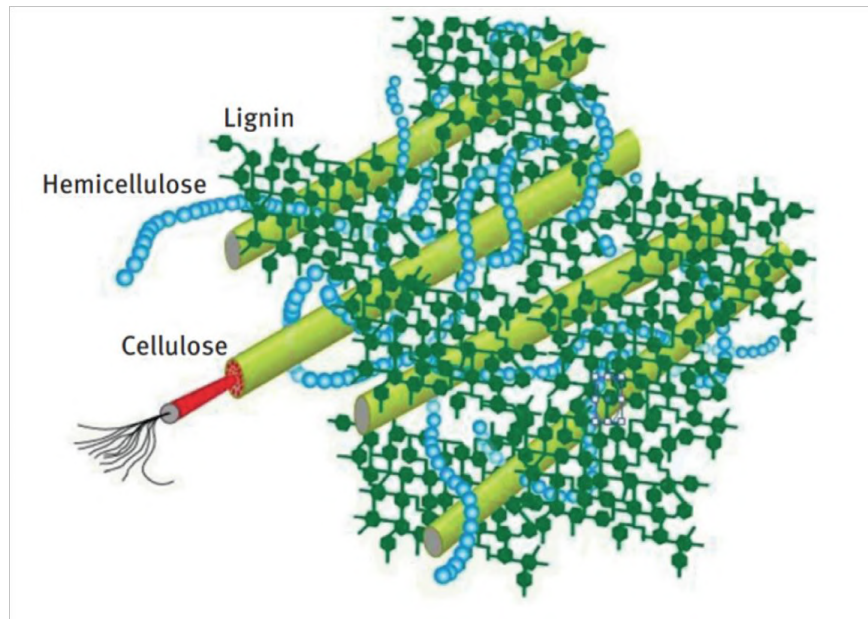


Fig. 2.1 Wood composite consisting of hemicellulose, cellulose, and lignin structure (extracted from [2])

Wood is most commonly treated as a homogeneous material although its intrinsic properties are anisotropic [64], as it is limited to characterize the complex interior structure and the thermal conductivity across the longitudinal is approximately two times larger than that of the radial and tangential direction, thus it is reasonably correct to be modeled under 1D [61, 65]. And in some cases, the thermal conductivity is estimated as the average value among different directions [66].

Another substitute inside wood involves the water which exhibits three types, i.e. bound water, liquid-free water, and water vapor [58]. Bound water is chemically bonded with the form of  $-OH$  groups within the skeleton, and the free water is retained through capillary forces [58]. The  $-OH$  groups may be present with more mass fraction in hemicellulose and cellulose than those in lignin [37, 58]. Usually, the free water is treated as bound water until the water mass fraction is higher than that in the fiber saturation point which occupies nearly 30 wt% of overall weight at ambient temperature [8, 64, 67]. It should be noted that the water content of wood specimens used for a laboratory test is usually around 10 wt% [67], which demonstrates that

these amounts of free water pertain to the bound water. When heated, the bound water diffuse to liquid-free water, then free water is evaporated to water vapor moving outwards [68]. However, with the presence of the chemical linkage for bound water within the wood skeleton, much more energy is needed compared with liquid water for its two stages transformation [64]. Indeed, the vaporization latent heat is generally required from liquid water to water vapor, while the desorption heat is added to bound water to evaporate [64].

The majorities of carbon fiber composites used have different types of fiber and matrix, also with different combination structures such as fiber layer direction. We focus here on the laminate carbon fiber polymer matrix composite. For synthetic polymer matrix, there are two sets including thermosets such as epoxy, and thermoplastics such as polyimide [69]. When heated, the thermoplastic can melt in contrast to the thermoset polymer leaving carbonaceous residue due to its cross-linked stable structure [11]. Figure 2.2 shows the molecular linkage difference for the thermoset and thermoplastic [16].

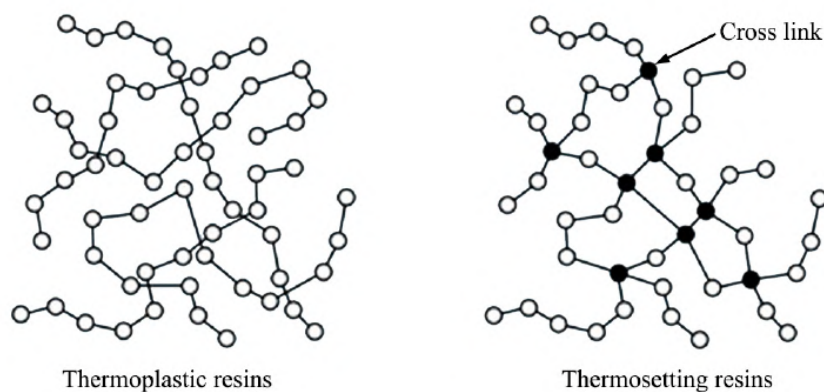


Fig. 2.2 Molecular linkage for thermoplastic and thermoset [16]

Owing to the performance of enduring capacity with relatively high temperature and pressure, carbon fiber thermoset composites, especially carbon/epoxy composites, have been largely exploited in different application fields [5–9, 11, 12]. The epoxy resin involves a glass transition temperature and, over this temperature, its structure main-

Table 2.2 The carbon/epoxy composite element analysis (dry basis) [23]

Elements	wt(%)
N	3.28
C	88.01
H	18.847
S	0.082
O	6.781

taining capability significantly changes [70]. The element analysis of the carbon/epoxy composite is shown in Table 2.2 [23].

Due to the different characteristics of carbon fiber and epoxy resin, it is observed that the thermal conductivity for longitudinal (parallel to carbon fiber) and transverse (perpendicular to carbon fiber) could behave with many differences [71]. In some literature, the term in-plane direction refers to the direction parallel to the fiber, while the through-thickness direction represents the perpendicular direction [19, 72]. The constituents for carbon/epoxy composite impose different mechanical, physical, and chemical properties. For example, in the direction parallel to carbon fiber, it involves good mechanical performance than that in the perpendicular direction. The combination of these two constituents makes it much more advanced than the original ones, and carbon fiber usually acts as the reinforcement with the epoxy resin to maintain the structure [16].

Due to the carbon/epoxy composite anisotropic thermal conductivity induced by carbon fiber, the length, and diameter, also the specific surface of carbon fiber plays the predominant role [14]. Carbon fiber consists of more than 90 wt% of carbon which is commonly constituted by polyacrylonitrile (PAN) treated under rigorous heat and mechanical conditions [16]. The diameter of the carbon fiber is nearly 3-5  $\mu\text{m}$  [16]. The characteristic of PAN fibers is quite physically stable for its graphite composition and the composite thermal resistance can be reduced when increasing carbon fiber mass fraction [71]. The water content in the polymer matrix is normally less than 1 wt%, thus it is reasonably correct to neglect the water effect inside the carbon/epoxy composite [68].

## 2.2 Pyrolysis phenomenon in the fire scenario

A charring layer of transient evolution is formed under the pyrolysis process, which is the main distinguishing feature for charring materials. The term pyrolysis refers to the reaction processes under which the micro material structure can thermally decompose, i.e. the chemical bond breaks among a group of complex molecular structures, releasing a large amount of gas volatiles [4]. The pyrolysis process schematic in case of charring materials (wood) in fire conditions can be seen in Figure 2.3 under bench-scale tests. In the following parts, some preliminary descriptions are presented regarding the pyrolysis process and modeling research in the case of the fire scenario.

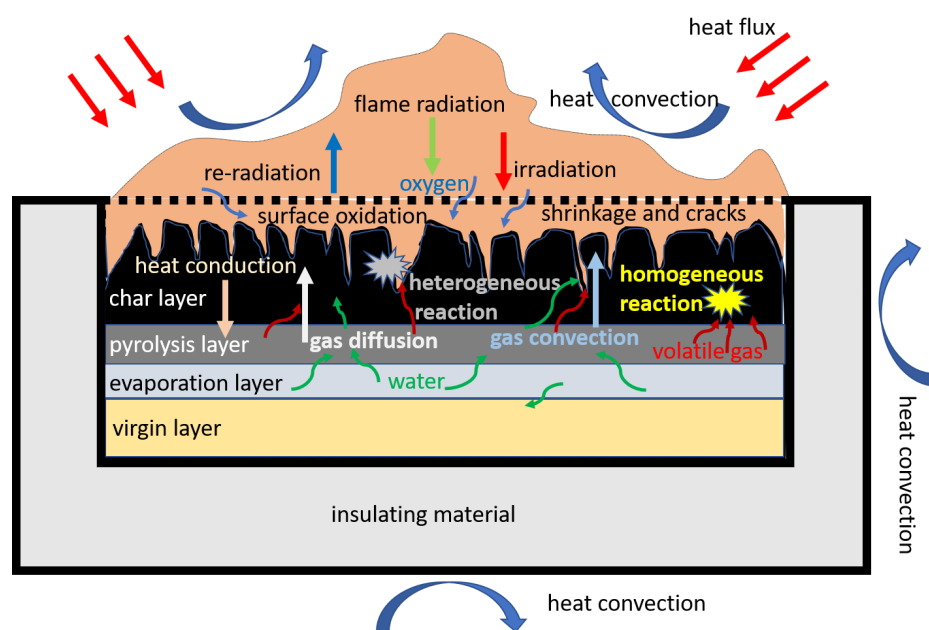


Fig. 2.3 The pyrolysis process schematic in case of charring materials (wood) in fire conditions under bench-scale tests

### 2.2.1 Pyrolysis process description

Due to the high susceptibility of several phenomena to the pyrolysis process, a comprehensive pyrolysis modeling study should be given more attention. This

part presents a detailed pyrolysis process (without oxidation) for charring composite materials concerning wood and carbon/epoxy composite pyrolysis, and their similarities and differences will be summarized. Different factors influencing the pyrolysis process are also reviewed. The pyrolysis modeling background and development are presented. Several assumption considerations of comprehensive pyrolysis models are evaluated, which focus on the kinetic reactions, heat and mass transfer, the boundary condition, and the physical structure change. Then, the four principal pyrolysis models in the fire community are described and evaluated: pyrolysis parts of FDS, FireFOAM, ThermaKin, and Gpyro.

The complex pyrolysis process of charring materials involves physical, chemical, and thermal phenomenon, such as heterogeneous or homogeneous reactions, different forms of heat transfer, complicated decomposition kinetics, internal pressure accumulation, gas and species transport, moisture evaporation within the wood, the heat of decomposition, material structure shrinkage and swelling, and overall material properties change at different pyrolysis stages, etc [65]. The following parts will present the macroscopic observation, heat, and mass transfer aspects, chemical reaction parts, and physical structure change aspects during the pyrolysis process. Due to the high similarity of the pyrolysis process in the fire scenario, they are integrated as one while the different features are reviewed. Some differences concerning chemical reaction can be viewed for wood and carbon/epoxy composite. For the heating up process of carbon/epoxy composite, this material firstly attains the glass transition temperature before pyrolysis chemical reactions take place [73]. Another very important difference is the water influence. It deserves much attention for wood, while the water influence on carbon/epoxy composite is quite minor and can be neglected [32].

### **2.2.1.1 Macroscopic observation of pyrolysis of composite materials**

From a macroscopic view, there exist four layers within charring material pyrolysis which involve char layer, thermal decomposition layer, evaporation layer, and virgin layer [61], and sometimes the dried material layer is also included, as for wood. As

aforementioned, there is a very less amount of water inside the carbon/epoxy composite, thus the evaporation and dried layer could be neglected. The char front is separated by char zone and pyrolysis zone, and it is believed at the temperature of approximately 573 K [74]. It should be noted that this separation of char and pyrolysis layer due to the visibility is not scientifically accurate. Because the pyrolysis reaction is not infinitely fast and some fractions of the pyrolysis zone are inside the so-called visible char layer. When describing the pyrolysis process, the one-dimensional assumption is usually taken to simplify the boundary influence from different sides and to focus on the intrinsic thermophysical and chemical response. Figure 2.4 is a schematic representation of a pyrolyzed charring solid with the different zones under 1D [75]. It includes char, pyrolysis, and virgin zones, and the heat flow is from irradiant heat flux, convection, and heat radiation loss. The pyrolysis front here is at the approximate middle location of the pyrolysis zone and it involves the maximum chemical reaction rate. Thus, the charring depth and corresponding charring rate prediction for wood pyrolysis should be performed cautiously especially for precise analysis.

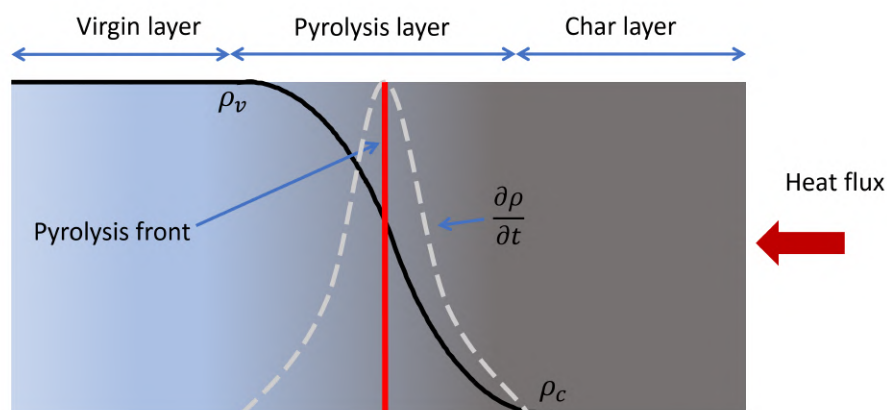


Fig. 2.4 Schematic illustration of different zones for charring solid pyrolysis under 1D (adapted from [74])

### 2.2.1.2 Heat and mass transfer aspect

For the heat boundary in the fire scenario, it can be from thermal radiation, thermal convection, and heat conduction. The most common fire heating scenario is under thermal radiation and convection from the outer heat source, and the material surface will absorb heat and conduct the heat to the interior condensed phase when heated [65, 76]. This behavior of heat absorption depends on the heat source, material surface physical properties such as optical properties, the atmosphere flow condition, etc. For example, some materials are treated as semi-transparent material, the in-depth radiation needs to be seriously considered for accuracy [4]. But for the charring materials in the fire community, they are usually treated as opaque materials without in-depth radiation absorption [77].

In the initial stage of the pyrolysis process inside the condensed phase, the material temperature increases by heat transfer, which is characterized by thermal diffusivity [78]. Due to the quasi-homogeneous properties of wood, the difference of thermal strain for each direction is relatively small [57–59]. However, the thermal strain at a different location can be varied seriously for the anisotropic carbon/epoxy composite [45, 46]. This behavior can affect the thermal response in the condensed phase. The heat absorbed at the surface is not only transferred to the interior sites by heat conduction, but also by heat radiation inside the pores [4]. This radiative heat is more predominant near the surface of high temperature due to the high radiation dependency on temperature [79]. Moreover, this phenomenon can be more important when the fully developed char is present with larger porosity [32]. This char layer formation plays a dominant role in thermal insulation behaving as a heat barrier. Figure 2.5 shows the porous char residue under heat flux conditions for carbon/epoxy composite [80]. Thus, it could influence the mass loss rate and temperature evolutions [81, 82]. Indeed, the char formation has a chemical and physical influence on the pyrolysis process. Chemically, it can undergo heterogeneous reactions to absorb or release heat, thus affecting the pyrolysis reaction. Physically, it acts as the porous thermal barrier to limit the heat and mass transfers, thus the more mass fraction of char produced, the

stronger the material's tendency to be thermal resistant. It is one of the most important exploring directions for retardant-flame materials [11, 82]. Many studies consider the thermal conductivity in the condensed phase as effective thermal conductivity [83]. The thermophysical parameters, especially the specific heat capacity and thermal conductivity, are highly temperature-dependent [4]. For example, these values could increase several times larger over different pyrolysis temperature ranges [46].

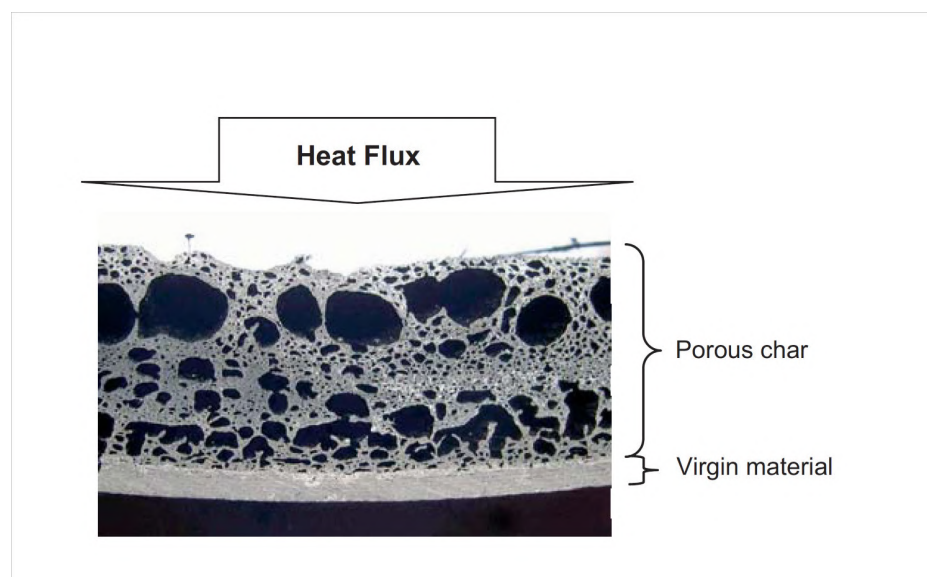


Fig. 2.5 Porous char residue under heat flux condition for carbon/epoxy composite [80]

For the detailed heat transfer inside the material pores, the thermal convection between the gas and solid could behave much more heavily than gas species heat diffusion due to the high pressure and velocity [37]. The thermal convection could be more prominent at the surface layer due to the larger difference between relatively cooler gas and hotter solid [18]. Specifically for the water inside the pores under heating conditions, the bound water diffuse and the liquid water evaporates to vapor [61]. The water vapor under high heat flux can be much earlier to move out to the surface in comparison with that under low heat flux or for thick materials, thus, the water vapor cooling effect can last longer under low heat flux [83].

The gas species including water vapor can migrate outward to the hot char surface or inward to the cool virgin region such as the water condensation due to

the accumulated gas volume pressure. However, a very limited amount of gas species move inward to the interior sites due to the much larger permeability in the char layer compared with those in the virgin layer [61, 66]. These gas species can be transported by convection and species diffusion, and the gas flow could behave differently at a different location due to the difference of species intensity, species categories, gas pressure, the porosity of the condensed matrix, etc [37]. It should be highlighted that the gas blowing effect at the surface could happen and influences the boundary thermal radiation and convection transfer to the condensed phase. However, due to the relatively medium heat flux under ambient pressure which is controlled by boundary heat radiation [58], the gas species velocity at the surface is not very high and this effect is usually neglected.

### 2.2.1.3 Chemical reaction aspect

When the temperature attains the threshold of the heat of thermal decomposition, the chemical reactions take place and different gas volatiles are released due to the micro molecular bond breakage [84]. For wood and carbon/epoxy composite, the reaction form could be quite different due to their different chemical structures.

The chemical reactions are finite and experience over different ranges of temperature, which lead to the decreasing of material density, releasing of gas species, and forming of some portions of carbonaceous residue involving very high porosity [84]. For example, the temperature ranges for the thermal decomposition of wood components are estimated as: hemicellulose 200-260 °C, cellulose 240-350 °C, and lignin 280-500 °C [65]. It is predicted that lignin yields more char fraction than that of hemicellulose and cellulose [66]. It is generally also believed that wood pyrolysis can produce the final char yield with approximately 20 wt% [58]. Char formation and its properties are governed by many parameters such as interior pressure and temperature, which also depend on gas species imposing high reaction tendency within char [84]. The reaction is controlled by kinetics under low temperature and is governed by heat and mass transfers under high temperature [58]. It should be highlighted that this char layer

has heavy internal heterogeneity as discussed previously although it exhibits visibly some black residue. When the gas species flow through the surface char layer, the homogeneous and heterogeneous reactions among the char and gas species may take place under high temperature and longer residence time. Thus, these reactions could affect the final char residue yield [85], the total mass loss rate, and the temperature development in the condensed phase. The majorities of permanent gases are CO, CO<sub>2</sub>, CH<sub>4</sub>, H<sub>2</sub>, and N<sub>2</sub> [37]. In the fire safety community, the heat of pyrolysis for the three components are normally treated as endothermic, while the detailed study shows that they can also be exothermic [65]. Indeed, different intrinsic structures of materials and different heat fluxes can lead to highly diversified char residue, and its related parameters such as porosity and permeability should be obtained by corresponding experiments under specific conditions. Wood and char thermal conductivity are normally considered homogeneous [86]. During the advancement of the pyrolysis process, the density at the material's surface decreases fast to a constant char density which accounts for the termination of the pyrolysis process at the surface.

The pyrolysis of carbon fiber/epoxy composite mainly occurs at the range from 550 K to 750 K and the average value of final char residue consists of 72.4% [23]. It is found that the released gas species in the carbon/epoxy composites and pure epoxy resin are quite similar during the pyrolysis process and the carbon fiber mass fraction loss is approximately 0.8% from 573 K to 773 K [23]. Due to the high thermal stability of carbon fiber in an inert atmosphere and relatively medium temperature, it is estimated that carbon fiber does not involve in the pyrolysis reaction [87]. However, these carbon fibers could influence deeply the thermal response and chemical reaction of the resin matrix [84].

#### **2.2.1.4 Physical structure change**

For the physical structure change during the composite pyrolysis process, the more concentration is made for carbon/epoxy composite, as its structure change is more complex than wood.

During the pyrolysis process of wood, the whole structure can shrink due to gas volatile molecules escape which can't support the skeleton structure integrity [83]. It forms a new porous char structure which can crack induced mainly by thermal strain at different levels randomly. The extent of shrinkage for the surface char layer is higher than that in the virgin layer due to its heavy structure change. It should be mentioned that the char layer may also swell for wood under high heat flux [58]. Thus, it shows the similar behavior of carbon/epoxy composite in the description following. The swelling takes place for that a large number of gas species could be trapped inside the fragile elastic char pore layer under high pressure and the swelling could be caused by cracks. The wood shrinkage extent is smaller in the longitudinal direction, while heavier in the radial and tangential direction [37]. The shrinkage also happens during the drying process but it is not much prominent compared with that in the pyrolysis process [58]. The shrinkage during drying is mainly induced by bound water diffusion and free water evaporation and a recovered structure can be present when it absorbs moisture [58].

Carbon/epoxy composite pyrolysis can lead to structural damage including thermal delamination, cracks in the char layer, and the fiber and matrix interface debonding [88, 89]. These physical phenomena are quite hard to predict numerically. In the virgin layer, the delamination and cracks can also take place, mainly due to the cohesion capacity diminution between fiber and resin, also among the interfacial plies [20, 29, 90]. Figure 2.6 [41] shows the thermal delamination process due to the internal gas pressure increase by gas accumulation which can't migrate quickly outwards due to some resistance and long residence time. When this pressure strength surpasses the material structure strain, delamination and cracks could occur [41]. A swelling ratio of 2.2 is found by some experiments based on the thickness variation of carbon/epoxy composite during pyrolysis [8].

The thermal delamination and cracks are influenced by the coupling of thermal and mechanical loadings, which are non-linear problems hard to characterize even under the same operation conditions [89]. The macroscopic observations of thermal delamination

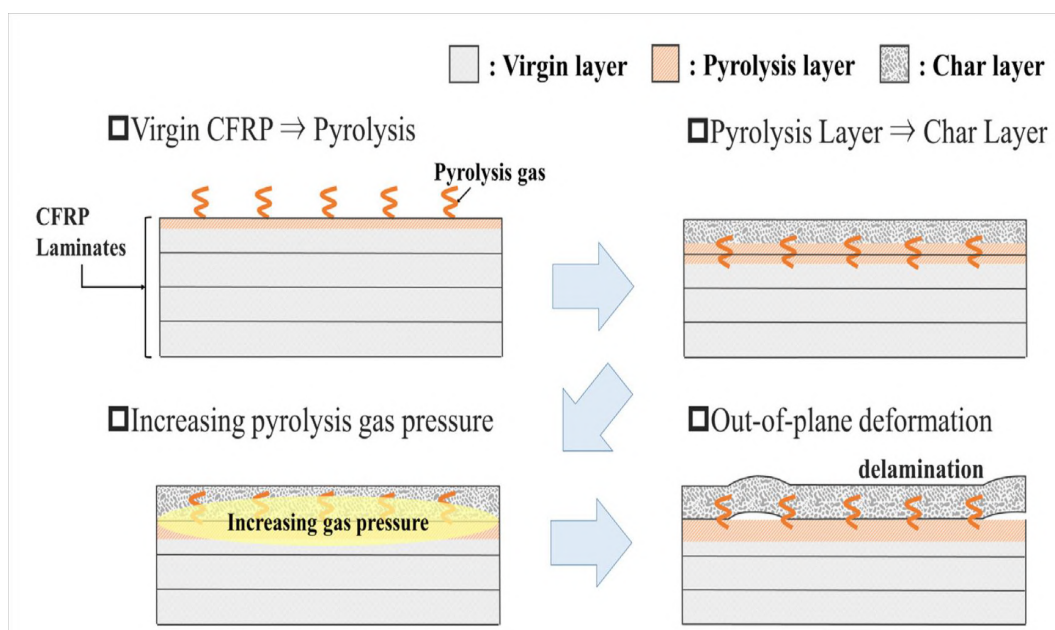


Fig. 2.6 Thermal delamination process of carbon fiber reinforced polymer (CFRP) composite during pyrolysis [41]

of different heat fluxes from  $20 \text{ kW/m}^2$  to  $50 \text{ kW/m}^2$  are conducted, as shown in Figure 2.7 [30]. More obvious delamination and cracks can present in the char layer than that in the virgin layer, which shows that the thermal and mechanical influences are higher in the char layer. Figure 2.8 illustrates the microscopic cross-sectional view of the fire-damaged composite laminate [29].

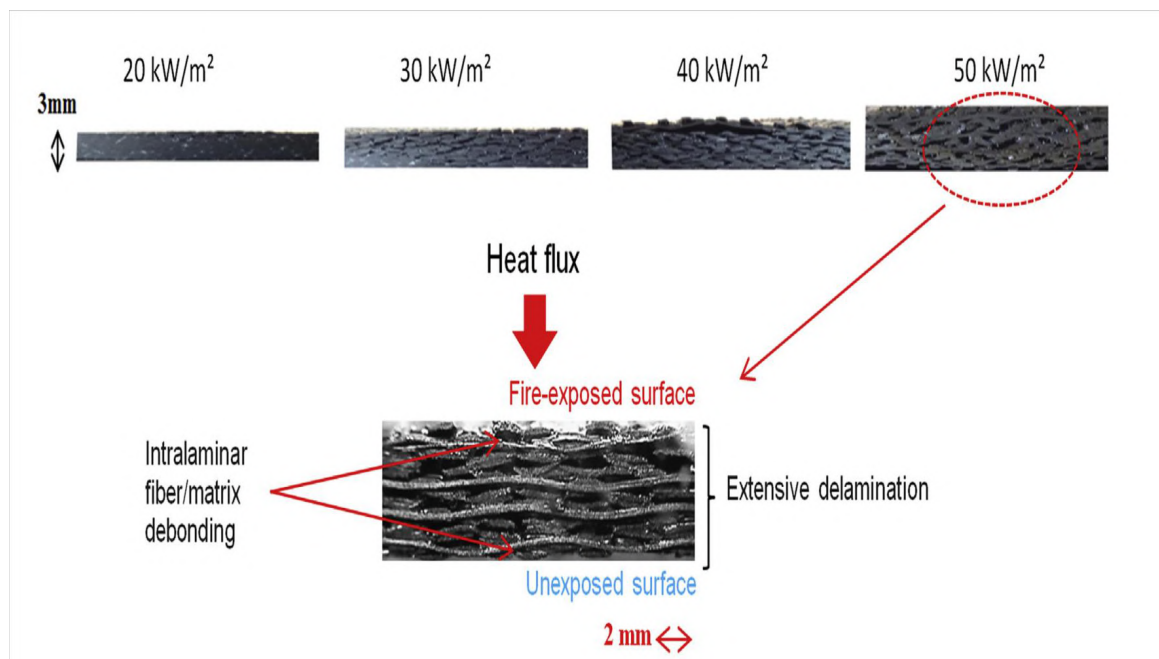


Fig. 2.7 Macroscopic observation of thermal delamination of fiber laminated composite at different fire heat fluxes [30]

All these physical structure changes in the virgin and char layer, including thermal delamination, cracks, shrinkage, and swelling, can influence strongly the pyrolysis process including heat and mass transfers [66, 74, 84]. For example, the shrinkage effects can lead to lower heat flux absorption from the ambient environment and the

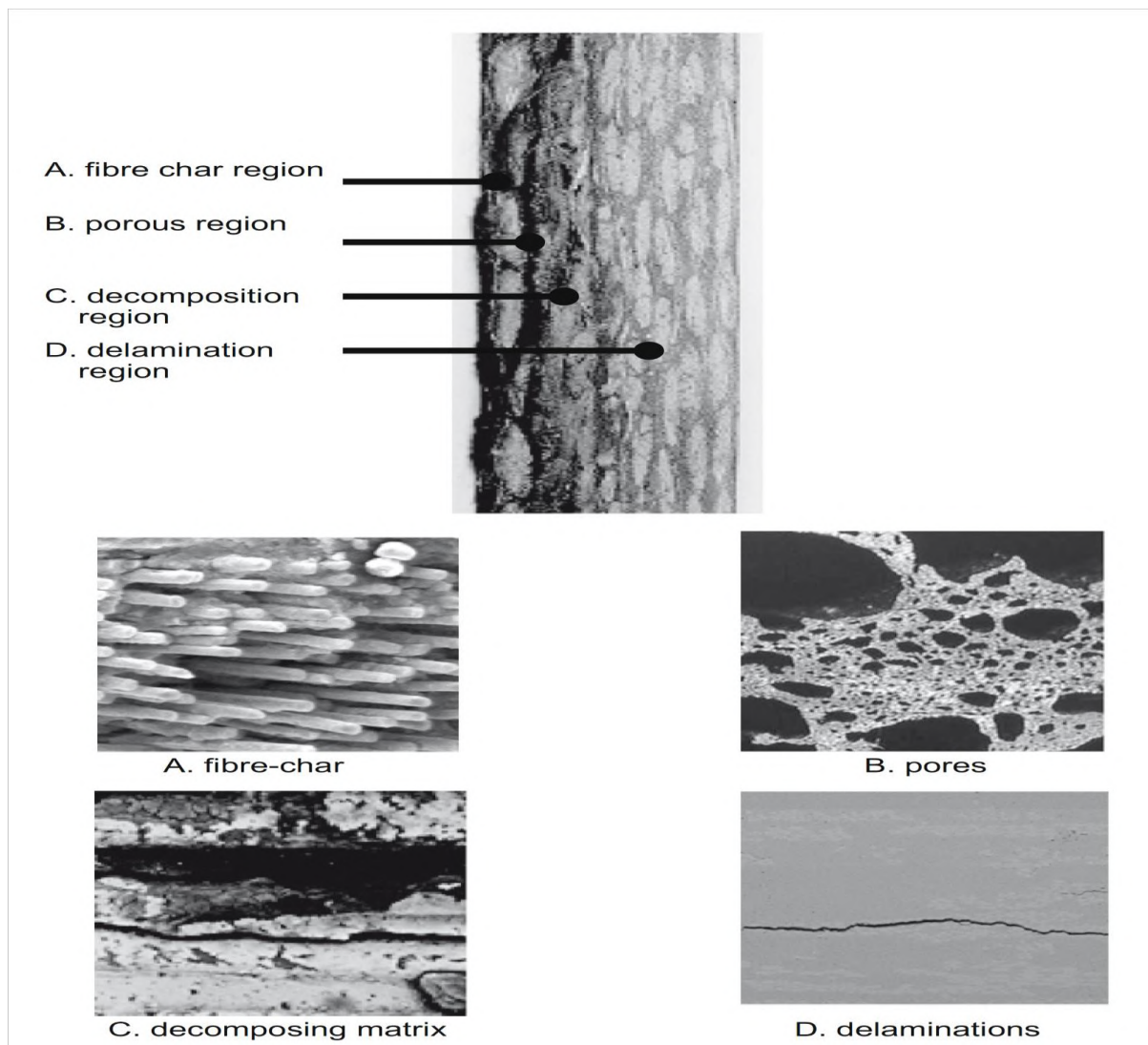


Fig. 2.8 Microscopic observation of fire-damaged composite [29]

delamination can reduce the heat conduction while increasing the permeability for gas transport.

To summarize the pyrolysis process description of composite materials, in the case of wood and carbon/epoxy materials, many complex physicochemical processes are involved during the pyrolysis process. Depending on fire conditions, these processes are more or less linked and predominant. But to deal with a pyrolysis model able to describe correctly the wide range of fire conditions, the main physical phenomenon should be considered with more or less accuracy in the model. This part is described in the following part.

### 2.2.2 Pyrolysis process modeling

There are two kinds of pyrolysis models, i.e. semi-empirical pyrolysis models and comprehensive ones. Semi-empirical models account for the thermal analysis in a macroscopic view. The material thermal properties can be directly estimated from the bench-scale experiments [32] and the chemical reaction of infinite-rate or simple one-step global reaction model is employed [35, 77, 91].

Another classification of pyrolysis models concerns numerical solution methods which involve the analytical models, integral models, and comprehensive numerical equation models [92]. Analytical models account for the infinite-rate kinetic model without gas volatiles convection [66]. As demonstrated, this assumption is not realistic and can only be used when under high heating rates and materials with larger thickness. Indeed, these models could be viewed as thermal models neglecting the participation of microchemical reactions. The integral models also assume the infinite-rate kinetic model with different temperature distributions in the material [93].

When using the finite-rate kinetic models under one-dimensional configuration, the pyrolysis reactions occur at a certain range of temperature and moving reaction zones due to heat transfer. Thus, the instantaneous density can be interpolated by virgin and char density [75]. While for infinite-rate kinetic models, the virgin and char layers are simply separated by a thin pyrolysis front. This one has the iso-thermal

temperature, i.e. pyrolysis temperature [75]. Thus, the infinite-rate kinetic model, or named the pyrolysis front model, is used mostly under high heating rates for that the pyrolysis reaction is controlled by heat and mass transfer, i.e. the pyrolysis reaction is instantaneously terminated due to a much smaller reaction time scale [75]. It can be concluded at this point that the analytical model, the integral model, and the semi-empirical model in this work can be viewed as the same category. Thus, only comprehensive ones, for which the main pyrolysis assumptions are captured to solve complicated partial differential equations, are focused due to their higher accuracy.

Normally, a comprehensive pyrolysis model includes some procedures for preparation. For example, the conservation equations for mass, momentum, and energy, the kinetic and thermo-physical parameters for model inputs. Also, some related experimental data to validate the model are required [94]. For conservation equations, they are a set of mathematical expressions that account for the description of different thermophysical and chemical phenomena occurring inside the condensed phase. Some complex phenomena such as shrinkage and swelling can also be integrated into some advanced comprehensive pyrolysis models. Based on the detailed pyrolysis process understanding, some assumptions are always adopted for their complexity to characterize the real and whole phenomenon involved. As the parameters for modeling input, they are some basic material properties such as kinetic and thermophysical parameters, as well as the boundary condition parameters which involve incident heat flux, heat convection coefficient, ambient temperature, and pressure, etc. The related numerical parameters are also needed to be set, for example, the time step, the mesh size, and the discretization parameters. All these procedures are extremely important to account for some reliable modeling results. Thus, the following parts will present some basic background and development concerning all these comprehensive pyrolysis modeling procedures.

There are two sub-models for comprehensive pyrolysis modeling: kinetic model, heat and mass transfer model. Without heat and mass transfer influence, the kinetic model is described for obtaining the kinetic parameters under thermally thin theory.

The chemical reaction can influence much the heat and mass transfer process, thus these kinetic parameters can be integrated into the heat and mass transfer model to calculate them simultaneously. This pyrolysis modeling methodology has been applied in many studies such as [95]. The consideration points for a comprehensive pyrolysis model, which is favored firstly under one-dimension including heat conduction, pyrolysis kinetics, gas mass transport, gas pressure build-up, and some other physical parameters to characterize such as shrinkage or swelling [74, 88, 96].

The finite-rate kinetic model accounts for the Arrhenius equation by three kinetic parameters, i.e. the pre-exponential factor, the activation energy, and the reaction order, which is usually adopted as a first-order reaction model in the fire community [97]. Concerning moisture evaporation modeling, there are three major drying models: the equilibrium model, the heterogeneous reaction model, and the heat sink model [37]. The equilibrium model assumes that the bound water is in equilibrium with water vapor which is normally employed in low heating rate conditions. The heterogeneous reaction model involves the Arrhenius equation by a first-order reaction, which is usually treated as the fourth component compared with the three components in wood. This reaction model is employed by many studies due to its simplicity to be integrated into the pyrolysis model such as [68, 74, 98]. The heat sink method is a semi-empirical model assuming a specific evaporation temperature and a thin infinite reaction front, which is applied mostly under high heating rates for large samples [37].

Some statistics show that the most charring material pyrolysis modeling studies involve wood for the past decades [68, 92]. They include heat conduction, pyrolysis kinetic reactions, gas volatiles transport, internal pressure distribution, volume variation, moisture evaporation, physical porosity, and permeability. Concerning the pyrolysis modeling development history for synthetic composite such as carbon/epoxy composite, it is firstly based on the one-dimension model describing the wood pyrolysis [29, 84] of which the heat transfer and the first-order Arrhenius equation is considered as well as the gas volatiles for immediate outward migration. Detailed development information can be found in [68]. It could be concluded that wood plays a dominant

role in test usage during advanced comprehensive pyrolysis modeling development, for their similarities and relatively high complexity in comparison with other advanced composite materials.

As noted in [99], for comprehensive pyrolysis modeling work which involves approximately several input parameters (for example, different thermo-physical parameters components, the kinetic parameters) there are many physical and chemical mechanisms to be included, such as the in-depth radiation absorption and pore radiation transfer. However, these input parameters can lead to much uncertainty of the model [100], and some assumptions are usually adopted during the modeling process. It is reasonably correct to neglect some phenomena which have minor effects on the pyrolysis process, depending on the corresponding experiments, and to seek the balance between accuracy and complexity when analyzing some specific pyrolysis scenarios. There are many assumptions considered in performing the pyrolysis modeling study, for example, the thermal equilibrium assumption [41, 87, 98]. When calculating the energy conservation equations, the local thermal equilibrium assumption between the gas and solid is considered almost for all pyrolysis models [67]. And when the gases flow out the surface char layer, the thermal equilibrium is assumed for that the heat capacity of gas is relatively small in the fire-related boundary condition. Thus, there is no heat convection consideration between solid and gas [32].

Due to the difference of materials components, some simplifications and approximations are conducted to be treated as homogenous and isotropic [87, 90] to account for simplified conservation equations, such as the homogeneous approximation for wood [32]. The thermophysical parameters of samples are usually considered as temperature-dependent [87, 91] and the thermal conductivity does not include the pore radiation [99]. The kinetic reaction schemes are usually treated as single-step [92, 98] or multi-step [87]. The pyrolysis reaction product is treated as inert gas without thermal convection [41, 58, 87, 101]. The in-depth radiation absorption is neglected and the material is treated as non-transparent. This is usually applied in the fire

scenarios [36, 32, 87, 101], for example, the charring materials are usually assumed as non-transparent with the presence of a constant emissivity value [102].

It is always assumed that there is no volume change including shrinkage, swelling, and cracks [74, 98, 101]. It is also estimated that the volume of the condensed phase is fixed while the density changes during the pyrolysis of thermally thick materials, although the shrinkage, swelling, and density variation occur simultaneously in reality [75, 103]. Due to the high porosity and internal pressure, the assumption that the gas immediately moves outward without resistance is always treated for fire scenarios to diminish the complexity while not influence too much the accuracy [33, 77, 103]. When considering gas transport, it is usually influenced by pressure and is described by Darcy's law [41, 87]. The diffusion of gases is much slower than the convection of gas volatiles [58, 65, 66, 98], thus the energy and mass of diffusion could be neglected [92]. Indeed, in some studies, the gas transfer coefficient is usually treated as homogenous with a relatively high value of  $2 \times 10^5$  m<sup>2</sup>/s. Thus, the gas produced is instantaneously moved out of the material, and its heat and mass transfer is very small to influence the mass loss rate [36]. The gas species are usually treated as ideal gases with identical thermophysical properties [41, 74] and the homogenous reactions among gas species are neglected in the solid [74].

Many comprehensive pyrolysis models have been developed during the last decades of which some very basic and important mathematical formulations and assumptions are still being applied to describe the typical physical and chemical phenomenon for pyrolysis modeling. For example, the pyrolysis models of Kung and Henderson are integrated into the current generalized pyrolysis models such as FDS, ThermaKin, and Gpyro [8, 32]. Some new phenomenon expressions are then supplemented, such as more complicated reaction schemes, the gas transport consideration, etc [32]. The main points are presented in the following parts.

### 2.2.2.1 Chemical reaction model

The kinetic modeling needs to be improved since the pyrolysis process is highly dependent on the thermal decomposition kinetic parameters and the reaction schemes [35]. The kinetics for thermal decomposition can be very complex and the Arrhenius equation describes the pyrolysis reaction rate based on temperature, mass concentration, and the related kinetic parameters. The corresponding kinetic parameters are mainly estimated based on non-isothermal TGA experiments [10, 18, 40, 35, 104].

The thermal decomposition kinetics can be described as follows [23, 105, 106]:

$$d\alpha/dt = k(T)f(\alpha) \quad (2.1)$$

$$\alpha = \frac{m_0 - m}{m_0 - m_f} \quad (2.2)$$

$$f(\alpha) = (1 - \alpha)^n \quad (2.3)$$

Where  $\alpha$  denotes the extent of conversion,  $t$  the time,  $T$  the temperature,  $f(\alpha)$  the conversion function,  $k(T)$  the reaction rate dependent on temperature,  $n$  the reaction order,  $m_0$  the initial mass,  $m_f$  the final mass,  $m$  the instantaneous mass.  $k(T)$  can be expressed by the Arrhenius equation [107] as follows:

$$k(T) = A \exp\left(\frac{-E_a}{RT}\right) \quad (2.4)$$

Where  $A$  denotes the pre-exponential factor,  $E$  the apparent activation energy,  $R$  the universal gas constant which is 8.314 J/(K mol). The final kinetics expression is formulated as follows:

$$d\alpha/dt = A \exp\left(\frac{-E_a}{RT}\right) (1 - \alpha)^n \quad (2.5)$$

The activation energy accounts for the minimum energy for starting the reaction, higher activation energy implies that the reaction is hard to start and much energy needs to be absorbed. This is related to environmental pressure, temperature, and reaction advancement [23, 108]. The pre-exponential factor involves the reaction frequency which is governed by intrinsic molecular vibration and collision [10, 109]. A high pre-exponential factor implies that the reaction could take place easily [10]. The reaction order is the exponent to represent the material mass concentration changing behavior during thermal decomposition [102].

As aforementioned that the kinetic is usually predicted by the non-isothermal TGA experiments under given heating rates  $\beta$ .

$$\beta = dT/dt \quad (2.6)$$

Thus, the kinetics can be expressed as:

$$d\alpha/dT = \frac{A}{\beta} \exp\left(\frac{-E_a}{RT}\right) (1 - \alpha)^n \quad (2.7)$$

In the fire community, the assumption of first-order kinetics is usually performed by many studies such as [95, 97]. Some studies show that the  $n^{\text{th}}$  order kinetic model can't employ identical parameters to estimate the kinetics under different heating rates [87]. Some studies show that the  $n^{\text{th}}$  order reaction scheme is more accurate [2, 11] and the reaction order can impose much effect on the mass loss. Indeed, the  $n^{\text{th}}$  order reaction schemes are employed when prescribing complicated thermal decomposition with parallel or multi-step reactions [11]. For example, for the pyrolysis of the three wood components, hemicellulose and cellulose account for the initial mass loss, while the last phase of mass loss involves the lignin decomposition. Thus, the first-order model does not fit the multiple independent parallel reaction scheme [67]. Then, the fourth-order reaction model is employed for carbon/epoxy composite thermal decomposition study [23].

Different kinetic reaction schemes are employed for biomass thermal decomposition [110]. Usually, the one-step global reaction scheme, the multi-step reaction scheme, and the independent multiple parallel reaction scheme are performed for biomass [92, 106].

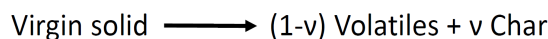


Fig. 2.9 One-step global reaction scheme of wood thermal decomposition [106]

Figure 2.9 presents a one-step global reaction scheme for wood [66], where  $v$  is the stoichiometric value of char. The virgin wood thermally decomposes to gas volatile and char. A competition of char and volatile formation process can take place. For this assumed one-step global reaction scheme, it is favored when we concentrate on the macroscopic pyrolysis production yield and mass loss. Thus, this scheme is adopted widely in engineering fields [58].

For the following figures concerning Figure 2.10, the left one is the typical multi-step reaction scheme for biomass pyrolysis [66] and the tar is the intermediate production as well as the presence of gas and char for the first step. Then the tar continues to decompose to char and gas. The right form is the sole intermediate activate yield for the first step, then, it can decompose to form char, gases, and tar during a second step. It could well predict the wood thermal decomposition kinetics and is usually employed in the fire community pyrolysis modeling [4, 58].

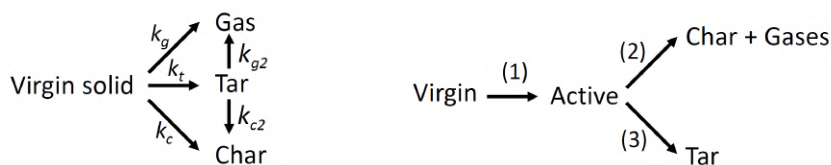


Fig. 2.10 Multi-step reaction schemes of wood thermal decomposition [66]

Wood is usually treated as homogeneous material due to its nature and complex structure for different directions [57–59] and its thermophysical properties of the three components are regarded as uniform even though they involve different chemical reactions. The wood thermal decomposition is usually treated as the combination

of the kinetics of different components, and the decomposition temperature range for hemicellulose, cellulose, and lignin are approximately at the range of 200-260 °C, 240-350 °C, and 280-500 °C, respectively [68, 74]. The hemicellulose, cellulose, and lignin approximately consist of a mass fraction of 25-35%, 40-50%, and 16-33%, respectively, and lignin can produce the most amount of char residue [65]. However, some studies assume the char yield is the same under the same thermal decomposition condition for these three components [60]. The activation energy for hemicellulose changes among 80-116 kJ/mol, the cellulose varies among 195-286 kJ/mol, and the lignin changes among 18-65 kJ/mol [61]. The independent three parallel reaction scheme for wood thermal decomposition can be expressed in Figure 2.11 [58, 111].

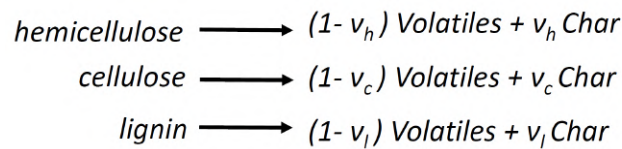


Fig. 2.11 Parallel reaction schemes of wood thermal decomposition [111]

Where  $\nu_h$ ,  $\nu_c$ ,  $\nu_l$  denote the stoichiometric value for the char produced by hemicellulose, cellulose, and lignin, respectively. The decomposition kinetics form for each of them can be expressed with the Arrhenius equation described earlier.

When it comes to the reaction mechanisms of epoxy resin pyrolysis, they display quite similarly with the pyrolysis kinetics of wood thermal decomposition. Different kinetic mechanisms are estimated and employed in relevant studies. It is demonstrated that the epoxy resin (thermoset polymer) thermal decomposition is diversified by different experimental conditions and different reaction model alternatives [108]. A large number of reactions can participate simultaneously, they behave endothermically or exothermically [84]. Thus, the polymer is usually treated as a one-step global reaction scheme due to its complexity [68]. This one-step global reaction model can be found in many studies such as [9, 112, 45], and it can be illustrated in Figure 2.12.

While others [87] treat the epoxy resin polymer as a mixture of components, and each component involves a one-step global reaction scheme. Thus the epoxy resin

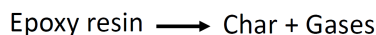


Fig. 2.12 One-step global reaction schemes of epoxy resin decomposition [112]

decomposition can be implemented with some parallel reactions and this reaction mechanism can be seen in Figure 2.13. The overall epoxy resin reaction rate can be integrated by each of them, however, the mass fractions of epoxy resin to decompose for each reaction is hard to estimate.

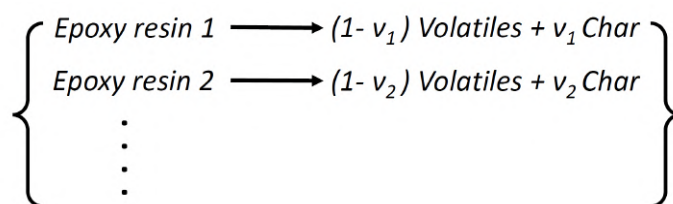


Fig. 2.13 A multiple parallel reaction schemes of epoxy resin (polymer) thermal decomposition [87]

And some others treat the polymer decomposition as a consecutive two-step reaction scheme since two reaction peaks are found in the DSC experiment [46]. This consecutive two-step reaction mechanism is presented in Figure 2.14 [46, 71, 108]. It is assumed that an intermediate form of epoxy resin is produced, then this intermediate one continually decomposes to final char residue and gases.



Fig. 2.14 A two-step reaction scheme of epoxy resin thermal decomposition [46]

To conclude, a one-step global reaction scheme sometimes could not predict well the TGA mass loss rate curve, due to the complexity of composite structure which involves many different reactions over different temperature ranges [32, 92]. The advantage of employing the one-step global reaction scheme is that it could reduce the number of model input parameters. Also, this reaction scheme can be used to test the chemical homogeneity of different components of composites. Finally, a one-step

global reaction scheme is also applied in the fire community to represent the charring material pyrolysis behavior to directly form char and gas [91].

For the multi-step reaction scheme, the kinetics and thermophysical parameters of intermediate products are quite hard to characterize. For example during wood pyrolysis, the competitive production, and the reaction of the intermediate liquid tar of which the properties are sensitive with heating rates [37]. The multiple independent parallel reaction scheme can represent the composite decomposition behavior with different kinetics concerning the different components. The advantage of the independent parallel reaction scheme is that it can be easily employed to predict the specific single component pyrolysis behavior [2, 106]. However, this kind of scheme involves many kinetic parameters and the minor interactions for each component are usually neglected [58]. It should be noted that sometimes, the different reaction schemes adoption such as wood is quite flexible. For example, hemicellulose thermal decomposition can be assumed with a two-step reaction scheme with intermediate solid production, cellulose can decompose with two independent parallel reaction schemes, and lignin can be treated as a one-step global reaction scheme [65]. As described in the following parts, the different reaction schemes are employed to fit the TGA mass loss rate curve mathematically to obtain the kinetics parameters [76]. Then, the reaction schemes can influence the kinetics significantly, and these kinetic parameters are normally treated as dependent on the reaction model. For example, the multi-step reaction schemes can lead to a relatively low decomposition rate, and the heavy reaction overlap accounts for the independent parallel reaction schemes when under high heating rates [11]. Thus, the first-order reaction model is commonly applied for the independent parallel reaction scheme [61].

#### **2.2.2.2 Heat and mass transfer model**

The heat is transported from the solid surface to the interior location by thermal conduction, the material absorbs energy to thermally decompose at given conditions [35]. These phenomena are fundamental considerations for comprehensive pyrolysis models. The pyrolysis model of Kung [113] is one of the most important comprehensive pyrolysis

models. It was introduced based on the one-dimensional study for wood slabs. In this approach, the most important chemical and thermophysical phenomenon are included, such as heat conduction, kinetics, the heat of pyrolysis, and gas convection. The Arrhenius equation of first order is adopted to describe the finite pyrolysis kinetics and the energy conservation equation is expressed as follows:

$$\rho C_{ps} \frac{\partial T}{\partial t} = \frac{\partial}{\partial x} \left( k \frac{\partial T}{\partial x} \right) + M_g \frac{\partial h_g}{\partial x} + \frac{\partial \rho}{\partial t} \left[ Q_p - \frac{\rho_w}{\rho_w - \rho_f} h_a + \frac{\rho_f}{\rho_w - \rho_f} h_c + h_g \right] \quad (2.8)$$

Where  $h_g$ ,  $h_a$ ,  $h_c$  denote the gas, solid, and char specific enthalpy variation,  $k$  the thermal conductivity,  $C_{ps}$  the solid specific capacity,  $M_g$  the gas volatile mass flux,  $\rho_w$  the virgin density,  $\rho_f$  the char density and  $Q_p$  the endothermic heat of reaction.

Based on the Kung pyrolysis model for wood pyrolysis, one composite pyrolysis model was developed by Henderson [114]. This one includes the heat conduction, the pyrolysis kinetics, the heat of reaction, and the heat convection. Its energy conservation equation can be expressed as:

$$\rho C_p \frac{\partial T}{\partial t} = k \frac{\partial^2 T}{\partial x^2} + \frac{\partial k}{\partial x} \frac{\partial T}{\partial x} - \dot{m}_g C_{pg} \frac{\partial T}{\partial x} - \frac{\partial \rho}{\partial t} (Q_i + h - h_g) \quad (2.9)$$

Where  $h_g$ ,  $h$  denote the gas and solid enthalpy,  $k$  the thermal conductivity,  $C_p$  the solid specific heat capacity,  $C_{pg}$  the gas specific capacity,  $\dot{m}_g$  the gas mass flux,  $\rho$  the density, and  $Q_i$  the endothermic heat of reaction.

This model also considers the finite rate kinetics and uses the Arrhenius equation with  $n^{\text{th}}$  order. It does not consider the gas accumulation, the thermal expansion, and the assumption of thermal equilibrium is considered. The thermal conductivity is dependent on temperature and decomposition extent, which are interpolated by virgin and char thermal conductivity by the mass fraction. The specific heat capacity is also the interpolation of the specific heat capacity of virgin and char. The fourth right side accounts for the heat of consumption or generation, the third right side denotes the gas convection heat, the second term on the right side represents the thermal conductivity

change for different decomposition stages, the left term and the first right term are the internal energy change in the solid and the heat conduction flux.

The gas transport involves convection and diffusion during the pyrolysis process of charring materials. Convection mass transport is normally performed by Darcy's law which depicts the correlation among the gas velocity, porous pressure, dynamic gas viscosity, and permeability. The diffusion transport is normally implemented by Fick's diffusion law, which describes the lumped molecule movement induced by the concentration difference, and it is sometimes performed by multi-phase diffusion [37]. The transport of water in the porous wood is usually treated to obey Darcy's law and Fick's diffusion law, and the evaporation rate follows the Arrhenius equation [8]. The gas is usually assumed as an ideal gas and the ideal gas law is usually combined within Darcy's law. Usually, the convection is much faster than the diffusion during the pyrolysis process, thus, the diffusion can be neglected [37, 66]. Gas mass transport in the porous material and steady-state Darcy's law is formulated as [41].

$$\mathbf{v} = -\frac{\mathbf{K}}{\mu} \nabla P \quad (2.10)$$

Where  $\mu$  denotes the dynamic viscosity coefficient,  $\mathbf{K}$  the permeability tensor,  $P$  the pressure,  $\mathbf{v}$  the gas velocity. The gas is assumed as ideal and the gas state equation can be expressed as:

$$P = \frac{\rho RT}{M} \quad (2.11)$$

Where  $\rho$  denotes the gas density,  $M$  the gas molecular weight,  $R$  the universal gas constant, and  $T$  the temperature of the gas.

### 2.2.2.3 Physical structure change model

As noted, modeling shrinkage or swelling during the pyrolysis process is quite complex. It can be influenced by surface heat flux, interior temperature distribution, experiment duration, material construction toughness, material homogeneity, sample

size, and shape, etc [29, 83, 115]. The existing models for these predictions usually involve the presence of some empirical considerations. For example, the shrinkage factor is used to characterize the shrinkage behavior, which involves the instantaneous and initial volume ratio changing linearly without consideration of cracks [86]. Some other shrinkage evaluations are based on materials' internal porosity, conversion extent, experiment observations, determination with different heat flux, and the assumed shrinkage velocity, as described in [68]. Many studies assume that no shrinkage or swelling occurs (such as [65]). Others are based on experiments and the swelling factor of carbon/epoxy composite is predicted by a variation order of two [9]. To conclude, the modeling work of shrinkage or swelling is still one of the most challenging studies in the comprehensive pyrolysis modeling development.

#### 2.2.2.4 Boundary conditions

The boundary conditions for pyrolysis is usually controlled by radiation and heat convection in the fire scenario. Indeed, it is performed as the radiation absorption from ambient heat flux, heat convection, and the re-radiation at the surface when under no flame condition [89]. The gas blowing effect is sometimes considered by the empirical formulation which is based on the heat convection coefficient [116]. As aforementioned, it is usually neglected for relatively low gas velocity and ambient pressure in the fire scenario. Some pyrolysis studies consider in-depth radiation absorption such as [117]. However, charring materials are usually treated as non-transparent with the absence of in-depth radiation absorption [118]. The transmissivity is negligible, thus the material surface only involves absorptivity and reflectivity. Detailed information can be found in [119]. The absorptivity is usually assumed equal to emissivity by Kirchhoff's law for the surface radiation emit which is usually applied in the engineering analysis [119]. When considering a constant heat flux pyrolysis scenario, the thermal boundary condition at the surface is usually expressed as [18, 116].

$$-k \frac{dT}{dt} = \alpha \dot{q}_e'' + \varepsilon_s \sigma (T_s^4 - T_\infty^4) + h_c (T_s - T_\infty) \quad (2.12)$$

Where  $q_e''$  denotes the irradiant heat flux,  $T_s$  denotes the surface temperature,  $T_\infty$  the ambient temperature,  $h_c$  the surface heat convection coefficient,  $\alpha$  the absorptivity,  $\varepsilon_s$  the emissivity, and  $k$  denotes the thermal conductivity.

At the bottom surface, it is usually assumed impermeable [116] and the thermal boundary condition is usually performed in two ways: thermal adiabatic, thermal radiation and convection [119, 120]. However, for many studies concerning pyrolysis in fire scenarios such as cone calorimeter, the sample back surface is protected by thermal insulation materials [121]. Due to the low temperature at the back surface of insulation materials, the bottom surface thermal boundary condition is only influenced by heat convection [5].

### 2.2.2.5 Pyrolysis model evaluation

The pyrolysis model in Fire Dynamics Simulator (FDS) [44], Thermal Kinetic Model of Burning (Thermakin) [122], Gpyro [32], and pyrolysis model in FireFOAM [123] developed by FM global are the most used pyrolysis models in the fire community. They are all generalized comprehensive pyrolysis models that integrate the finite rate reaction, transient heat transfer, and mass transfer to solve different sets of conservation equations for CFD numerical analysis.

FDS pyrolysis model involves the one-dimensional heat transfer process considering different pyrolysis reactions. A three-dimensional beta version could be performed currently and the different gas and solid production occur for the reaction. It can also consider the in-depth radiation process. The computation domain can be cubic, cylinder, and spherical. The surface boundary conditions consist of heat convection and radiation and a similar surface boundary condition or adiabatic can be performed at the back surface. Several assumptions are taken, for example, gas volatiles release infinitely to the surface, local thermal equilibrium, no gas mass transport, and negligible gas condensation. The shrinkage and swelling prediction can be conducted based on material density variation during the pyrolysis process [44].

FireFOAM is a large eddy simulation solver permitting to study fire-related scenarios such as gas and condensed phase. It is developed based on OpenFOAM which is an open-source CFD package. Only the surface pyrolysis phenomenon is considered, the interior condensed phase is assumed inert. Thus, energy conservation is exclusively implemented for the boundary condition [39, 77].

The Thermakin model can implement transient kinetics, heat transfer, and mass transfer process. For example, the first-order or second-order Arrhenius equation can be solved, heat convection transfer and in-depth radiation are considered [124]. Currently, it can also study the flame spread [43]. The reaction schemes can be performed with parallel or multi-step forms [43]. One-dimensional and two-dimensional pyrolysis processes can be performed and transient swelling problems can also be estimated [82, 125]. The thermal conductivity and specific heat capacity in Thermakin are treated as temperature-dependent. Instantaneous heat convection is assumed with the absence of gas momentum. Gas mass transport is governed by a concentration gradient [10, 126]. The target material is treated as a mixture containing different layers of components [76]. These components have their intrinsic properties, for example, density, specific heat capacity, and thermal conductivity. The boundary conditions of material sides for Thermakin2D is assumed adiabatic and impenetrable [43]. Inverse modeling has been widely conducted by using Thermakin, such as the work to estimate the thermophysical parameters of carbon fiber composite with related experiments [21].

Gpyro is an open-source pyrolysis model, which can study zero-dimensional, one-dimensional, two-dimensional, and three-dimensional problems, respectively. All the parameters such as specific heat capacity and thermal conductivity used in Gpyro are treated by average volume or mass fraction, and thermal equilibrium is assumed for the finite gas release. The bottom surface is usually treated as impenetrable and only heat convection is considered due to the low re-radiation under low temperature. The side surface is considered adiabatic. Material surface regression as well as in-depth radiation are integrated into the model [60]. The conservation equations in Gpyro involve gas phase mass and species, condensed phase mass and species, momentum,

and energy. Darcy's law is assumed for gas transport [111]. An inverse modeling analysis can be performed consisting of different optimization algorithms such as the genetic algorithm (GA) to estimate the model input parameters [34, 100]. The homogeneous or heterogeneous reactions of gas species in the condensed phase are considered. The condensed phase thermophysical parameters, i.e. specific heat capacity, thermal conductivity, and density, are treated as temperature dependent, while the gas specific heat capacity is treated as constant [42]. The density, specific heat capacity, and thermal conductivity variation with temperature can be expressed as follows [42]:

$$\phi(T) = \phi(0) \left( \frac{T}{T_r} \right)^n \quad (2.13)$$

Where  $\phi(T)$  denotes the density, specific heat capacity, or thermal conductivity value at the given temperature,  $T_r$  the reference temperature,  $\phi(0)$  the value of  $\phi(T)$  at  $T_r$ , and  $n$  specifies whether  $\phi$  increases or decreases with  $T$ .

The shrinkage or swelling study in Gpyro can also be performed [4] in the one-dimensional study. The radiation inside the pores can be considered to account for effective thermal conductivity, and the gas species involve identical diffusion coefficients [42, 127]. Different thermal conductivity and permeability values in different directions can be specified [127].

As shown previously, the comprehensive pyrolysis models combine the heat and mass transfer model and the kinetic model. They could be the common practice to predict pyrolysis behavior [37]. It can be concluded that each of these pyrolysis models has different assumptions for simplicity. However, the fundamental phenomenon is considered such as the Arrhenius equation, heat transfer, heat of decomposition, and thermal equilibrium assumption. Other mechanisms are implemented alternatively, for example, the gas convection transport described by Darcy's law, the gas species diffusion, the different boundary configuration, different material dimensions, parameters dependency on temperature, in-depth radiation, material shrinkage or swelling, etc. Some discussions about their main features and differences can also be found in [10, 43, 99, 104, 128, 129].

Due to the complexity of the pyrolysis process, it is not possible to consider many different physical and chemical mechanisms. With the presence of some underlying phenomenon, it can be quite reasonably acceptable while neglecting the ones imposing minor effects. Moreover, it can also balance the model uncertainty and computation cost. The model validation work has been widely conducted to compare the results performed by different pyrolysis models, they can be found in [34, 128–130]. Indeed, the model validation process involves many problems, for example, the initial detailed material properties, char residue uncertainties, shrinkage, crack and swelling, kinetic parameters, etc [58]. Also, many complicated materials involve anisotropic properties, then, the consideration of corresponding tensor analysis needs to be specified such as thermal conductivity and permeability, and some thermophysical parameters are highly temperature-dependent [58, 89]. For example, the carbon/epoxy composite is usually assumed as isotropic and this assumption could give us many errors for its constituents which have distinguished intrinsic properties, such as much higher thermal conductivity of carbon fiber than that of epoxy matrix [7, 14]. However, very limited studies concern the anisotropic characteristics of composite materials [58].

The model used in this work has some similarities compared with these mentioned pyrolysis models. For example, the assumption with no shrinkage/expansion or crack/delamination is involved. Each elementary reaction is implemented with an  $n^{\text{th}}$  reaction model in the Arrhenius equation form. The thermophysical properties, i.e. specific heat capacity and thermal conductivity, are specified to vary on the dependence of temperature. Darcy's law is formulated to characterize the pressure and gas flow behavior. However, some different features can be found. The thermal conductivity tensor is inherited to implement the energy conservation equation. Three-dimensional simulations coupling with flexible boundary condition implementation can be achieved including thermal radiation and convection boundary condition at different surfaces. Detailed model description in this study is presented in Chapter 3.

## 2.3 Multi-scale experiment and parameters estimation

There are three main steps for pyrolysis modeling: conservation and boundary equations, input parameters, and model validation. The conservation and boundary equations involve different pyrolysis mechanisms and relevant assumptions described mathematically. The input parameters, for example, the kinetics, thermophysical and numerical parameters, etc., are employed for model implementation. The validation work involves a comparison between the model prediction and experimental data [100].

Due to the complexity of overlap thermophysical and chemical mechanisms during the pyrolysis process, studies at different scales are usually performed to separate them for simplicity and detailed analysis [10, 130]. For the experimental data used for model validation, it could be milligram-scale, bench-scale, and large-scale under different configurations [129]. The milligram-scale and bench-scale studies are commonly employed for pyrolysis experiments and pyrolysis modeling for their cost efficiency and scientific accuracy [11, 130]. The TGA and cone calorimeter are widely applied concerning milligram-scale and bench-scale experiments in the fire community such as the work from [22, 129]. This multi-scale study is usually adopted for pyrolysis modeling validation work. The common idea is to obtain the kinetic parameters from TGA experiments coupling with related model fitting optimization methods. These kinetic parameters are integrated into thermophysical parameters in order to validate the heat and mass transfer process in cone calorimeter experiments as noted in [121, 51].

The sample size has a significant effect on pyrolysis behavior such as milligram-scale TGA and bench-scale cone calorimeter experiments and some dimensionless numbers or parameters are usually adopted to characterize this behavior. The Py number is usually applied for describing pyrolysis controlled by heat or by a chemical process, while the Biot number is used to differentiate the thermally-thin or thermally-thick materials [37, 38, 58, 131]. The interaction map for Py and Biot number is shown in Figure 2.15 [38].

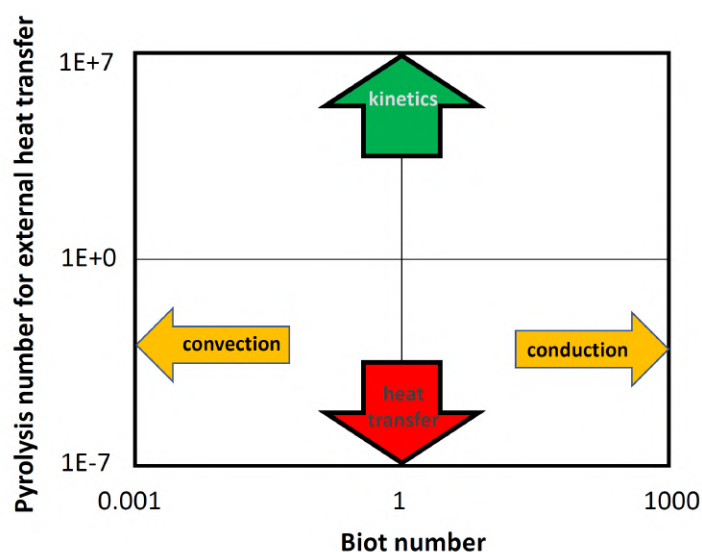


Fig. 2.15 Chemical reaction/heat transfer map for biomass pyrolysis (adapted from [38])

TGA milligram-scale studies are often applied for chemical kinetics study without considering the heat and mass transfer. The cone calorimeter is dedicated to fully understand the pyrolysis performance coupling with kinetic and thermal behavior. TGA experiments should be performed at different heating rates and cone calorimeter experiments should be conducted under different heat flux to minimize the error for model validation [11] which essentially analyzes the temperature evolution and mass loss profile [76].

### 2.3.1 Milligram-scale TGA and kinetics

As a milligram-scale thermal analysis experiment, the heat and mass transfer are assumed negligible for TGA with thermally-thin theory [132]. Thus, it is usually used to study the pure chemical reaction performance under 0D [21]. Milligram-scale TGA and DSC experiments are usually coupled to collect the kinetics, specific heat capacity, and heat of pyrolysis. TGA performs the mass change, DSC describes the heat flow change, and the heat of pyrolysis is implemented as the enthalpy change at a given temperature between solid reactants and gaseous products weighted by unit

mass [133, 134]. The kinetic parameters are often extrapolated from TGA experiments and usually concentrated on the sample weight variation history, i.e. mass loss rate and char yield [38]. TGA experiments can be performed under an oxidative or inert atmosphere, this should be highlighted when considering different application scenarios. For example, in the TGA experiments for the carbon/epoxy composite, the oxygen could influence the pyrolysis process below 400 °C and the char residue formation over the temperature range of 400-500 °C [108]. TGA experiments can also be conducted under iso-thermal or non-iso-thermal heating conditions. As it can't avoid the initial stage for heating up when performing iso-thermal analysis under given temperatures, and unknown complicated chemical reactions could take place during this heating up process, the non-iso-thermal method is normally utilized under controlled heating rates [106]. Very light and small samples and relatively low heating rates are required to eliminate the influence such as the thermal lag and the temperature gradient imposed in the condensed phase [97, 76, 130, 135].

Kinetic parameters estimation usually involves different TGA heating rates such that the compensation effect could be avoided [37]. For high heating rates aforementioned, it can trigger the thermal lag and temperature gradient inside the sample. Thus the homogenous thermal properties can't attain and can influence the kinetics [10]. Indeed, the kinetic parameters are influenced significantly by TGA heating rates [11, 102], which produce different final char yields for some materials decomposition [38, 136]. Some studies show that the kinetic parameters obtained from low heating rates could not predict well those under high heating rates [103, 132]. Other ones can obtain generalized kinetic parameters over different heating rates [76]. Thus, it is reasonably believed the kinetic parameters obtained by different heating rates are quite sensitive, although many studies demonstrate that unique kinetic parameters should be extracted under different heating rates [51]. The range of heating rate performing in TGA is limited, typically from 0.1 K/min to 50 K/min [84], due to its accuracy consideration [76, 51, 132].

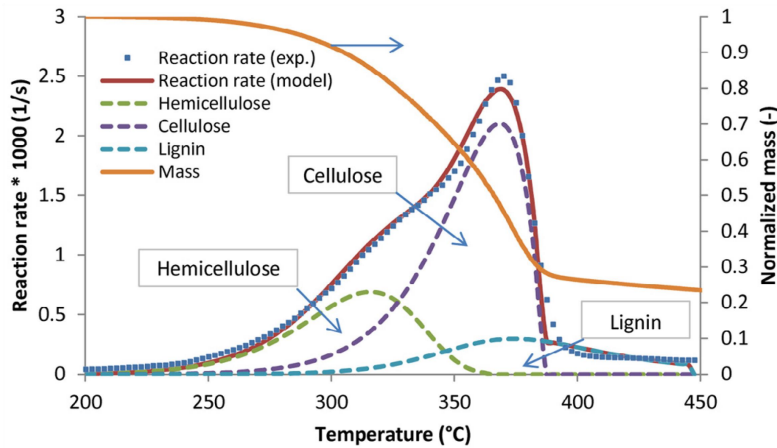


Fig. 2.16 Experimental and model prediction of mass loss profile of three pseudo-components of wood pyrolysis [37]

There are two main kinds of methods to obtain the kinetic parameters based on TGA experiments, i.e. model-free and model-fitting method [105]. With the complexity of different material components composition, the kinetic mechanism involves mixed chemical and physical processes, and the model-fitting method is usually favored and adopted [52, 105, 137]. The model-fitting method is performed by a prescribed kinetic model, then the kinetic parameters are predicted by fitting the TGA experimental curves employing different optimization algorithms. And usually, the independent multiple parallel reaction scheme is employed to study the kinetics for each component [106]. Figure 2.16 shows a case for wood pyrolysis to obtain kinetic parameters of different components using the model-fitting method [37]. The fitness level could be promoted when choosing more independent parallel reactions [106].

### 2.3.2 Bench-scale cone calorimeter

The mostly used bench-scale experiments for fire scenarios are cone calorimeter [138] and fire propagation apparatus (FPA) [139]. The two experiments are quite

similar, they all have a well-defined heat radiation configuration and one-dimensional heat conduction can be reasonably assumed [43]. The mass loss rate and temperature evolution data can be gathered [10, 140]. Moreover, many other parameters related to combustion can be collected such as the time to ignition, heat release rate, etc [102, 140]. The major difference involves the radiant system used by each device. The infrared lamp heaters in FPA could not guarantee a complete range of radiative wavelength used in the fire scenario [10, 130], and some theoretical radiation studies show that this radiation wavelength difference between FPA and cone calorimeter could account for the different pyrolysis results under the same configurations [94].

The standard cone calorimeter (ISO 5660) [138] is often utilized under ambient atmosphere, and it involves the sample surface area of  $100 \times 100 \text{ mm}^2$  with a thickness of several millimeters. The conical heater is mounted to provide a controlled irradiance from 0 to  $100 \text{ kW/m}^2$  by heat flux gauge calibration at the center of the sample top surface. The distance between the cone heater and sample top surface is usually fixed to 25 mm [11, 141, 142]. The piloted ignition can be triggered by the spark igniter [121] and the mass loss history is calibrated by a load cell and related data collection system [102]. The sample holder and thermal insulation material are usually wrapped around the sample sides and bottom surface, as aforementioned that the cone calorimeter is assumed reasonably as one-dimensional. Thus the heating loss from sides is usually neglected [128]. A schematic of the experiment setup of the cone calorimeter is shown in Figure 2.17 [54].

In some studies, the sample sides and bottom surface, or just the bottom surface, are also wrapped with a thin aluminum layer such that no gas can release to the sample holder to ensure the sample completeness and provide a perfect impenetrable boundary condition [36, 82, 140, 141, 143]. It could be a factor influencing the in-depth temperature evolution although it is quite thin and no difference of mass loss rate present in some work such as [9]. And for the back surface boundary condition, a heat convection condition is performed [18], or an adiabatic assumption is considered due to the thermal insulation material [54, 55]. The radiation at the back is usually

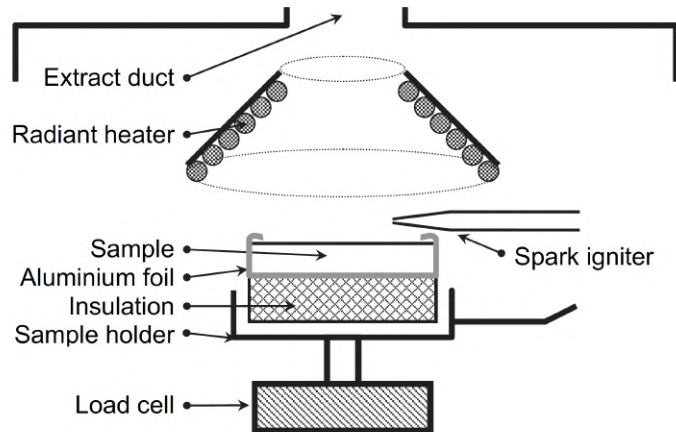


Fig. 2.17 Cone Calorimeter setups [54]

neglected due to the quite low temperature of the bottom surface of insulation materials. However, the heating up process for the bottom surface under different heat flux and experiment configurations can behave quite differently [54].

The surface temperature distribution before ignition is quite uniformed for the horizontal orientation. For the vertical orientation, its center can attain the highest temperature and the temperature of the upper edge and lower edge involve the medium and the lowest, respectively. The top surface temperature is quite non-uniformed for two orientations when under flame configuration [72]. Consequently, the horizontal cone calorimeter is mostly employed and recommended to study the material flammability due to its relatively higher accuracy.

As demonstrated, the boundary condition can be quite varied when manipulating different cone calorimeter experiments. For example, the heat convection coefficient for different cylindrical sample surface is found to be approximately 3-11 W/m<sup>2</sup>/K for cone calorimeter experiments under a controlled atmosphere [82]. Generally, an assumed or approximated value is allocated for pyrolysis modeling work such as heat convection coefficient. For example, this convection coefficient can be predicted with the correlation of heat flux [71, 144] with empirical evaluations [87], or with some literature data such as 10 W/m<sup>2</sup>/K which is usually adopted [18, 36], while some studies consider this value as 15-25 W/m<sup>2</sup>/K [54]. Indeed, the heat convection coefficient

is influenced by gas velocity, sample geometry, the temperature variation, etc [94]. Thus, it is reasonably correct to consider a higher heat convection coefficient when the buoyancy effect dominates during the pyrolysis process in comparison with pure heat conduction tests.

For the sample temperature measurement during the pyrolysis process under cone calorimeter, the commonly used are the thermocouples embedded in the sample [145] and the infrared camera to predict the surface temperature such as [10, 82, 89, 96, 145, 120]. The benefit of using an infrared camera during the pyrolysis test is that the temperature and mass evolution history can be collected simultaneously without contact with the sample [130]. The sample surface is sometimes painted black during the pyrolysis process to correct the emissivity which can seriously affect the temperature evolution [76, 82, 130].

The thermocouple temperature measurement applies the Seebeck thermoelectric effect for sensing the temperature difference, i.e. the feedback of the junction of two dissimilar wires [146]. Thus, the junction can determine the accuracy of temperature measurement results and many factors can influence the junction performance such as the diameter and environment configuration. Usually, very thin and shield protective implementations are considered [146]. For the environmental factors of the junction, many factors can influence the errors of thermocouple measurement. For example, the catalytic reaction effects, heat flow convection, heat conduction, and radiation, especially at high temperature and transient chemical reaction scenario [146–149]. As shown in Figure 2.18 with a schematic of the heat transfer process for a thermocouple [148]. At high temperature and small gas velocity ( $Ma=0.2$ ), the radiation errors possess the largest uncertainty of which some energy is radiated to the environment [147], the conduction and the catalytic effect is relatively quite small [148].

The thermocouple junction contact and its location shift within the material are quite uncertain due to the complex structure change during pyrolysis [76], especially at high temperatures [76]. There are two common ways to perform the thermocouple setup, the first one is to be inserted horizontally which is perpendicular to the gas

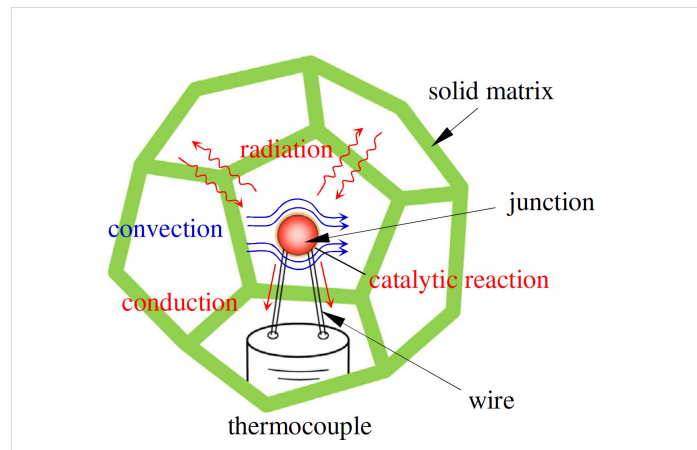


Fig. 2.18 Heat transfer of the thermocouple junction in solid materials [148]

migration direction such as [60, 4, 76, 150], the counterpart is to be inserted vertically such as [18, 71, 72, 151].

### 2.3.3 Parameters estimation

For pyrolysis modeling work, the input parameters are of importance. Normally, these parameters are from experiments, literature references, laboratory experiences, or even assumed data. Due to the complexity of the pyrolysis process coupling of physical, chemical, and mechanical mechanisms, the transient material parameters under complex boundary conditions for laboratory tests are not practical. Thus, the inverse modeling method is a good alternative [70, 125] which is the parameter estimation process by fitting experiment data and obtain the related parameters [97, 127]. For example, the effective thermal conductivity for the experiment is quite hard to characterize due to the diversified distribution of pore size to describe the pore radiation effect. The pore size is highly non-uniformed in the char layer especially at a high temperature which contributes much of the effective thermal conductivity [55, 67, 83]. The parameters usually involve high dependency on the temperature and the varied boundary condition. The inverse modeling method has been widely used to obtain correct and reliable data for model validation and some optimization methods are usually integrated to obtain the target optimal parameters [77]. For example, the heat convection coefficient in cone

calorimeter can be collected by inverse modeling [144]. The consideration of constant values for specific heat capacity and thermal conductivity could be the main reasons accounting for worse prediction of in-depth temperature evolution, and it can influence the pyrolysis rate [58]. Some parameters estimation are based on the extent of reaction degrees, such as the specific heat, thermal conductivity, porosity, and permeability which are treated as the linear interpolation of virgin and char values [41, 92].

However, inverse modeling has some requirements such as the experiment accuracy and a comprehensive model. This model can describe multiple physicochemical processes and specific boundary conditions [32]. Due to the complexity of kinetic mechanisms, the inverse modeling work for obtaining the kinetic parameters is quite dependent on the reaction schemes prescribed which could provide some errors. In order to make the kinetic parameters reliable for different configurations, the kinetic parameters obtained from inverse modeling are sometimes compared to those calculated by the model-free method [56, 95]. And the common compensation effect is usually avoided by conducting the inverse modeling work by different heating rates [152]. Indeed, some parameters obtained from the inverse modeling can be model-specific due to the uncertainty from many aspects. For example, when using cone calorimeter experimental mass loss rate and temperature profile coupling with genetic algorithm method to obtain optimal parameters, it is sensitive to the experiment data, the model assumption simplicity, and boundary condition [53]. These parameters are obtained from model estimation and could be of non-physical meaning for practical usage [153]. However, based on the accurate assumption representation used in the model, this method has the capability and flexibility to predict different parameters that have the true physical meaning of materials properties to be applied in a large range of scenarios as noted in [10, 99, 117]. Indeed, the inverse modeling method can be applied to predict the parameters based on the milligram-scale and bench-scale experiments. Relevant optimization process are mainly performed by different optimization algorithms [36, 76, 99, 116, 117, 124].

Sometimes, the manual optimization way can also provide optimal results [104] such as the steady or transient heat conduction process. One of the most used optimization methods is the genetic algorithm (GA) and related comparison between the experiment data and optimization value can be found [32, 100, 116]. TGA experiments coupled with the genetic algorithm optimization are usually employed to obtain the kinetic parameters with different reaction schemes involved [137]. Indeed, in the fire scenario, the optimization process usually involves the evolution algorithms of interest which possess the robustness for multi-variable optimization such as GA (genetic algorithm), Shuffled Complex Evolution (SCE), and Stochastic Hill Climbing (SHC) [10, 52, 53, 91, 99, 104, 97, 117, 133, 152]. Some work shows that GA and SCE could provide better fitness than SHC [104]. The iteration process for these evolution algorithms is followed. Firstly, many individuals are initialized which accounts for the probability of target parameters. Then, the individuals are selected to fit the experimental data and progress the reproduction toward another generation while keeping the convergence. Lastly, the optimal parameters can be gained over many population numbers under prescribed fitness function [10, 104].

The bench-scale experimental data can be applied for parameters estimation, and it can be also used for model validation while employing micro-scale experiments to estimate the parameters such as [153]. Indeed, inverse modeling has been used to obtain the charring material kinetic parameters and heat of reaction using TGA and DSC experiments with the pyrolysis model Thermakin [132]. The thermal conductivity and specific heat capacity are obtained under different heat fluxes based on bench-scale mass loss rate and temperature data at the top surface or bottom surface [32, 125].

Due to the large number of input parameters to be estimated [91, 94], some priorities should be given. For example, the specific heat capacity of wood and char play an important role in model validation, while the gas specific heat capacity influence could be negligible [58]. Thus, it is sensible to predict the most uncertain parameters such as specific heat capacity, thermal conductivity, boundary parameters, and heat

convection coefficients, while other physical parameters such as density and emissivity can be captured in advance.

## 2.4 Conclusion

This chapter provides a complete background for pyrolysis modeling study. Firstly, the target porous charring materials are focused on wood and carbon/epoxy composite in this study. Their fundamental chemical and physical properties are evaluated, especially different components inside the materials. Similarities and differences are discussed, wood can be assumed as isotropic while carbon/epoxy composite involves anisotropic properties considering thermal conductivity differences at different directions.

The pyrolysis processes of these two materials in the fire scenario are described under chemical, heat, and mass transfer as well as physical structure change aspects. Similarities of char layer formation pose a great effect on the pyrolysis process, while wood shrinkage and carbon/epoxy composite delamination make these two materials pyrolysis with a large difference. Different types of pyrolysis models are evaluated from simple to comprehensive pyrolysis models. The comprehensive pyrolysis model is given emphasis which mainly couples with chemical reactions, heat, and mass transfer. The elementary models concerning these three parts are formulated mathematically which mainly employ the Arrhenius equation and Darcy's law. Then the pyrolysis models developed in the fire community are described briefly, their benefits and inefficiencies are evaluated.

The pyrolysis model validation process involves the comparison of model prediction against the experimental data. Milligram-scale TGA and bench-scale experimental cone calorimeter tests are introduced and described when considering different characteristic length scales under thermally thin and thermally thick theory. Different input parameters to implement the pyrolysis model are discussed, and they are mainly collected with chemical and thermophysical parameters. The kinetic properties are specified

to control the pyrolysis reaction while the thermophysical properties determine the heat and mass transfer process. Kinetic parameters are mainly estimated by TGA experiments by fitting with the corresponding mass loss profiles based on pyrolysis modeling. The curve fitting inverse analysis method is usually employed to characterize the thermophysical properties as a supplementary of the experimental way.

Based on the aforementioned pyrolysis modeling process description with different aspects, the following chapter will present a new pyrolysis model PATO to overcome some inefficiencies of current pyrolysis models in the fire community. This model involves volume averaging theory assumption, and relevant conservation equations containing thermal conductivity and permeability tensor are described. It can be implemented with flexible convective boundary conditions on different surfaces. Employing this model, the kinetic parameters, thermophysical parameters, and boundary condition parameters are also collected with some level of accuracy. They are estimated with different simulation options to be inherited as the input parameters to finally validate this pyrolysis model.

# Chapter 3

## Description of the PATO solver

The Porous material Analysis Toolbox based on OpenFOAM (PATO) [154] is an open-source (GNU GPL) numerical solver released by NASA to analyze the heat and mass transfer process of reactive porous materials, for example, the charring material pyrolysis behavior. This solver solves the partial differential equations by the finite-volume method. PATO also integrates Mutation++ as a third party library which is developed by Von Karman Institute for Fluid Dynamics [155]. The Mutation++ is used for computing equilibrium chemical reactions which include the database for gas chemical compositions, thermodynamics, and transport. PATO is developed initially for the charring ablator, i.e. the Phenolic Impregnated Carbon Ablator (PICA), which is utilized in the thermal protection system for aerospace vehicle re-entry involving rigorous boundary heating conditions. This boundary accounts for the high-enthalpy gas flow. The gas under the aerothermal environment with high pressure and the temperature is controlled by convection heat flux while radiation heat flux is less predominant. The boundary layer is treated as thermal equilibrium for chemical reaction, heat transfer, and mass transfer, which deal with the interaction among ambient gas, pyrolysis gas, and surface char layer. PATO can solve zero-dimensional, one-dimensional, two-dimensional, and three-dimensional problems.

The main features and handling process in PATO can be collected as follows: different solid phases and individual gas phase are introduced in the solver and are

scaled based on the volume averaging theory. The solid pyrolysis, gas species release, heterogeneous reactions, and homogeneous reactions are treated as local thermal equilibrium for solving the conservation equations. Solid mass (pyrolysis), solid species, gas mass, gas species, gas momentum, internal energy conservation equations, and boundary equations are solved in PATO. It involves two major reaction forms for gas, finite-rate chemistry which accounts for the species, and equilibrium chemistry for the elements. The chemical reactions are mainly treated as equilibrium chemistry model in the boundary layer. It is assumed that the substrate density change with the presence of constant interior volume, although the most important surface recession consideration such as ablation is included.

The detailed description of conservation equations including boundary implementation, the different relevant technical terms, simulation options, and the input parameters description are presented as follows. It should be noted that all the material originally consists of different solid phase and only one gas phase.

### 3.1 The theory of volume averaging

Due to the complex and heterogeneous structure of wood and carbon/epoxy composite, for numerical simulation, the conservation equations and corresponded properties inside the porous medium are usually described based on the volume averaging method [156]. This one is also applied in PATO and a schematic for wet wood upon pyrolysis under volume averaging theory can be shown in [64]. The volume is selected to include all the condensed phase and gas phase while it constitutes a much smaller space compared to the whole material. This complex porous volume is described as a representative elementary volume (REV) and it is homogenous material containing different phases to be treated as a continuum [64, 157]. Figure 3.1 shows the schematic averaging volume consideration of different solid phases in porous materials [157].

The different solid phases and gas phases of volume fraction are equal to one and are described as follows:

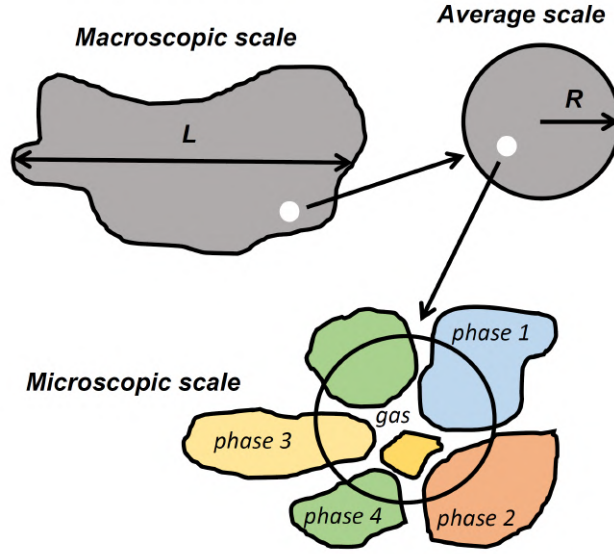


Fig. 3.1 Principle of the averaging volume containing multiple solid phases and single gas phase (adapted from [157])

$$\sum_{i \in [1, N_p]} \epsilon_i + \epsilon_g = 1 \quad (3.1)$$

Where the  $N_p$  is the number of solid phases,  $\epsilon_g$  the gas volume fraction (porosity),  $\epsilon_i$  the volume fraction for the solid phase.

The quantity  $\psi_i$  for phase  $i$  in the average volume of the condensed phase can be expressed by:

$$\psi_i = \frac{1}{V} \int \psi_i dV \quad (3.2)$$

Where  $V$  is the averaging volume of the entire porous material.

The intrinsic quantity  $\psi_{i, \text{intrinsic}}$  can be expressed as:

$$\psi_{i, \text{intrinsic}} = \frac{1}{V_i} \int \psi_i dV \quad (3.3)$$

Where  $V_i$  is the volume occupied by phase  $i$  and the volume fraction can be expressed as:

$$\epsilon_i = \frac{V_i}{V} = \frac{\psi_i}{\psi_{i, \text{intrinsic}}} \quad (3.4)$$

And the material density can be expressed as:

$$\rho = \epsilon_g \rho_g + \sum_{i \in [1, N_p]} \epsilon_i \rho_i \quad (3.5)$$

Where  $N_p$  is the number of the solid phase.

This formulation is applied to PATO to calculate the material density containing different solid phases in which the intrinsic density and volume fraction data should be prescribed. To give some examples for an explanation, the wood intrinsic density and volume fraction are listed in Table 3.1. The intrinsic density of hemicellulose, cellulose, and lignin in the wood are assumed as identical.

Table 3.1 The description for the sub-components of wood

Solid-phase	Subphase	Name	Intrinsic density	Volume fraction
1	None	hemicellulose	1500 [64]	0.0780 [158]
1	None	Cellulose	1500 [64]	0.1213 [158]
3	None	Lignin	1500 [64]	0.0809 [158]
4	None	water	1000 [64]	0.0467 [158]

For carbon/epoxy composite, the intrinsic density and volume fraction are listed in Table 3.2.

Table 3.2 The description for the sub-components of carbon/epoxy composite

Solid-phase	Subphase	Name	Intrinsic density	Volume fraction
1	None	Carbon fiber	1800 [15]	0.50 [159]
2	2	Epoxy resin	1220 [112]	0.38 [159]

The pyrolysis process involved in porous media is difficult to tackle because of the many physics and large range of local times and lengths scales. The concept of Representative Equivalent Volume allows the pyrolysis process to treat all complexities with a global point of view. With this technique, one major difficulty is introduced concerning the calculation of intrinsic physical parameters of each component involved

in the condensed phase which is treated as “apparent” values. These values have to be estimated by using upscaling techniques which are complicated to handle due to the potential large range of times and length scales involved during pyrolysis. We can point out that this field is still a challenge in the research community.

## 3.2 Pyrolysis kinetics

The pyrolysis kinetics of composite materials is a complex process. In the present study, basic chemical mechanisms for wood and carbon composite are used in which only parallel reactions are defined. As a first step, these kinds of mechanisms have been chosen only for their simplicity because of the lack of interactions between components. This is the first step to achieve before dealing with more complex chemical mechanisms. Indeed, these models are quite acceptable when the chemistry is infinitely fast and the overall pyrolysis process still govern by heat transfer into the porous media [75]. But depending on burning conditions, when the chemistry becomes finite rate, such models are not qualified, and more complex mechanisms should be used to capture the competition process between chemistry and heat transfer. In that case, the time and length scales of these two processes are in the same order of magnitude. This aspect will be discussed in the results part. So, in the following part, the chemical aspect of the pyrolysis model is introduced through a progress variable dealing only with a set of parallel reactions.

Each solid-phase  $i$  can involve different sub-phase pyrolysis mechanisms, and  $j$  denotes the sub-phase, thus the pyrolysis process can be expressed as:

$$P_{i,j} \rightarrow \sum_{k \in [1, N_e]} \zeta_{i,j,k} A_k \quad (3.6)$$

Where  $i \in [1, N_p]$ ,  $j \in [1, P_i]$ ,  $k$  denotes the gas element,  $N_e$  denotes the number of gas elements, and  $A_k$  is the specific gas element produced by the subphase  $j$  in the solid phase  $i$ ,  $\zeta_{i,j,k}$  is the related stoichiometric coefficient of the gas element production.

In this work, wood is treated as isotropic material, i.e. the thermal conductivity and permeability tensor is neglected, while for carbon/epoxy composite, these values are non-uniform for different directions. When tackling independent parallel reaction schemes for wood, the four solid phases are water, hemicellulose, cellulose, and lignin, respectively.

In this work, each solid phase accounts for only one reaction and it is assumed that the pyrolysis production is Nitrogen which is considered as a tabulated gas properties simulation option. Assuming that pyrolysis gases released is nitrogen is a strong assumption. However, the idea is to assume that pyrolysis gas released are “non-reactive”, but it should be treated as a “reactive” gas volume as a perspective of this work. The description of pyrolysis items concerning each component of wood is listed in Table 3.3.

Table 3.3 Pyrolysis parameters for each component in wood (estimated in this study)

Solid-phase $i$	Sub-phase $j$ of $i$	Pyrolysis reaction $P_{i,j}$	Element $A_k$	Stoichiometric coefficient $\zeta_{i,j,k}$
Hemicellulose	None	$P_{1,1}$	{C, H, O, N}	{0,0,0,1}
Cellulose	None	$P_{2,1}$	{C, H, O, N}	{0,0,0,1}
Lignin	None	$P_{3,1}$	{C, H, O, N}	{0,0,0,1}
Water	None	$P_{4,1}$	{C, H, O, N}	{0,0,0,1}

For carbon/epoxy composite, the condensed phase involves solid phases of carbon fiber and epoxy resin. Epoxy resin thermally decomposes by consecutive reaction schemes. Indeed, as mentioned above, a more complex mechanism than parallel simple one is needed in many cases to describe correctly the pyrolysis process. Such mechanisms are under implementation in PATO and will be a perspective part of this work. Here, independent parallel reaction schemes are used and carbon fiber does not participate in the pyrolysis reaction. The resin is assumed to involve two reactions according to related DSC curves and the inert gas is also assumed for the pyrolysis gas volatiles production. The pyrolysis parameters can be shown in Table 3.4:

Linear Arrhenius equation is performed for pyrolysis type and can be expressed as:

Table 3.4 Pyrolysis parameters for each component in carbon/epoxy composite

Solid-phase $i$	Sub-phase $j$ of $i$	Pyrolysis reaction $P_{i,j}$	Element $A_k$	Stoichiometric coefficient $\zeta_{i,j,k}$
Carbon fiber	None	None	None	None
Epoxy resin	Resin 1	$P_{2,1}$	{C, H, O, N}	{0,0,0,1}
Epoxy resin	Resin 2	$P_{2,2}$	{C, H, O, N}	{0,0,0,1}

$$\partial_t \chi_{i,j} = (1 - \chi_{i,j})^{m_{i,j}} T^{n_{i,j}} A_{i,j} e^{-\frac{E_{i,j}}{RT}} \quad (3.7)$$

$$\forall i \in [1, N_p], \forall j \in [1, P_i] \quad (3.8)$$

Where  $A_{i,j}$  is the pre-exponential factor,  $E_{i,j}$  the activation energy,  $R$  the molar gas constant,  $m_{i,j}$  the reaction order,  $n_{i,j}$  the temperature coefficient, and it is neglected in this study ( $n_{i,j} = 0$ ). The  $\chi_{i,j}$  is employed to denote each pyrolysis reaction advancement (the extent of reaction  $P_{i,j}$ ), i.e. the subphase  $j$  reaction of solid-phase  $i$ , with the range of  $0 < \chi_{i,j} < 1$ , and the total advancement of pyrolysis  $\tau$  can be described as:

$$\tau = \sum_{i \in [1, N_p]} \sum_{j \in [1, P_i]} \frac{\epsilon_{i,0} \rho_{i,0} F_{i,j} (1 - \chi_{i,j})}{\sum_i^{N_p} \sum_j^{P_i} \epsilon_{i,0} \rho_{i,0} F_{i,j}} \quad (3.9)$$

And each solid phase  $\rho_i$  and total transient solid density  $\rho$  can be formulated as:

$$\rho_i = \frac{\epsilon_{i,0} \rho_{i,0}}{\epsilon_i} \left( 1 - \sum_j^{P_i} \chi_{i,j} F_{i,j} \right) \quad (3.10)$$

$$\rho = \sum_{i \in [1, N_p]} \rho_i \epsilon_i \quad (3.11)$$

The production rate of the gas element  $k$  during thermal decomposition for all sub-phases  $N_p$  in the solid phase can be expressed by summation:

$$\pi_k = \sum_{i \in [1, N_p]} \sum_{j \in [1, P_i]} \zeta_{i,j,k} \epsilon_{i,0} \rho_{i,0} F_{i,j} \partial_t \chi_{i,j} \quad (3.12)$$

Where  $\epsilon_{i,0}$  is the initial volume fraction of solid-phase  $i$ ,  $\rho_{i,0}$  is the initial intrinsic density of solid-phase  $i$ . Thus the  $\epsilon_{i,0} \rho_{i,0}$  is the initial apparent density of solid-phase  $i$ ,  $F_{i,j}$  is the mass fraction to be thermally decomposed to gas volatiles for solid-phase  $j$  in the solid-phase  $i$ .

Thus the total material pyrolysis rate is described as the summation of all pyrolysis gas element  $k$  production rate and can be expressed as follows:

$$\Pi = \sum_{k \in [1, N_e]} \pi_k \quad (3.13)$$

For wood pyrolysis reaction coefficients, the related pyrolysis reaction parameters can be listed in Table 3.5 for illustration:

Table 3.5 Pyrolysis reaction parameters for each component in wood

Pyrolysis reaction $P_{i,j}$	Reactants	$F_{i,j}$	$A_{i,j} (s^{-1})$	$E_{i,j} (J/mol)$	$m_{i,j}$	$n_{i,j}$
$P_{1,1}$	Hemicellulose	0.96	$6.22 \times 10^9$	$1.34 \times 10^5$	3.39	0
$P_{2,1}$	Cellulose	0.80	$9.47 \times 10^{18}$	$3.51 \times 10^5$	1.05	0
$P_{3,1}$	Lignin	0.74	$3.95 \times 10^5$	$8.25 \times 10^4$	0.47	0
$P_{4,1}$	Water	1.0	$3.48 \times 10^{11}$	$8.74 \times 10^4$	3.28	0

For carbon/epoxy composite pyrolysis the reaction coefficients are listed in Table 3.6.

Table 3.6 Pyrolysis reaction parameters for each component in carbon/epoxy composite

Pyrolysis reaction $P_{i,j}$	Reactants	$F_{i,j}$	$A_{i,j} (s^{-1})$	$E_{i,j} (J/mol)$	$m_{i,j}$	$n_{i,j}$
$P_{1,1}$	Carbon fiber	None	None	None	None	None
$P_{2,1}$	Resin 1	0.47	$1.58 \times 10^{14}$	$1.99 \times 10^5$	1	0
$P_{2,2}$	Resin 2	0.25	$6.31 \times 10^8$	$1.4 \times 10^5$	1	0

### 3.3 Conservation equations

#### 3.3.1 Solid mass conservation equations

Based on the volume averaging theory, the solid phase mass conservation is expressed by using the progress variable  $\chi_{i,j}$  derived in the pyrolysis model described before.

$$-\partial_t(\epsilon_i \rho_i) = \sum_{j \in [1, P_i]} \zeta_{i,j,k} \epsilon_{i,0} \rho_{i,0} F_{i,j} \partial_t \chi_{i,j} \quad (3.14)$$

#### 3.3.2 Gas mass conservation equations

The gas mass is produced by solid pyrolysis and it varies at different time and different space locations. It can be expressed as follows:

$$\partial_t(\epsilon_g \rho_g) + \partial_{\mathbf{X}}(\epsilon_g \rho_g \mathbf{v}_g) = \Pi \quad (3.15)$$

Where  $\epsilon_g$  is the gas volume fraction (porosity),  $\rho_g$  the gas density,  $\mathbf{v}_g$  the gas velocity,  $\Pi$  the pyrolysis term which is described by the Arrhenius equation. The total and surface pyrolysis rate can be expressed as:

$$\dot{m}_{pg} = \epsilon_g \rho_g \mathbf{v}_g \quad (3.16)$$

Where  $\dot{m}_{pg}$  is pyrolysis gas production rate,  $\mathbf{v}_g$  the vector gas velocity. The  $\dot{m}_{pg}$  designates the pyrolysis rate for converting the virgin materials to gas volatiles per unit second per unit volume.

#### 3.3.3 Gas momentum conservation equations

Momentum conservation equation is used to simulate the pressure and gas velocity which need to specify the permeability and porosity of virgin and char. The volume-

averaged gas momentum equation in the porous volumes is expressed according to Darcy's law, and it can be expressed as:

$$\mathbf{V}_g = -\frac{1}{\epsilon_g} \left( \frac{1}{\mu} \underline{\underline{\mathbf{K}}} + \frac{1}{p_g} \underline{\underline{\beta}} \right) \cdot \partial_{\mathbf{x}} p_g \quad (3.17)$$

Where  $\underline{\underline{\mathbf{K}}}$  is the permeability tensor,  $\underline{\underline{\beta}}$  is the Klinkengerg correction to account for the slip effect in the pore, it is usually neglected when the Knudsen number is very small. The virgin and char permeability are second-order tensors for wood. In this work, the permeability for virgin and char are treated as isotropic for wood, and carbon/epoxy composite with non-isotropic properties in different directions.  $\mathbf{V}_g$  is the gas velocity,  $\epsilon_g$  the gas volume fraction,  $p_g$  the gas pressure,  $\mu$  the dynamic gas viscosity. And the perfect gas law can be expressed as:

$$p_g = \frac{\rho_g R_g T_g}{M_g} \quad (3.18)$$

Thus:

$$\rho_g = \frac{M_g p_g}{R_g T_g} \quad (3.19)$$

Where the  $R_g$  is the gas constant number,  $T_g$  the gas temperature,  $M_g$  the gas molecular weight. The momentum equation can be introduced in the gas mass conservation equation and described as:

$$\partial_t \left( \frac{\epsilon_g M_g p_g}{R_g T_g} \right) - \partial_{\mathbf{x}} \left( \frac{M_g p_g}{R_g T_g} \left( \frac{1}{\mu} \underline{\underline{\mathbf{K}}} + \frac{1}{p_g} \underline{\underline{\beta}} \right) \cdot \partial_{\mathbf{x}} p_g \right) = \Pi \quad (3.20)$$

### 3.3.4 Energy conservation equation

The energy can be consumed or produced in the chemical reaction. In this work, the endothermic reaction is considered and they are formulated based on the volume averaging theory as mentioned. The energy conservation is formulated based on the local thermal equilibrium assumptions, and it can be expressed as:

$$\partial_t (\rho_t e_t) + \partial_{\mathbf{X}} (\epsilon_g \rho_g h_g \mathbf{V}_g) = \partial_{\mathbf{X}} \cdot (\underline{\mathbf{k}} \cdot \partial_{\mathbf{X}} T) + \mu \epsilon_g^2 (\underline{\underline{\mathbf{K}}}^{-1} \cdot \mathbf{v}_g) \cdot \mathbf{v}_g \quad (3.21)$$

Where  $\rho_t$  is the total density,  $e_t$  the total energy per unit mass,  $\epsilon_g$  the gas volume fraction,  $\rho_g$  the gas density,  $h_g$  the gas enthalpy,  $\mathbf{V}_g$  the gas velocity,  $\mathbf{k}$  the effective thermal conductivity tensor,  $N_g$  the elemental composition of gases  $k$  gas element. The second term on the right denotes the viscous energy dissipation which is very small. In this work, the wood is treated as isotropic material, thus the thermal conductivity is identical for the three directions. For laminate carbon/epoxy composite, the thermal conductivity is treated as a second-order tensor,  $T$  is the temperature, and  $\rho_t e_t$  is the total energy of all solid phases and the gas phase, and it can be expressed as:

$$\rho_t e_t = \epsilon_g \rho_g e_g + \sum_{i \in [1, N_p]} \epsilon_i \rho_i h_i \quad (3.22)$$

Where  $i$  denotes the solid phase,  $N_p$  the number of solid phases,  $\epsilon_i$  the solid phase volume fraction,  $\rho_i$  the solid phase density,  $h_i$  the enthalpy solid-phase  $i$  and its evolution can be expressed by specific capacity:

$$\partial_t h_i = c_{p,i} \partial_t T \quad (3.23)$$

The previous equation can be rearranged as:

$$\partial_t (\rho_t e_t) = \partial_t \left( \epsilon_g \rho_g \left( h_g - \frac{p_g}{\rho_g} \right) \right) + \partial_t \left( \sum_{i \in [1, N_p]} [(c_{p,i} \epsilon_i \rho_i \partial_t T) + h_i \partial_t (\epsilon_i \rho_i)] \right) \quad (3.24)$$

A detailed enthalpy implementation is applied and formulated as follows:

$$h_s = \int_{T_0}^T c_p dT \quad (3.25)$$

$$h_{\text{detail}} = h_s + h_p \quad (3.26)$$

Where  $h_{\text{detail}}$  is the charring enthalpy for specific solid-phase  $i$ ,  $h_s$  the sensible enthalpy, and  $h_p$  the decomposition heat for solid-phase  $i$ .

The effective thermal conductivity is the most important item for heat transfer and the energy equation is usually expressed as temperature-dependent and solved implicitly as follows:

$$\begin{aligned} & \sum_{i \in [1, N_p]} [(\epsilon_i \rho_i c_{p,i}) \partial_t T] - \partial_X \cdot (\underline{\mathbf{k}} \cdot \partial_X T) = \\ & - \sum_{i \in [1, N_p]} [h_i \partial_t (\epsilon_i \rho_i)] - \partial_t (\epsilon_g \rho_g h_g - \epsilon_g p_g) + \partial_X (\epsilon_g \rho_g h_g \mathbf{V}_g) \end{aligned} \quad (3.27)$$

$$h_g = \int_{T_0}^T c_{p,g} dT \quad (3.28)$$

Where  $h_g$  is the gas enthalpy. In this work, the thermal conductivity and specific heat capacity parameters are temperature-dependent which are the most sensitive transport parameters. Based on the volume averaging theory, the weight mass averaged thermal conductivity, specific heat capacity, enthalpy, the volume fraction of gas, absorptivity, and emissivity can be described as the interpolation with virgin and char properties based on total pyrolysis advancement in the condensed phase. It could be emphasized that this technique is the simplest way to obtain ‘‘apparent’’ parameters when the volume averaging technique is used. Indeed, only the virgin state and final state of the pyrolysis process are used to handle apparent parameters. However, during the pyrolysis process, many intermediate states (between virgin and char) occurs probably affecting ‘‘apparent’’ thermochemical parameters. A more detailed upscaling technique should be used in perspective to be better described those ‘‘apparent’’ parameters that could evolve in function of temperature and pyrolysis states.

$$c_p = \tau c_{p,v} \frac{\rho_v}{\max(\rho_v, \rho_c)} + (1 - \tau) c_{p,c} \frac{\rho_v}{\max(\rho_v, \rho_c)} \quad (3.29)$$

$$k = \tau k_v \frac{\rho_v}{\max(\rho_v, \rho_c)} + (1 - \tau) k_c \frac{\rho_v}{\max(\rho_v, \rho_c)} \quad (3.30)$$

$$\alpha = \tau \alpha_v \frac{\rho_v}{\max(\rho_v, \rho_c)} + (1 - \tau) \alpha_c \frac{\rho_v}{\max(\rho_v, \rho_c)} \quad (3.31)$$

$$\varepsilon = \tau \varepsilon_v \frac{\rho_v}{\max(\rho_v, \rho_c)} + (1 - \tau) \varepsilon_c \frac{\rho_v}{\max(\rho_v, \rho_c)} \quad (3.32)$$

$$h = \tau h_v \frac{\rho_v}{\max(\rho_v, \rho_c)} + (1 - \tau) h_c \frac{\rho_v}{\max(\rho_v, \rho_c)} \quad (3.33)$$

$$\epsilon_g = \epsilon_{g,c} + (\epsilon_{g,v} - \epsilon_{g,c}) \sum_{i \in [1, N_p]} \sum_{j \in [1, P_i]} \chi_{i,j} \quad (3.34)$$

The mass fraction of different solid phases  $Y_i$  can be described as:

$$Y_i = \frac{\epsilon_i \rho_i}{\rho} \quad (3.35)$$

$$\rho = \sum \epsilon_i \rho_i \quad (3.36)$$

$$h = \sum Y_i h_i \quad (3.37)$$

Where  $\epsilon_i$  is the volume fraction of different solid phases,  $\rho_i$  the intrinsic density of different solid phases,  $\rho$  the volume-averaged bulk solid density. Thus the porosity  $\phi$  of material is given by:

$$\phi = 1 - \sum \frac{\rho_s}{\rho_i} \quad (3.38)$$

### 3.4 Boundary conditions

There are several options to select in PATO to implement the boundary conditions. In this work, the radiative fire boundary condition is used, which is revised based on the radiative boundary condition in PATO without pyrolysis and ablation blowing. The heat convection loss only occurs at the side, and the bottom is adiabatic with a thick thermal insulation material. The boundary condition in PATO concerning aerothermal heating boundary condition which has complex surface energy and mass balance model can be found in [160, 161]. The radiative fire boundary condition is applied which includes the heat irradiation, re-radiation, and convective heat transfer subjected to pyrolysis condition. The boundary conditions have been described in Chapter 2 and re-formulated consistent with this work as follows. During our work, all the experiments have been conducted in the inert experiment, so oxidation or flame is not involved:

$$-k \frac{dT}{dt} = \alpha \dot{q}_e'' + \varepsilon \sigma (T^4 - T_\infty^4) + h_{top} (T - T_\infty) \quad (3.39)$$

Where  $\dot{q}_e''$  denotes the ambient heat flux,  $T$  the surface temperature,  $T_\infty$  the ambient temperature,  $h_{top}$  the surface heat convection coefficient,  $\alpha$  the absorptivity,  $\varepsilon$  the emissivity, and  $\sigma$  the Stefan-Boltzmann constant. The material is treated as a gray body and the emissivity and absorptivity are assumed to be 0.96 because the sample surface is painted in black. The bottom surface is specified as adiabatic with the same ambient temperature. The convective boundary condition concerning cone calorimeter sides is formulated as:

$$-k \frac{dT}{dt} = h_{side} (T - T_\infty) \quad (3.40)$$

Where  $h_{side}$  is the convective heat transfer coefficient at sides.

## 3.5 Modeling work protocol

The general method for pyrolysis modeling work is to predict mainly the experimental mass loss, mass loss rate, and temperature evolution at surface or bottom [125, 5, 97, 134, 130], and these experiments involve different scales and corresponding data are extracted. However, some studies [162] have demonstrated more parameters should be taken into account to evaluate the model. Those parameters can be in-depth temperature evolution at different locations, char or pyrolysis front evolution, and the ratio variation trend of the pyrolyzing gas species at different time scales.

As reviewed in [34], pyrolysis modeling work includes different steps. Firstly, the TGA micro-scale and cone calorimeter bench-scale tests are carried out to obtain the experimental data, a mathematical pyrolysis model is established combining with the Arrhenius equation, heat transfer, and mass transfer model, as also showed in the literature review. Secondly, the parameterization work by numerical optimization or inverse analysis to fit the experimental data under a comprehensive pyrolysis model. Finally, some simulations are conducted to obtain the corresponding predicted results and to analyze the results especially the discrepancies involved.

Thus, this study will concentrate on the application of experiments with different scales, i.e. milligram-scale TGA and bench-scale cone calorimeter. The TGA experiment is employed to study the pyrolysis kinetics, heat transfer, and mass transfer phenomena are preliminarily neglected. Mass loss and derived mass loss rate are extracted to estimate the kinetic parameters. The cone calorimeter is widely employed to obtain the corresponding mass loss history, the derived mass loss rate is the elementary pyrolysis parameter to analyze the heat release rate, this permits to characterize the material flammability and other fire properties [163, 138]. The temperature evolution and pyrolysis front propagation can also be studied under different thermal configurations. Again, these two equipment involve standard experimental manipulation which can provide reliable boundary conditions and present reproducible results.

As previously reviewed in Chapter 2, wood and carbon/epoxy composite are chosen in this study as the targeted charring composite materials. The TGA and cone calorimeter experiments are conducted under an inert environment in this study, thus without the presence of oxidation and flame. Concerning the parameterization process for model input at bench scale, the fundamental kinetic parameters are used to implement the chemical reactions which are estimated by coupling with the Dakota optimization [164]. The main thermal parameters are obtained by inverse analysis based on PATO or from reliable reference data. This methodology has been applied widely in many studies such as the research group [96]. For the inverse analysis work, the relevant thermal properties and boundary conditions, including heat convection coefficient, specific heat capacity, the thermal conductivity of virgin and char, are estimated by fitting the pure heat conduction model prediction against the cone calorimeter experimental data. The inverse analysis concerning the temperature evolution is measured by thermocouples. When conducting the inverse analysis of char thermal properties, the char samples chosen are the final residue after the termination of the virgin pyrolysis experiment. And the thermocouples setup are fixed from the virgin to char samples when conducting char inverse study. The strategy used here is to decouple as much as possible all physical and chemical processes to validate the model, and then investigate them one by one before investigate their interactions that could be complex due to the large range of time and length scales involved during pyrolysis .

### 3.6 Modeling assumption and simulation options

Due to the complexity of pyrolysis process in fire conditions, some assumptions are made in this modeling study, and the corresponding phenomena considered and neglected can be seen in Figure 3.2 based on Figure 2.3 in Chapter 2.

Species or element diffusion is not considered in this work, so the element or diffusion mass and energy are not solved. No volume moving or change is considered,

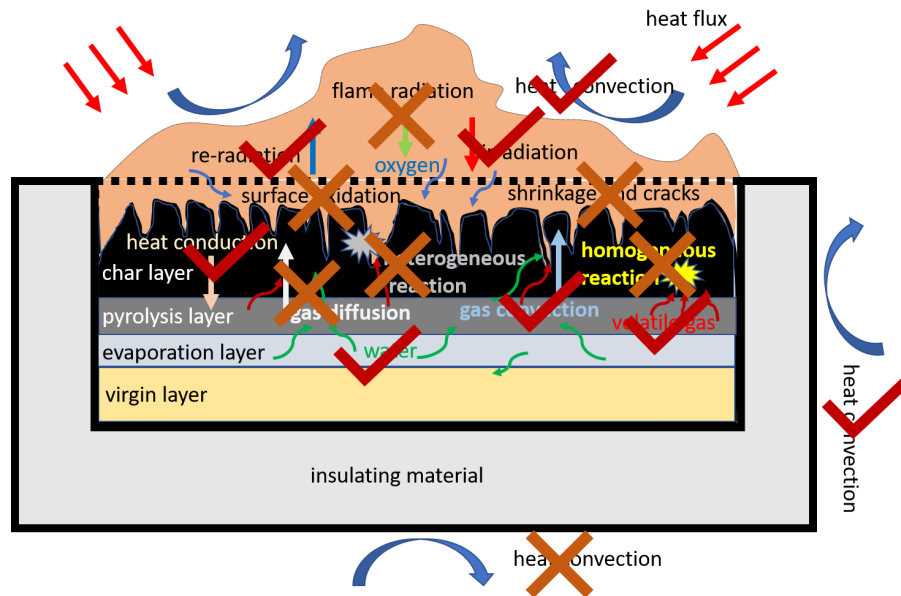


Fig. 3.2 Pyrolysis process assumptions with considered and neglected phenomena in this study

the char ablation phenomenon is not considered and the carbon epoxy composite thermal swelling and wood shrinkage are neglected. The total volume is assumed as constant with the variation of density of each solid phase. The pyrolysis release gas species are assumed as inert gases that have identical thermal and transport properties with Nitrogen, this assumption is also applied in other studies such as [91]. The material is assumed non-transparent thus the in-depth radiation is neglected. The option of tabulated gas properties is chosen and some of the typical simulation options in PATO are shown in Table 3.7.

The local thermal equilibrium is considered between the gas volatiles and solid phase and the gas in the tabulated gas option involves the uniformed Nitrogen as aforementioned. The gas-related properties are present to solve the momentum conservation equation. The momentum conservation equation for gas volatiles is considered to obtain the pressure and gas velocity evolution. The gas volatiles reaction concerning homogenous and heterogeneous is neglected, and the energy is mainly from heat conduction and pyrolysis in the condensed phase.

Table 3.7 Simulation options involved in this study

Gas properties	Energy type	Material properties	Pyrolysis	Gas mass
None	Pure conduction	Pure conduction	None	None
Tabulated gas	Pyrolysis	Porous	Arrhenius	None
Tabulated gas	Pyrolysis	Porous	Arrhenius	Darcy Law

### 3.7 Conclusion

The present Chapter has permitted to present the PATO model used in this study, detailed volume averaging theory is described and corresponding conservation equations are provided as well as the expressions of related material properties. Different kinetic reaction mechanisms concerning wood and carbon/epoxy composite pyrolysis are explained. The boundary conditions at different material surfaces employed in this study are presented to implement the simulations which mainly include TGA, pure heat conduction, and cone calorimeter simulations. Lastly, some model assumptions and corresponding simulation options are given. Based on the PATO model, the objective is now to model the thermal decomposition of the wood studied at the particle scale. In the following parts, the wood micro-scale TGA experiment and the kinetics parameters optimization work are presented in Chapter 4.

## Chapter 4

# Particle scale modeling of the wood pyrolysis

This chapter is dedicated to the modeling of thermal decomposition of wood at the particle scale, i.e. at the TGA (Thermogravimetric Analysis) scale. The approach used is “comprehensive”, it is different from the common manipulation of average kinetic parameters used for all heating rates [76, 51].

The objective of this part is to define a mechanism of thermal decomposition of wood to be implemented into the PATO model and then to obtain each set of parameters for the Arrhenius kinetic equation of each reaction at the corresponding heating rates. Coupled with the kinetic equation, two different reaction mechanisms are used: one-global reaction and one independent parallel multi-reaction schemes to evaluate the effect of reaction schemes choice on the kinetic parameters. The kinetic parameters are obtained first by one heating rate and after they are analyzed to simulate another heating rate case. In parallel to the kinetic study, the heating rate influence on the pyrolysis reaction is also analyzed. Finally, the optimized kinetic parameters (by model fitting method) are evaluated with those found in the literature. All this work is conducted with 0D and 2D axis-symmetry TGA simulation cases to study the heat transfer phenomenon at this scale with the PATO model.

## 4.1 TGA experimental procedure

When conducting the pyrolysis kinetics study, the Thermogravimetric Analysis (TGA) is widely studied to extrapolate the kinetics of materials pyrolysis, as discussed in [100]. Although the TGA experiments are often conducted at multiple heating rates, it is still concerned that they are applicable to estimate the pyrolysis kinetics to other heating rates [10]. Indeed experiments at different heating rates are conducted to quantify the sensitivity of the prescribed kinetic model and to evaluate the validity of the kinetic parameters [135, 82]. This concern has been called by many studies such as [108] to acknowledge the influence of heating rates at different pyrolysis conditions. Even though good fitness can be achieved by the model fitting method to obtain reliable kinetic parameters, it tends to predict poorly the mass loss rate under given heat flux for large samples pyrolysis [10, 165]. Indeed, the fact relies on that TGA heating rates employed are quite different from the heating rates for real materials pyrolysis such as in cone calorimeter experiments [166]. This observation is also found from the experimental data in this study. Moreover, similar to TGA experiments, cone calorimeters are also conducted with multiple heat flux [96, 4, 104] and the low heating rate is observed at low heat flux while with a high heating rate under high heat flux [104]. Again, due to the transient temperature evolution trend, the heating rate at each location within the material can differ seriously versus time [103]. To summarize, the correlation between heating rate and pyrolysis kinetics need to be studied in detail.

As mentioned before, when a solid is exposed to external heat flux, the heating condition is a dynamic process and it depends on the pyrolysis state of the solid and the space location. The heating rates of TGA in this study are linked to the materials heating behavior in the cone calorimeter under different heat flux (this will be discussed in Chapter 5). It is observed that the representative heating rate can be around 10 K/min to 20 kW/m<sup>2</sup>, and more in some specific conditions for example 50 K/min under 50 kW/m<sup>2</sup>. The choice of these two heating rates could be discussed but a compromise is made by choosing the most representative value and what is possible to achieve by experiment in TGA. In order to explore the heating rate influence on the pyrolysis

reaction, it is chosen to extract one set of kinetic data for each heating conditions. The use of different sets of kinetic data aims to point out the interaction between the chemical, heat, and mass transfer processes during cone calorimeter experiments. A common strategy often used in the fire community is to extract one set of kinetic data for many heating conditions to have a kind of “average” data set taking into account heating rate interaction with kinetics [51]. However, this strategy just minimizes the “error” of the model dealing with heating rate influence and does not take into account this parameter “physically” in the model.

The Mettler-Toledo type of TGA thermal balanced apparatus is used to obtain thermal information for TGA data, this apparatus is displayed in Figure 4.1. The Douglas Fir wood is used in this work and the TGA experiments are conducted under an inert atmosphere with a purging Nitrogen flow rate continuously of 90 mL/min to sweep the gaseous volatiles and to limit the influence of the oxygen.



Fig. 4.1 TGA apparatus of Mettler-Toledo type

To engage the experiment data uncertainties, each TGA experiment is repeated at least 3 times to guarantee reproducibility. The virgin samples are firstly powdered with a weight of approximately 5-7 mg. Before the prescribed temperature evolution set for different heating rates, the furnace should last several minutes under ambient temperature to attain the thermal equilibrium within pure nitrogen. Then, the apparatus stopped by decreasing the furnace temperature to ambient temperature. In the second run, the sample is thermally decomposed in the furnace with different

heating rates at the temperature range of 300-1000 K. Thus, the material mass loss profile can be collected.

## 4.2 TGA Experimental results

For the following experimental and numerical results, the term NML refers to normalized mass loss calculated by the ratio of instantaneous mass profile over the initial mass. The term MLR refers to the mass loss rate which is derived by the mass loss profile over time or temperature. The overall NMLR represents the normalized mass loss rate which specifies the ratio of instantaneous reaction rate over the corresponding maximum reaction rate through the decomposition process.

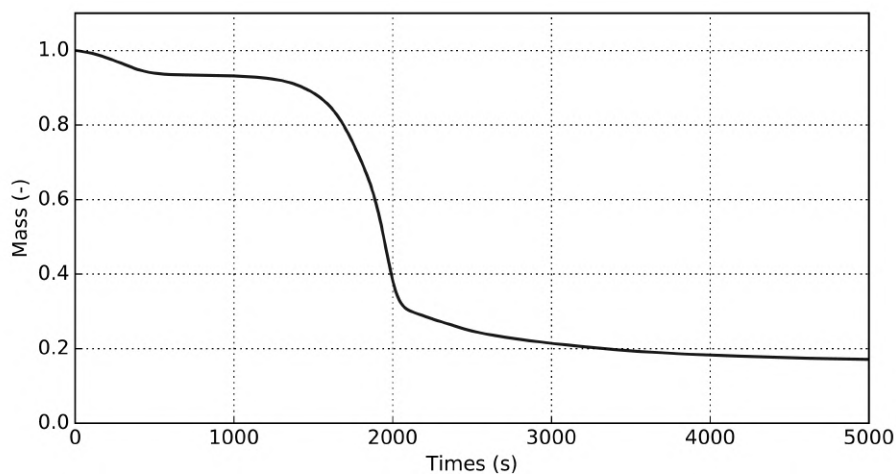


Fig. 4.2 Average experimental NML at 10 K/min of TGA experiment

Figure 4.2 and Figure 4.3 involve the average experimental NML conducted at the same conditions with three times under 10 K/min and 50K/min. The difference among experimental data is calculated to be less than 5%, which demonstrates good experimental repeatability. For results analysis, the mass loss curves calculated by averaging the experimental data are retained [135], as shown in the following Figure 4.4 with the comparison of NML between 10 K/min and 50 K/min.

The TGA experimental MLR and NMLR curves for the two heating rates, i.e. 10 K/min and 50 K/min, are shown in Figure 4.5 and Figure 4.6. Results have been

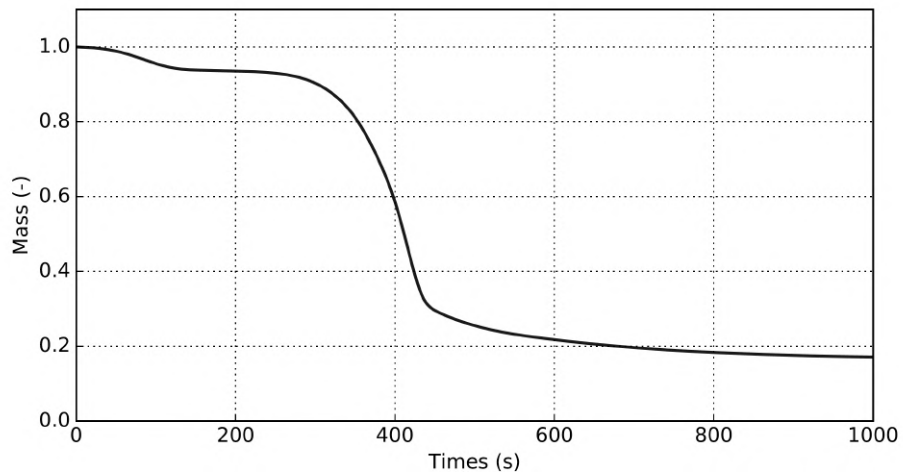


Fig. 4.3 Average experimental NML at 50 K/min of TGA experiment

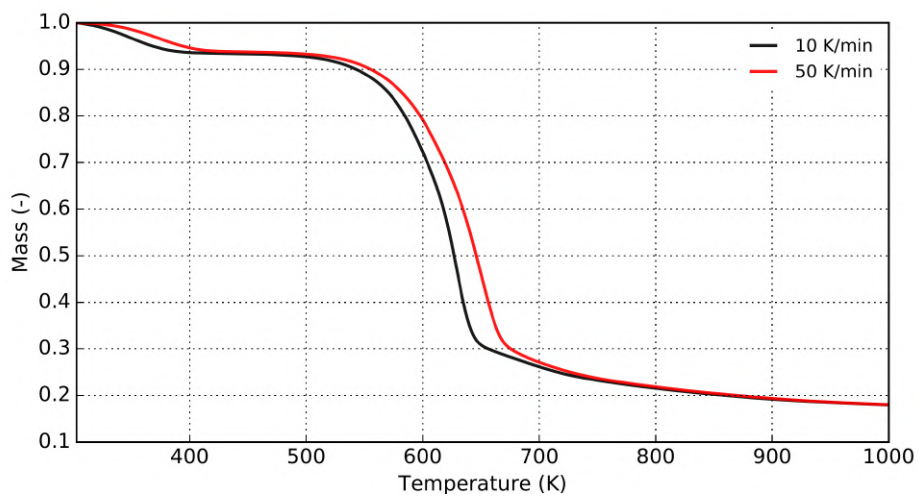


Fig. 4.4 Comparison of experimental NML under 10 K/min and 50 K/min

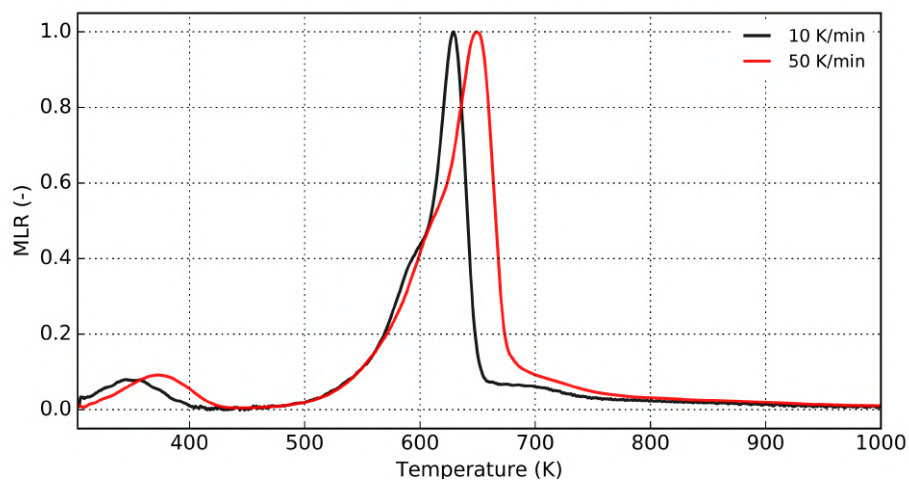


Fig. 4.5 Experimental MLR under 10 K/min and 50 K/min

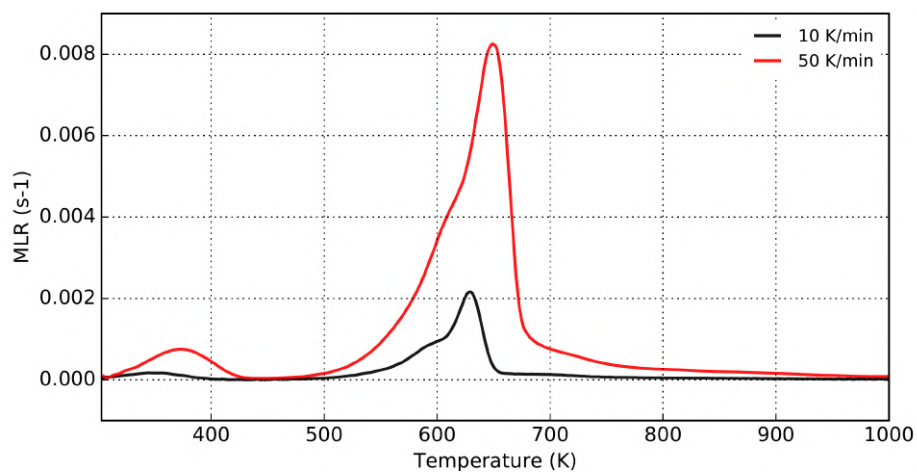


Fig. 4.6 Experimental MLR under 10 K/min and 50 K/min

plotted in function of the temperature of the sample to avoid the time dependence on the kinetics into the plots. Consequently, the heating rate influence on pyrolysis phenomena can be pointed out. With a higher heating rate, the overall reaction rate is higher as shown in Figure 4.5, but the reaction advancement is less as can be seen in Figure 4.4. Indeed, for a given temperature, the total mass loss under 50 K/min is less than the one for 10 K/min Figure 4.4. The maximum MLR is achieved at 629 K for 10 K/min while it is at 649 K for 50 K/min, some level of deviation is presented with a delay of 20 K, as it is classically shown in the literature [56].

It can be seen from figure 4.4 that the higher material remaining mass fraction tends to be present under higher heating rates, before approximately 800K. This observation agrees with the finding that more mass fraction of material residues could be present under a higher heating rate, with the presence of a lower amount of volatile gases released [65]. Here, the mass residue represents the remaining mass involving reaction and the final mass residue is the mass residue after the termination of pyrolysis. However, the final mass residue consists of approximately 20 wt% of the initial one for both heating rates, thus, the final mass residue fraction seems to be independent of the heating rate. Indeed, during this whole pyrolysis process, there exist different factors influencing the mass residue fraction such as the heating rate, final experiment temperature, atmospheric pressure, retention time for released gas, inorganic presence, etc [37].

For both heating rates, the higher reaction rate is achieved when 50 wt% of the mass is consumed and this value could be viewed as an “equilibrium” state. For a mass fraction of the virgin material more than 50 wt%, the kinetic process is governed by the temperature rise of the sample, because there still exists enough mass to decompose while accelerating the process. When it comes to less than 50 wt% of virgin mass fraction, the remaining virgin mass is not sufficient to maintain the reaction rate rising with the temperature. The remaining mass becomes the limited parameter on the overall reaction process. This typical value of virgin mass fraction could be viewed as a

“stoichiometric value” to make a comparison with the stoichiometric mixture fraction value of a gas mixture at which the reaction rate is maximum.

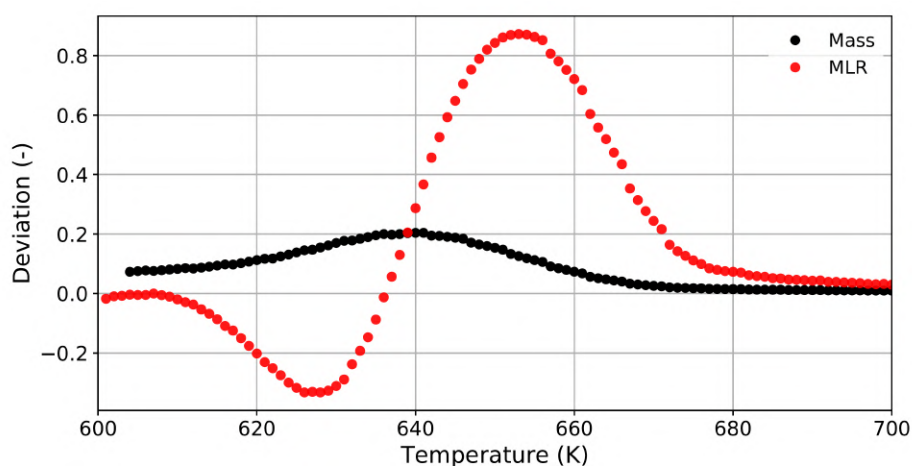


Fig. 4.7 Deviation of NML and NMLR between 10 K/min and 50 K/min

Figure 4.7 plots the deviation of experimental NML and NMLR between the 2 heating rates. The curves are calculated against the data difference, i.e. the data at 10 K/min subtracted by the data at 50 K/min. The maximum NML difference occurs at 641 K and can reach more than 20 wt% of the initial mass. Regarding the NMLR, the maximum difference occurs at 656 K and reaches more than 85% for relative error on NMLR. The heating rate does not affect in the same order of magnitude of NML and NMLR values in terms of relative errors.

Regarding NMLR evolution neglecting the water evaporation part, it is found that the first peak is attributed to hemicellulose thermal decomposition reaction, the second peak which corresponds to the highest MLR value is related to cellulose reaction and the third one involves the lignin reaction (Figure 4.6) [37]. Thus, when observing the NMLR curves (Figure 4.6), only the reaction concerning cellulose thermal decomposition seems to be affected by the heating rate in terms of the onset temperature range. The 2 other reactions regarding hemicellulose and lignin seem to be not affected by the heating rate evolution due to the presence of curves superposition. To confirm such phenomenon peak deconvolution is made to extract reaction rates of each component.

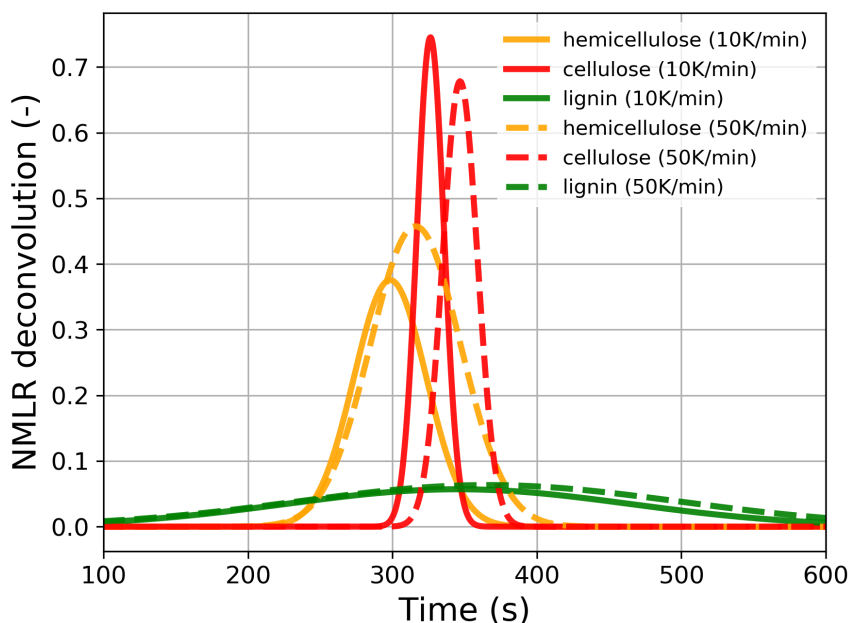


Fig. 4.8 Deconvolution of experimental NMLR at 10 K/min and 50 K/min (the solid line is 10 K/min, the dashed line is 50 K/min)

Figure 4.8 presents the experimental deconvolution of NMLR (overall NMLR summed by different components) curves by using a sum of bell-shaped functions [167]. Those curves involve two heating rates for each component, i.e., hemicellulose, cellulose, and lignin. The solid curves are the deconvolution peaks of experimental NMLR at 10 K/min and the dashed ones involve 50 K/min.

We focus on the pyrolysis process concerning the pyrolysis of hemicellulose, cellulose, and lignin. The two reaction peaks regarding lignin pyrolysis under the two heating rates are superposed relatively well (slight deviation present at the second half part of reaction peak) thereby demonstrating that the reaction is not affected too much given different heating rates. Moreover, the heating rate doesn't affect the onset temperature of the hemicellulose reaction. Indeed, good superposed curves at the onset of reaction temperature point for hemicellulose reaction can be noticed under the two heating rates. However, the reaction rate peak magnitude is much higher in the case of 50 K/min and the duration range of temperature is also larger. It can

be so demonstrated that a higher heating rate tends to promote the intensity and duration of hemicellulose reaction. However, the reaction rate peak value is smaller for cellulose decomposition reaction at 50 K/min and the onset temperature to start the reaction is higher. Thus, a higher heating rate seems to weaken the cellulose thermal decomposition process, with a larger temperature range of reaction when the heating rate increases. This analysis is based on curve deconvolution with a mathematical method. Regarding such consideration conclusions made should be confirmed with a physical model involving each reaction.

To summarize this part of experimental results at the TGA scale, wood pyrolysis is a complex phenomenon involving reactions with its major components, such as cellulose, hemicellulose, and lignin. It is demonstrated that the heating process can interact with the global pyrolysis process. However, one part of the overall complexity is that each reaction of thermal decomposition is not affected in the same way by the heating process.

The last point is fundamental and involves the complexity to deal with this effect in a numerical model. As the way to include this dependence into the pyrolysis model is fundamental, it is chosen in this study to avoid this point for simplicity firstly (two heating rates chosen to obtain each set kinetics) and it should be treated as a perspective work.

### 4.3 TGA Pyrolysis modeling study

Before conducting modeling work, some basic sample information is collected. The density of the Douglas Fir wood is measured and is equal to 467 kg/m<sup>3</sup>. The free moisture content has been measured and varies from 8 to 12 wt% of the virgin wood. A mean value of 10 wt% has been chosen and is fixed in the numerical model. Such value is under the classical plot of the equilibrium moisture content (%) as a function of the temperature and relative humidity of the atmosphere [158]. The initial mass fraction of components (cellulose, hemicellulose, and lignin) have also been fixed into

the numerical model following [158], which specifies that for each component mass fraction softwood, it involves around 42 wt% of cellulose, 27 wt% of hemicellulose, 28 wt% of lignin, and 3 wt% of extractives, respectively. In this study, the extractives are neglected due to their slight mass fraction.

Due to the complexity and uncertainties of kinetics, in order to assess the predictability for different reaction schemes, simple one-step global and complex independent parallel reaction schemes with  $n$ th order reaction model are proposed to describe the material thermal decomposition behavior. To evaluate the assumption without the presence of heat transfer through the sample in TGA experiments, the specified results with modeling study of 0D and 2D axis-symmetry are analyzed. For the mass transfer part in the modeling study of 2D axis-symmetry, it is assumed that the diffusion of gas species has no effect on thermal decomposition and they are specified as nitrogen. The model-fitting method is adopted to estimate the kinetic parameters and stoichiometric coefficient, i.e.,  $A$ ,  $E$ , and  $n$ , fitting the TGA experiment curves mathematically. This modeling fitting process is predicted by Genetic Algorithm (GA) [168, 169], which is performed in the Dakota optimization package [164]. The Genetic Algorithm is widely used for optimization study to obtain kinetic and thermal parameters in current fire scenario research [53].

The two reaction schemes are shown in Figure 4.9 with a one-step global reaction scheme, and in Figure 4.10 with four independent parallel reaction scheme. The four parallel reactions correspond to four wood components: water, hemicellulose, cellulose, and lignin, respectively. The overall pyrolysis rate is described by the linear combination of reaction rate concerning these four pseudo-components, and it can be seen in Chapter 3 with the PATO model description. The reaction rate concerning each component obeys the non-linear Arrhenius varying with temperature and mass. Based on the initial mass for each component,  $F$  denotes the mass fraction of gas volatiles,  $\nu$  denotes the mass fraction of residue char. And the  $\nu_h, \nu_c, \nu_l$  are the mass fraction of residue char produced by hemicellulose, cellulose, and lignin, respectively.

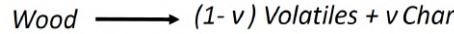


Fig. 4.9 One-step global reaction scheme of wood pyrolysis

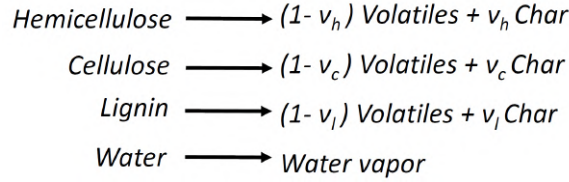


Fig. 4.10 Four independent parallel reactions scheme of wood pyrolysis

The optimization process is based on the comparison between simulation and experimental data, i.e., mass loss and mass loss rate. When using the Genetic Algorithm method, the number of generations of optimization plays a key role in obtaining good predictions. The number of 200 generations [137] is mostly used when studying TGA result optimization, which could provide high optimization efficiency. The Genetic Algorithm parameters set in this work are consistent with [97] which uses 200 populations and 200 generations. Based on the Dakota optimization analysis, the fitness between the experiment and simulation data are achieved, and the best sets of corresponding kinetic parameters are obtained concerning the two reaction schemes, which are listed in Table 4.1 for the one-step global reaction scheme and Table 4.2 for the parallel reactions scheme. The objective fitness value in Dakota is calculated with 0.00015 by the comparison between experimental and optimized mass loss profile, and the acquisition of qualified kinetic parameters is approval, detailed information regarding best sets of fitness value in Dakota can be seen in [164].

Table 4.1 Optimized kinetic parameters with the one-step global reaction scheme

10 K/min	Optimized values	50 K/min	Optimized values
F	$8.0305833137 \times 10^{-1}$	F	$7.7772829178 \times 10^{-1}$
A	$1.0000000000 \times 10^{19}$	A	$6.8159095570 \times 10^{19}$
E	$2.4402745742 \times 10^5$	E	$2.5254334794 \times 10^5$
n	2.9493770101	n	2.7306261927

Table 4.2 Optimized kinetic parameters under independent parallel reaction scheme (1,2,3,4 denote hemicellulose, cellulose, lignin, and water reaction, respectively)

10 K/min	Optimized values	50 K/min	Optimized values
F1	$9.6184767013 \times 10^{-1}$	F1	$8.6749124251 \times 10^{-1}$
A1	$6.2172706189 \times 10^9$	A1	$5.4443491175 \times 10^9$
E1	$1.3384861088 \times 10^5$	E1	$1.2732139592 \times 10^5$
n1	2.3933359170	n1	2.8815899840
F2	$8.0523331343 \times 10^{-1}$	F2	$8.6882034543 \times 10^{-1}$
A2	$9.4720434232 \times 10^{18}$	A2	$4.2096335072 \times 10^{19}$
E2	$2.5130681782 \times 10^5$	E2	$2.5490106863 \times 10^5$
n2	1.0566099598	n2	1.7822540401
F3	$7.4496529402 \times 10^{-1}$	F3	$7.4004100475 \times 10^{-1}$
A3	$2.9532717773 \times 10^5$	A3	$4.7759652153 \times 10^5$
E3	$8.2465715205 \times 10^4$	E3	$8.6791730014 \times 10^4$
n3	4.6943364114	n3	4.5472070796
F4	1.0	F4	$7.7772829178 \times 10^{-1}$
A4	$2.4865188829 \times 10^{11}$	A4	$2.9877698212 \times 10^{12}$
E4	$8.7379599184 \times 10^4$	E4	$9.4821330763 \times 10^4$
n4	2.2880878236	n4	2.6829532421

The Figures 4.11 and 4.12 represent the experimental and optimized data of NML and MLR for the two reaction schemes at 10 K/min and 50 K/min, respectively.

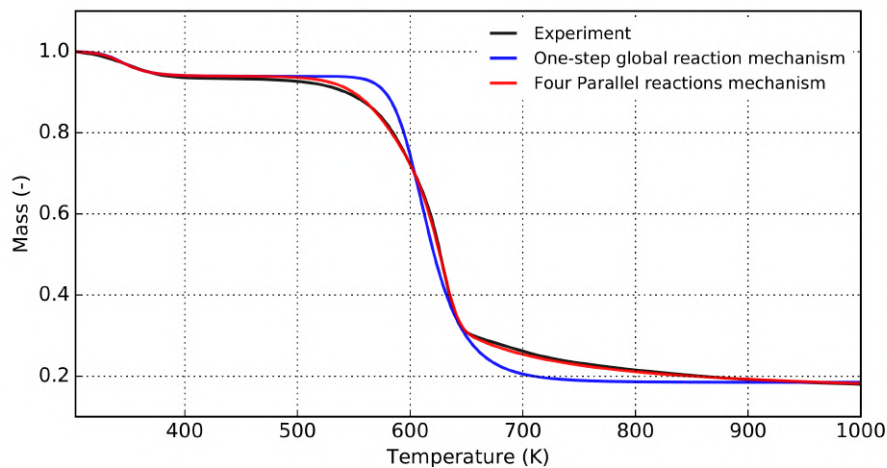


Fig. 4.11 Experimental and optimized NML under different reaction schemes for 10 K/min

Observing the corresponding predicted data, for both heating rates, the two schemes fit well for the water evaporation process (the optimized peaks before 400

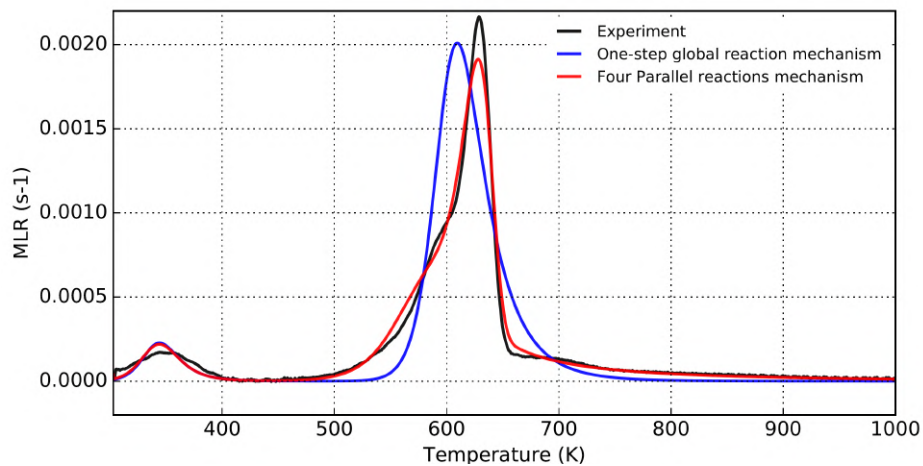


Fig. 4.12 Experimental and optimized MLR under different reaction schemes for 10 K/min

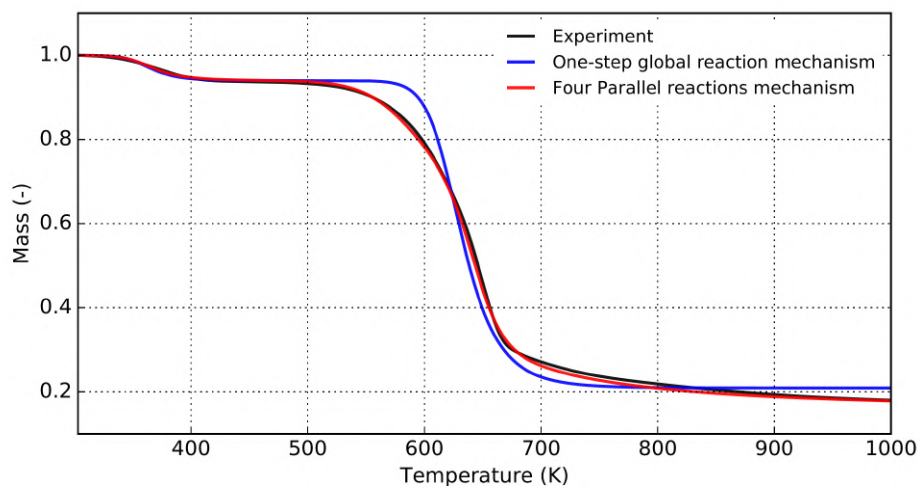


Fig. 4.13 Experimental and optimized NML under different reaction schemes for 50 K/min

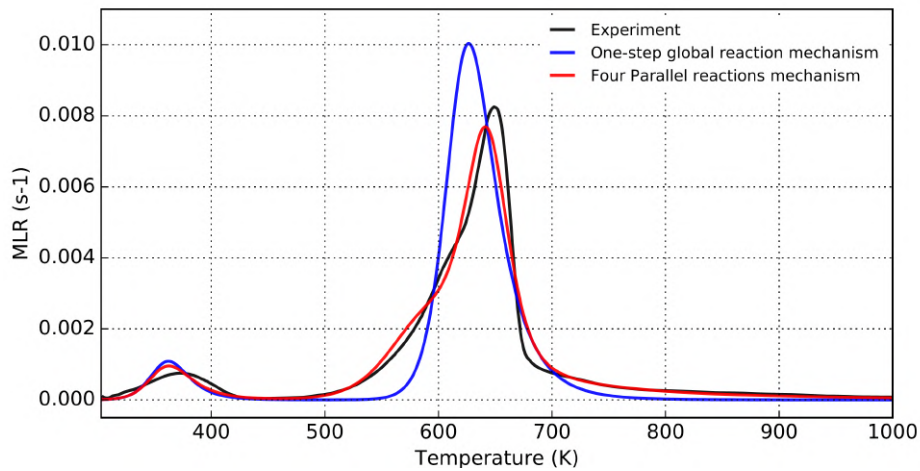


Fig. 4.14 Experimental and optimized MLR under different reaction schemes for 50 K/min

K), so the water evaporation is independent of pyrolysis reaction schemes. However, compared with the parallel reaction scheme, the one-step global reaction scheme doesn't capture well the MLR peak value and the temperature range at which the pyrolysis reaction occurs, this can be seen from approximately 500 K to 800 K. Thus, it seems that the kinetics are not predicted qualitatively well with the one-step global reaction scheme compared with the parallel one. This observation can be caused by its inability for characterizing the complex thermal behavior for different components over a wide temperature range. However, from a macroscopic view, targeting experimental and numerical mass loss profile, the one-step global mechanism success to represent the overall pyrolysis trend, so such a mechanism could be applicable to describe the pyrolysis process when a fire is fully developed. Indeed, the virgin mass evolution (Figure 4.11) is well captured when 40 wt% to 70 wt% of virgin mass remains to react. This range is around the so-called "stoichiometric value" introduced before, which corresponds to the maximum reaction rate of the overall pyrolysis process where the heating process is less interacting because reactions are fast. When reactions are slower under high temperatures, the pyrolysis process is governed by the remaining mass to react which mainly depends on lignin thermal decomposition. This one is not captured by the one-step global mechanism. For low temperatures, where reactions are governed

by the heating process, the simple mechanism fails to capture such a trend. It could not describe correctly solid ignition phenomena which depend on pyrolysis gas release when hemicellulose begins to decompose and the end of the process governing the remaining mass fraction of char (indeed, the thermal decomposition of lignin results in a high char yield).

For both heating rates, the independent parallel reaction scheme fits quite well, with an error of less than 10% [56, 135], the TGA experimental curves of NML and MLR, although there exist some minor. When observing the mass loss rate profile, the model under-predicted the peak magnitude around 5-8% for both heating rates. This error is approximated by the standard deviations between experiment and simulation upon the temperature. This peak magnitude error could be attributed to the initial mass and sensitive stoichiometric values. Indeed, the overall peak and shoulder profile are the linear combinations of different components thermal decomposition as aforementioned, i.e. hemicellulose, cellulose, and lignin. They could have quite different reactivity under the temperature stages and yield a different mass fraction of final residue as mentioned above. Thus, this relatively slight discrepancy is quite acceptable for the optimized values.

The optimized stoichiometric values obtained in this work for the reactions of thermal decomposition of hemicellulose, cellulose, and lignin concerning the independent parallel reaction scheme are consistent with the literature [111]. They correspond to a gaseous volatile mass fraction of approximately 80 wt%, the lignin can supply the largest mass residue.

It can lead to different kinetic triplets within a relatively wide range for different heating rates, as can be found in [51]. When analyzing the kinetic values for different heating rates, the variation of pre-exponential factor and activation is relatively small, which shows no compensation effect between activation energy and pre-exponential factor. The compensation effect implies that a larger pre-exponential factor corresponds to a smaller activation energy. However, it seems that the heating rate doesn't influence the activation energy and the pre-exponential factor linearly. For example, the optimized

activation energy for hemicellulose reaction under a high heating rate is lower but the pre-exponential factor is also lower compared with those under a low heating rate. The activation energy value for hemicellulose and cellulose is approximately 100 kJ/mol and 250 kJ/mol and are within the range of variation reported in the literature [37, 24]. It is apparent that the optimized reaction order value for lignin is relatively high compared to the one for hemicellulose and cellulose decomposition. As noted, in some studies, a 1st order reaction model could predict well hemicellulose and cellulose thermal decomposition, while for lignin, it is not appropriate when under multiple heating rates condition [51]. It could be concluded that the reaction order for lignin is quite hard to determine.

### 4.3.1 Numerical comparison under different heating rates

As already mentioned, when analyzing the experimental data, the heating rate of the sample is one of the key parameters that govern the pyrolysis process. To examine the detailed thermal decomposition behavior of wood components under different heating rates, the comparison of numerical prediction is carried out regarding NML, MLR, and NMLR. Figure 4.15-4.17 shows the NML, MLR, and NMLR of the three wood components and water at 10 K/min (solid lines) and 50 K/min (dashed lines).

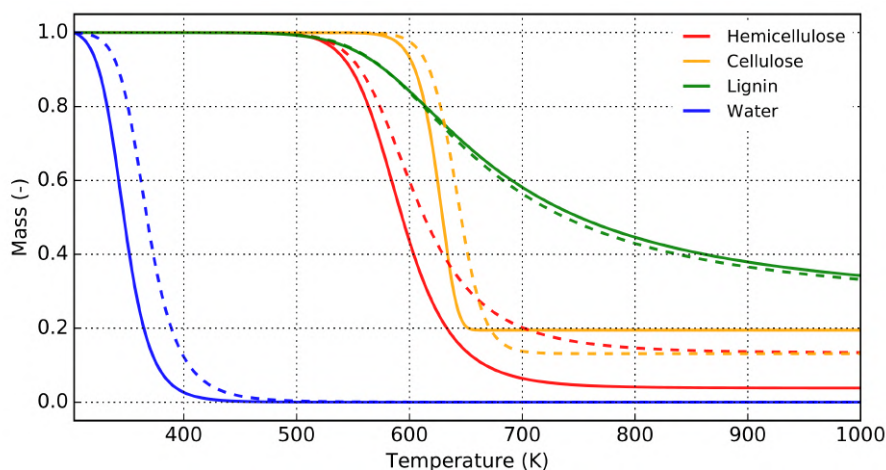


Fig. 4.15 NML profile for wood components for 10 K/min (solid lines) and 50 K/min (dashed lines)

It can be observed from Figure 4.15, that the thermal decomposition of water, hemicellulose, cellulose, and lignin correspond to different temperature ranges with different mass residue. Their decomposition temperature ranges are respectively: 300-450 K, 500-750 K, 550-750 K, 450-1000 K. The thermal decomposition of hemicellulose and cellulose occurs relatively over a short temperature range while the lignin decomposes experience a wide temperature range. This is attributed to the overall slow thermal decomposition of wood.

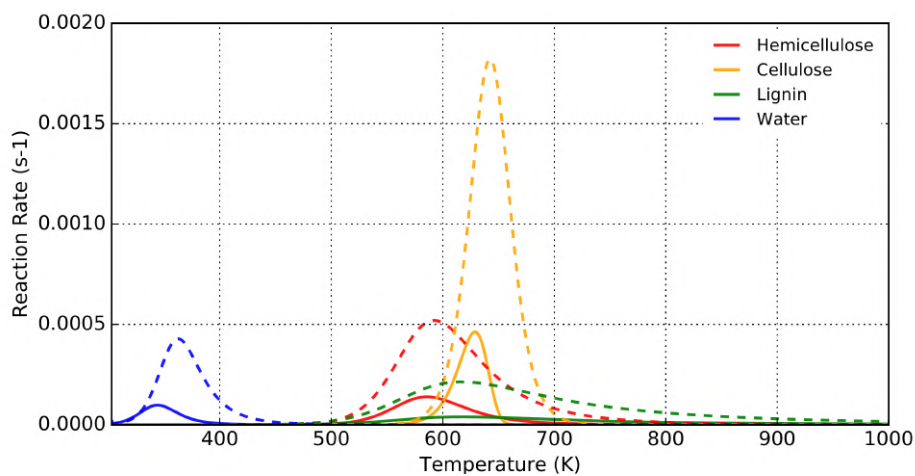


Fig. 4.16 MLR profile of wood components for 10 K/min (solid lines) and 50 K/min (dashed lines)

When observing Figure 4.16, at a higher heating rate, the shoulder and the peak reaction rate for all the components shift apparently to the sites at higher temperature with a much serious increment of peak value, this is consistent with the observation [135]. This lag in higher temperature can be due to a kinetic effect or to a thermal gradient, as noticed that the thermal gradient under high heating rates can shift the MLR curve to a higher temperature range with a higher peak value [135].

As pointed out, when analyzing experimental results and deconvolution plots, the heating rate affects the kinetic of each reaction in different ways. In Figure 4.17, the corresponding numerical results confirm that the heating rate has nearly no impact on the lignin thermal decomposition. Indeed, the NMLR of lignin decomposition at 10 K/min and 50 K/min are quite superposed. Conversely, the thermal decomposition of

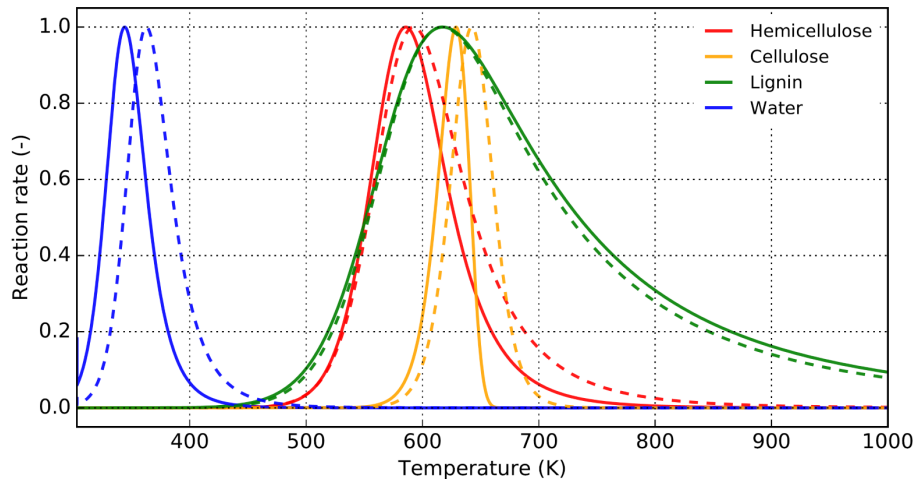


Fig. 4.17 NMLR profile of wood components for 10 K/min (solid lines) and 50 K/min (dashed lines)

hemicellulose and cellulose are affected by the heating process. The two reactions are extended to higher temperatures for higher heating rates. When observing the NMLR from 10 K/min to 50 K/min in Figure 4.17, the onset of cellulose reaction is shifted to higher temperatures, thus the beginning of the cellulose reaction is delayed. However, this variation trend isn't present for hemicellulose reaction, the beginning reaction of hemicellulose is not affected too much by the heating process. The reaction rate concerning the rising part of the hemicellulose decomposition is nearly the same at 10 K/min and 50 K/min. The shift to higher temperatures is observed mainly when the hemicellulose reaction rate begins to decrease. From Figure 4.17, we also observe the lignin reaction rate shows a very slight difference under different heating rates, and it can be specified as invariant when comparing the difference in the case of hemicellulose and cellulose reaction. As already mentioned, even though the heating rate can affect the remaining mass fraction, when temperatures reach very high values (approximately 1000 K), the mass fraction of the total char residue is nearly the same for the two heating rates (Figure 4.4). This can be argued with Figure 4.15. Indeed, the lignin decomposition can produce the largest mass fraction of char residue at the end of the pyrolysis process, and this char residue doesn't change with heating rate. However, the heating process changes the mass fraction of char residue given by the cellulose

and hemicellulose reactions (Figure 4.15). For cellulose, the higher heating rate can give less residue by approximately 5 wt% while more residue (approximate 15 wt%) is present for hemicellulose reaction. The dependence of the residue mass fraction on the heating process is not so clear and seems to depend locally on each reaction evolved in the pyrolysis process. Detailed finite rate chemistry is probably necessary to capture numerically correctly the char front dynamic during the pyrolysis process. This one is also strongly linked with possible heterogeneous reactions when the surrounding atmosphere is oxidative.

### 4.3.2 Analysis of the influence of the kinetic parameters

To analyze deeply the role of the heating process on pyrolysis reaction, the error generated by the kinetic data extraction is investigated. This part concentrates on a parallel reaction scheme to investigate the reaction behavior for different components. To capture correctly the chemical reaction for the two heating rate cases, we choose to extract different kinetic parameters by using the Genetic Algorithm optimization for each heating case. As discussed above the kinetic data extracted for the two heating cases are different. It is firstly argued that the heating process can influence the chemistry otherwise the two sets of kinetic data should be approximatively the same when taking into account experimental errors.

But it is not the right way to proceed like this because heating process influences are involved in the kinetic values triplet and the physical sense of such a method is questionable. To “quantify” in which manner the heating process changes the chemistry, the kinetic parameters optimized at 10 K/min are used to simulate the thermal decomposition at 50 K/min. Correspondingly those optimized at 50 K/min are used to simulate the pyrolysis at 10 K/min. The discrepancies in the two simulations are analyzed and will give us more understanding of heating interaction during the pyrolysis process.

Figure 4.18 shows the comparison between the optimized NMLR and simulated NMLR using the kinetic parameters by the different heating rates. Two different curves

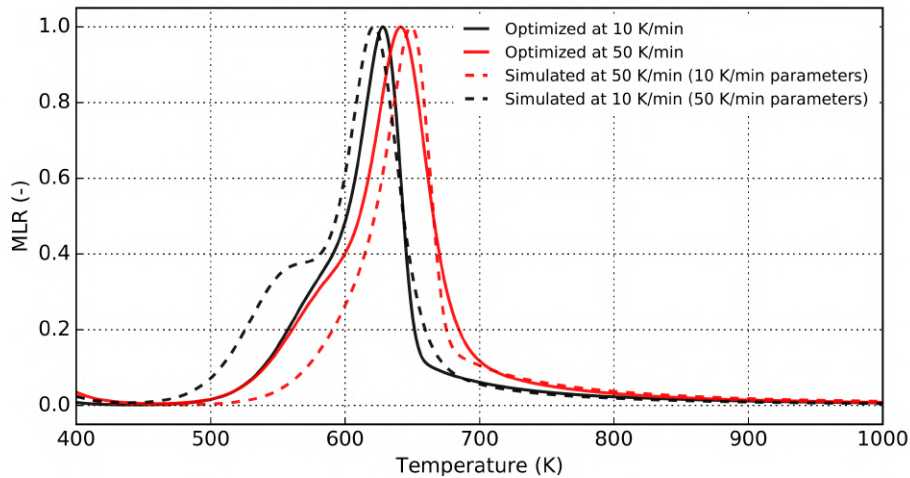


Fig. 4.18 Optimized NMLR at 10 K/min (black solid line) and simulated at 10 K/min (black dashed line) with kinetic parameters optimized at 50 K/min (correspondingly for other two curves at 50 K/min)

regarding one heating rate can be observed. To specify a little, the black solid line is the optimized NMLR at 10 K/min against the experimental data of 10 K/min. The black dashed line is the simulated NMLR at 10 K/min using the kinetic parameters from the 50 K/min which correspond to the optimized values against experimental data at 50 K/min. Correspondingly, the red solid line is the optimized NMLR at 50 K/min against the experimental data of 50K/min. The dashed red line is the simulated NMLR at 50 K/min using the kinetic parameters from the 10 K/min which correspond to the optimized values against experimental data at 10 K/min.

Figure 4.19 permits to plot the NMLR discrepancy evolution between the two curves for each heating rate as described. To observe a positive discrepancy value at the onset temperature of pyrolysis, the discrepancy for 10 K/min corresponds to the optimized NMLR data subtracted by the simulated NMLR data. The discrepancy for 50 K/min corresponds to the simulated NMLR data subtracted by the optimized NMLR data.

Figure 4.20 plots the comparison for different components regarding the optimized reaction rate and simulated reaction rate using the kinetic parameters by different heating rates. To specify a little, the solid line is the optimized reaction rate at 10

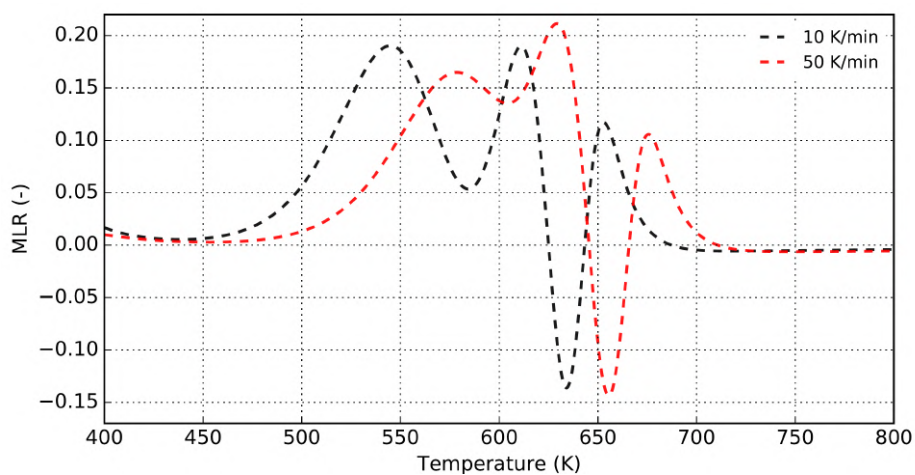


Fig. 4.19 NMLR difference between optimization and simulation at 10 K/min (correspondingly at 50 K/min)

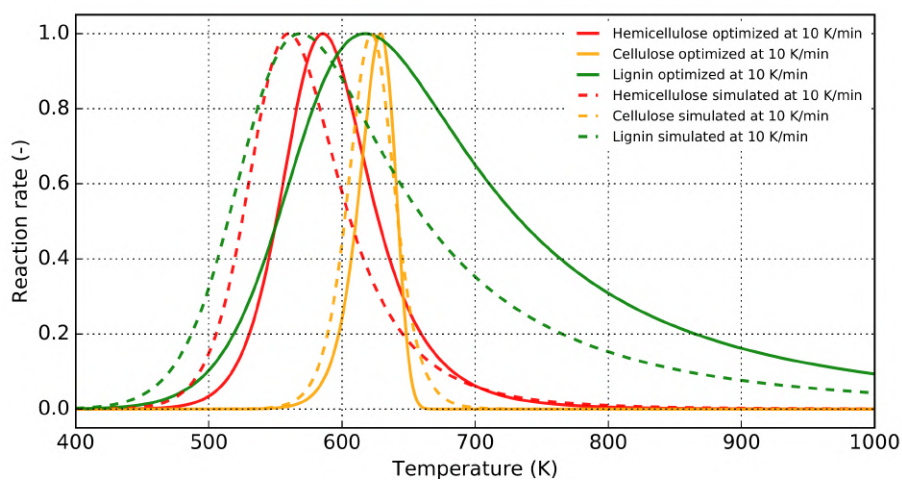


Fig. 4.20 Reaction rates of wood components at 10 K/min (optimized and simulated)

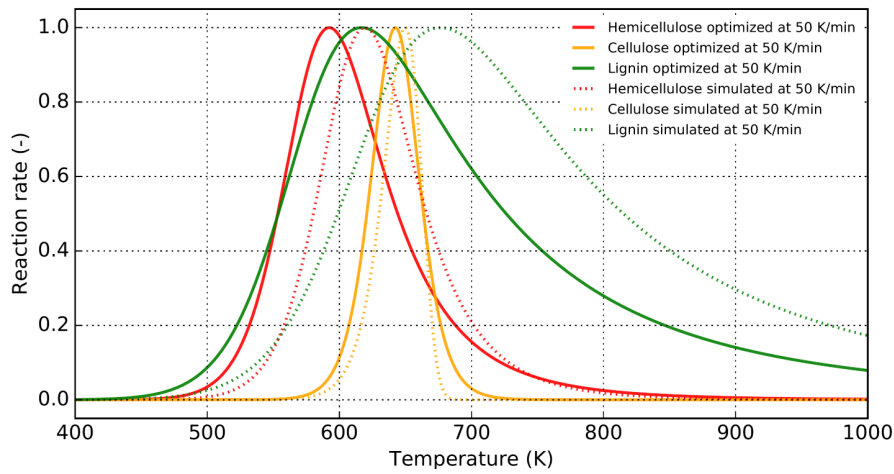


Fig. 4.21 Reaction rates of wood components at 50 K/min (optimized and simulated)

K/min against the experimental data. The dashed line is the calculated reaction rate at 10 K/min using the kinetic parameters from the optimization of 50 K/min. Correspondingly, Figure 4.21 shows the comparison at the case of 50 K/min, the solid line is the optimized reaction rate, and the dashed line is the calculated reaction rate.

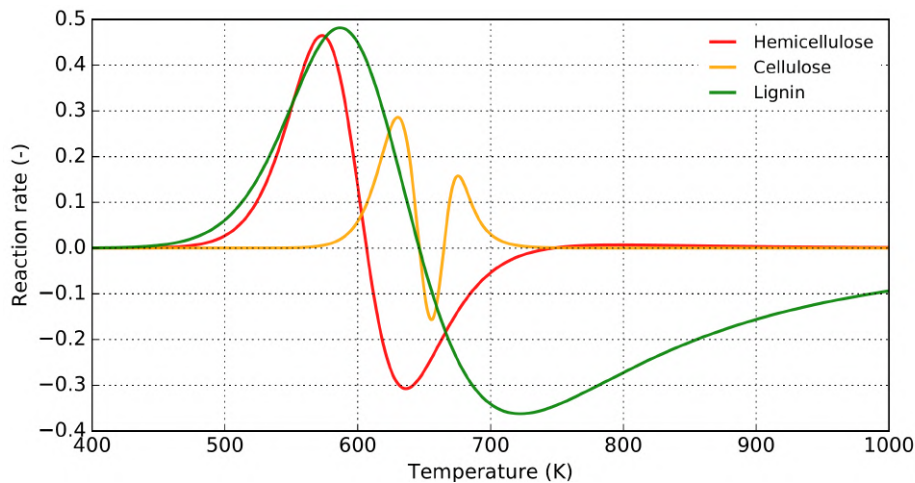


Fig. 4.22 The difference of each wood component reaction rate between optimized and simulated at 10 K/min

Figure 4.22 and Figure 4.23 concern each component reaction rate difference at 10 K/min and 50 K/min, respectively. The same manipulation taken with overall NMLR difference (Figure 4.19), the difference at 10 K/min corresponds to the optimized reaction data subtracted by the simulated reaction rate, while at 50 K/min, the

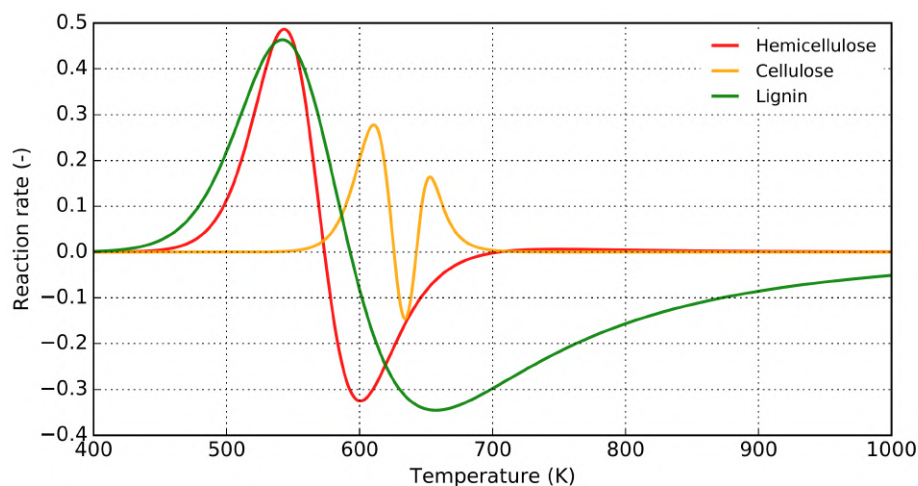


Fig. 4.23 The difference of each wood component reaction rate between optimized and simulated at 50 K/min

difference represents the simulated reaction rate subtracted by the optimized reaction rate data.

As displayed from the above figures (Figure 4.18-4.23), significant discrepancies are observed in the two heating cases. When simulating a low heating rate case (10 K/min) with optimized kinetic parameters at 50 K/min, all reactions are shifted to lower temperatures (Figure 4.18). The opposite trend (i.e., all reactions are shifted to higher temperatures) is observed when a high heating rate case (50 K/min) is simulated with optimized parameters at 10 K/min). But when observing Figure 4.19 which plots the discrepancies between the simulated and optimized data for each heating rate, we can find that the curves are not superposed and the shape changes notably at the beginning of the pyrolysis process. Then, the heating condition has a “nonlinear” impact on the pyrolysis process. When we focus on the difference of reaction rates for each component in the two heating cases (Figures 4.20 and Figure 4.21), the same behavior is observed: reaction rate of each component is shifted to lower temperatures at 10 K/min while it involves an opposite shift trend at 50 K/min, as discussed previously regarding Figure 4.18. But the reactions of the three components are not impacted in the same manner. For the two heating cases, hemicellulose and lignin reactions are much sensitive to

kinetic data change (under different heating rates) than the cellulose with much larger shifts, i.e., higher reaction rates difference (Figure 4.22 and Figure 4.23).

One strategy to deal with heating rate impact is to optimize the chemistry and to find a kind of “average set of kinetics” minimizing errors when simulating different heating conditions with the same set of kinetic data, as mentioned above. It is demonstrated here that this strategy should fail to capture correctly the heating rate impact on pyrolysis, especially when a multiple reactions mechanism is used in a numerical model thereby minimizing these global errors.

The heating condition seems to have a non-linear interaction with the pyrolysis process. Here “linear” means that the difference of kinetic data should be approximately the same when low heating case change to high heating case and the opposite, and also the impact of heating condition change on each component reaction rate involve the same extent.

The parallel mechanism used here cannot be used when the heating condition is a key parameter in the pyrolysis process. It has been shown that it is especially applicable for conditions when the reaction is slow compared to the heat transfer process, because slow reactions are very sensitive to kinetic parameters, as seen in literature review Chapter 2. One strategy to take into account the heating process reaction into the pyrolysis model could be chosen by using mechanisms with competitive and consecutive reactions. Such mechanisms would allow defining some prior reactions pathway in function of the heating process. In this work, it has been chosen to continue using the independent parallel reactions to point out the advantages and drawbacks of such mechanism correlated with the heating condition at the cone calorimeter scale. But the implementation of such a mechanism should be a serious perspective of this work.

### 4.3.3 Analysis of the 0D and 2D modeling influence

Two regimes have been identified during the thermal decomposition of wood. The first involves faster chemistry occurring when cellulose decomposes (smaller temperature range in Figure 4.20 and Figure 4.21). It has been demonstrated that this regime

is not too sensitive to the heating process. The heating rate at which the kinetic parameters are extracted could not affect too much the prediction of such reaction which is consistent with the former conclusion. The second one involves slower chemistry when hemicellulose and lignin react (larger temperature range in Figure 4.20 and figure 4.21). The slower chemistry is influenced by a limited number of factors among them. Firstly, at high temperatures, the chemistry (represented by reaction rate) is governed by the remaining mass to burn. At low temperatures, the chemistry is governed by the heating process making the sample temperature rise. As the heating process plays an important role in the thermal decomposition, 2D simulations have been conducted to analyze the possible thermal gradients into the solid in TGA configuration. Also, to verify if conclusions made with 0D modeling are consistent with the 2D cases, and to explore that if the kinetics under the heating rates studied can represent those encountered in real fires concerning.

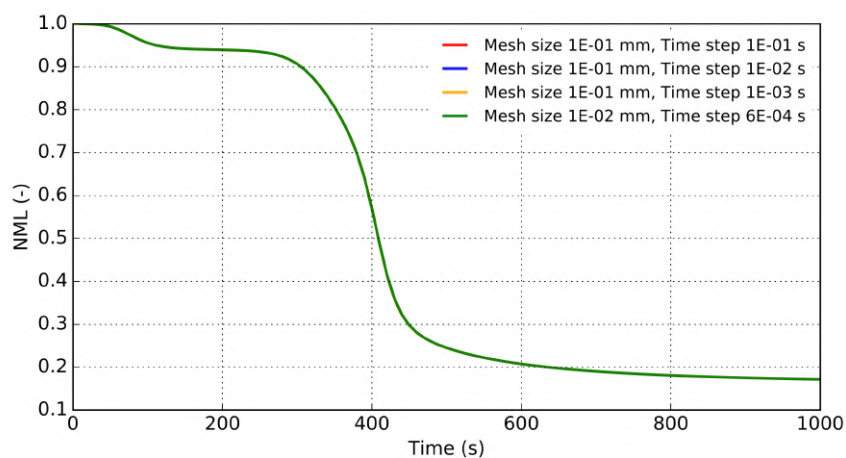


Fig. 4.24 Mass evolution for different mesh sizes and time steps

In order to analyze the assumption of no presence of significant heat and mass gradient in the sample during the TGA experiment, two simulation cases are performed with the PATO model: the case for 0D which neglects the heat and mass transfer, and the case for 2D axis-symmetry considering the heat and mass transfer. Different mesh sizes and time steps have been tested to guarantee the independence of results against mesh and time step. As shown in Figure 4.24, four sets of mesh size and time step are

tested thus guarantee that results are independent of mesh size and time step. The mesh size varies between 0.1mm and 0.01 mm, while the timestep varies with 0.1 s, 0.01 s, 0.001 s, and 0.0006 s, respectively.

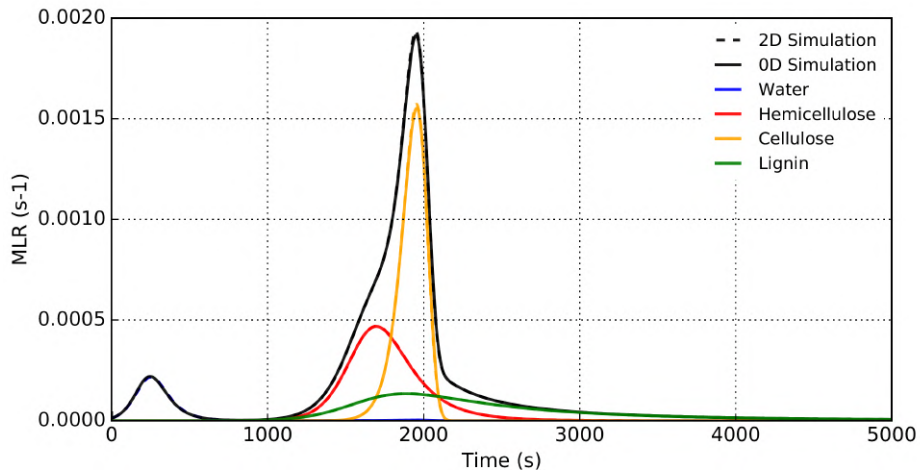


Fig. 4.25 MLR for 0D and 2D mesh at 10 K/min

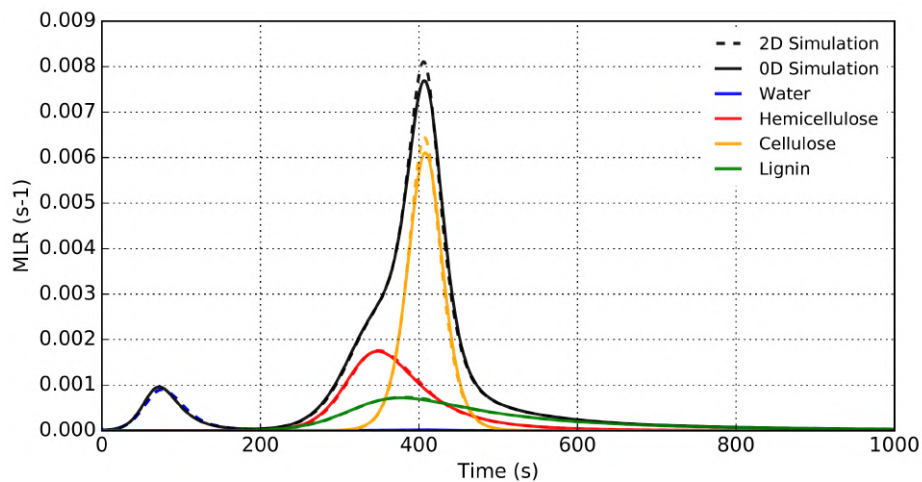


Fig. 4.26 MLR for 0D and 2D mesh at 50 K/min

Figure 4.25 and Figure 4.26 shows MLR with 0D and 2D mesh, at 10 K/min and 50 K/min, respectively. These two figures permit to study the influence of the 0D and 2D modeling. It shows that only the cellulose decomposition peak magnitude has a minor difference which accounts for approximately 5% at 50 K/min. For the heating rate of 10 K/min, no apparent differences are observed. Even though it seems that the

overall thermal decomposition is not affected significantly by heat and mass transfer into the sample (2D modeling) at 50 K/min, all processes need to be deeply analyzed across the thickness of the solid. Indeed, Figure 4.25 and Figure 4.26 plot the integral of all reaction rates over space and demonstrates that this overall reaction rate is not too much dependent on heat and mass transfer, however, this is not guaranteed when it comes to the reaction rate of each location through the thickness of the sample. The following part is focused on the simulation case at 50 K/min because Figure 4.25 and Figure 4.26 show that the most differences are under 50 K/min.

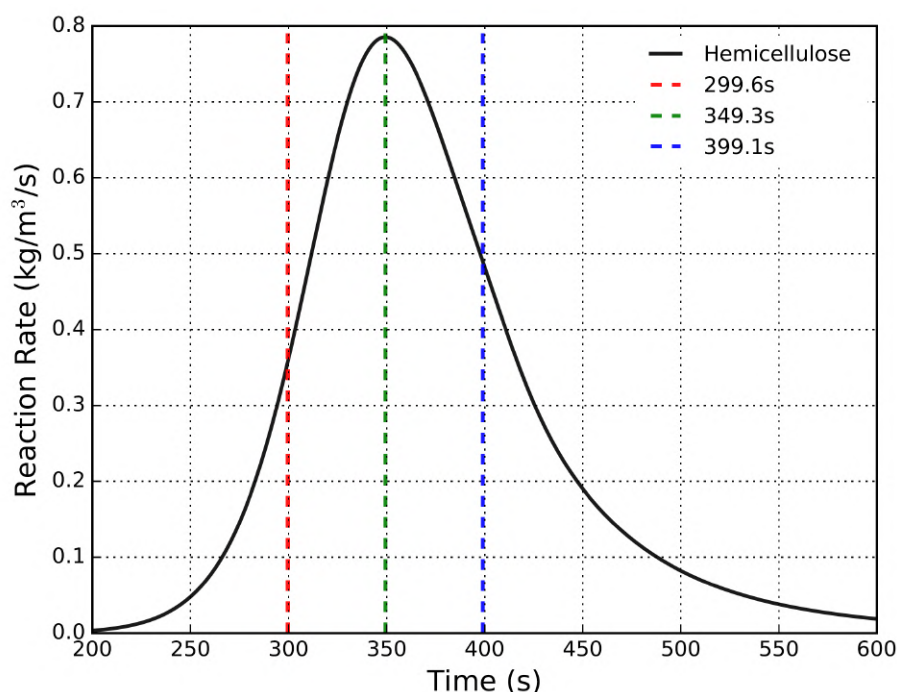


Fig. 4.27 Three characteristic time points for hemicellulose reaction rate

In this part, for 2D simulations, different characteristic times are concentrated to explore the reaction behavior. The characteristic time regarding hemicellulose, cellulose, and lignin reaction rate are shown in Figure 4.27-4.29, respectively. The curve of reaction rate has been cut into three characteristic time points regarding the reaction rate peak time, the time before and after this peak, respectively. For hemicellulose, they are at 299.6 s, 349.3 s, and 399.1 s, for cellulose, they are at 371.4 s, 407 s, and 442.7 s, while for lignin they are at 304.8 s, 382.1 s, and 459.4 s. Those

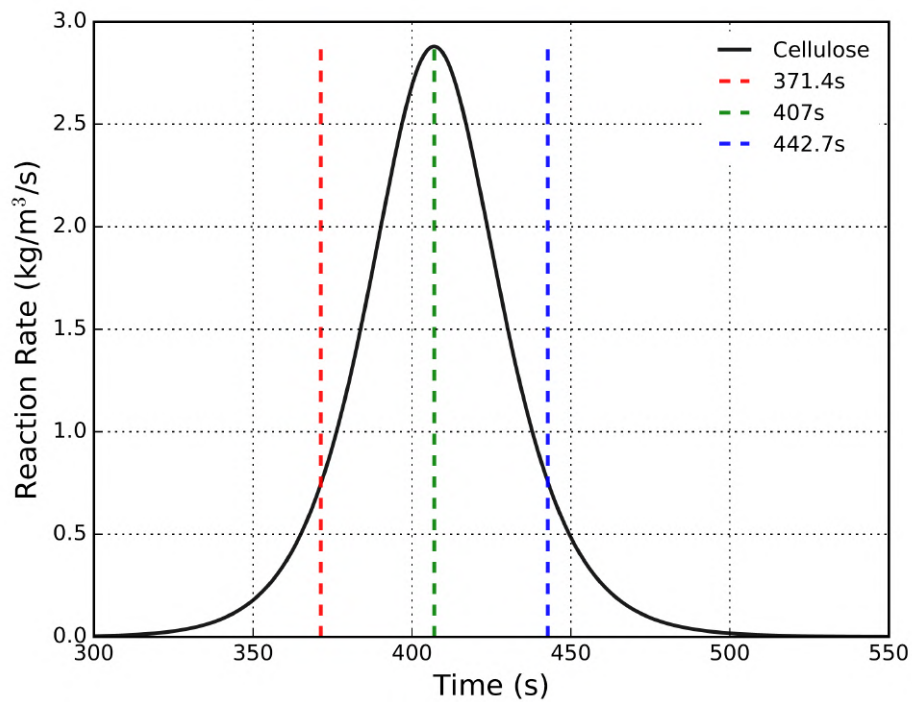


Fig. 4.28 Three characteristic time points for cellulose reaction rate

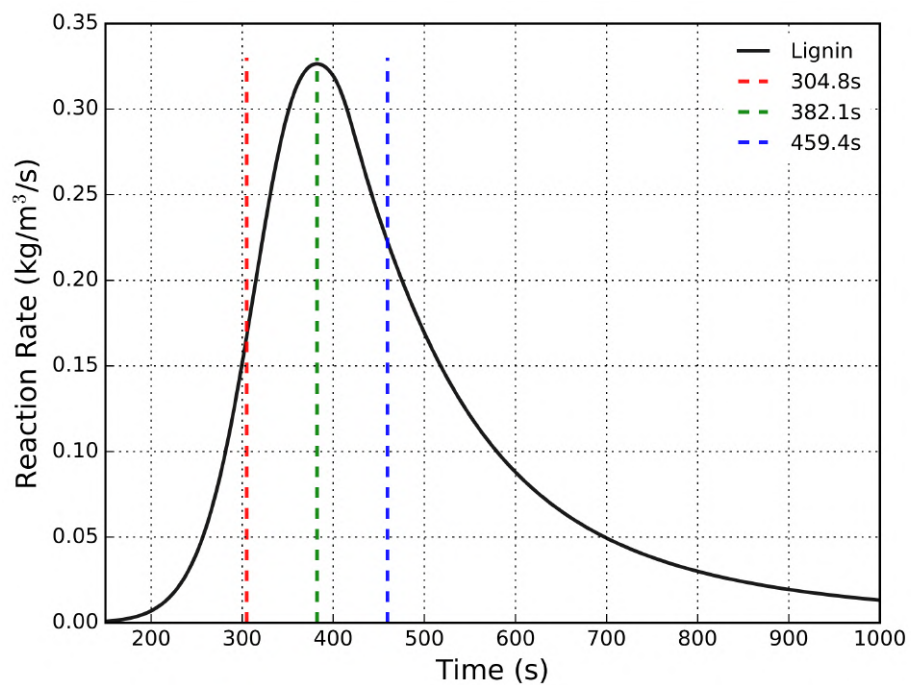


Fig. 4.29 Three characteristic time points for lignin reaction rate

characteristic time are different for each component reaction because these components involve different reaction temperature ranges [65]. The first and third characteristic time involve the same interval against the second one (peak time). This technique makes easiest the analysis a function of the material thickness.

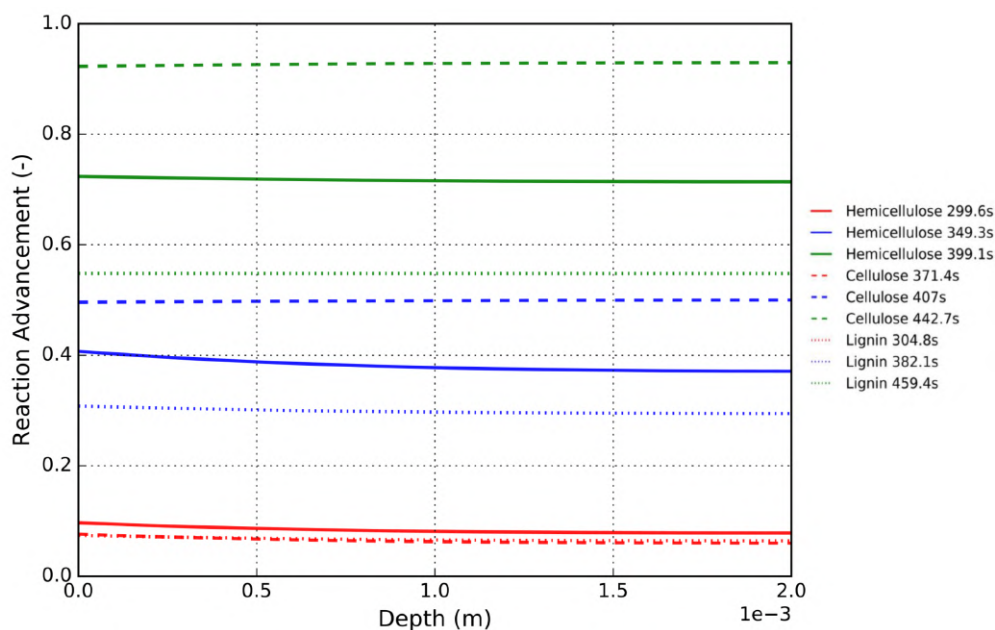


Fig. 4.30 Reaction advancement of hemicellulose, cellulose, and lignin through the sample thickness at the different given characteristic time

Figure 4.30 plots the advancement of each reaction across the thickness of the sample for three characteristic times for each component reaction defined before. Solid lines correspond to hemicellulose reaction, dashed lines concerning cellulose reaction and dotted lines involve lignin reaction of thermal decomposition. Blue lines correspond to the time at which the maximum reaction rate is observed for each component reaction. Red lines correspond to the characteristic times before the peak of reaction rate and green lines are the characteristic time after the reaction rate peak. The x-axis corresponds to different depths through the thickness of the solid, 0.0 m represents the surface and 0.002 m corresponds to the middle position of the sample, and the total thickness of the sample is 0.004 m.

Observing Figure 4.30, the advancement of the reactions is quite constant across the thickness of the solid. A larger difference is observed for hemicellulose reaction (solid line) at the time when the reaction rate is maximum (blue solid line). Consequently, in the 0D model, the results which describe a “stoichiometric value” have been introduced. We have shown that the global maximum reaction rate is observed when the advancement of such a global reaction is around 0.5. However, for the 2D model, Figure 4.30 highlights the differences concerning reaction advancement of each component which behaves as a function of the thickness. The main differences are for hemicellulose and the advancement of approximately 0.41 is observed at the surface and 0.38 in the center at the characteristic time of 349.3 s. This demonstrates that a reaction advancement gradient is formed through the solid thickness.

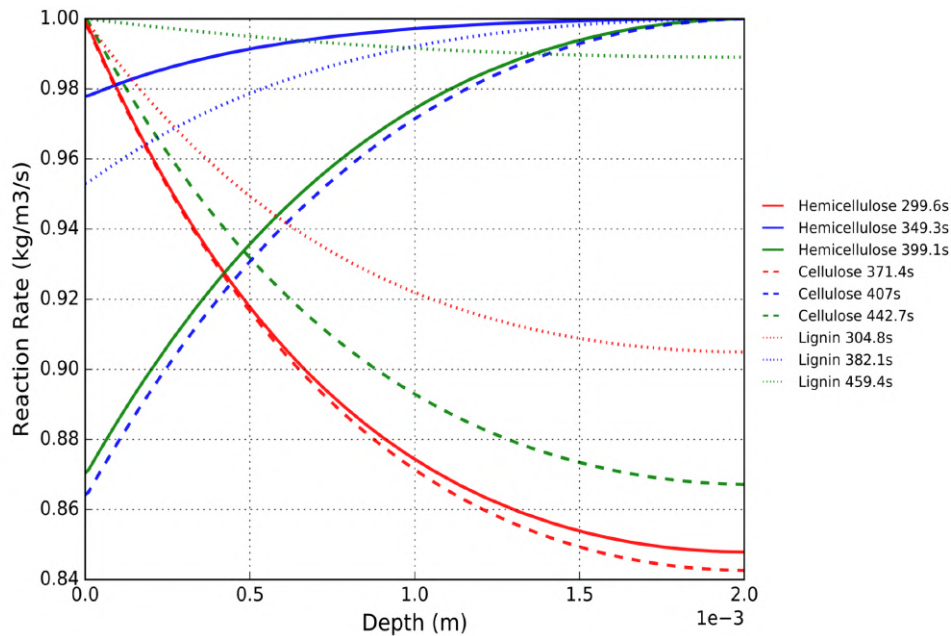


Fig. 4.31 Normalized reactions rates of hemicellulose, cellulose, lignin through the sample thickness at the different given characteristic time

To compare each reaction across the thickness of the sample, the normalized reaction rates have been plotted in Figure 4.31. This one plots reactions rate divided by the maximum reaction rate reached by each reaction at given time. A value of 1.0

means that the maximum reaction rate has been reached at the given time and space location. A value different to 1.0 means that reaction gradient still remains.

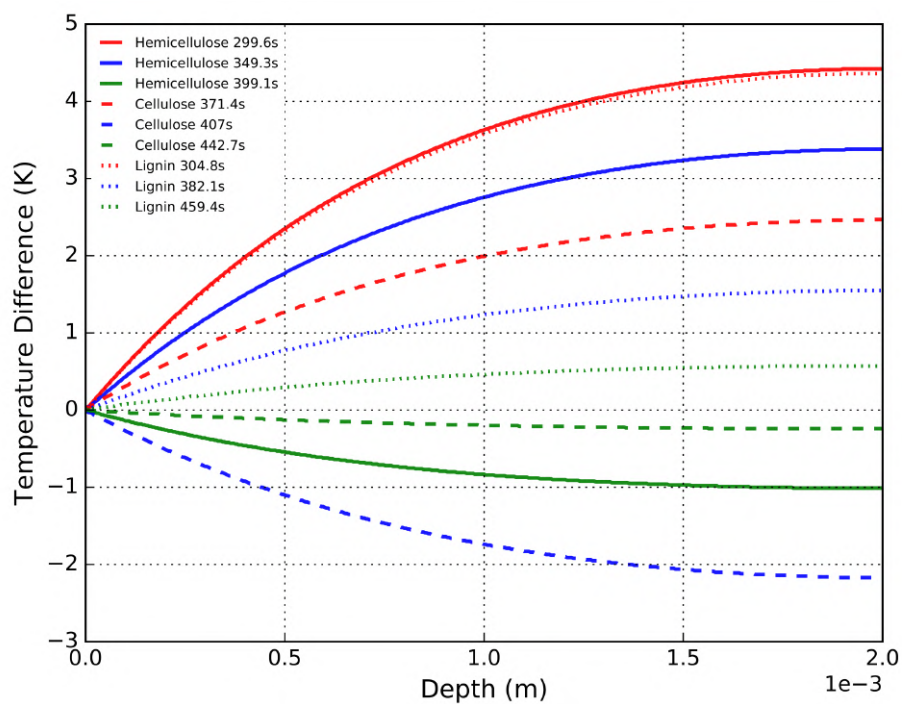


Fig. 4.32 Temperature difference for each reaction of hemicellulose, cellulose, lignin through the sample thickness at the different given characteristic time

Figure 4.32 plots the temperature difference across the sample thickness at the given characteristic time. At a specific time, the temperature difference is related to the difference between the temperature of the surface and the temperature across the thickness. Figure 4.33 plots the evolution of the calculated heating rate (temperature derivative versus time) in a function of the solid thickness at a different characteristic time.

In Figure 4.31, at the characteristic time before the maximum reaction rate (red curves), hemicellulose and cellulose reactions show higher reaction rate gradients with a difference of around 15% of the reaction rate between the surface and the center of the sample. Lignin is less influenced by a reaction rate difference of less than 10%. The heating rate could explain the same order of magnitude of the reaction rate gradient despite a lower temperature difference. For cellulose reaction, we observe a higher

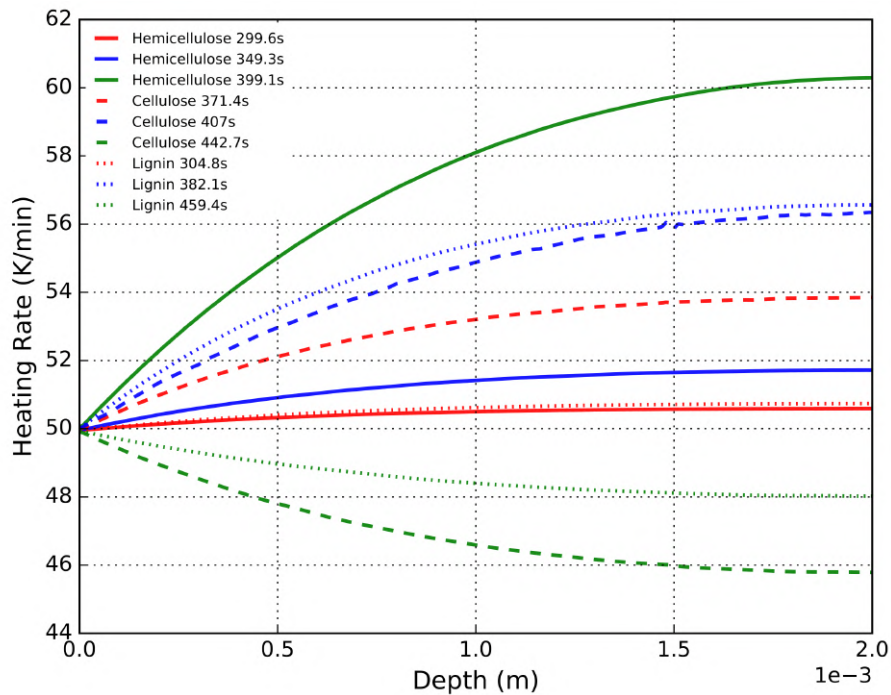


Fig. 4.33 Heating rate for each reaction of hemicellulose, cellulose, lignin through the sample thickness at the different characteristic time

heating rate evolution that reaches 54 K/min comparing hemicellulose reaction where the heating rates still close to 50 K/min. As we argue before, a higher heating rate tends to shift reactions to higher temperatures which could explain comparable reaction rate gradient with hemicellulose reaction with a less temperature difference.

At the time when reaction rates are maximum corresponding to blue curves in Figure 4.31, we observe less reaction rate gradient for hemicellulose and lignin. Their reaction rate at the surface and middle locations (involve maximum reaction rate) of the sample is around 5%. However, this reaction rate difference is around 15% for cellulose accompanied by a 2 K difference between the surface and the middle of the sample, and a heating rate greater than 50 K/min (around 56 K/min). We can note that at these characteristic times, when reaction rates are maximum, the maximum value of the reaction rate is located at the middle of the sample and different smaller values are observed at the surface, demonstrating that reaction fronts move from the surface to the middle of the sample thickness. Differences are more important for

cellulose reaction probably because the reaction front is thinner and when it moves to the center of the solid, it causes higher reaction rate gradients.

For the characteristic time after the reaction rate peak (green curves), we observe a similar trend for lignin and cellulose reactions (Figure 4.31). While higher reaction rate gradients for cellulose reaction, an opposite trend for hemicellulose reaction rate which could be explained by high heating rate value at that time corresponding to the solid green line in Figure 4.34.

With such behavior discussed above, we can conclude that heat and mass transfers interact with pyrolysis reactions when the global heating rate is more than 50 K/min. However, this can behave in different ways depending on the observation of the kinetic characteristic of each reaction. Indeed, depending on the characteristic time scale of the reaction (slow or fast reaction), heat and mass transfers do not have the same impact on reactions. So the link among reactions, heat, and mass transfers is complex and it depends locally on characteristic time and length scales of chemical reactions, heat, and mass transfer processes. These interactions need to be correctly captured by the model to describe correctly the overall pyrolysis process. Here we point out some interactions at the TGA scale at 50 K/min. Even though this interaction extent is quite low because of the small thermal gradients involved, it is necessary to describe it in our model. Indeed, in the case of cone calorimeter experiments, where high thermal gradients are involved, the interaction between the heating and pyrolysis reaction process should become stronger and if the model does not capture it correctly, some important discrepancies could be involved.

## 4.4 Conclusion

Chapter 4 is dedicated to the modeling of the thermal decomposition of wood at the particle scale. Experiments have been performed using the TGA apparatus under an inert atmosphere, for two heating rates: 10 K/min and 50K/min. From the mass loss and mass loss rate evolutions, two reactions scheme have been proposed: a

---

global-one step and multi-parallel reactions. The unknown kinetic parameters have been determined by the DAKOTA into the PATO model. The modeling evolutions of the mass loss and the mass loss rates have been compared to the experimental ones to analyze the influence of the reaction scheme. The influence of the heating rate on the kinetic parameters is analyzed. Thus, the kinetic parameters optimized by one heating rate are compared by the kinetic parameters extracted from other heating rates. Finally, 2D modeling with the PATO model permits to explore the interaction of the heat and mass transfers at this specific particle scale. Based on this work, the objective is now to characterize the availability of the model to represent the thermal decomposition of wood at a larger scale.



# Chapter 5

## Cone calorimeter experiments and model validation for wood pyrolysis

Chapter 4 permits to discuss some interesting points about wood pyrolysis at the TGA scale, which is mainly concentrated on the chemical part. Due to the strong link between the chemical and thermophysical processes during the real fire pyrolysis scenario, this chapter focuses on the wood pyrolysis at a larger bench-scale, with the cone calorimeter apparatus. Experiments are conducted in order to characterize the thermal decomposition of wood, with both heat and mass transfers. The kinetic parameters obtained from Chapter 4 are implemented to describe the pyrolysis phenomena at this larger scale and the material heating process will be discussed. The boundary convective and thermo-physical parameters are predicted specifically under the experimental conditions concerning the cone calorimeter. Moisture evaporation is targeted, the wet wood and dry wood pyrolysis are studied numerically at different time and length scales.

## 5.1 CACC experiment description and temperature measurement

The controlled atmosphere cone calorimeter (CACC) utilized in this work is developed from the standard cone calorimeter of ISO 5660 [138]. It is applied as a pyrolysis apparatus characterizing the thermal decomposition of wood samples under an inert atmosphere. The schematic of CACC is shown in Figure 5.1. In order to obtain an inert atmosphere for pyrolysis condition, a continuous nitrogen gas flow rate is kept at approximately 185 L/min in order to maintain a well-ventilated condition. The oxygen concentration in the CACC chamber is extremely low ( $< 1$  vol%) which is proved to be reliable for maintaining an inert environment. The surface boundary condition is relatively uniform and constant, avoiding a flame heat flux which is the main source of fluctuations during classical cone calorimeter experiments.

The experimental chamber (ambient conditions in the room where the CACC is placed) involves an ambient temperature of approximately 300 K with 1 atm. To decrease the radiation from the surrounding wall in the chamber, the inner chamber wall is coated with black paint with high emissivity (0.9). The water cooling circuit system is mounted underneath the sample holder. They provide an ambient temperature in the chamber and limit the radiation transfer between the wall and the sample such that a well-defined boundary with ambient temperature is obtained. Different heat fluxes are employed and the setting is realized using a calibrated Schmidt-Boelter gauge placed above the center and at 25 mm above the sample surface of the top material surface. The heat flux gauge is also painted black.

In order to have a more complete understanding of the thermal decomposition of the wood, both the mass loss and the temperature evolution at different places are measured. The mass loss history is monitored by balance equipment supported by a load cell. The temperature measurement is conducted through the setting of thermocouples (Type K) inside the wood sample. For the experimental mass loss and temperature measurement, at least three times of tests are given to maintain

reproducibility, and the experimental data are recorded with high precision for every 0.02 s. The normalized mass loss data is derived by the initial and instantaneous mass, and the mass loss data are filtered to obtain the mass loss rate data which are available to compare with the model prediction. The results obtained show that the temperature and mass loss are quite reproducible, permitting to give less uncertainty for the model validation.

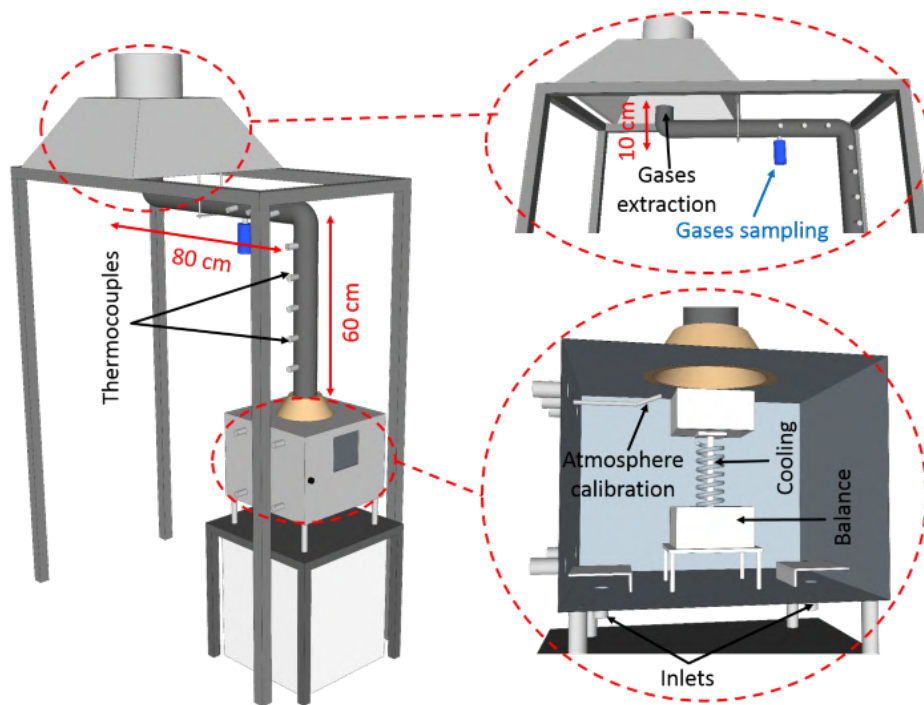


Fig. 5.1 CACC apparatus

To verify the validity of the uniform distribution of the incident heat flux at the surface of the sample given by the cone heater, a Monte Carlo simulation of the cone heater radiation distribution has been made, the results are plotted in Fig 5.2.

It can be observed that the heat flux distribution along the radial coordinate is not fully uniform. The black square represents the sample size (rectangular with a length of 100mm) as mentioned in the standard cone calorimeter (ISO 5660). The heat flux can vary approximately 20% from the center to the corner of the sample. To minimize this 2D effect, we choose to use a cylindrical sample with a diameter of 80mm to guarantee a closer 1D behavior, although a small heat flux gradient remains.

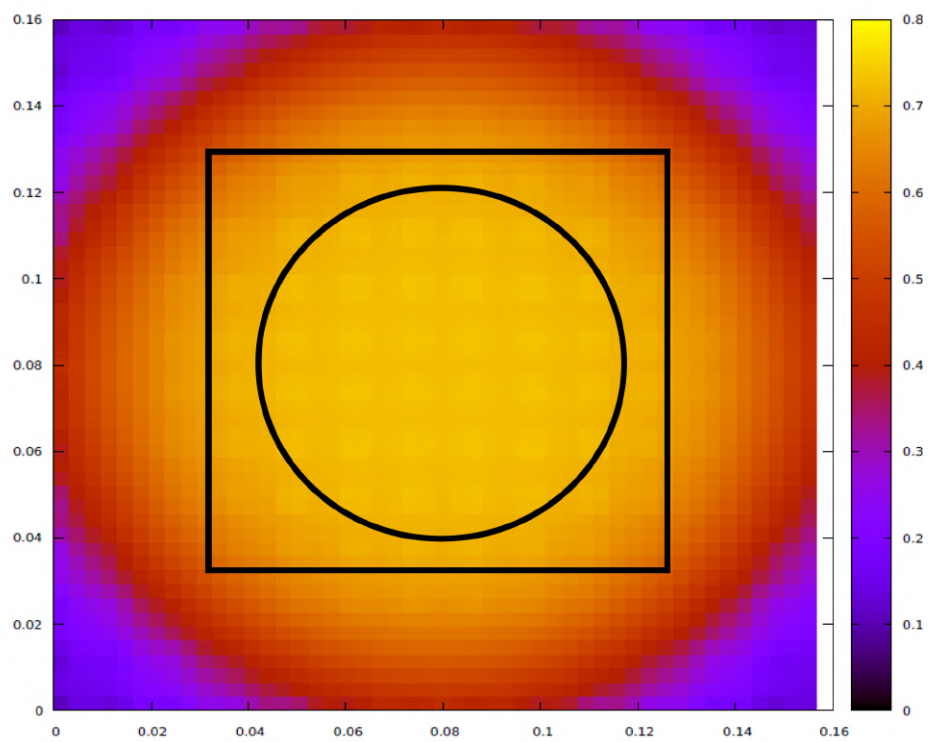


Fig. 5.2 Monte-Carlo heat flux distribution at the top surface of axis-symmetry under  $20 \text{ kW/m}^2$

A function regarding heat flux factor along the radial space is implemented as the surface boundary condition in the model to take into account these gradients identified in Figure 5.2 and to reflect the real boundary conditions during the cone calorimeter experiments.

The sample holder is made of thick cylindrical silicate insulation material. The Douglas fir wood is selected, cylindrical samples (the diameter and thickness are 80 mm and 21 mm, respectively) are employed due to their facility to prepare and to adjust fully the real heating condition as mentioned. The specific heat capacity and thermal conductivity are obtained by inverse modeling, and other related parameters are based on the previous laboratory experiments and literature.

The original wood samples account for approximately 10 wt% of water content. A common choice, such as realized by [137], is to employ the drying oven with more than 24 h or 48 h at about 373K before the cone calorimeter experiments. However, it has been observed that the delay required to prepare the experiment (so between the sample extraction of its conditioning and the beginning of the test) favors the evolution of the humidity content. Then, the humidity considered during the modeling can be different from the real experimental one. In order to avoid this water influence for wood pyrolysis, an alternative manipulation is selected in this study, with heating performed in CACC under 5 kW/m<sup>2</sup>. The duration of the water evaporation experiment is prolonged until no apparent mass residue variation is observed. The sample shape profiles are examined without changing through the water evaporation process. The surface temperature is tested at approximately 473 K and the bottom temperature is found to be approximately 400 K. It is specified that the sample doesn't have any pyrolysis involvement and a dried wood sample is obtained under such manipulation condition.

After the evaporation experiment, the cone heater is switched off and the sample is cooled without moving it from the cone box until to reach the ambient temperature. The Nitrogen flow is continuously conducted to prevent humidity absorption during the sample cooling. This method has some advantages. Firstly, it minimizes manual

manipulation of the sample to reduce the experimental errors and to prevent humidity absorption. Secondly, during the water evaporation process, the mass loss and temperatures inside the sample are recorded. Then, only the evaporation process is simulated, allowing to validate the evaporation model and to determine the initial mass fraction of free water which is estimated to be 10 wt%.

The silicate is chosen as the insulating material to serve as the sample holder. Some studies use a thin Aluminum layer between the wood and the insulating material to avoid the volatiles release providing impenetrable boundary conditions or to enhance the thermal contact with the sample holder [21]. As demonstrated in [21], in the cone calorimeter experiment with or without the Aluminum layer between the sample and sample holder, the mass loss history and temperature evolution are similar. So, there are no heat and mass transfer influences from the Aluminum layer. In this study, no Aluminum layer is added and the thermal contact resistance is defined as one displaying perfect heat conduction between the sample and silicate. The silicate board is cut with a cylinder for the wood sample as shown in Figure 5.3.



Fig. 5.3 Experimental sample holder of cylindrical silicate

Although many studies are performed considering insulating materials, it is usually not considered in the modeling work and adiabatic boundary conditions are mostly applied, such as [4]. As described in the literature review, this consideration of the boundary conditions could lead to different errors despite the presence of low temperature at the insulating surface. In this work, the silicate and porous charring materials are coupled in the model. More over, the silicate sample holder is generally treated as impenetrable for mass transfer [21], however, it is a highly porous material. In this work, the sub-material, i.e. silicate, is treated as a porous material. The silicate density and related thermal properties are consistent with [36]. The density of silicate

is  $245 \text{ kg/m}^3$  and the most important specific heat capacity and thermal conductivity evolution versus temperature are presented in Figure 5.4 and Figure 5.5 from [36].

Silicate could contain some free water giving errors when the sample is heated up especially in mass loss recording. To prevent as much as possible all experimental errors and to correctly validate the model, the same procedure as the one for the sample humidity removal has been applied for silicate to remove its humidity.

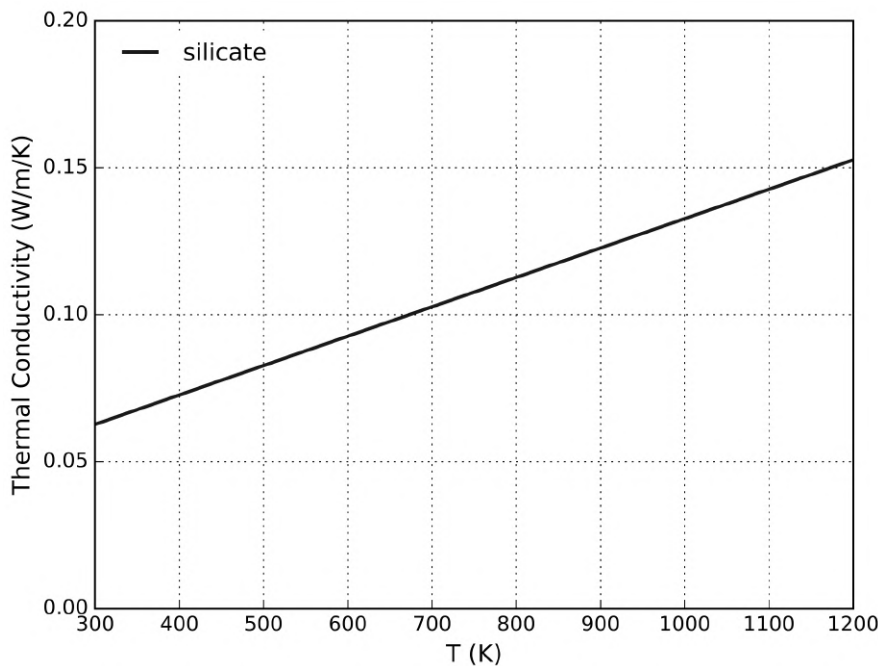


Fig. 5.4 Thermal conductivity of porous silicate

The temperature is measured through thermocouples embedded in wood samples with stainless steel sheathed K-type thermocouples. In order to capture the temperature profile through the thickness of the sample, three holes horizontal to the top surface with a diameter of 0.5 mm are drilled to place the thermocouples. For thermocouples setup, the locations from the top surface are 4 mm, 11 mm, and 17 mm, respectively. During the tests, the sample edge temperature could be non-uniform compared with the one in the center as noted in [82]. Thus, the thermocouple junctions in the holes are placed near the center of the sample. In this study, the locations of thermocouple junctions are mounted away from the center axis less than 10 mm, and the thermal parameters of

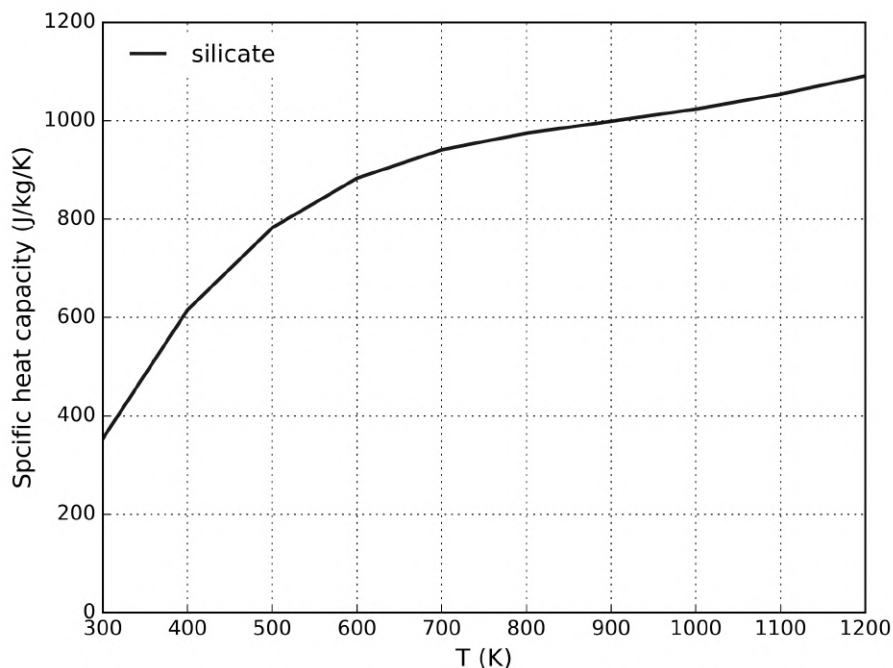


Fig. 5.5 Specific heat capacity of porous silicate

thermocouple junctions can be viewed in [148]. The experimental schematic description for this experiment is shown in Figure 5.6. In order to attain a thermal equilibrium in the cone chamber, the temperature measurement is delayed for several minutes after the start-up of gas flow.

As shown in Figure 5.6, three holes are drilled at the side of the silicate to connect the thermocouples with the sample. The thermocouple locations are set as  $T_{top}$ ,  $T_{middle}$ , and  $T_{bottom}$  temperature probes which are 4 mm, 11 mm, and 17 mm beneath the surface as described.

The emissivity and absorptivity for all materials are assumed as constant and equal. The sample is treated as opaque and the in-depth radiation is neglected. In order to minimize the radiation from the surface of the sample to the environment, the surface of the sample has been painted black. Even if a “black” char layer is formed quickly at the surface of the sample, it is assumed in the numerical model at the boundary surface that the emissivity of virgin wood is close to 0.96. Indeed, at the initial time of the tests, the first peak of the MLR is governed mainly by the

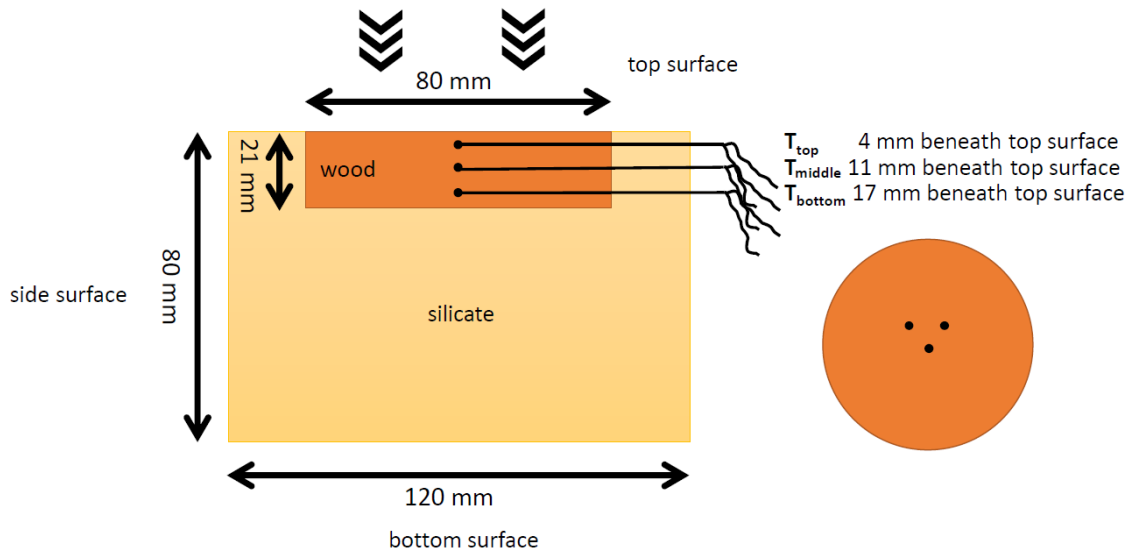


Fig. 5.6 Schematic illustration of temperature measurement for wood pyrolysis

heat balance at the surface, which is treated as a boundary condition in the present model. In order to minimize the error made on the term regarding the radiation from the surface that needs to specify the emissivity of wood, this assumption has been chosen. The boundary conditions at the bottom are specified as “zero-gradient” for temperature and fixed ambient pressure. For the 2D axis-symmetric model, the fixed pressure is specified on sides but heat losses by convection have been taken into account due to non-zero velocity on the sides coming from the Nitrogen flow. As noted in [170], the initial stage of pyrolysis mainly takes place at the surface of the sample, i.e., the appearance of the first mass loss rate peak. However, with the advancement of pyrolysis through the thickness, the side boundary condition tends to have some effect on heat dissipation and to influence the mass loss to some extent. The cone calorimeter tests tend to be treated as the one-dimensional case, as demonstrated in [125]. Thus, in this study, the cylindrical wood numerical simulations are taken as one-dimension and axis-symmetrical two-dimension. The modeling work in this study for wood pyrolysis simulation concerning 1D and 2D axis-symmetry is illustrated in Figure 5.7. The mesh is displayed over the 2 directions for the axis-symmetrical case and only through the thickness for the 1D case.

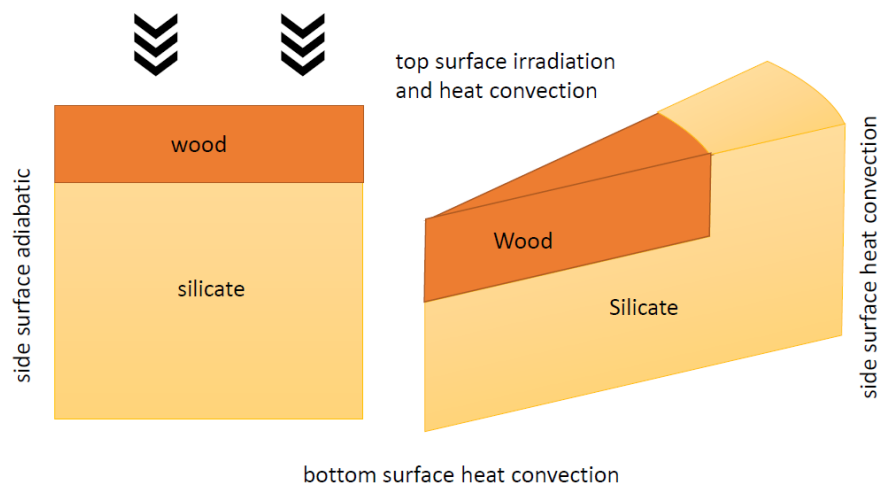


Fig. 5.7 Schematic of modeling configuration for wood under 1D and 2D axis-symmetry

The experimental work conducted to perform the modeling can be summarized as follows: firstly, the wet wood samples undergo water evaporation at a heat flux of  $5 \text{ kW/m}^2$  to produce dried wood samples. At the same time, mass loss and temperatures are recorded to validate the water evaporation process implemented into the model. Then, pure heat conduction of dried wood is conducted under the heat flux of  $5 \text{ kW/m}^2$  again to capture the temperature-dependent specific heat capacity and thermal conductivity by inverse analysis through the temperature evolution at three locations. In the following, wood pyrolysis tests under  $20 \text{ kW/m}^2$  and  $50 \text{ kW/m}^2$  are made to preserve the final char matrix. The char containing thermocouples are kept in the cone with Nitrogen for cooling at ambient temperature. Finally, the experiments concerning char heat conduction under  $20 \text{ kW/m}^2$  and  $50 \text{ kW/m}^2$  are conducted to perform the inverse analysis such that the char thermal conductivity and specific heat capacity with different heat fluxes can be captured. These parameters are applied to simulate wood pyrolysis cases under different heat fluxes. Considering the sensitivity of mass balance imposed by thermocouples, the experimental manipulation of the mass loss and the temperature measurement by thermocouples are separated.

## 5.2 Inverse analysis to obtain heat convection coefficient

An inverse analysis is conducted in this work with an Aluminum block (AU4G) to predict the convective heat transfer coefficient. Although some changes can take place due to the flow scenarios in the chamber during different heat flux and pyrolysis stages, the convection heat transfer coefficient in this work is assumed as constant. The Al sample with a cylindrical contour similar to the wood sample is employed to obtain the temperature at different locations under the heat flux of  $20 \text{ kW/m}^2$ . The thermocouple setup is also the same as the one for wood. However, the Al heat conduction thermocouple setup involves a single temperature probe due to its high thermal conductivity and the corresponding temperature measurement, the illustration is shown in Figure 5.8. Indeed, it has been verified by experiments in this study that the temperatures are quite homogeneous along the centerline by measuring the temperatures at different locations. Thus, only the temperature in the middle of the Al sample is shown. The boundary condition for pure heat conduction is the same as that of wood pyrolysis which considers the heat convection of the top surface and side surface. Due to the low absorptivity and high emissivity of Aluminum which could lead to high uncertainties interacting with the ambient atmosphere. Before the measurements, the surface of the Al block is coated with black paint with an absorptivity and emissivity of approximately 0.96. These two values are assumed to be identical with those of wood and char surface which are treated as constant in PATO. The ambient temperature in this study is monitored as 300 K.

In this study, an Al block sample with well-defined thermal properties to reduce the errors is employed to conduct the inverse analysis. The properties are listed in Table 5.1 [171].

In this work, the heat convection coefficient is defined as a single constant value across the sample surface under 1D and 2D. However, the heat loss by convection depends on many factors and could change over the surface. One of these factors is

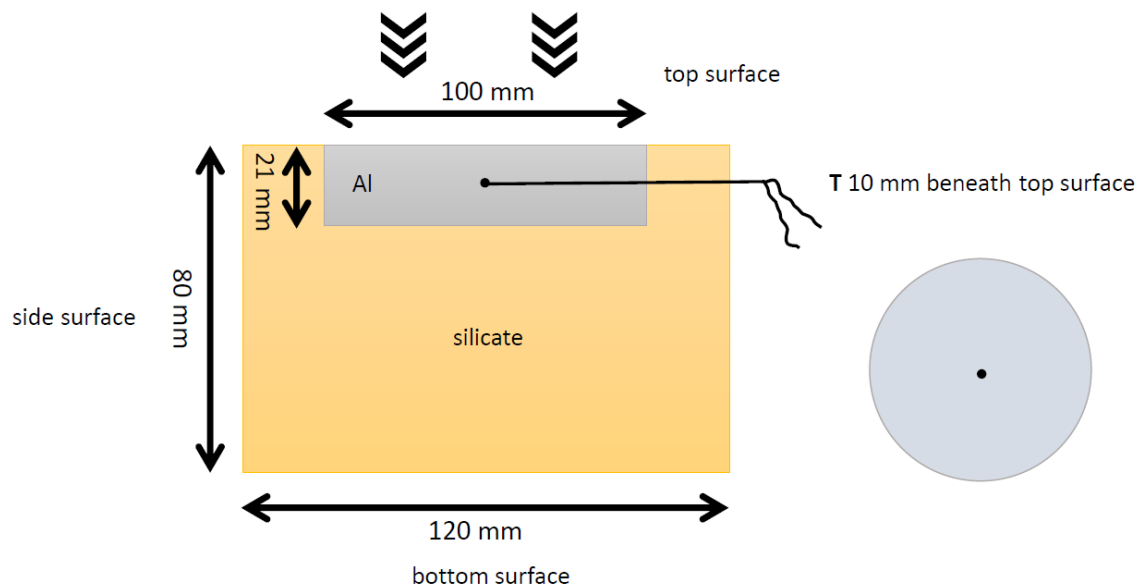


Fig. 5.8 Schematic illustration of temperature measurement for the Al block sample

Table 5.1 Thermal parameters of Aluminum block sample [171]

Aluminum properties	Value	units
Density	2750	$Kg/m^3$
Specific heat capacity	$4.94 + 0.00296 \times T$	$J/mol/K$
Thermal conductivity	$76.64 + 0.2633 \times T - 0.0002 \times T^2$	$W/m/K$
Emissivity (surface black paint)	0.96	-
Absorptivity (surface black paint)	0.96	-

the difference between the surface temperature of the sample and the temperature of the surrounding gases. Due to the non-uniform heat flux distribution along with the radial directions of the sample surface, a flux mapping boundary condition at the top surface is employed for the 2D axis-symmetry case in PATO, taking into account the view factor of the cone calorimeter regarding the sample surface which is shown in Figure 5.2 (heat flux distribution at the surface).

The heat convection coefficient at the sample surface is hard to measure but only this value is unknown in the boundary of the pure heat equation of Al. It can be then predicted. The inverse 1D and 2D analysis contain the heat convection coefficient of top and sides, as shown in the following Figure 5.9. The objective is to obtain a good fitting between the predicted and the experimental temperature evolution for Al

plate pure heat conduction by assigning and optimizing the heat convection coefficient. The thermal contact between the Al plate and the silicate is defined as perfect. The experiment for Al heat conduction is performed under  $20 \text{ kW/m}^2$  and it is assumed to be the same value for top surface heat convection coefficient under different heat fluxes with or without pyrolysis. This aspect is discussed previously. The moderate difference of buoyancy flow under different heat flux is neglected. As noted in [172] under the CACC experiment, it is found that the shape of material has little effect on the results, however, the difference tends to be present under different surface locations.

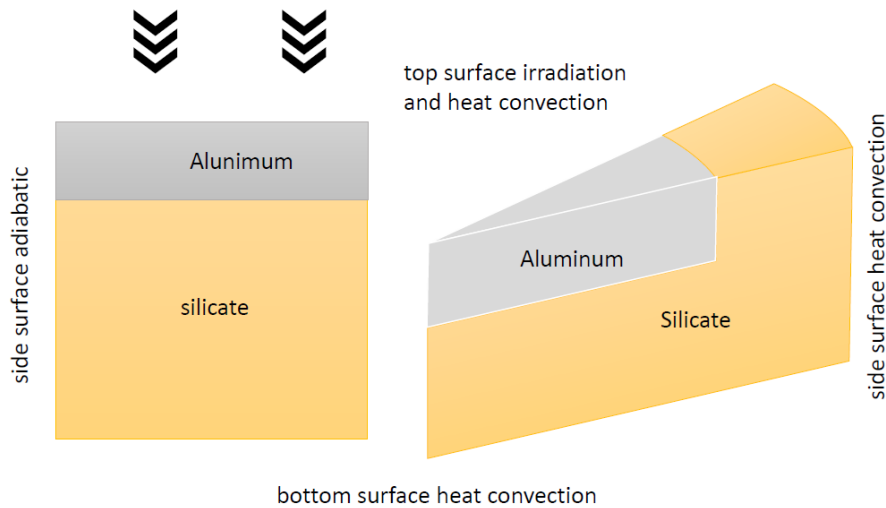


Fig. 5.9 Schematic of modeling configuration for Aluminum under 1D and 2D axis symmetry

A set of heat convection coefficients are assigned for model prediction, and the comparison between the measurement and prediction concerning temperature evolution for Al pure conduction is shown in Figure 5.10 (heat flux of  $20 \text{ kW/m}^2$ ). Under 1D and 2D simulations, different sets of heat convection coefficients are tested. Compared with 1D simulation, a better good agreement is achieved concerning the heat convection coefficients between 3 and  $5 \text{ W/m}^2/\text{K}$  at the top surface under 2D. These values are quite low but consistent with the one obtained by [130] where a Copper sample is employed under different heat fluxes. The bottom convection is neglected due to its perfect thermal insulation with a thickness of approximately 60 mm for the silicate

sample holder, this is similar to the reported one by [82]. The heat convection coefficient of the side surface is obtained by the 2D simulated cases and it is estimated to evaluate between 0 and 4 W/m<sup>2</sup>/K, and it is observed that the side heat convection seems to be less important compared with that at the top surface. It can be noted that different mesh sizes and time steps have been tested to ensure the independence of the results. For 1D simulations, a mesh size of 0.1 mm and a time step of 0.001 s have been used, and for 2D simulations, a mesh size of 1 mm and a time step of 0.01 s have been used.

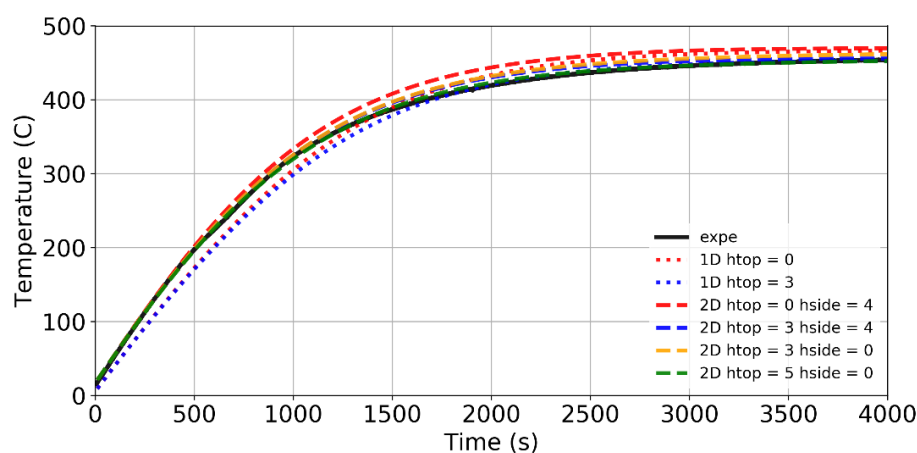


Fig. 5.10 Temperature evolution between measured and model-predicted for Al heat conduction under 1D and 2D subjected to incident irradiance of heat flux of 20 kW/m<sup>2</sup>

The prediction curves, at the heat conduction transient stage, are not well captured by the 1D modeling but are well captured by the 2D simulation. It can be viewed that the deviation is larger from the onset to the strong transient stage for 1D simulation. However, this trend does not appear under the 2D simulation. It is likely to be caused by thermal effect uncertainty between the Al block and the silicate sample holder during the experiments. Indeed, due to the large different thermal properties for these two materials, the temperature gradient should be high at the beginning of the test between the contact sides of silicate and Al sample which enhances the heat transfer by conduction. The thermal diffusivity coefficient of silicate is approximately two orders of magnitude lower than that of Al [36, 171]. At the beginning of the test, the temperature of silicate over the small thickness is increasing faster than that of Al

causing some temperature gradients between the two materials. At approximately 1700 s, the silicate has sufficient time to heat up and to propagate heat through its thickness, making temperature gradients with the Al sample (on sides) less important. The temperature differences given by 1D and 2D models are then negligible. When the heat transfer attains a steady state, these two models give quite similar results. The heat convection coefficient extraction is not easy and depends on many parameters, as discussed in Chapter 2. It has been demonstrated that this coefficient is between 3 and 5 W/m<sup>2</sup>/K at the surface and between 0 and 4 W/m<sup>2</sup>/K at the sides. However, the configuration used to extract these data is a non-reactive case that could differ from the pyrolysis case. Then, these values should also be used with caution when simulating a reactive case. Indeed, the heat convection process seems not affecting a lot the heat transfer in the Al sample. However, this value could affect the pyrolysis front shape close to the sample sides making the pyrolysis process not a real 1D case, this is will be discussed in the following part.

### **5.3 Inverse analysis to obtain wood thermophysical parameters**

Due to the diversity of wood types and the heterogeneity of such material depending on many parameters (tree growth conditions, humidity, composition, etc.), the range of physical parameters related to wood is found to be large in literature. Moreover, physical parameters like heat capacity and conductivity are complicated to measure due to the high uncertainty of dedicated experimental methods. Char is also a material that could have a large range of physical values due to the conditions at which they are obtained as well as the methods of determination. For these reasons, the specific heat capacity and thermal conductivity for virgin wood and char are quite unreliable. Then, in this study, similar to Al pure heat conduction conducted to determine the heat convection coefficient, an inverse analysis is also conducted to predict the specific heat capacity and effective thermal conductivity for wood and corresponding char samples.

The method concerns the temperature profile at different locations. The numerical simulations are performed under one-dimensional and two-dimensional axis-symmetry.

The thermal parameters of wood are obtained based on dry wood pure heat conduction experiments, which need to undergo a drying process under the incident heat flux of  $5 \text{ kW/m}^2$  as described earlier. After the termination of the drying experiment, the hot wood sample attached to the thermocouples is kept to the sealed cone calorimeter box without oxygen to arrive at ambient temperature. Then, the pure heat conduction experiments of the dry wood sample are repeated under an identical heat flux of  $5 \text{ kW/m}^2$  to avoid the chemical reaction involvement.

It should be noted that this inverse analysis is performed by a manual tuning process based on the prescribed linear functions dependent on temperature. It has been tested in this study that constant values of interest could not provide acceptable fitting with experimental data. Indeed, the temperature has a great influence on their properties which can involve several times larger than the original value (see Chapter 2). In this study, the specific heat capacity and thermal conductivity are treated to be dependent on temperature.

The thermal process for temperature evolution can be divided into two stages: the transient and the steady one, which is only governed by thermal conductivity. As noted in [61], the variations of specific heat capacity and thermal conductivity involve a compensation effect. To consider this compensation effect between the thermal conductivity and the specific heat capacity during thermal process prediction, the priority is to determine the thermal conductivity which is the most influential parameter at the final stage (more than the specific heat capacity). Then, based on the reference data at the room temperature, and the evolution trend dependent on temperature, the thermal conductivity of the transient stage is extrapolated. Finally, the specific heat capacity is predicted to fit the experimental temperature curve. The comparison between experimental and predicted temperature evolution of wood at different locations is shown in the following Figure 5.11.

As aforementioned, the values from reference data are mainly based on the room temperature, and these values are employed as the initial value to extrapolate the linear change of thermal properties as a function of the temperature. The values considered at room temperature in this study are based on the properties of the softwood from [173] which involves a value of 0.2 W/m/K for wood thermal conductivity, 0.09 W/m/K for char thermal conductivity, 1000 J/kg/K for char specific heat capacity and 2000 J/kg/K for wood specific heat capacity, respectively. The Douglass Fir wood thermal properties from [53] are also referred to, the thermal conductivity is 0.18 W/m/K, the specific heat capacity is 2860 J/kg/K and the char specific heat capacity is 1600 J/kg/K, respectively. These values are collected to predict the wood temperature evolution at three locations.

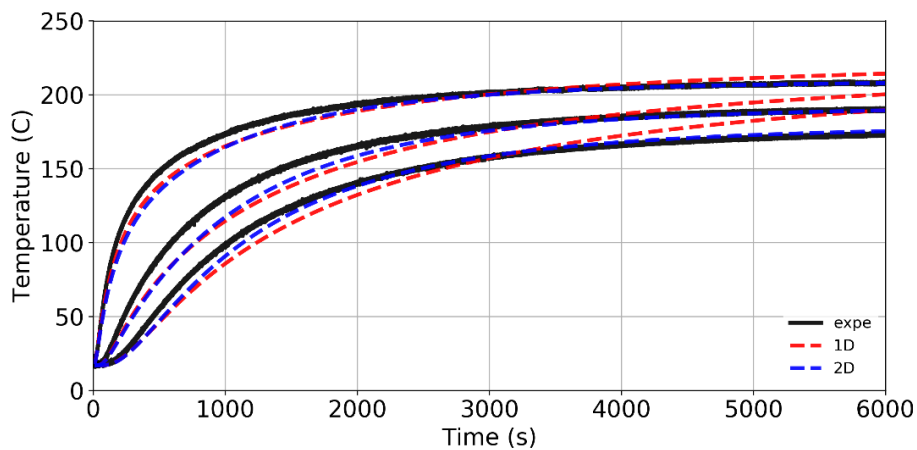


Fig. 5.11 Experimental and predicted temperature evolution of wood pure heat conduction at different locations

The heat transfer process is globally well captured by 1D and 2D models. For steady-state temperature profiles at the three locations corresponding to the end of the heating process (at approximately 6000 s), the 1D model fails to capture the heating while the 2D models capture it very well. It could be pointed out the important role of the boundary conditions, specifically concerning the insulated sides. Indeed, the temperatures recorded at the centerline are greatly affected by the boundaries of the sides. We can note, compared with the 1D model, a better prediction of the transient

stage is given by the 2D model, as also observed for the Al pure heat conduction. For wood heat conduction, the two models are matching up quite well for top temperature location. The difference is increasing at the bottom temperature. The heating rate (the derivative of the temperature) is less important when penetrating through the thickness of the sample which is nearly constant. Thus, the side effect regarding the boundary conditions tends to be more serious in the heating process when the heating rate is slow. When the time is sufficient, silicate material is heated up and the heat could be conducted to wood material by sides. If this assumption is real, much attention should be paid especially when simulating pyrolysis cases with quite low heat transfer and chemistry processes, and the 2D side effect could become non-negligible on the overall pyrolysis process. We can note that this effect is pointed out in a cone calorimeter configuration which could be reasonably approximated globally as a “1D experiment”. Then for a fully 3D configuration, this effect can be enhanced.

The temperature evolution in Figure 5.11 is examined without water evaporation plateau which is similar to the heat conduction of Al. This verifies the assumption of no water in the dry wood sample. At the final stage, constant temperatures at approximately 473 K are present without the presence of pyrolysis reaction. Although some discrepancies are present when comparing the experiment and prediction profile, the errors are within the reasonable acceptance and it is believed that the predicted values concerning specific heat capacity and thermal conductivity can represent the effective thermal properties.

In order to assess the optimized wood specific heat capacity and thermal conductivity which are temperature dependent, they are compared with the reported ones [64, 59, 174, 81] which are frequently employed in the literature. The comparison between the specific heat capacity in this work and the reported ones is shown in Figure 5.12, the corresponding comparison for thermal conductivity is shown in Figure 5.13.

It can be observed from the comparison of specific heat capacity and thermal conductivity evolution versus temperature, the predicted wood thermal parameters are

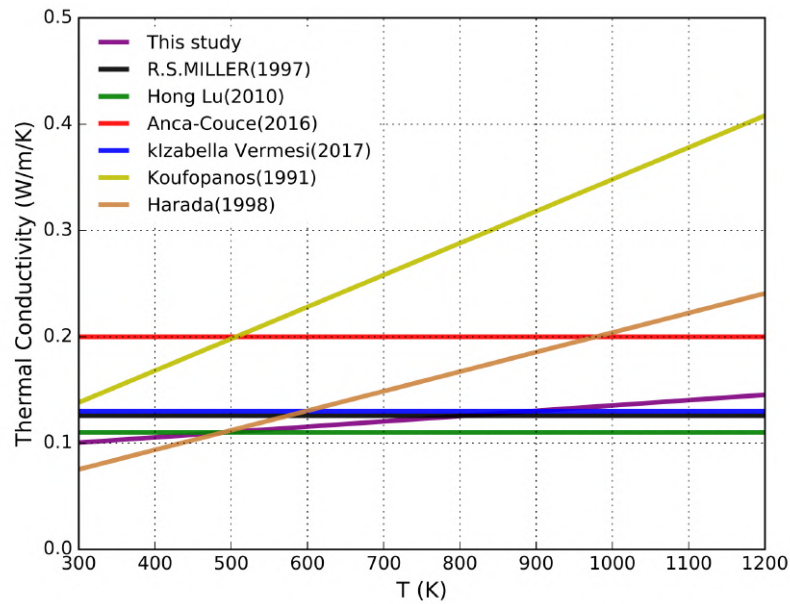


Fig. 5.12 Comparison of wood thermal conductivity of reported and predicted values in this study. (R.S.MILLER(2017) [175], Long Hu(2010) [176], Anca-couce(2016) [177], KIZabellaVermesi(2017) [4], Koufopoulos(1991) [178], Harada(1998) [179])

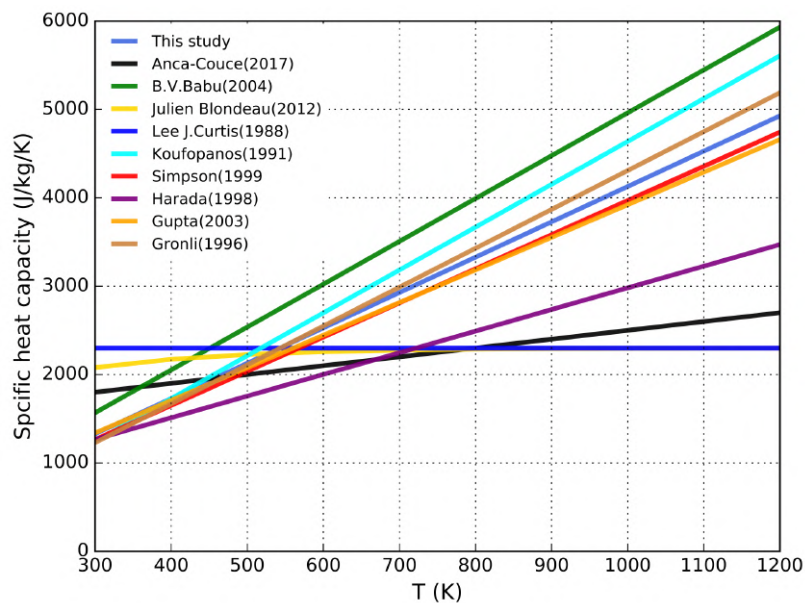


Fig. 5.13 Comparison of wood specific heat capacity of reported and predicted values in this study.(Anca-couce(2017) [177], B.V.Babu(2004) [180], Julien Blondeau(2012) [181], Lee J.curtis(1988) [182], Koufopoulos(1991) [178], Simpson(1999) [183], Harada(1998) [179], Gupta(2003) [59], Gronli(1996) [62])

within the range of uncertainty of reported data, which demonstrates the true physical behavior is captured in this work. As shown in [135], the predicted parameters are quite model-specific, thus it is reasonable to display some moderate difference in the range of values.

## 5.4 Inverse analysis to obtain char thermophysical parameters

Due to the fragile and porous structure to sustain a complete material matrix, the experiments for measuring temperature are quite hard to conduct. Inverse analysis or literature data is an alternative for reference. The inverse analysis to obtain char thermal parameters are conducted with the char pure heat conduction. However, the char structure depends on many parameters such as pyrolysis conditions. Indeed, the heating conditions and chemical reactions are responsible for char production, the remaining char matrix could be more or less porous with different mechanical properties depending on cracks formed perpendicular to virgin wood fibers. Cracks are often directly related to heat flux received at the surface of the sample. For those reasons, two tests of pure heat conduction have been performed on two different char matrices obtained by pyrolysis tests at two heat fluxes, i.e., 20 kW/m<sup>2</sup> and 50 kW/m<sup>2</sup>. The objective is to verify if the char matrix and the associated thermal parameters are or not highly dependent on heat flux conducted to form the char matrix.

After the termination of the wood pyrolysis experiment at 20 kW/m<sup>2</sup> and 50 kW/m<sup>2</sup>, the char sample is fixed in the sample holder and in the chamber until it arrives at the ambient temperature. The comparison between experimental and predicted for the char thermal parameters under 20 kW/m<sup>2</sup> and 50 kW/m<sup>2</sup> are shown in Figure 5.14 and Figure 5.15, respectively.

At the heat flux of 20 kW/m<sup>2</sup>, the overall model prediction concerning different locations fits the experimental data fairly well, especially at the transient stage. For the middle and bottom thermocouple locations, the deviation is quite reasonable to predict

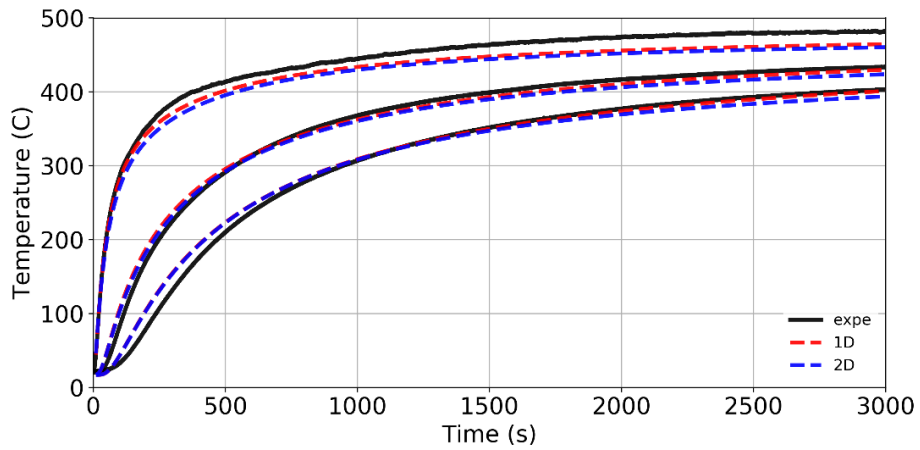


Fig. 5.14 Temperature evolution of char pure conduction at different locations at the heat flux of  $20 \text{ kW/m}^2$

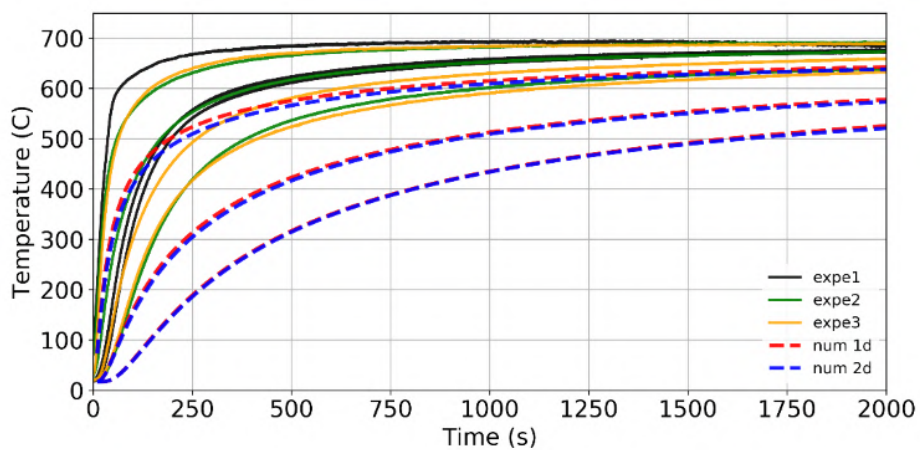


Fig. 5.15 Temperature evolution of char pure conduction at different locations at the heat flux of  $50 \text{ kW/m}^2$

well the specific heat capacity and thermal conductivity. The temperature evolution at the top location is predicted well at the onset of the heat conduction stage. However, the temperature is under-predicted at the intermediate and final stages which mainly due to the experimental moderate surface shrinkage and crack presence such that the specific surface could absorb irradiant heat flux leading to an increase of temperature. The presence of cracks allows radiation penetration over a thin layer, increasing the temperature near the surface. As the radiation effect on the sample is not taken into account in the model, it could explain the discrepancies observed for the temperature evolution at the steady-state heating process. The temperature is well captured for the middle location during the transient state because cracks are not fully formed and probably the in-depth radiation could be negligible. The char pore radiation also increases much at a high temperature. It could cause many more differences and this model does not consider this phenomenon which tends to be the partial reason for providing this underestimation result.

For the temperature evolution at  $50 \text{ kW/m}^2$ , quite large discrepancies are observed regarding the three temperature evolutions between the experiments and predictions. Under this heat flux condition, the char surface temperature prediction is of high uncertainty due to the serious cracks and shrinkage of the char layer surface, as seen in Figure 5.15. Indeed, if we compare temperature profiles at the three locations of experiment 1 (black curves), we can see that middle and bottom temperatures are nearly the same, which means that the two thermocouples were in the same crack. The temperature in the crack is governed by the in-depth radiation process explaining why the crack locations have the same temperature profile. Excepting such typical cases, experiments are quite reproducible meaning that when the char matrix is highly porous with many cracks, the in-depth radiation governs the heating process of the char matrix. As the model used doesn't include an in-depth radiation effect, the pyrolysis modeling at high flux could be not well captured. This point will be discussed in the following pyrolysis modeling part of 5.6.

The experiments for temperature evolution are observed to involve a high degree of repeatability at 20 kW/m<sup>2</sup>. When subjected to the high heat flux of 50 kW/m<sup>2</sup>, the experiments can involve serious scatter due to its strong unreliable physical boundary conditions. Indeed, the surface and inner structure of the sample under 50 kW/m<sup>2</sup> accounts for poor integrity, and much serious deviation is believed to be present when simulating based on the original mesh. The char structure for 50 kW/m<sup>2</sup> is quite fragile and many cracks are present, especially at the surface which is quite different from the original wood sample.

Indeed, using the inverse analysis method to obtain char thermal properties, the realistic char layer is quite hard to quantify with a relatively large deviation between experimental and numerical simulation. They could be attributed to the unreliable rough boundary condition as noted in [82]. And the experiments under well-controlled boundary conditions could achieve much accuracy for model prediction. At the final stage, with fully formed porous char, the radiation through the pore dominates the heat transfer to the back surface. At the heat flux of 50 kW/m<sup>2</sup>, the char is comprised of more pores than that at 20 kW/m<sup>2</sup> due to the high heating rates especially at the surface [37], as noted in [82], the char porosity could attain 0.96.

Based on the above analysis regarding the char thermal parameters obtained under two heat flux different levels of discrepancies are obtained. The values under 50 kW/m<sup>2</sup> are quite unreliable compared with reality, and they are not appropriate to predict the corresponding pyrolysis process at 50 kW/m<sup>2</sup>. Due to the observation that the temperature evolution is predicted with higher accuracy under 20 kW/m<sup>2</sup>, and the errors are approximately negligible compared with experimental uncertainties. Thus, the char thermal parameter value obtained by 20 kW/m<sup>2</sup> is adopted as the input parameters to simulate the pyrolysis cases for these two heat fluxes. The char conductivity extracted is an “apparent” value considering the porous char matrix as a component. However, the choice has been made without considering the thermal conductivity value of the in-depth radiation process, because it has been demonstrated that the in-depth radiation is a key process at high heat fluxes. Then, a physical

model should be added to take it into account rather than including its effect into an “apparent conductivity”. The second reason is to quantify the real impact of this value on the pyrolysis process. The data from the inverse analysis under lower heat flux is preferable due to the relatively higher reliability although the thermal behavior at high temperatures is not well captured. The uncertainty level is found to be approximately 10% for the inverse analysis in this work, and they are within the range of deviations of experimental uncertainties of 10% [56, 135].

In order to assess the physical meaning of char thermal parameters predicted in this study, the reference data are collected to compare. Figure 5.16 and Figure 5.17 show the comparison of thermal conductivity and specific heat capacity of char between the reported and the predicted in this study.

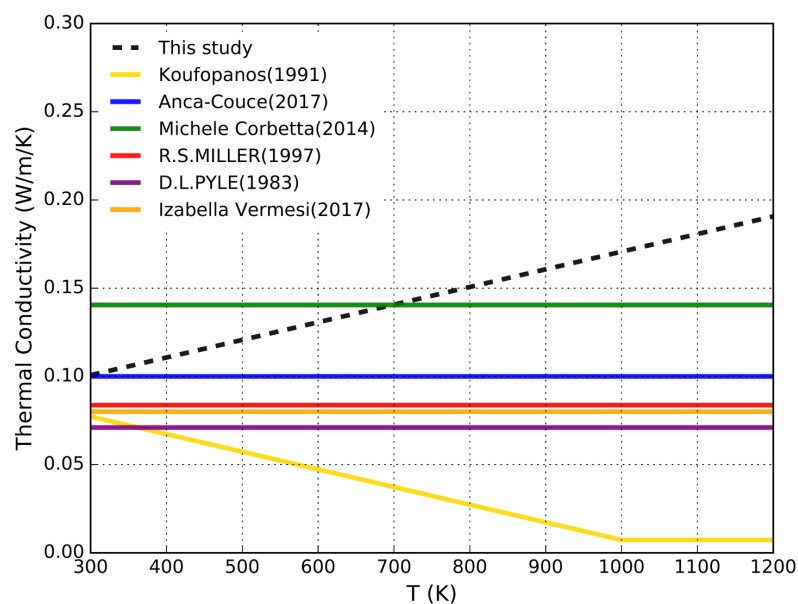


Fig. 5.16 Comparison between predicted and reported char thermal conductivity. (Koufopoulos(1991) [178], Anca-couce(2017) [177], Michele Corbetta(2014) [38], R.S.MILLER(1997) [175], D.L.PYLE(1983) [184], Vermesi(2017) [4])

Observing these two figures, the discrepancy for char thermal conductivity is within the limit of errors, which is consistent with the literature data especially at the temperature range of 300-700 K. The specific heat capacity is close to the literature data presented. In this study, the effective thermal conductivity accounts for the

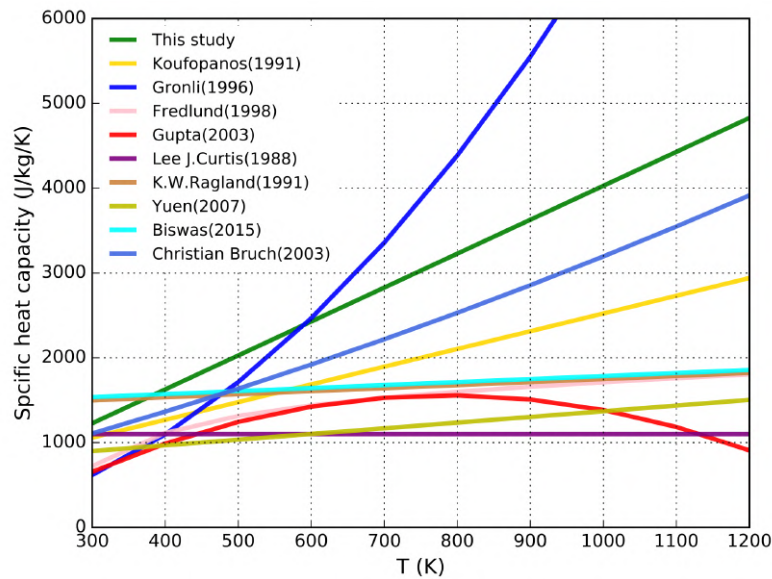


Fig. 5.17 Comparison between predicted and reported char specific heat capacity. (Koufopoulos(1991) [178], Gronli(1996) [62], Fredlund(1988) [185], Gupta(2003) [59], Lee J.curtis(1988) [182], K.W.Ragland(1991) [186], Yuen(2007) [187], Biswas(2015) [188], Christian Bruch(2003) [189])

radiation through the pore excepted for the case at  $50 \text{ kW/m}^2$  where in-depth radiation is a highly dominant process to be included in an apparent conductivity value. Thus, the value could be higher than the reported in the literature but it is assigned to be reasonably accurate within the limit of literature uncertainties.

## 5.5 Model validation for moisture evaporation

As reported in [58] for wood drying, due to the higher pressure in wood, the drying temperature could cause some errors when the temperature of  $373 \text{ K}$  is assumed. There still exists some amount of free water after this drying process [190]. Thus, the common drying method at a temperature of approximately  $373 \text{ K}$  is not taken in this study. As noted previously, the drying process in cone calorimeter under the incident heat flux of  $5 \text{ kW/m}^2$  doesn't involve the presence of pyrolysis reaction.

The drying process is not sensitive to the thermal process and it is found that the water evaporation rate is nearly the same concerning different values of thermal

conductivity and specific heat capacity [57]. The thermal conductivity and specific heat capacity could primarily involve some variations due to the moisture content difference. However, the moisture content is approximately 10 wt% in this study which has a minor contribution to display apparent difference. For the thermal conductivity and specific heat capacity concerning wet and dry wood, it is found in some studies that the difference is quite small within the error of approximately 5% [116], and the majority amounts of water evaporation account for the evaporation temperature of 373 K which is quite low. It is reasonably treated as identical in this study for wet and dry wood. In reality, some water evaporation simulations are conducted previously under  $5 \text{ kW/m}^2$  for collecting different sets of wood specific heat capacity and thermal conductivity. The mass loss history and the temperature evolution present quite similar results. Conversely, it is found that these results are quite changeable with the variation of chemical kinetics and heat of evaporation. The water evaporation kinetic parameters are based on the literature data where the reaction order is assumed to be 1, the activation energy is  $88000 \text{ J/kg}$ , the pre-exponential factor is  $5.132 \times 10^6 \text{ s}^{-1}$  and the heat of evaporation is endothermic with  $2.4 \times 10^6 \text{ J/kg}$  [191, 98].

The water evaporation regarding mass loss, mass loss rate, and temperature evolution profile are presented in Figure 5.18-5.20.

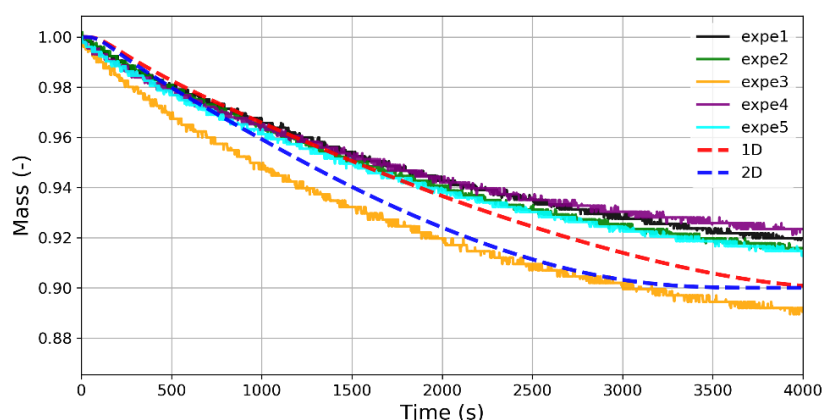


Fig. 5.18 Mass loss for water evaporation of wet wood under  $5 \text{ kW/m}^2$

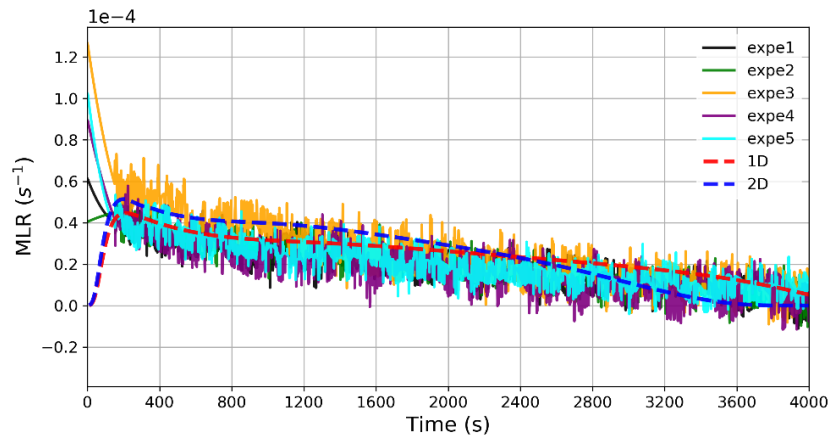


Fig. 5.19 Mass loss rate for water evaporation of wet wood under  $5 \text{ kW/m}^2$

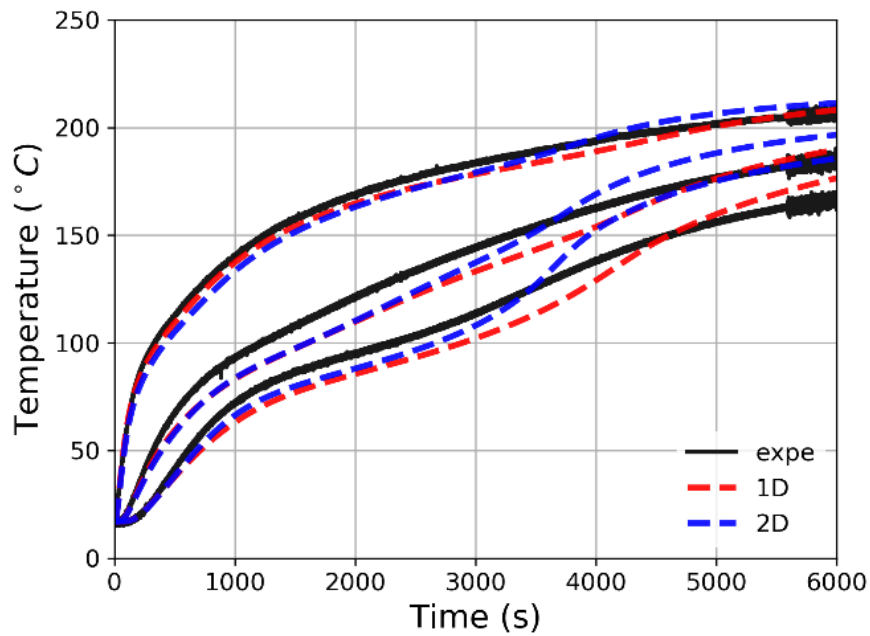


Fig. 5.20 Temperature evolution at different locations for water evaporation of wet wood under  $5 \text{ kW/m}^2$

It can be observed from the figures that the prediction is within the range of experimental uncertainties for both mass loss and mass loss rate profiles. Indeed, as shown in Figure 5.18, the percentage of water can vary between 8 wt% and 11 wt% caused by wood heterogeneity. We can also note that wood evaporation does not reach a steady state during the experiments and that probably increases uncertainties on these values. As mentioned before, a fixed value of 10 wt% has been used in modeling. The temperature plateau presents at a temperature of approximately the boiling point of water. Good fitness is achieved at the initial evaporation stage while some discrepancies are present at the final stage especially for the 2D simulated cases. The deviation between the predicted under 1D and 2D models at the final stage is also observed, which is discussed earlier.

The discrepancy between the measured and predicted could be due to the water transport inside the sample induced by high bulk gas pressure. Indeed, with the pressure elevated in the pore at this heat flux, the moisture could potentially move downward to the bottom of the sample which is cooler [58]. This effect of water vapor moving downward is captured by the model, but the water vapor is assumed to be Nitrogen in the model, noted in Chapter 3, which is one of the drawbacks of model assumptions in this study. The transport properties of Nitrogen are different from  $H_2O$  and could explain one part of the discrepancies. However, the assumption of local thermal equilibrium made in the model is probably much stronger because the model is assumed with no heat exchange between gas in the pores and the solid.

Figure 5.21-5.23 plot simulated slices of water reaction rate at three different characteristic times, 500 s, 1700 s, and 3500 s, respectively. A velocity vector colored by pressure is also added in these figures. As the water evaporation front moves downward, the pressure gradient is achieved on the bottom edge of the evaporation front pushing the water vapor into the bottom direction. When the evaporation front passes through the water vapor, they turn around to the top surface of the sample. Another uncertainty tends to be from the silicate which is added to the simulation and is treated as a porous material, and the silicate is dried before the experiment to

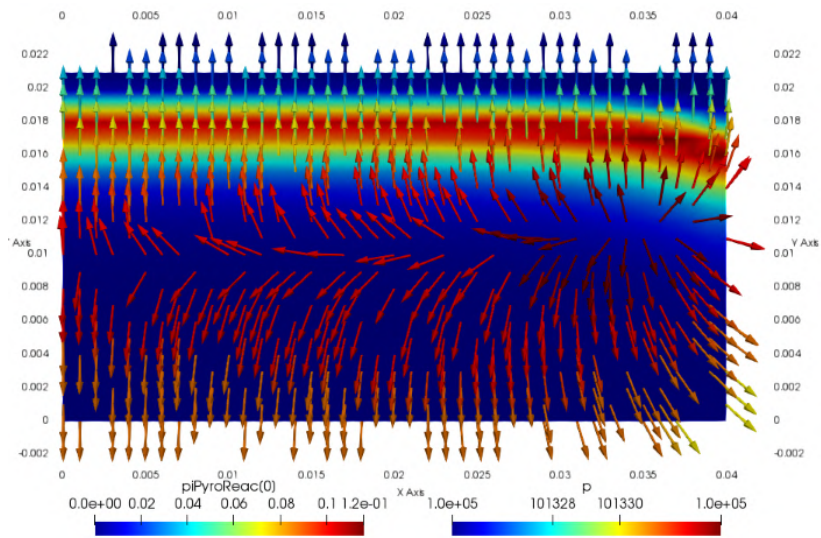


Fig. 5.21 Water reaction rate with velocity arrows colored by pressure at three characteristic time points: 500 s (a)

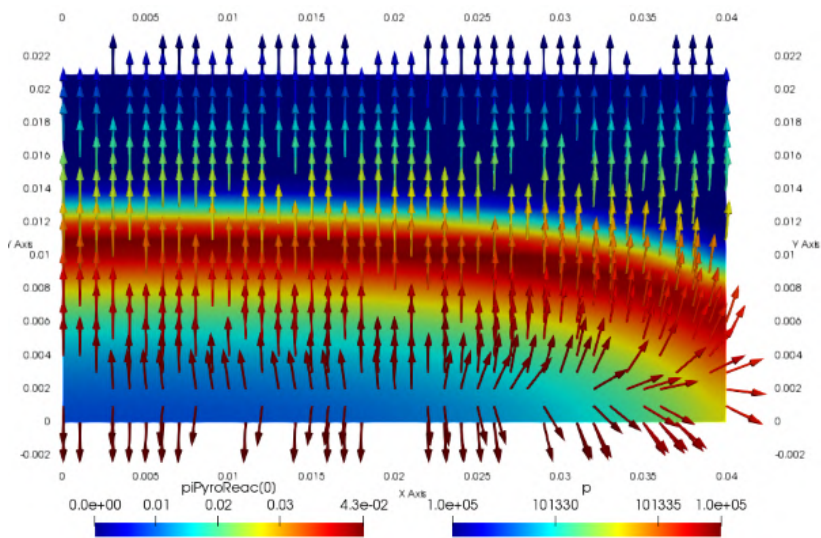


Fig. 5.22 Water reaction rate with velocity arrows colored by pressure at three characteristic time points: 1700 s (b)

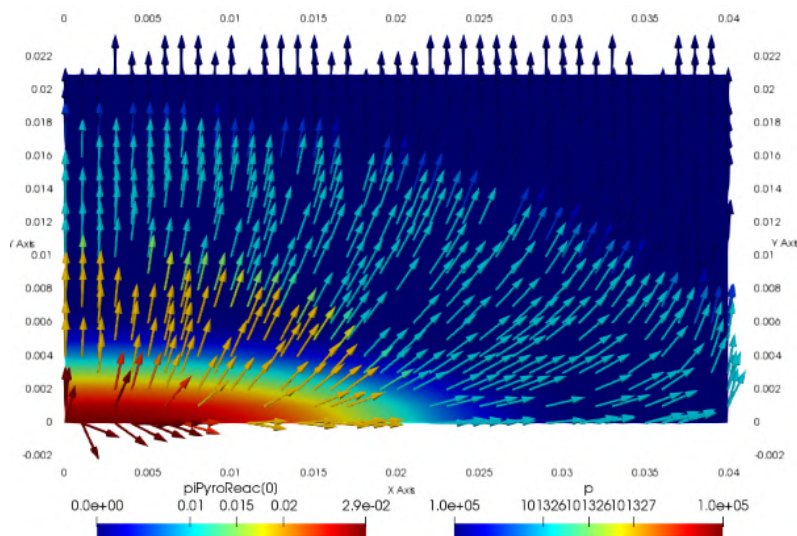


Fig. 5.23 Water reaction rate with velocity arrows colored by pressure at three characteristic time points: 3500 s (c)

limit the errors caused by inside water. Although some amount of water could still exist in the silicate after drying, however, this amount of water can continuously stay inside the sample during the process when subjected to the identical heat flux, and it doesn't influence the results. Due to the relatively high pressure in the wood, the water could migrate to the silicate at the sides which also could move to cooler silicate at the bottom. This effect is captured by the model as seen in Figure 5.21-5.23 where velocity vectors target the silicate. But again, the model assumes a local thermal equilibrium state which probably makes the 2D model over-predict the heat transfer from silicate to wood samples. It can be seen in Figure 5.21-5.23, silicate has an impact on reaction because the evaporation front is curved on sides due to the heat transfer increased by the silicate. At the beginning of the process, the silicate doesn't impact so much the reaction because the front curvature is not so apparent. This could explain that the temperature prediction at the top surface is well captured by the 2D model at the end of the entire evaporation process. But with time going forward, the water evaporation front is more curved and thicker. At the time of 3500 s, the boundaries are dominant

on the evaporation process because the water evaporation front is obvious non-1D, no water presents on sides but remains in the middle. As the water reaction is highly endothermic, the temperature jump could be viewed in Figure 5.20 at the same time of 3500 s and could explain that probably the 2D model doesn't capture correctly what happened on sides. Because water cooling is not taken into account in the model, heat transfer is enhanced on boundaries. Some amount of water in the wood could transport to the inner side and bottom of silicate due to the higher permeability of silicate, as noted, the moisture transfer is dominated by convective mass transport and the diffusion could be neglected [57].

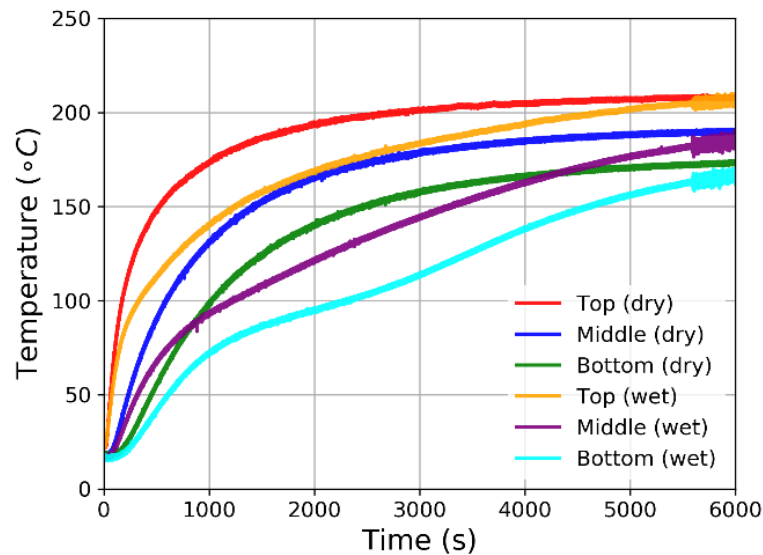


Fig. 5.24 Experimental temperatures evolution for dry wood and wet wood at three locations

The influence of water evaporation on heat transfer into the wood sample is mainly due to the enthalpy of reaction of water evaporation which is highly endothermic. This phenomenon is quantified in Figure 5.24 which plots temperature evolution at the three locations inside the sample for dry wood and wet wood involving the water evaporation process. It can be seen that the three locations are impacted by the water evaporation process until all water is removed. Indeed, in the end, temperatures for two cases (dry wood and wet wood) become the same when all water content is released. Figure 5.25

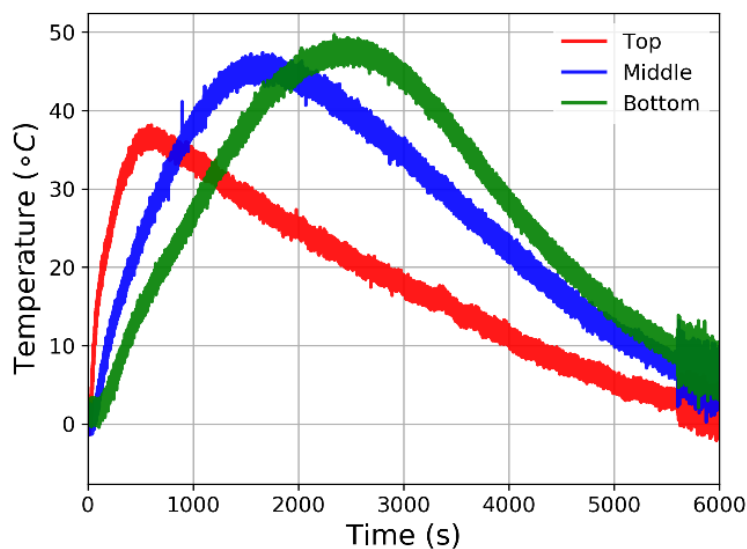


Fig. 5.25 Experimental temperature differences between dry wood and wet wood at three locations

plots the temperature difference between the two cases (dry wood and wet wood) at the three locations. The maximum temperature difference reaches around 50 °C for the bottom. The time at which the maximum temperature difference is reached for each location is different, and they correspond to 600 s, 1700 s, and 2500 s, respectively.

Figure 5.26 plots the reaction rate evolution as a function of the thickness of the sample for these three characteristic times. The peak of reaction rate for each time corresponds to the three locations mentioned above, meaning that the maximum temperature difference is obtained when the evaporation front reaches each location, especially when the reaction rate is maximum. Indeed, in Figure 5.26, we can see that the evaporation front changes across the thickness of the sample. The maximum value decreases and the front become thicker as a function of sample thickness, meaning that the evaporation reaction is fast near the surface and become slower when the front move towards the bottom of the sample.

Figure 5.27 shows the temperature profiles across the thickness of the sample for dry wood (dashed lines) and wet wood (solid lines) at three times. Figure 5.28 plots the temperature differences between the two cases. We can observe that the maximum

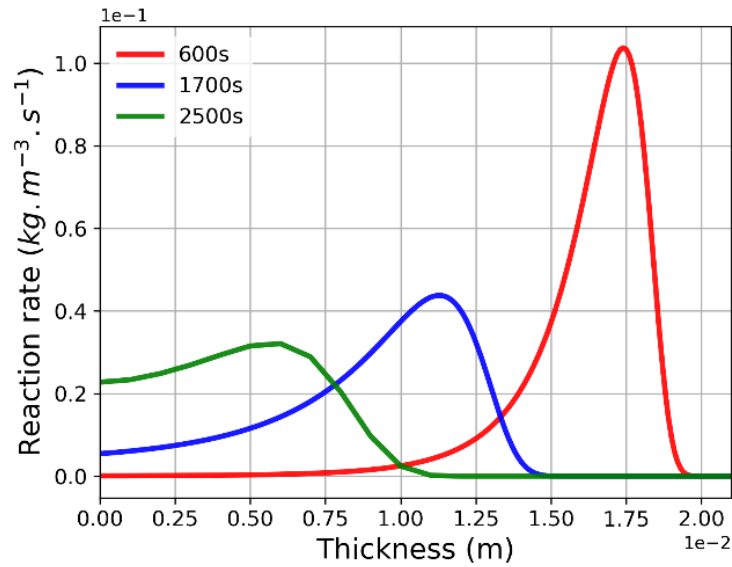


Fig. 5.26 Predicted reaction rate of wet wood evaporation through the thickness

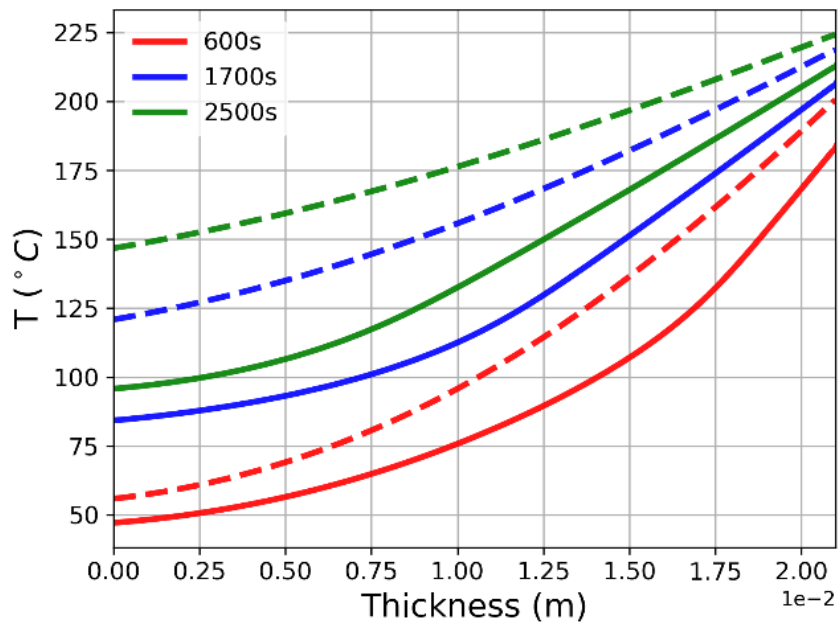


Fig. 5.27 Predicted temperature evolution through the sample thickness for dry wood (dashed lines) and wet wood (solid lines) at three characteristic time points

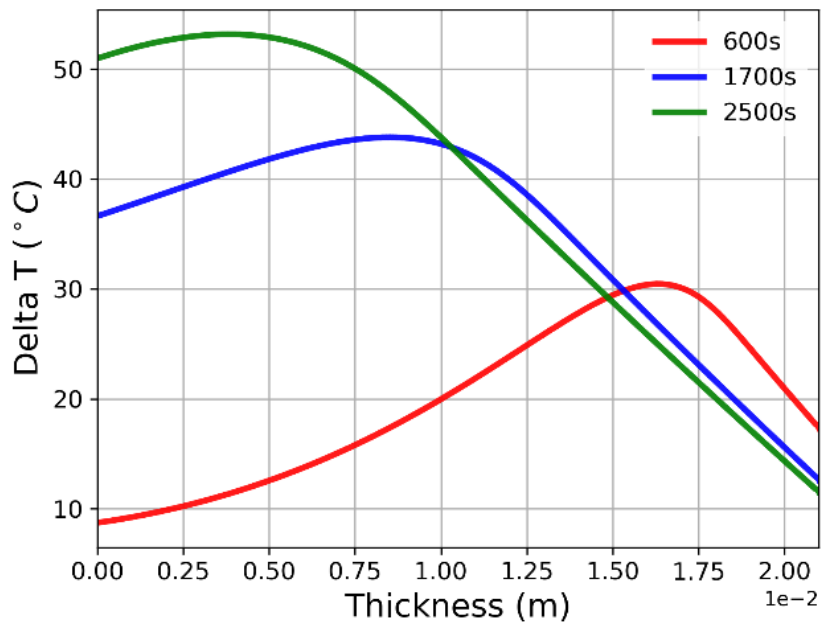


Fig. 5.28 Predicted temperature differences between dry wood and wet wood through the sample thickness at three characteristic time points

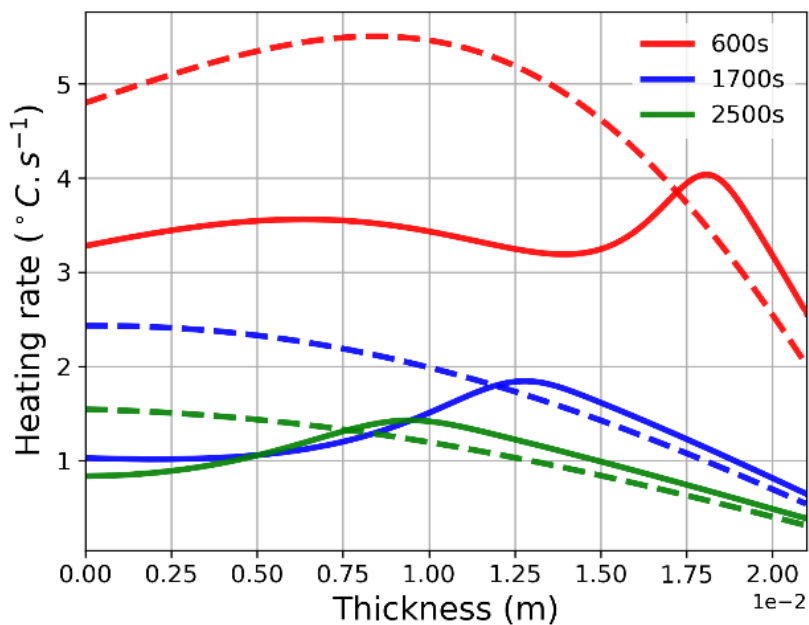


Fig. 5.29 Heating rate profiles across the sample thickness for dry wood (dashed lines) and wet wood (solid lines) at three characteristic time points

difference value for the three locations is close to those extracted by experiments and the locations of these maximum values correspond to the top, middle, and bottom surface of measured thermocouple locations. It implies that the dynamic of the evaporation front along the centerline is well captured by the model.

As pointed out in the TGA chapter, the heating rate is a key factor influencing the pyrolysis reactions and water evaporation. Figure 5.29 plots the heating rate profile across the sample thickness for dry wood (dashed lines) and wet wood (solid lines) at different characteristic times. The peak of solid curves corresponds to the water evaporation front. Downward the evaporation front for the three times, the heating rate is lower for the wet wood case because we have demonstrated before that the pressure in the downward front moves water vapor to the bottom and cool the “virgin” wet wood. For this reason, the temperature is lower and the heating rate is smaller. Upward the water evaporation front, the heating for the wet wood cases becomes nearly equal to the heating rate observed for the dry wood. Indeed, when water is evaporated, no cooling effect appears and the density of the wet wood becomes the same as the dry wood case, and a lower density can promote the increase of the heating rate.

## 5.6 Model validation for wood pyrolysis under different scenarios

Model validation is quite complex work that needs to account for many considerations such as the kinetics validity, parameters accuracy and reliability, boundary conditions, etc. One of the most uncertain factors should be assessed to validate the model under multiple heat flux because the interaction between chemistry, heat, and mass transfer could be more or less strong. Indeed, for high heat flux, the chemistry and heat transfer processes are rather different at different characteristic time scales. The chemistry could be fast compared to the heat transfer process. The pyrolysis front becomes thin and the chemistry could be described by a simple mechanism that is infinitely fast. However, when heat fluxes are quite low, the time scales of the two

competing processes are in the same order of magnitude and the chemistry becomes finite rate. To capture this phenomenon, the model needs to deal with more complex chemistry involving multi-step chemical mechanism.

In this study, the model validation work is conducted regarding wet and dry wood at the heat flux of 20 kW/m<sup>2</sup> and 50 kW/m<sup>2</sup>. The 20 kW/m<sup>2</sup> permits to deal with a low heat flux just above the critical heat flux for wood ignition (around 12 kW/m<sup>2</sup> when thermal decomposition is involved in air atmosphere), and a much higher one (50 kW/m<sup>2</sup>) that represents the classical average heat flux involved in a real fire. In order to avoid a flame, tests are performed under an inert atmosphere (Nitrogen). The kinetic and thermal parameters obtained under a given heat flux are usually employed to assess the validity at other heat fluxes as noted in [121], but the reliability of those parameters will be discussed in pyrolysis conditions tested in this study. The heat of decomposition of Fir wood is prescribed identically as  $-1.0 \times 10^5$  J/kg to each pseudo component mainly from the precise experimental data of softwood [56, 192, 75, 110]. The porosity of wood and char is 0.51 and 0.85, respectively. The wood and char permeability are estimated with  $1.0 \times 10^{-12}$  m<sup>2</sup> and  $1.0 \times 10^{-11}$  m<sup>2</sup>, respectively. Nitrogen is prescribed for the released pyrolysis gas volatiles and its thermal and transport properties are introduced from [110].

### 5.6.1 Model validation for temperature and mass loss profiles

As mentioned before, the value of the incident heat flux is one important parameter governing heat transfer into the solid as the rate of the chemistry. For a fixed incident heat flux, the rate of chemistry could also change because of the “thermally-thick” characteristic of the solid involved in the pyrolysis process. Indeed, as temperature gradients are assumed into the sample, the interaction between heat transfer and pyrolysis reaction could change and depends on time. Figures 5.30 and Figure 5.31 plot the experimental heating rates of the solid during pyrolysis at the three locations for the two different heat flux introduced before.

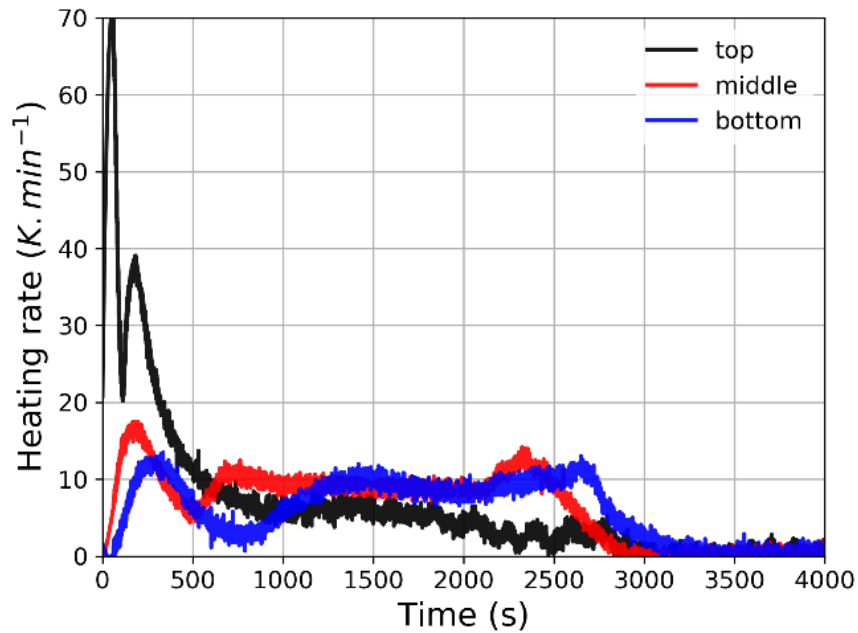


Fig. 5.30 Experimental heating rates for 20 kW/m<sup>2</sup> at three locations

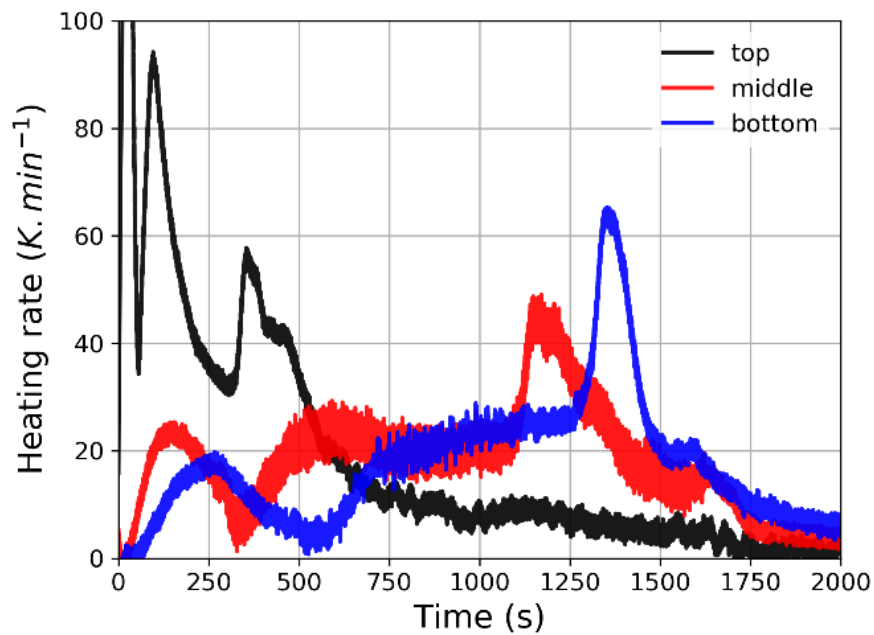


Fig. 5.31 Experimental heating rates for 50 kW/m<sup>2</sup> at three locations

For the two heat flux, a large range of heating rates is involved during the pyrolysis process, depending on time and space location in the sample. The major role of the heating rate on the chemical process has been demonstrated in Chapter 4. In consequence, this large range of heating rates involved when a thick solid is thermally decomposed which points out the complexity of the chemistry the model needs to capture. Under higher incident heat flux, the mean heating rate value is higher. It is interesting to underline that in the two cases, the highest heating rates, as well as the highest gradient of heating rates, are involved at the beginning of the pyrolysis process. During this beginning stage, the pyrolysis gases are released governing the ignition process when the thermal decomposition is involved in air. Then, to capture correctly the ignition process, the pyrolysis model should describe those first stages correctly when heating and gradients are high. As a perspective of this study, the heating parameter should be taken into account carefully in the chemical mechanism.

In this study, as introduced in Chapter 4, we decide to extract kinetic parameters by two different fixed heating rate values, rather than extracting parameters for a range of heating rates. Indeed, as parallel reaction mechanisms don't take into account heating rate which is a "physical parameter", we decided to employ two different constant values to address the role of heating rates in the chemistry description during the pyrolysis process. We have chosen 10 K/min because this value is an average of heating rates involved when pyrolysis is under 20 kW/m<sup>2</sup>. For 50 kW/m<sup>2</sup>, the average heating rate is not easy to quite clearly point out but 20 K/min seems to be the mean value. However, when observing the whole evolution trend, we decided to extract kinetic data at 50 K/min which is the highest value that can be handled with TGA to investigate pyrolysis when high heating rates are involved.

One of the most important drawbacks of a parallel reaction mechanism is that it doesn't take into account the heating rate into the chemical reaction. It fails to predict the final residual mass fraction making this mechanism inconsistent in terms of mass conservation. Figure 5.32 plots experimental and the 1D simulated total mass loss

evolution by using kinetic parameters extracted at 10 K/min for dry wood pyrolysis under 20 kW/m<sup>2</sup>.

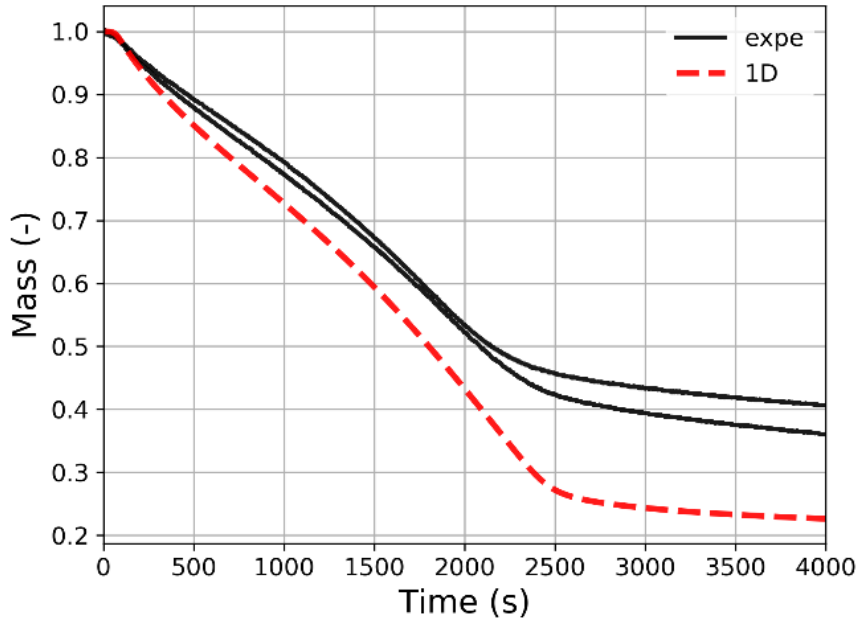


Fig. 5.32 Experimental and modeled total mass evolution for dry wood pyrolysis under 20 kW/m<sup>2</sup>

A large under-prediction of the final mass by the model is observed. Indeed, at the end of the process, low heating rates are involved, less than 5 K/min (Figure 5.30) while the chemical model used has been developed at 10 K/min. As demonstrated in Chapter 4, the model developed at a higher heating rate than in reality tends to under-predict the final mass residue. To avoid this phenomenon, the stoichiometric coefficients for hemicellulose, cellulose, and lignin reaction extracted at TGA scale have not been used but scaled by their proportion to conserve the mass for each experiment in the cone calorimeter. This scaling factor could be viewed as a “numerical parameter” and has to be removed in the future by improving the chemical mechanism used. However, it facilitates here for the comparison of predicted and experimental curves and does not modify the physics involved during the pyrolysis process.

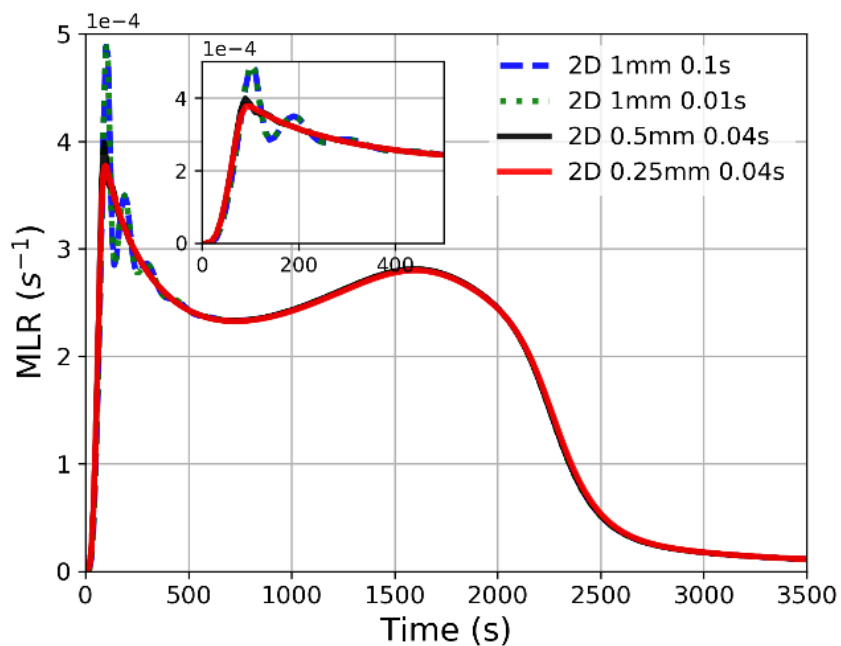


Fig. 5.33 Influence of mesh size and time steps during simulation for 2D model at 20  $\text{kW/m}^2$

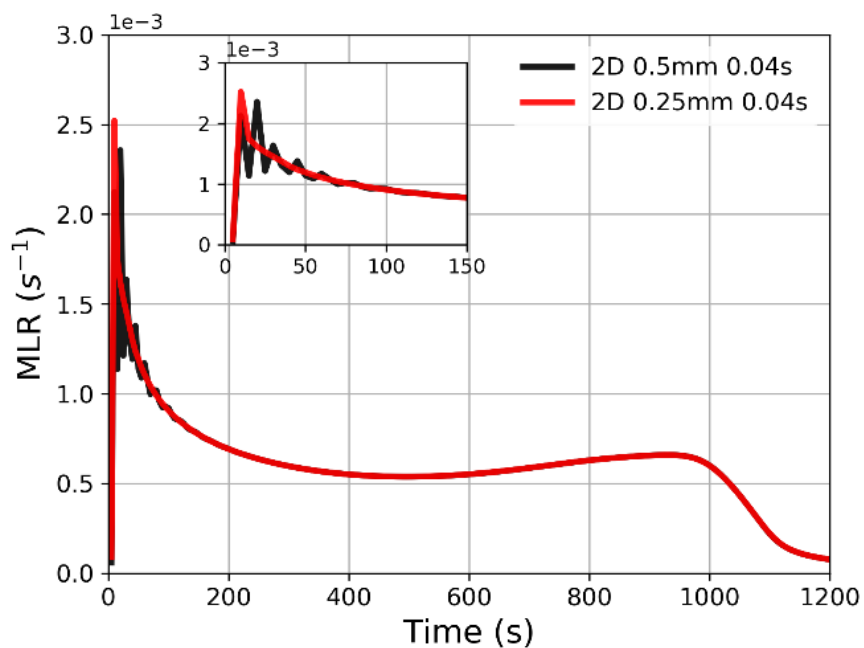


Fig. 5.34 Influence of mesh size and time steps during simulation for 2D model at 50  $\text{kW/m}^2$

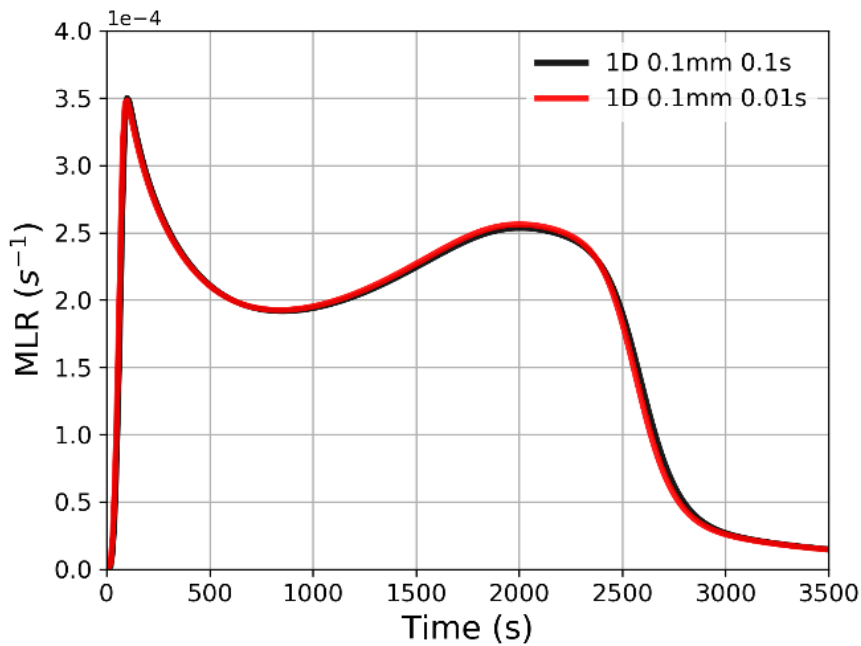


Fig. 5.35 Influence of mesh size and time steps during simulation for 1D model at 20 kW/m<sup>2</sup>

Figure 5.33-5.35 plots the sensitivity of mesh size and time steps on numerical results. The overall mass loss rate is plotted to represent the sum of the reaction rates over the space domain. Local scalars like in space have been also checked to verify if they are independent of mesh size and time step, and the sensitivity of those scalars follows the MLR one. It has been demonstrated that the heat transfer process is far less sensitive to mesh size and time steps than the chemistry process. In consequence, no plots are shown on that. Regarding 1D simulation, a constant mesh size of 0.1 mm and a time step of 0.1 s is sufficient to make results independent. For 2D simulation, a mesh size of 0.25 mm and a time step of 0.04 s has been chosen so that the results become independent of those numerical parameters. It has been checked that the numerical parameters chosen here are not independent numerical results for all conditions tested regarding heat flux of dry or wet wood pyrolysis cases.

For dry wood and wet wood exposed to the heat flux of 20 kW/m<sup>2</sup>, the comparison between the measured and predicted data are depicted in Figure 5.36-5.41, which

correspond respectively to mass loss, mass loss rate, and temperature evolution at different probes.

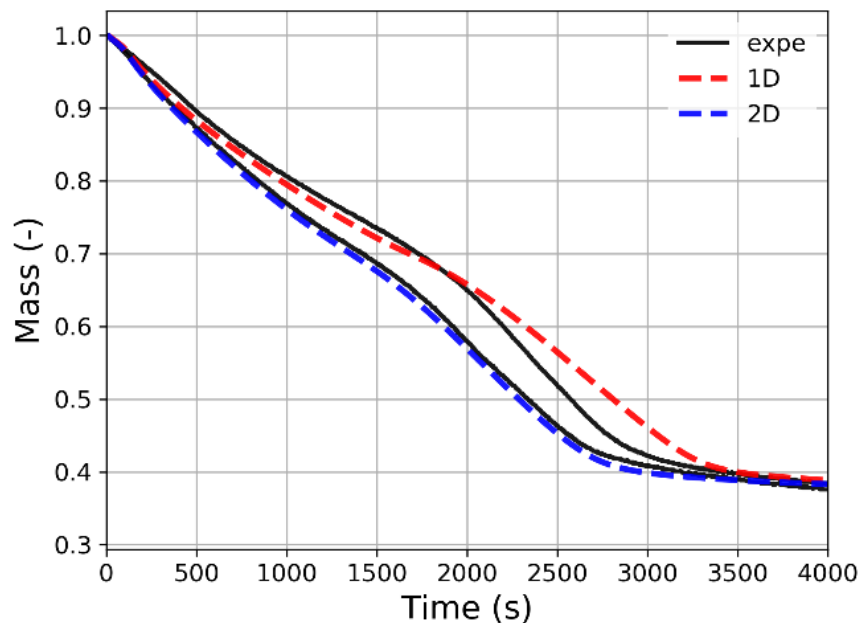


Fig. 5.36 Experimental and predicted mass loss profile for wet wood pyrolysis at the irradiant heat flux of  $20 \text{ kW/m}^2$

For experiments concerning wet and dry wood pyrolysis conducted at  $20 \text{ kW/m}^2$ , from the onset up to approximately  $373 \text{ K}$ , different heating and reaction behaviors are observed. The left minor peak of mass loss rate concerning water evaporation is reasonably correct for wet wood. The duration of water evaporation for different locations displays differently, the bottom temperature is at approximately  $373 \text{ K}$  and it can have a much longer duration. This demonstrates that water evaporation involves a relatively slow rate compared with the top and the bottom locations, where temperatures are higher promoting water evaporation. For the first peak concerning pyrolysis of wood, this peak for dry wood is higher and appears earlier compared with wet wood. This demonstrates that water could prolong the pyrolysis severely and a high reaction rate can be achieved. Indeed, the dry wood after the water evaporation process tends to be present with higher porosity. And all these physical phenomena could

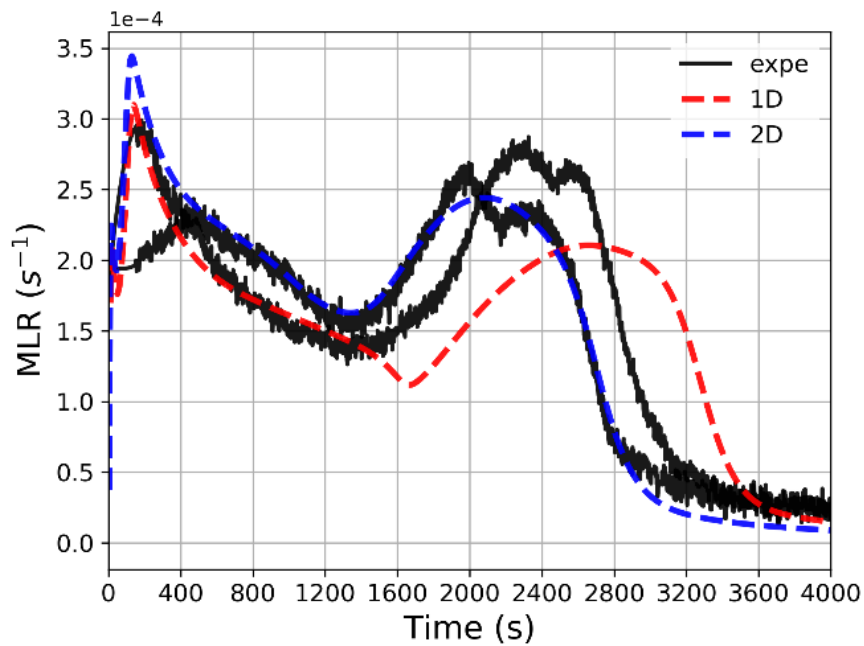


Fig. 5.37 Experimental and predicted mass loss rate for wet wood pyrolysis at the irradiant heat flux of  $20 \text{ kW/m}^2$

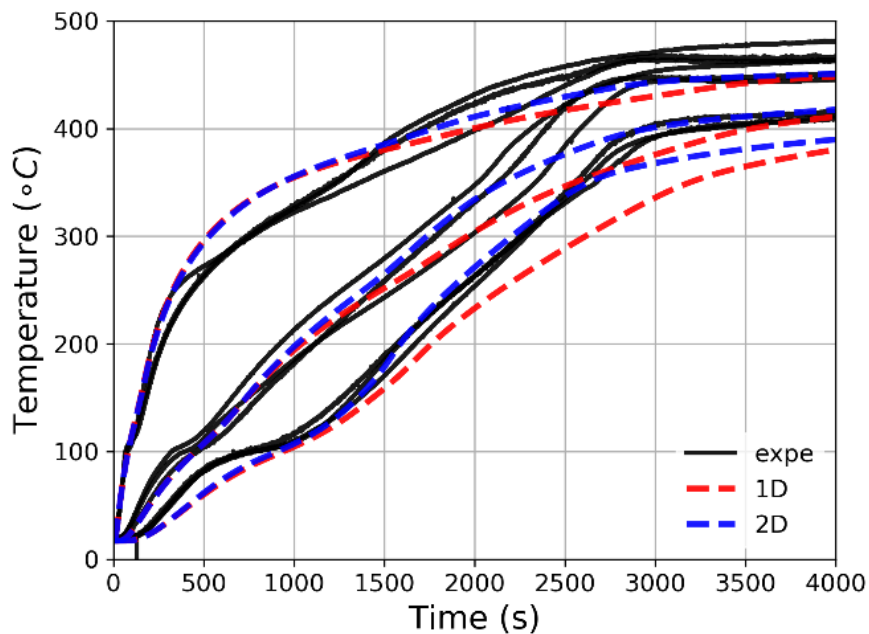


Fig. 5.38 Experimental and predicted temperature evolution for wet wood pyrolysis at the irradiant heat flux of  $20 \text{ kW/m}^2$

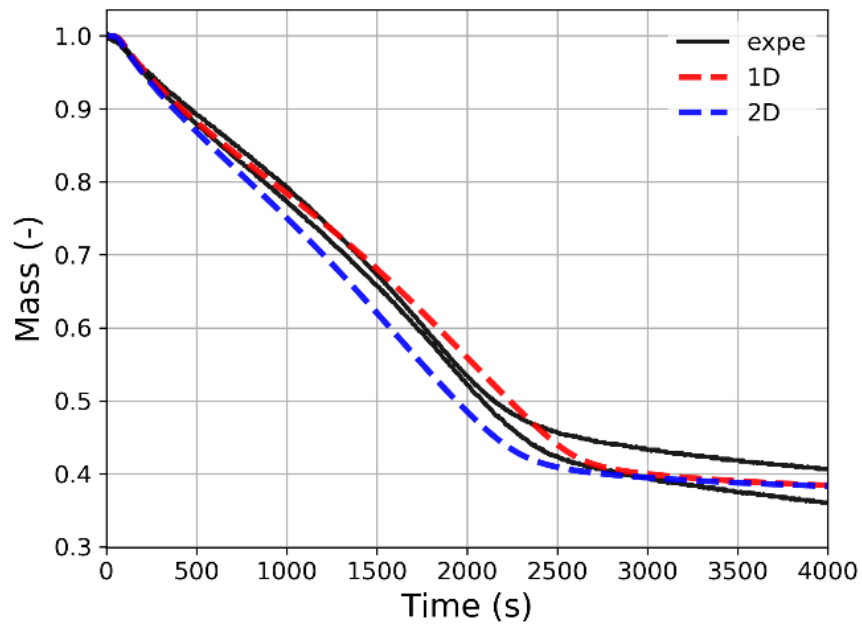


Fig. 5.39 Experimental and predicted mass loss profile for dry wood at the irradiant heat flux of  $20 \text{ kW/m}^2$

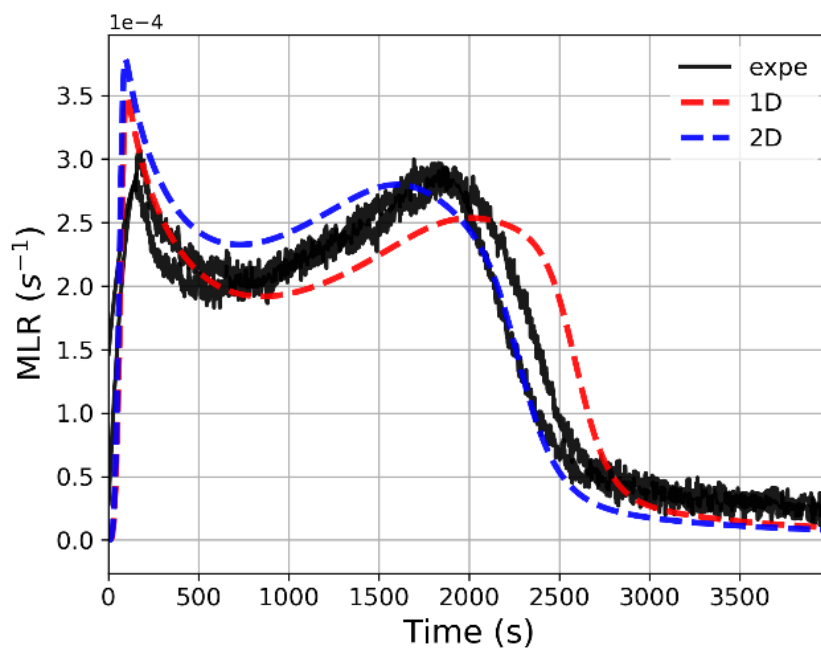


Fig. 5.40 Experimental and predicted mass loss rate for dry wood pyrolysis at the irradiant heat flux of  $20 \text{ kW/m}^2$

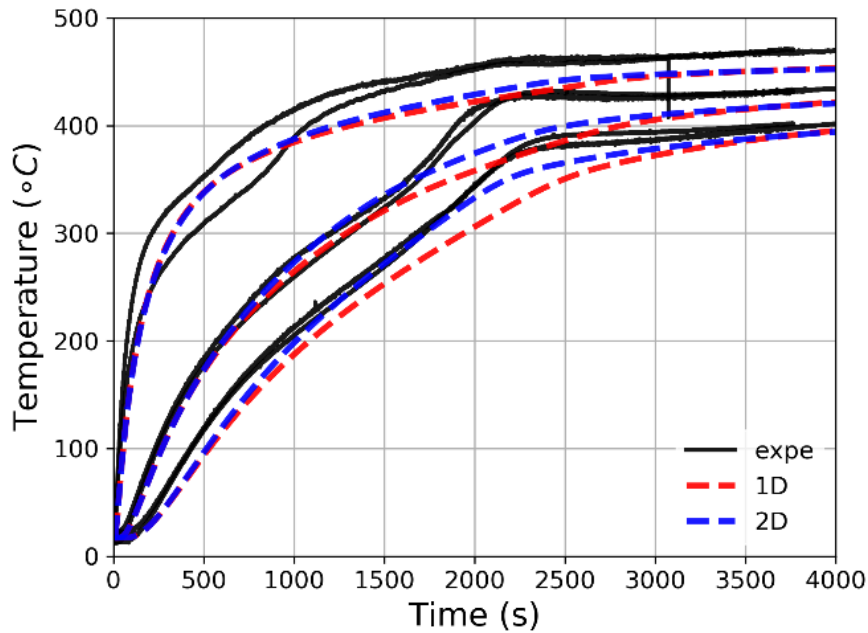


Fig. 5.41 Experimental and predicted temperature evolution for dry wood pyrolysis at the irradiant heat flux of  $20 \text{ kW/m}^2$

enhance the gas mass transfer, thus for dry wood pyrolysis, it could be subject to a higher mass loss rate. However, the final char yield fraction and temperature concerning wet wood and dry wood pyrolysis behave similarly, and no apparent differences are present. It is observed that approximately 25 wt% of mass residue is involved at  $20 \text{ kW/m}^2$  for wet and dry wood. Indeed, the water reaction does not interact with the pyrolysis reaction in the model, except for the temperature decrease enhanced by the water evaporation reaction which is endothermic. However, as the water reaction changes the local heating rate of the solid and due to the fact that this heating rate interacts with pyrolysis reaction as shown in Chapter 4, water evaporation should act on pyrolysis through the heating rate change. However, the pyrolysis model used here doesn't take into account this phenomenon. It is reasonably correct to expect that the final char yield is identical regarding the wet and dry wood. The water only tends to delay the pyrolysis process, and the corresponding reaction peak or temperature rise is limited. The water evaporation could change the material's porosity and permeability, thereby

influencing the pyrolysis behavior especially the gas flow. It has the trend to lose mass continuously which accounts for the lignin decomposition at a high-temperature range, and it could produce a partially charred residue. In this work, the different mass fractions of char are produced by different sub-components and the final char yield for different heat flux is treated as different due to the observation of experiment data.

The most apparent discrepancies for the two cases lie in the temperature evolution especially at the bottom location which is the most susceptible region by heat conduction. The water is also responsible for the decreasing magnitude of the second peak for wet wood pyrolysis. As depicted in Figure 5.38 and Figure 5.41, the wet wood involves a serious temperature evolution plateau especially at the bottom location, while no such plateau is present for dry wood pyrolysis. As noted that the moisture content accounts for approximately 10 wt% for wet wood and dry wood is defined to be completely dry, this plateau is mainly due to the endothermic of water evaporation and can delay the mass loss process.

The model predictions fit well the experimental mass loss and mass loss rate, except for the second peak temperature range. The model predicted earlier the mass loss rate at 20 kW/m<sup>2</sup> and this trend is found to be consistent with that at 50 kW/m<sup>2</sup> in the following part. As shown in Figure 5.36-5.40, different levels of deviation occur between the prediction and experimental results, and this deviation increases with an increase in temperature. Concerning the MLR at the peak temperature range, slight deviations are observed, and the final temperature stage involve a reasonable agreement especially in the 2D case. Indeed, the 1D model under-predicts the second mass loss rate peak magnitude, the time to reach the peak of the second mass loss rate is predicted with some delay. As we demonstrated in the water evaporation description part, the experiments in 2D for the boundary condition on sides are influenced by the silicate: the water evaporation front is curved on sides due to this side effect. For this reason, the 1D model gives acceptable results except for the end of the pyrolysis process when this side effect becomes non-negligible. Indeed, at the onset of pyrolysis and the final stage, no apparent difference is observed. During the temperature range of the

second peak, a deviation is present between 1D and 2D models. Some portions of heat are conducted to the wood side and induce a much higher temperature than at the center of the wood sample. Even though the 2D model captures better this effect, the second peak of MLR is well captured by the 2D model and some improvements should be done because some discrepancies remain for the temperature prediction at the end. The main cause is not clear to define. We can question if these discrepancies are due to boundary conditions which are not well defined or if it comes from the pyrolysis model which is too simple to capture correctly the pyrolysis process when the side effect becomes strong. However, we can consider globally that the model prediction is reasonably acceptable and the judgment is believed to comply with the uncertainty of experiments.

The comparisons between the measured and predicted data for wet wood pyrolysis under the irradiation of  $50 \text{ kW/m}^2$  are shown in Figure 5.42 to Figure 5.44, which involve respectively the mass loss, mass loss rate, and temperature evolution at different probes. The solid lines correspond to the experimental data and the dashed lines correspond to the prediction.

The comparisons between the experimental and predicted data for dry wood pyrolysis under the irradiation of  $50 \text{ kW/m}^2$  are shown in Figure 5.45 to Figure 5.47, which correspond to mass loss, mass loss rate, and temperature evolution at different probes, respectively.

When observing the experimental data for wet and dry wood pyrolysis under  $50 \text{ kW/m}^2$ , the experimental deviations among different runs involve different levels of discrepancy at different pyrolysis stage concerning the mass loss and the in-depth temperature evolution at three locations. For the mass loss rate profile following the first peak, due to the char formation with lower thermal conductivity, the plateau occurs with less heat conduction while involving endothermic pyrolysis reaction. This trend could delay for some time until the second peak, with a strong pyrolysis reaction of large remaining mass fraction due to the thermal feedback influence. The material temperature continuously increases, at the termination of the second peak, the whole

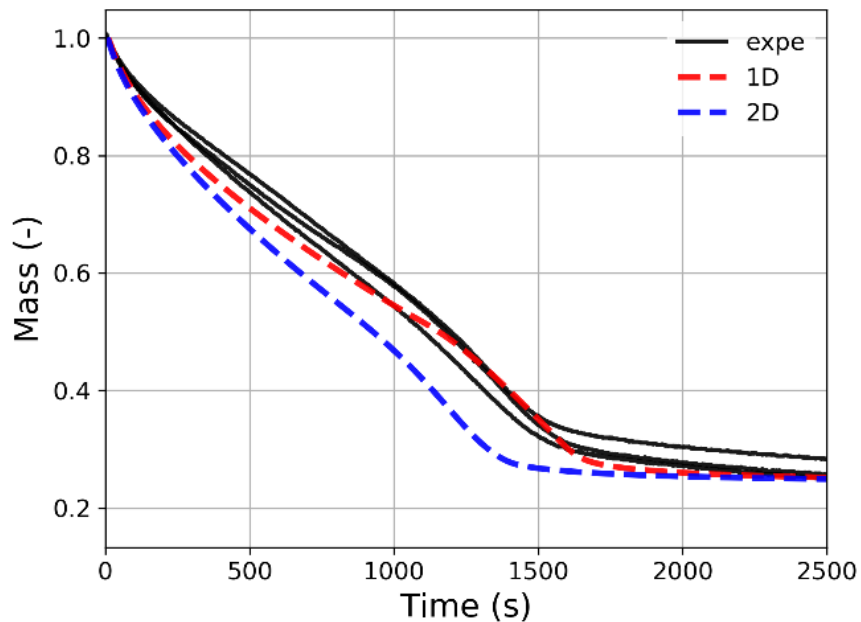


Fig. 5.42 Experimental and predicted mass loss for wet wood pyrolysis at the irradiant heat flux of  $50 \text{ kW/m}^2$

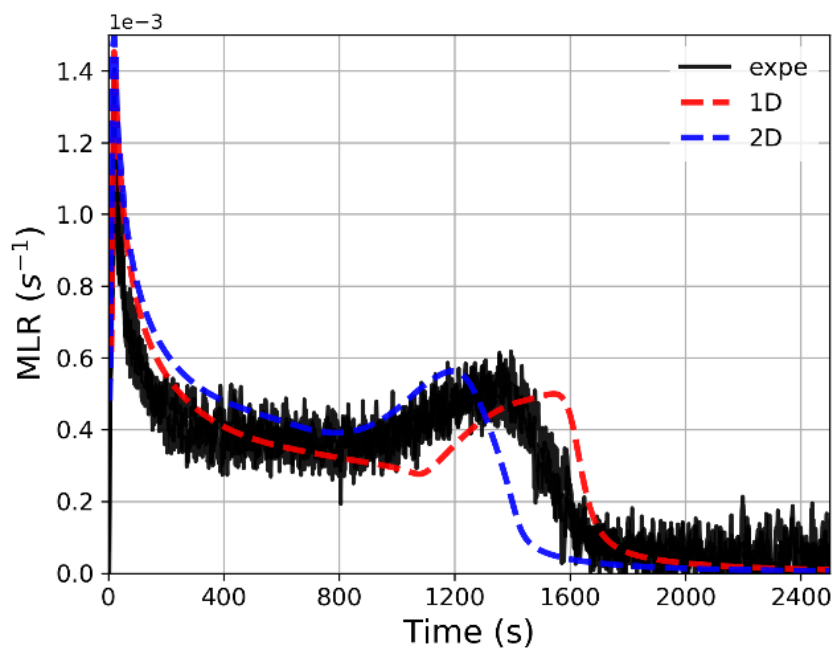


Fig. 5.43 Experimental and predicted mass loss rate for wet wood pyrolysis at the irradiant heat flux of  $50 \text{ kW/m}^2$

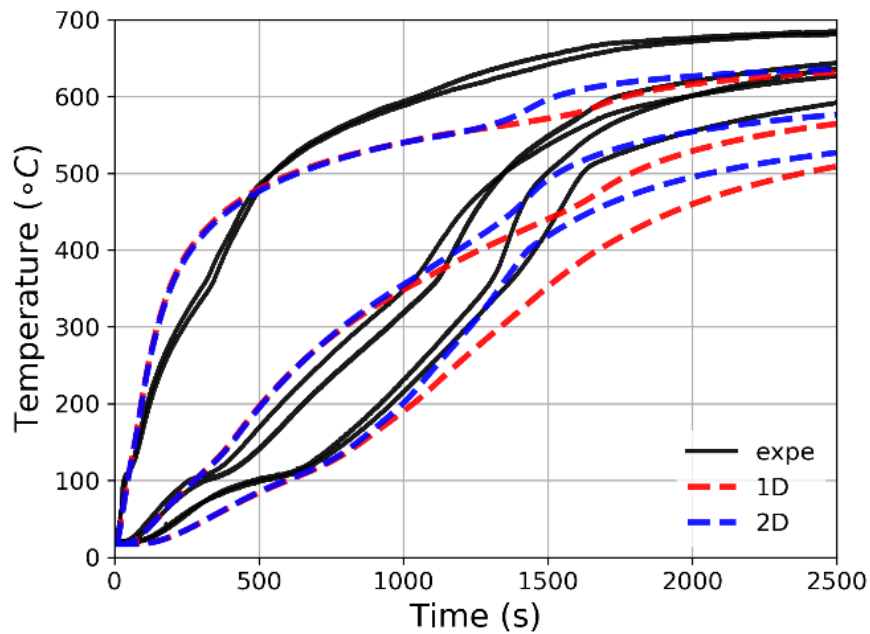


Fig. 5.44 Experimental and predicted temperature evolution for wet wood pyrolysis at the irradiant heat flux of  $50 \text{ kW/m}^2$

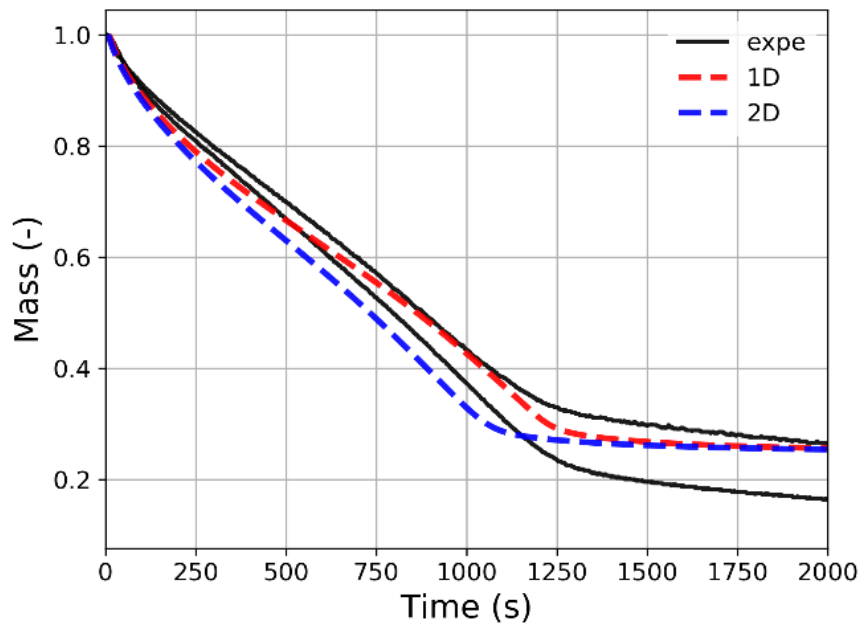


Fig. 5.45 Experimental and predicted mass loss rate for dry wood pyrolysis at the irradiant heat flux of  $50 \text{ kW/m}^2$

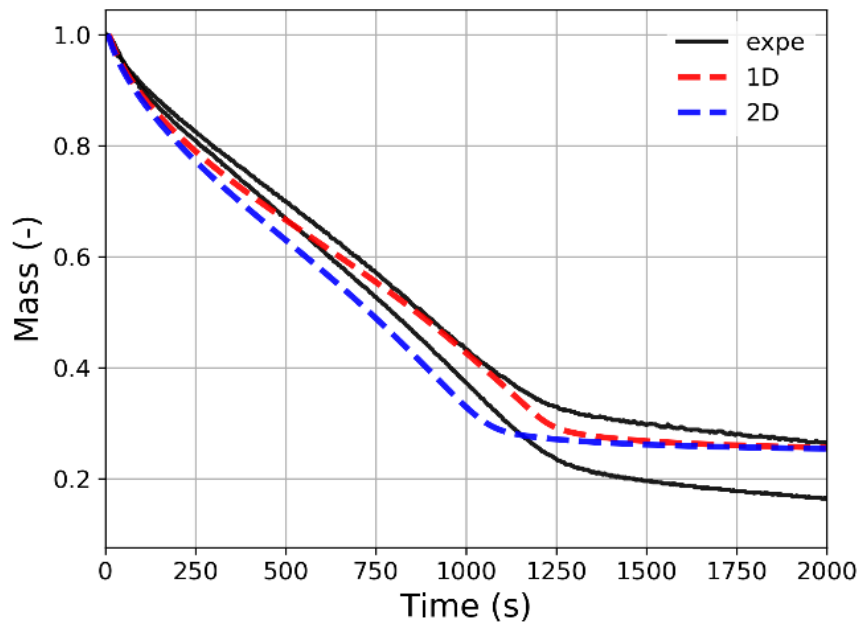


Fig. 5.46 Experimental and predicted mass loss rate for dry wood pyrolysis at the irradiant heat flux of  $50 \text{ kW/m}^2$

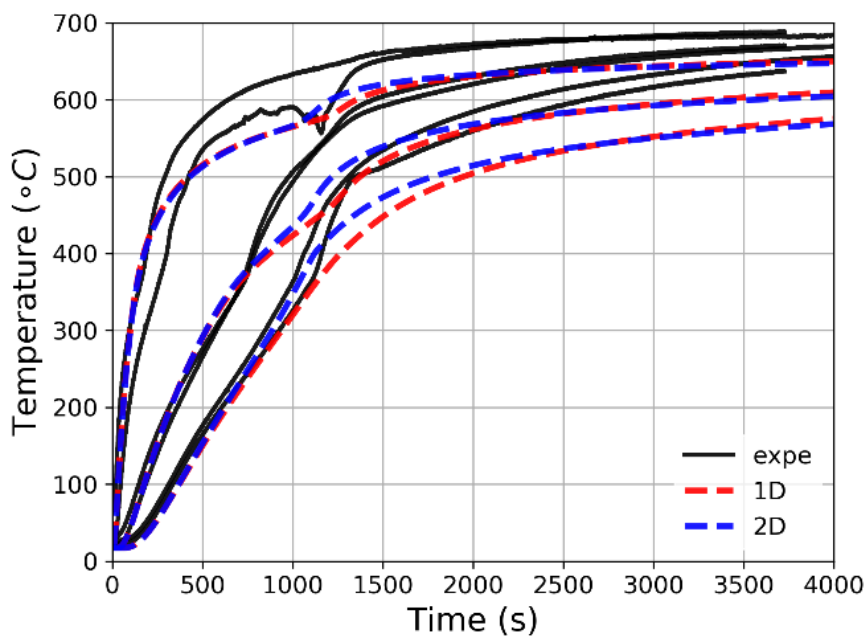


Fig. 5.47 Experimental and simulated temperature evolution for dry wood pyrolysis at the irradiant heat flux of  $50 \text{ kW/m}^2$

material could undergo a quasi-steady state, and the temperature evolution slows down with a long duration as displayed in the temperature profile at the end.

Similar to the trend regarding temperature evolution at  $20 \text{ kW/m}^2$  for wet wood pyrolysis, the temperature plateau occurs at approximately  $373 \text{ K}$  which accounts for the endothermic reaction of the water evaporation. This delays the temperature increases especially at the bottom location due to the relatively low temperature and longer duration of water vapor which absorbs much heat. As noted in [83], the cooling effect could influence the temperature at different locations. It is observed that it could be severe at the bottom location because the heating rate is small. The predictions coincide well with experimental data at both heat flux with exception of some deviations at the intermediate and final stages. Some factors could be responsible for these deviations. For example, the thermocouple position shifts induced by wood shrinkage and severe char cracks at the top surface location. It is consistent with the predicted presence of different levels of temperature deviation through the thickness. At a later stage, when the temperature reaches the threshold of pyrolysis reaction, the endothermic pyrolysis reaction can also cause a temperature profile plateau. However, it is not apparent with the presence of a smaller temperature evolution slope due to the minor influence at high temperature. It demonstrates that endothermic heat is more sensitive at low temperatures. After the plateau, the temperature increases sharply and absorbs a lot of heat to pyrolyze.

Under the 1D simulation, the mass loss rate is also predicted in good agreement concerning peak magnitude except for the appearance of the second peak, with some delay for approximately  $200 \text{ s}$  for wet wood pyrolysis. It can be seen that some improvements are achieved for 2D model prediction compared with that of the 1D model for the pyrolysis duration range of mass loss rate and temperature evolution, especially from  $800 \text{ s}$  to approximately  $1500 \text{ s}$  in the vicinity of the second peak. The most probable reasons could be attributed to side effects as discussed earlier. It is observed that the prediction accuracy trend is worse with the increasing time. This is mainly caused by the char formation with higher uncertainties at the final stage

at which the surface shrinkage and crack presence are more severe. Indeed, the char structure is more complete and thick at low heat flux, while at high heat flux, it is very fragile and the roughness is serious to absorb much radiation from the irradiant cone heater. The effective surface location tends to be much lower compared with the initial position which could enhance the heat transfer to the char surface. It is observed that the bottom temperature location involves the highest discrepancy. Indeed, from the overall temperature evolution profiles, the model fairly over-predicted the temperature at the top surface location. This structure change also facilitates the pyrolysis gases release with decreasing migration resistance outward, it could influence the mass loss rate variation. All these factors could provide underpredicted values compared with experimental data. Overall, the simulation results are qualitatively similar regarding both dimensionality models. The apparent difference involves the strong mass loss with the heat dissipation from silicate to the wood sides which can be seen in the two-dimensional simulation. It also corresponds to the sharp increase of temperature after the termination of heat pyrolysis heat absorption at the final stage. In conclusion, the 2D simulations could provide better agreement with experimental data in comparison with those in 1D.

### 5.6.2 Model validation for char front evolution

The model has been validated regarding mass loss and mass loss rate evolution which are overall scalars. Indeed, the mass loss rate plotted before is the sum over all the space domain of all reaction rates of the components of wood (water, hemicellulose, cellulose, and lignin). However, even though the model captured reasonably well the overall pyrolysis process, local scalars regarding pyrolysis should be investigated to ensure that the model can capture the instantaneous dynamics of the pyrolysis process. Indeed, local scalars could vary according to time and space. Figure 5.48 plots the evolution of the char layer as a function of space and time at  $20 \text{ kW/m}^2$ . To obtain some information about the char thickness dynamic, experiments have been stopped at different time and the char layers are measured. The measurement has been made with

a ruler which could be enhanced with a large deviation. However, it is a first simple approach and it will need to use a more precise experimental method to measure the char front as a perspective.

Different layers can be present through the sample in-depth direction: the virgin layer is the initial part without any reactions, the drying layer or pyrolysis layer represents the front where reactions are involved, the dried or char layer is the resulting layer when reactions finish.

The charring rate for wood pyrolysis is an important parameter to predict the fire behavior of wood, it represents the structural loading capacity [60]. To assess the char thickness evolution, the charred samples at the different experimental times are cut with a vertical cross-section. The wet wood pyrolysis experiment at  $20 \text{ kW/m}^2$  is stopped at 205 s, 605 s, 1005 s, 1805 s, and 2405 s, respectively. While at  $50 \text{ kW/m}^2$ , they correspond to 105 s, 405 s, 805 s, 1205 s, and 1405 s, respectively.

The char front propagation at different times of experiments are shown which are aligned together with the prediction, and they are shown in Figure 5.48 and Figure 5.50 under  $20 \text{ kW/m}^2$  and  $50 \text{ kW/m}^2$ , respectively. In the numerical figures, the density with blue color corresponds to char density and the crimson color describes the virgin density. As shown in Figure 5.49 and Figure 5.51, they represent the calculated specifically char front depth variation which is compared with the corresponding predictions.

The char front is highly sensitive to water content which tends to account for a higher pyrolysis rate for dry wood. The water delays the char front propagation rate through the in-depth direction for all cases due to the high endothermic reaction. Moreover, the water vapor could continue to absorb heat when migrating outward through the pyrolysis and char layer although this phenomenon is not considered in this study. At higher heat flux, the water evaporation rate is faster inducing higher bulk gas pressure. Thus the water influence could be moderate compared with that at low heat flux. The duration for the water evaporation process is approximately 1000 s for  $20 \text{ kW/m}^2$  and 700 s for  $50 \text{ kW/m}^2$ , respectively. At  $20 \text{ kW/m}^2$ , the heat transfer process is slow, the drying needs to absorb enough heat which designates a

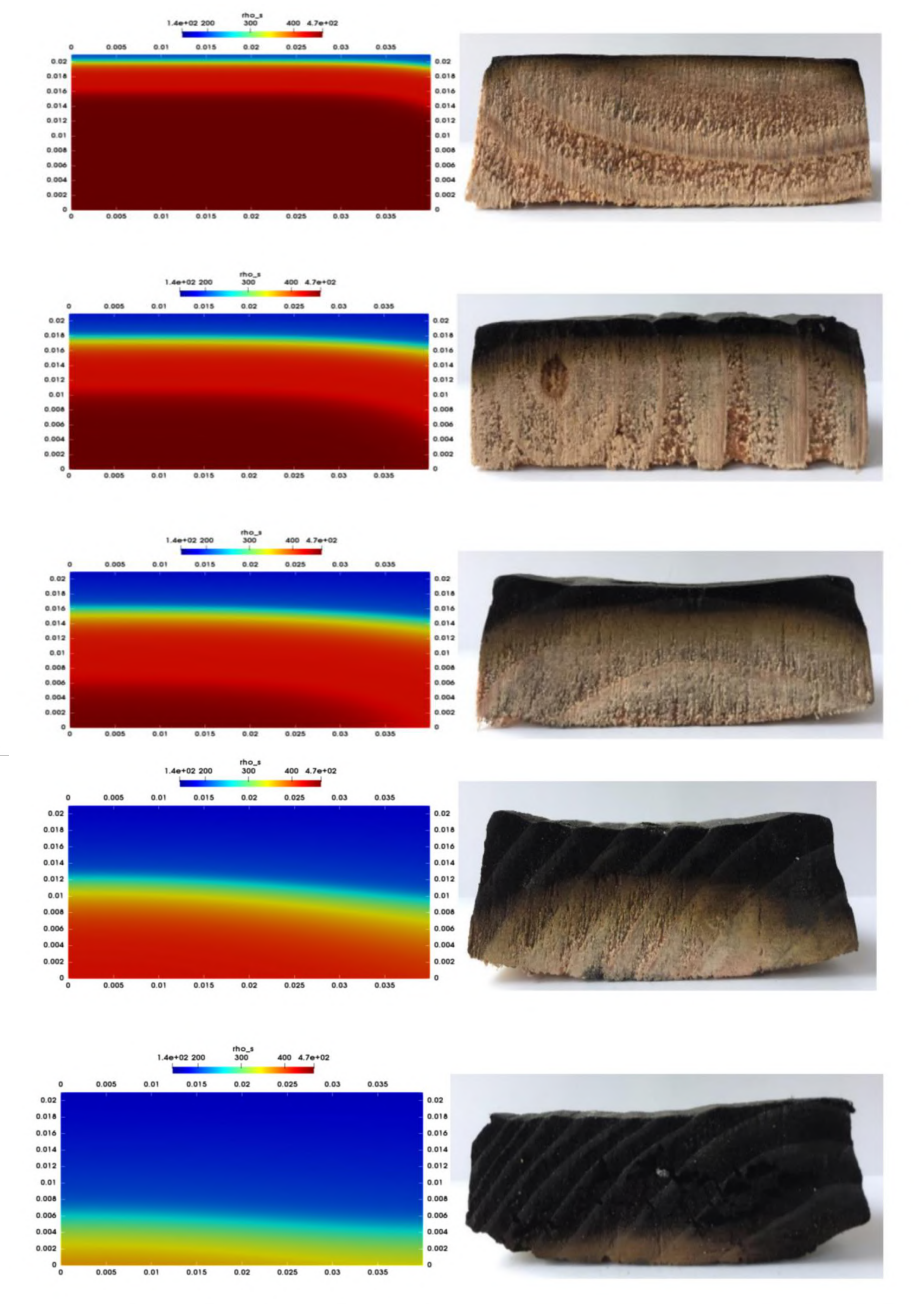


Fig. 5.48 Charring front propagation at different time (205 s, 605 s, 1005 s, 1805 s, and 2405 s) for wet wood pyrolysis under 20 kW/m<sup>2</sup>

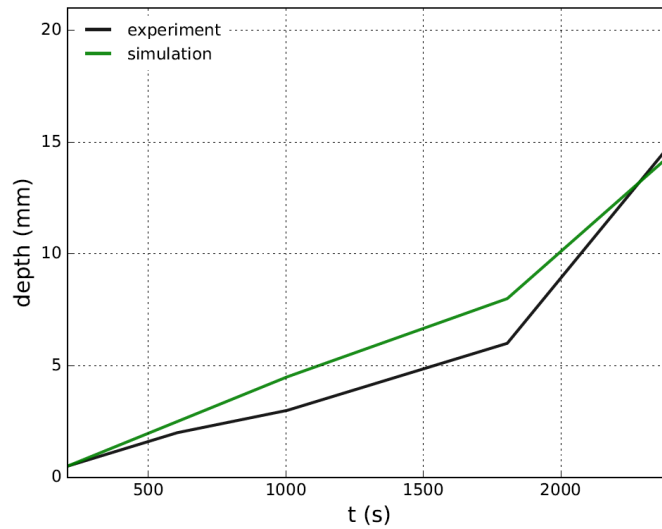


Fig. 5.49 Comparison of measured and predicted char depth at different times for wet wood pyrolysis under  $20 \text{ kW/m}^2$

long duration. Consequently, the char front propagation is much slower as can be seen in Figure 5.48 and Figure 5.50 comparing the thickness of the char layer at a different time for wet wood pyrolysis under  $20 \text{ kW/m}^2$  and  $50 \text{ kW/m}^2$ . The water content and heat flux are responsible for the char front development, as noted in [60], and the charring rate is very sensitive to the in-depth temperature evolution which is described as being influenced by its density, heat transfer, and kinetics interactions under different heat flux.

As shown in Figure 5.49 and Figure 5.51, char depth increase behaves differently at different incident heat flux. It is observed that the initial charring rate is higher and then decreases approximately linearly which attribute mainly to the surface char layer formation restricting the heat flow transport as a thermal barrier. This influence is more predominant at high heat flux with a steep slope at  $50 \text{ kW/m}^2$ . The kinetic scale is longer than the heat transfer scale at low heat flux, and the endothermic pyrolysis reaction could be present for a long duration. The char layer is thinner with limited heat transport downward to the bottom. Conversely, the heat propagation is faster than the kinetic reaction leading to a thicker pyrolysis layer at high heat flux. The char structure is more fragile with higher porosity and cracks due to the high heating

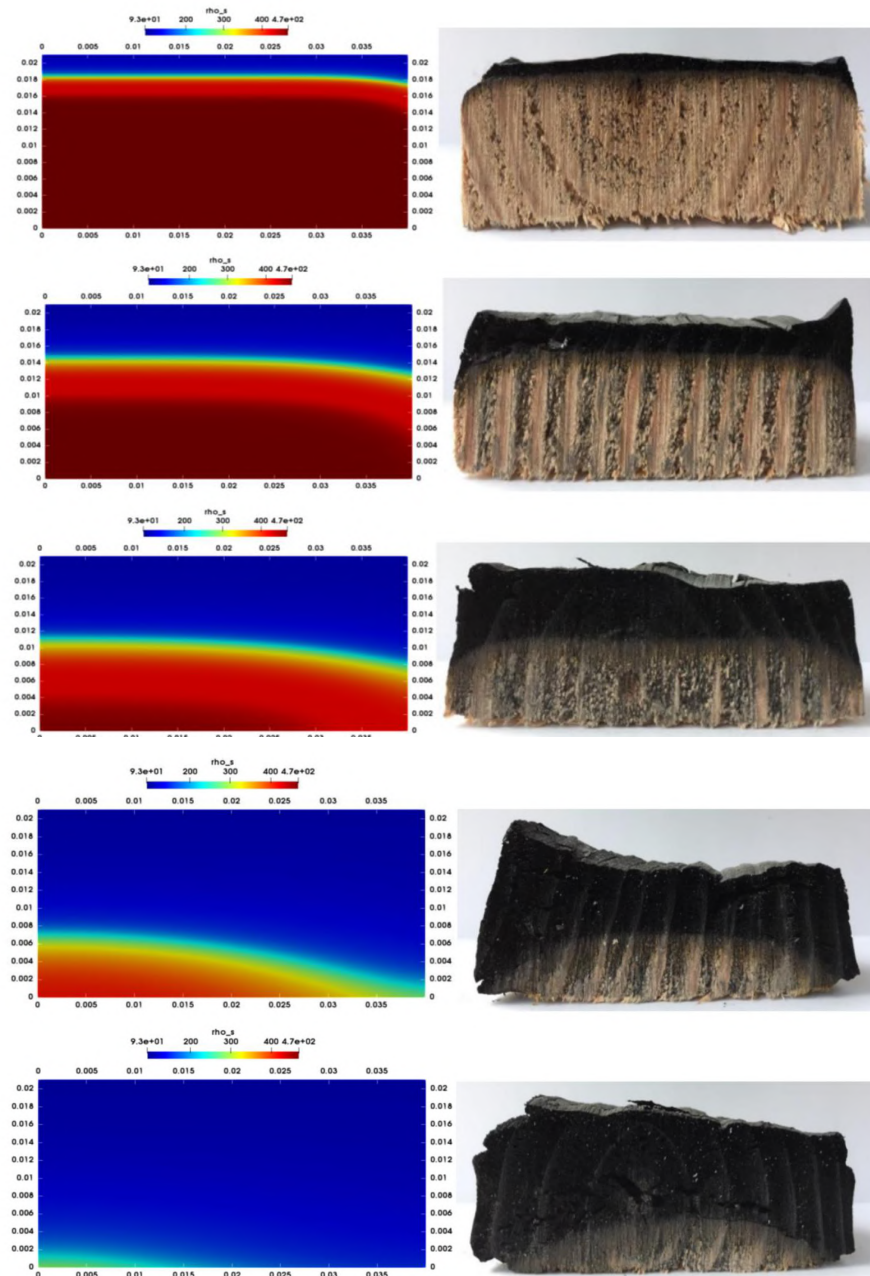


Fig. 5.50 Charring front propagation at different time (105 s, 405 s, 805 s, 1205 s, and 1405 s) for wet wood pyrolysis under 50 kW/m<sup>2</sup>

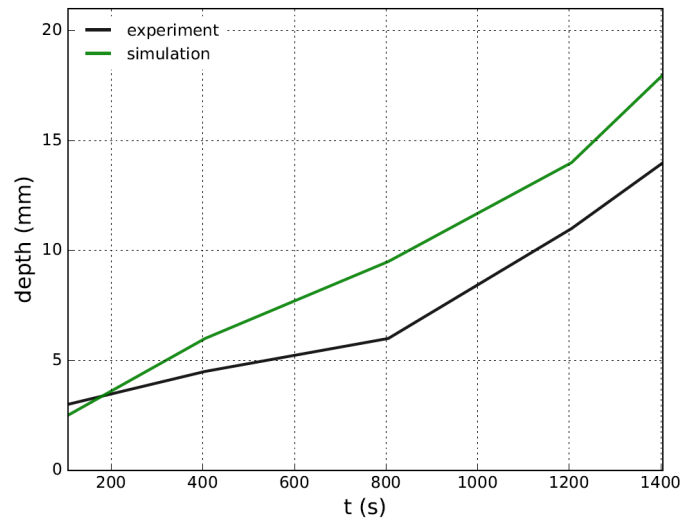


Fig. 5.51 Comparison of measured and predicted char depth at different times for wet wood pyrolysis under  $50 \text{ kW/m}^2$

rate. With the presence of the char layer formation at a given thickness to act as a thermal barrier, the char front propagation velocity decrease, and the layer tend to be thinner while the pyrolysis rate is lower at low heat flux. It matches reasonably well the experiment for  $20 \text{ kW/m}^2$ , however, the experimental char depth is over-predicted at  $50 \text{ kW/m}^2$  except for the initial stage of pyrolysis. The over prediction is about 2.5 mm for the whole pyrolysis process. However, the level of deviation concerning char depth at  $50 \text{ kW/m}^2$  is quite acceptable since serious shrinkage and crack are involved in leading to many uncertainties.

### 5.6.3 Numerical analysis with global and single scalars

The model has been validated for pyrolysis under wet and dry conditions for the two heat flux. The strength and weaknesses of the model have been discussed. Regarding those considerations, the pyrolysis process is investigated deeper in this section, only considering numerical results. The pyrolysis investigation is focused on the role of water in this process as the quantity of heat brings to the solid through incident heat flux. The analysis is focused on the overall process, first by analyzing

global scalars which have been averaged over all the physical space. In the second part, local scalars are discussed by analyzing their evolution in space and time.

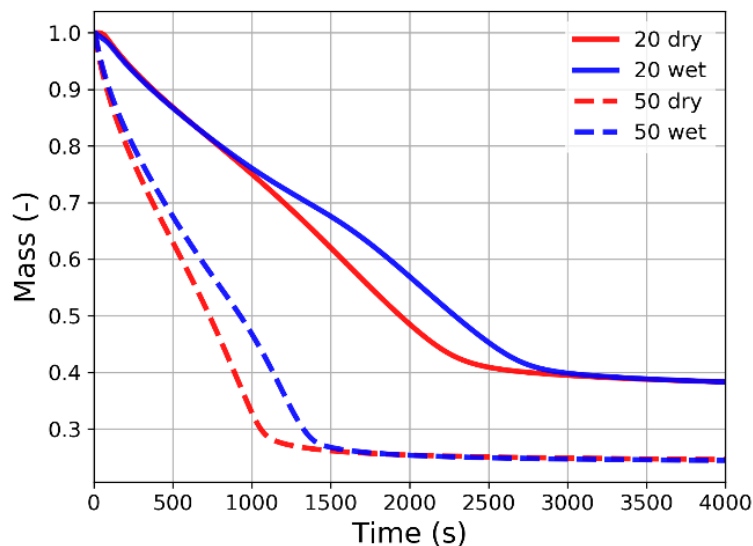


Fig. 5.52 Total mass evolution for dry and wet wood pyrolysis cases at 20 kW/m<sup>2</sup> and 50 kW/m<sup>2</sup>

Figure 5.52 plots the total (sum over all the physical space) mass evolution as a function of time for wet and dry wood pyrolysis cases at the two heat flux investigated. As previously discussed, water evaporation is an endothermic process and delays the pyrolysis due to the overall temperature decrease. The main phenomenon involved by the incident heat flux difference is the remaining mass of char when the pyrolysis process is over. Indeed, high heat fluxes involve generally higher temperatures that promote reactions and decrease the final mass fraction of residue. For the lower heat flux, the temperature at the bottom (green line of the left plot in the following Figure 5.55) doesn't reach 400 °C which is not sufficient to convert all lignin to char as demonstrated in Chapter 4. In this case, the remaining mass is a mixing of partially reacting wood and char. At 50 kW/m<sup>2</sup>, the remaining mass is fully formed by char with a mass fraction of around 20 wt%. This one is corresponding to the one obtained at the TGA scale.

Figure 5.53 and Figure 5.54 plot the total mass loss rate for dry and wet pyrolysis cases for 20 kW/m<sup>2</sup> and 50 kW/m<sup>2</sup>, respectively. Figure 5.55 and Figure 5.56 give details on all reaction rates for dry case (solid lines) and wet case (dashed lines) for 20 kW/m<sup>2</sup> and 50 kW/m<sup>2</sup>, respectively.

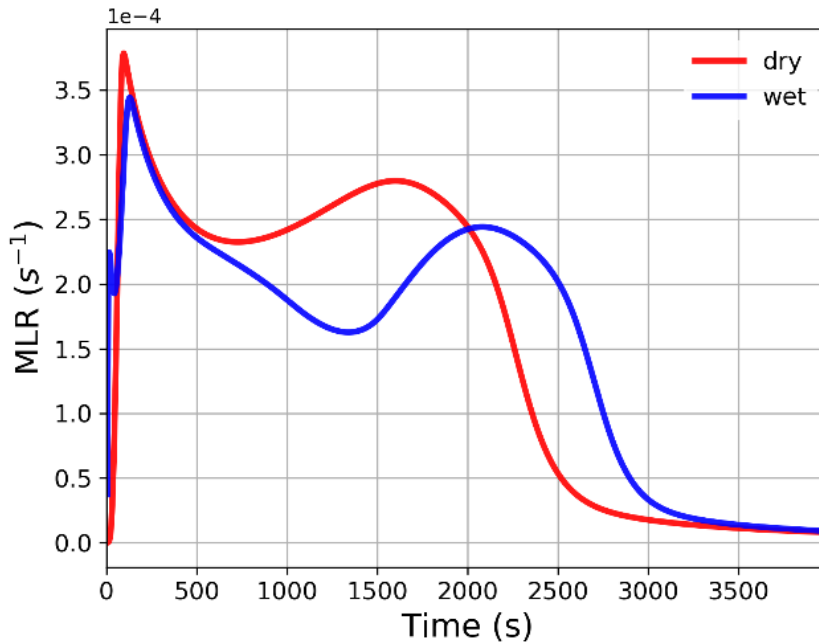


Fig. 5.53 Total Mass loss rate evolution for wet and dry wood pyrolysis cases at 20 kW/m<sup>2</sup>

The first peak of mass loss rate for wet wood at 20 kW/m<sup>2</sup> corresponds to the water evaporation. This peak doesn't present at 50 kW/m<sup>2</sup> which is overlapped with the surface pyrolysis peak, as it can be seen in Figure 5.56 where dashed blue curves represent the reaction rate of water evaporation. The water reaction rate peak appears earlier than cellulose for example at 20 kW/m<sup>2</sup> but overlaps for 50 kW/m<sup>2</sup> with other reactions. The higher heat flux involves an intensified first pyrolysis peak. The first peak magnitude at 50 kW/m<sup>2</sup> is more intensive than that under 20 kW/m<sup>2</sup>, while the temperature range, i.e. the duration time for sustaining the peak development, is wider at 20 kW/m<sup>2</sup> than that under 50 kW/m<sup>2</sup>. This tends to be caused by the char formation rate and thickness difference. The heating rate under 50 kW/m<sup>2</sup> is higher and the

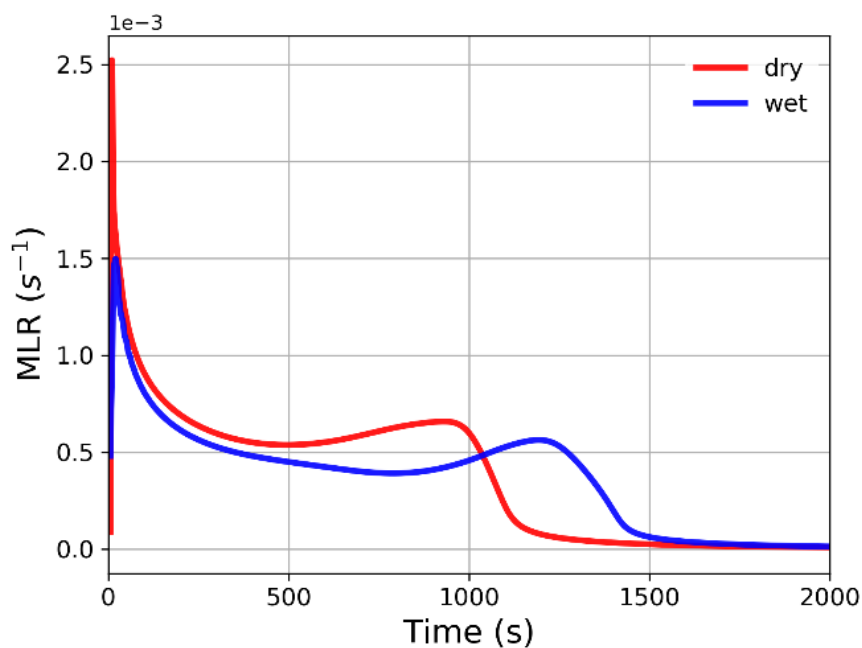


Fig. 5.54 Total Mass loss rate evolution for wet and dry wood pyrolysis cases at 50  $\text{kW/m}^2$

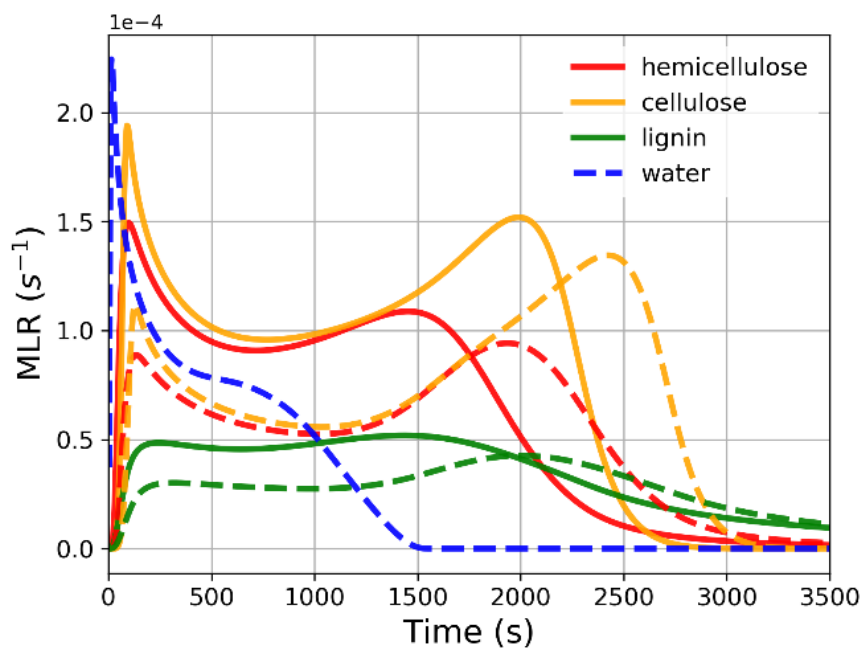


Fig. 5.55 Total reaction rates evolution for wet (dashed lines) and dry (solid lines) wood pyrolysis cases at 20  $\text{kW/m}^2$

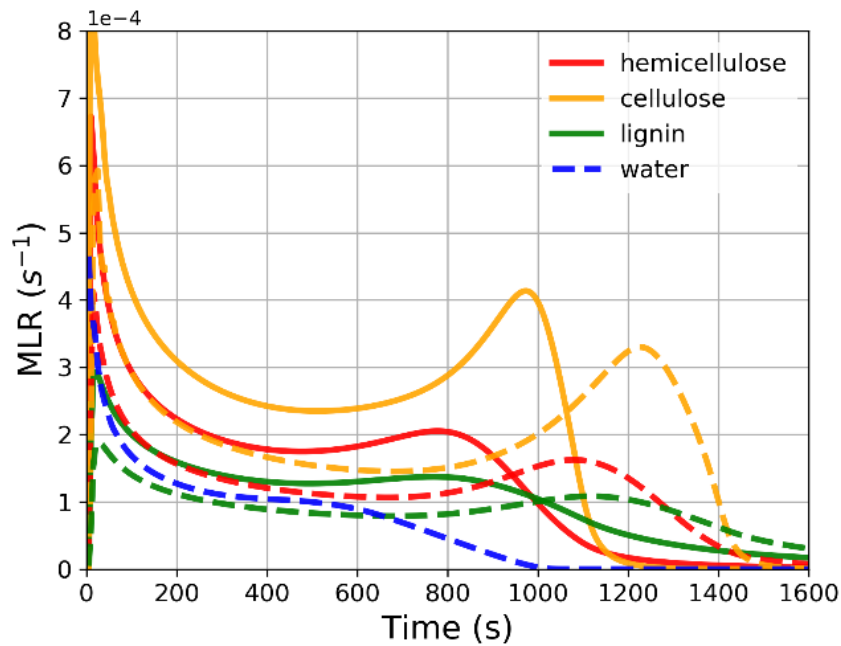


Fig. 5.56 Total reaction rates evolution for wet (dashed lines) and dry (solid lines) wood pyrolysis cases at  $50 \text{ kW/m}^2$

char layer formation is faster. Thus, the heat insulation effect occurs early to limit the heat propagation, and the mass loss rate experiences a sharp decrease. At  $20 \text{ kW/m}^2$ , the heating rate involved is slower which induces a longer pyrolysis process with the presence of a thicker formed char layer to achieve a wider mass loss rate peak duration. After the first peak, both cases are expected to enter the quasi-steady-state thermal process. As noted in [193], the pyrolysis could induce less amount of char residue at higher final temperatures, it is believed reasonably correct that the final char mass fraction tends to present some differences under different irradiant heat flux. Indeed, at lower heat flux, the final black substrate is comprised of a large amount of not fully decomposed solid residue due to the large pyrolyzed temperature for lignin which accounts for the main source of char yield compared to hemicellulose and cellulose. The carbon elemental composition is higher after the termination of pyrolysis at a final higher temperature from [193]. The reaction rate of water evaporation is globally higher than those of other reactions (hemicellulose, cellulose, and lignin) at  $20 \text{ kW/m}^2$

compared to  $50 \text{ kW/m}^2$  where the water reaction rate is lower than other reaction rates. The difference in MLR between dry and wet cases is also enhanced at a lower heating rate.

Figure 5.57 and Figure 5.58 plot the temperature evolution at the three locations introduced before (4 mm under the top surface, at the middle of the sample, and 4 mm above the bottom surface) for dry (solid lines) and wet cases (dashed lines), for the two heat flux of  $20 \text{ kW/m}^2$  and  $50 \text{ kW/m}^2$ , respectively. Figure 5.59 plots the temperature differences between dry and wet cases for  $20 \text{ kW/m}^2$  (solid lines) and  $50 \text{ kW/m}^2$  (dashed lines).

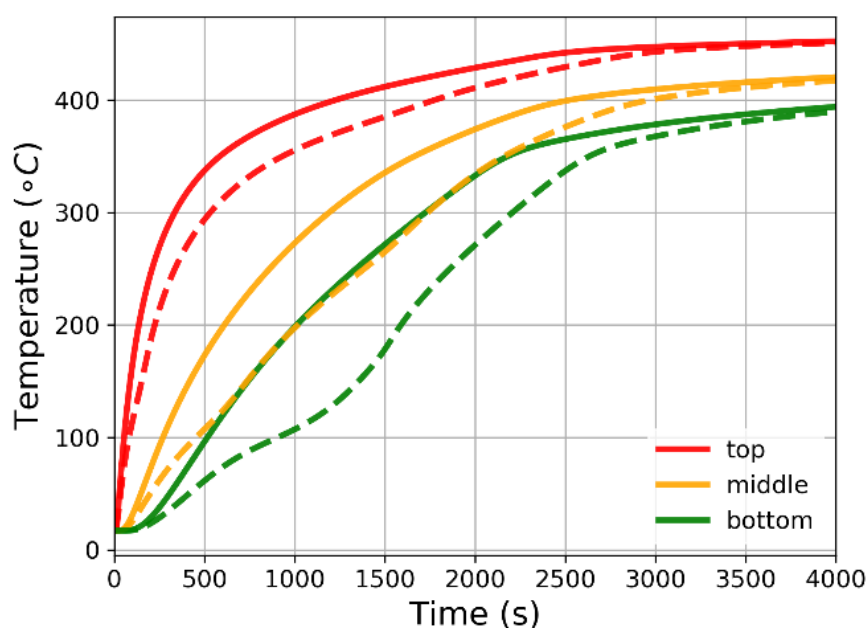


Fig. 5.57 Temperature evolution for dry (solid line) and wet (dashed lines) cases at  $20 \text{ kW/m}^2$

As mentioned earlier the temperature plateau due to water evaporation is enhanced for lower heat flux at the bottom of the sample. Indeed, low heat flux and space locations near the bottom promote low heating rates which involve slower water evaporation reaction which is endothermic and acts as a heat sink. When the water evaporation front moves downward from the top surface to the bottom of the sample,

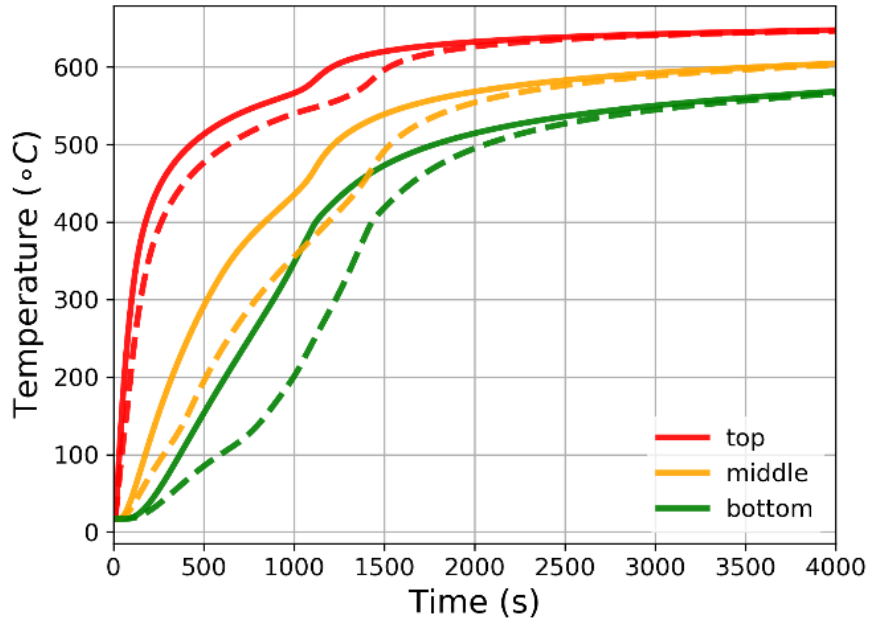


Fig. 5.58 Temperature evolution for dry (solid line) and wet (dashed lines) cases at 50 kW/m<sup>2</sup>

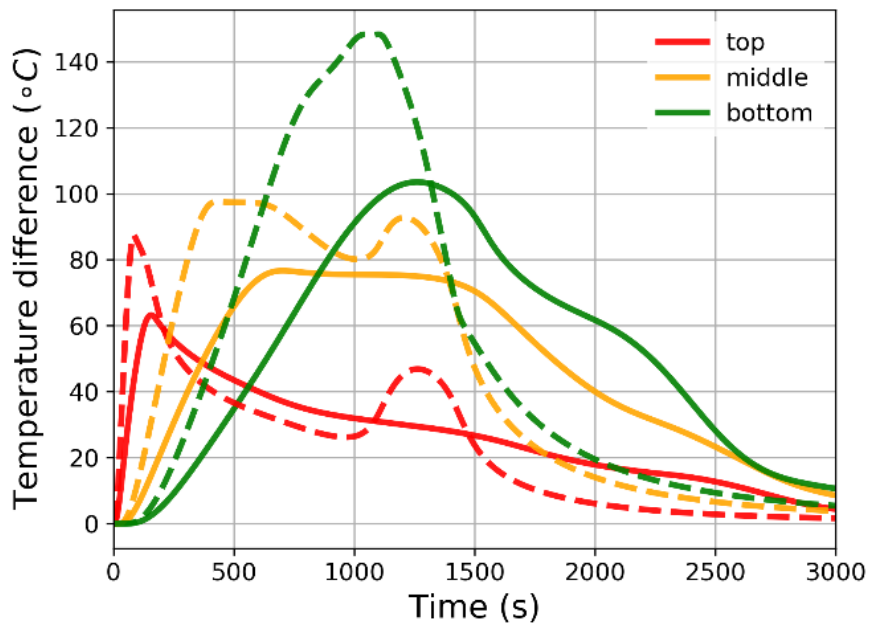


Fig. 5.59 Temperature difference between dry and wet cases for 20 kW/m<sup>2</sup> (solid line) and 50 kW/m<sup>2</sup> (dashed lines)

an over-pressure state is formed on the top edge (where the reaction begins) of the evaporation front, pushing water vapor formed downward and promoting the cooling of the sample downward to the evaporation front. This phenomenon could be seen in the following Figure 5.61. Locations near the bottom of the sample are cooled by this phenomenon which is taken into account in the model by gas convection effects in the energy equation.

The end of the pyrolysis process around 1000 s for 50 kW/m<sup>2</sup> (Figure 5.54) involves a temperature jump (Figure 5.58) because of the end of endothermic pyrolysis reactions. This jump is not visible for 20 kW/m<sup>2</sup> but still exists.

The temperature difference between dry and wet increases with the thickness coordinate, because it is exposed earlier due to a lower heating rate promoting a slower water evaporation reaction and also promoting the duration time of the heat sink. The temperature difference is also higher at 50 kW/m<sup>2</sup> than at 20 kW/m<sup>2</sup>, probably because the heat transfer by convection between water vapor and solid down to the water evaporation front is higher, and high heat flux can promote high pressure and also higher velocity into the solid matrix.

The gas transport of internal material is dominated by the pressure difference, the velocity magnitude is quite consistent with the pyrolysis rate during the pyrolysis process. Figure 5.60 plots the total pressure through all physical space in the function of time for wet and dry cases at 20 and 50 kW/m<sup>2</sup>.

Different pressure peaks appear at different phases of the pyrolysis process under different heat flux which is consistent with the pyrolysis reaction rate. The pressure evolution at different heat fluxes is different especially in the vicinity of the duration of the second peak of mass loss rate. The pressure at 20 kW/m<sup>2</sup> increases gradually to the pressure peak due to the pyrolysis gas accumulation and then drops gradually to the ambient pressure. While this trend for 50 kW/m<sup>2</sup> could display differently with the presence of a sharp decrease in the pressure after the termination of the mass loss rate peak of strong reaction. The reaction rate, the density change, and the reaction advancement of each sub-component are highly correlated to induce the

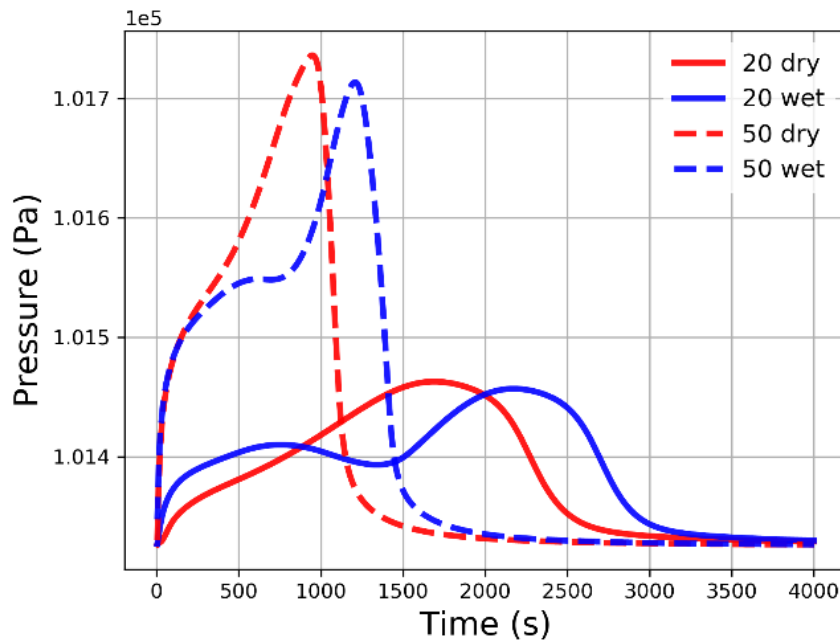


Fig. 5.60 Total pressure evolution for wet (dashed lines) and dry (solid lines) cases at 20 kW/m<sup>2</sup> and 50 kW/m<sup>2</sup>

pressure variation which determines the gas velocity during the pyrolysis process. For low heat flux, the reaction rate and the pyrolysis advancement are slow and produce the pyrolysis gases gradually through a thick pyrolysis layer, accompanied by a smaller temperature gradient. This trend could lead to a gradual pressure build-up with the presence of a relatively small gradient of permeability between the pyrolysis layer and the char layer. While for high heat flux with a thin pyrolysis layer, the fast accumulation rate of produced pyrolysis gases in a trapped region could induce the steep pressure peak shoulder. As noted in [65], the pressure peak could occur at an early stage of pyrolysis due to small permeability, while for high heat flux, the pressure peak appears at the end stage of pyrolysis due to the instantaneous gas accumulation which needs to migrate through long distance.

The overall behavior of pyrolysis has been investigated through the time-dependent analysis of integral scalars over all the physical space such as mass, MLR, each reaction rate, and pressure. To complete the analysis, the same scalars are analyzed in the next

Table 5.2 Pyrolysis front locations with different characteristic time for the 4 cases

—	20 kW/m <sup>2</sup> (dry)	20 kW/m <sup>2</sup> (wet)	50 kW/m <sup>2</sup> (dry)	50 kW/m <sup>2</sup> (wet)
Top	140 s	215 s	25 s	35 s
Middle	1500 s	2020 s	625 s	925 s
Bottom	2030 s	2510 s	1000 s	1330 s

part depending on time and space. Different characteristic time have been chosen and scalars have been plotted through the thickness of the sample along the centerline. For each case corresponding to dry and wet conditions for 20 kW/m<sup>2</sup> and 50 kW/m<sup>2</sup>, the time has been determined when the pyrolysis front is located at three different thicknesses: 1 mm under the top surface, 10 mm corresponding to the middle of the sample, and 4 mm above the bottom surface. These locations will be named in the following part as “top”, “middle”, and “bottom”, respectively. The corresponding different time for each case is given in Table 5.2.

Figure 5.61 and Figure 5.62 plot the pyrolysis front (which correspond here to the total reaction rate) slices for 20 kW/m<sup>2</sup> (Figure 5.61) and 50 kW/m<sup>2</sup> (Figure 5.62). For both figures, the three top pictures are for dry conditions and the three bottom figures are for wet conditions.

For the two heat fluxes, the pyrolysis front is thin near the top surface and becomes thicker when it moves to the bottom of the sample. However, the pyrolysis front stays nearly thin at 50 kW/m<sup>2</sup> during all the pyrolysis process and becomes thick in the case of 20 kW/m<sup>2</sup>. Indeed, at low heat flux, temperatures and corresponding gradients are smaller involving slow chemistry. In these conditions, the chemistry is a finite-rate and needs to be described by a multi-step reaction mechanism in the model to be captured correctly. At high heat flux, the chemistry stays nearly infinitely fast and could be captured quite correctly with a simpler kinetic mechanism. For the two heat flux, the pyrolysis front is quasi 1D at the beginning but becomes 2D when it moves to the bottom of the sample, which is as a function of the time. Indeed, the front is curved on the sides of the sample near the border with the silicate material. This phenomenon is increased at 50 kW/m<sup>2</sup> because of higher temperatures and higher thermal gradients

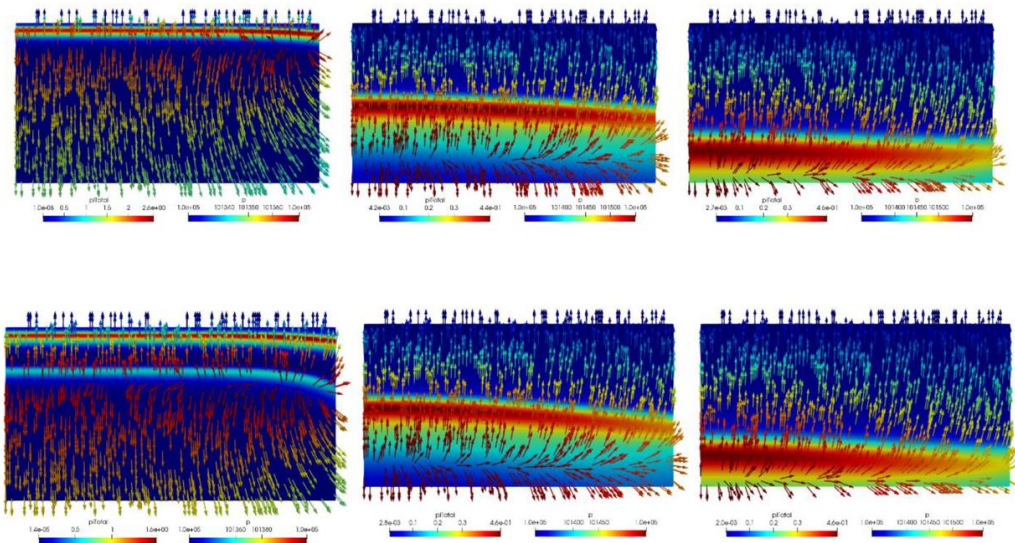


Fig. 5.61 Pyrolysis and water evaporation front for dry (top slices) and wet case (bottom slices) at  $20 \text{ kW/m}^2$

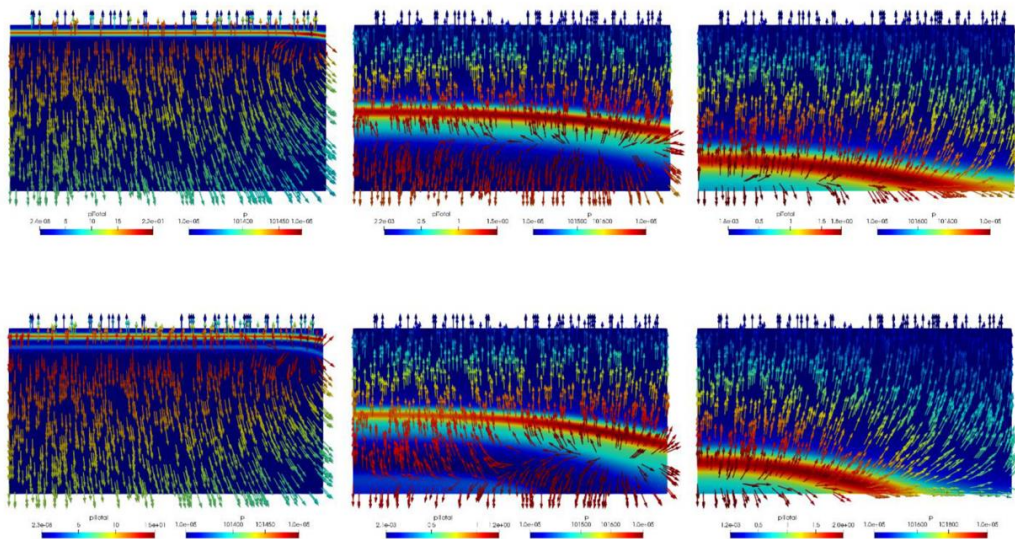


Fig. 5.62 Pyrolysis and water evaporation front for dry (top slices) and wet case (bottom slices) at  $50 \text{ kW/m}^2$

on the sides, between the sample and the silicate. Those gradients are due to the different thermal properties of wood and silicate. For dry cases for the two heat fluxes, an overpressure state is established on the top edge of the pyrolysis front. When the pyrolysis front moves to the bottom, the gas is first pushed to the bottom before being released at the top surface. Indeed, when the virgin wood is burned, char is formed which is more porous than virgin material making the pressure decreasing and allowing gas to migrate across the front until to reach the top surface and then being released into the atmosphere.

For wet wood cases, this phenomenon changes. The over-pressure state pushing the gas down is established on the top edge of the evaporation front which enhances the cooling of the sample bottom as mentioned earlier. On the bottom edge of the evaporation front, the gas is then pushed in the top direction through the pyrolysis front. The pressure generated at the top edge evaporation front is higher than the pressure at the top edge of the pyrolysis front discussed for the dry case. The pyrolysis gases don't go to the bottom but are directly pushed to the top surface of the sample. However, when the evaporation front reaches the bottom surface, the pyrolysis gases are then pushed down like in the dry cases. For high heat flux, the pyrolysis front collapses with the evaporation front because the chemistry is fast. In this case, the evaporation front could influence the pyrolysis process. For lower heat flux, the evaporation front is far from the pyrolysis front because the pyrolysis chemistry is slow compared to the evaporation rate. The evaporation front acts probably only as a heat sink on the pyrolysis process and could not interact in a physical way on pyrolysis.

In order to analyze deeper the pyrolysis front, Figure 5.63 plots the reaction rates evolution across the sample thickness for different pyrolysis front locations: 1 mm, 6 mm, and 10 mm under the surface for 20 kW/m<sup>2</sup> (left plot) and 1 mm, 6 mm, 10 mm and 17 mm under the surface for 50 kW/m<sup>2</sup> (right plot). The pyrolysis front location corresponds to the position of the cellulose reaction rate peak (orange line). Wet cases are represented by dashed lines and dry cases by solid lines. Figure 5.64 and Figure 5.65 plot in the same manner the heating rates and temperatures.

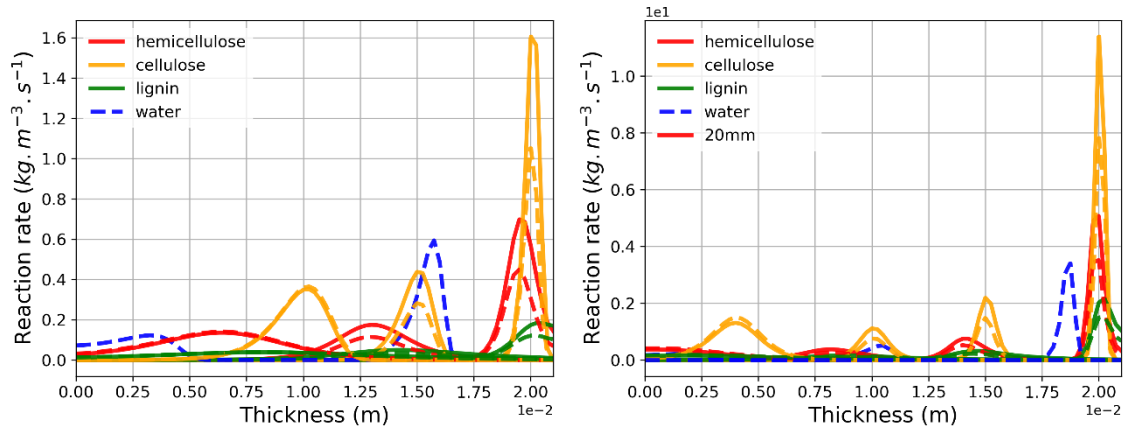


Fig. 5.63 Reaction rates evolution across the sample thickness for three pyrolysis front locations for dry (solid lines) and wet (dashed lines) cases at 20 kW/m<sup>2</sup> (left plot) and 50 kW/m<sup>2</sup> (right plot)

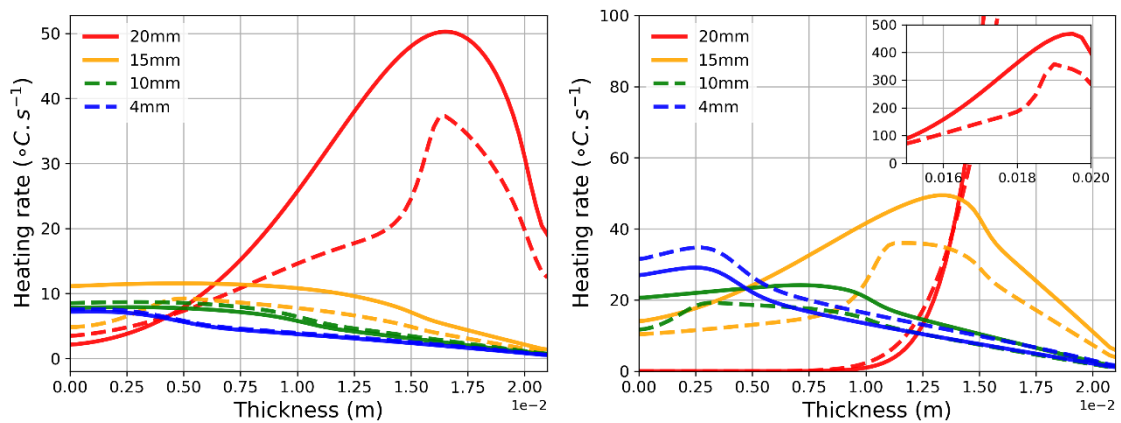


Fig. 5.64 Heating rate evolution across the sample thickness for three pyrolysis front locations for dry (solid lines) and wet (dashed lines) cases at 20 kW/m<sup>2</sup> (left plot) and 50 kW/m<sup>2</sup> (right plot)

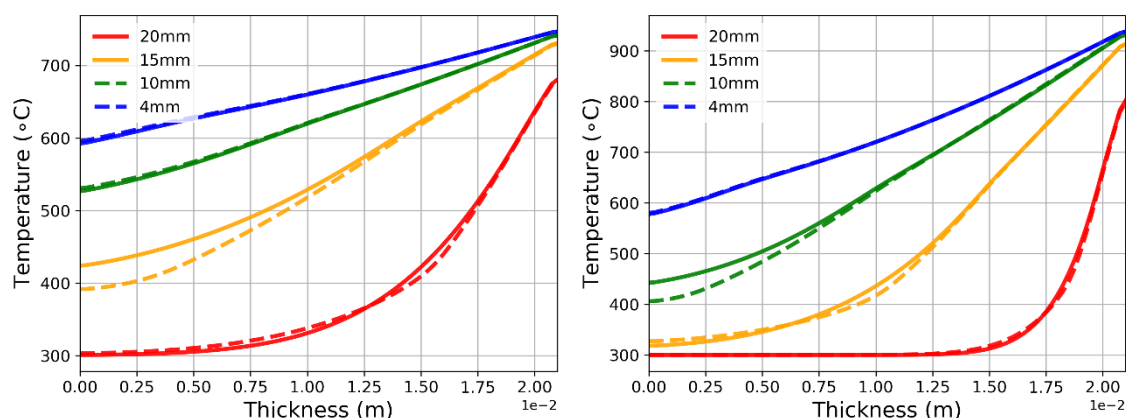


Fig. 5.65 Temperature evolution across the sample thickness for three pyrolysis front locations at  $20 \text{ kW/m}^2$  (left plot) and  $50 \text{ kW/m}^2$  (right plot) for dry (solid lines) and wet (dashed lines) cases

At  $50 \text{ kW/m}^2$ , at the beginning of the pyrolysis process, high reaction rates are involved compared to those obtained at  $20 \text{ kW/m}^2$ , and all reactions are nearly overlaid which denote the infinite fast chemistry with a thin reaction zone. When reactions are infinitely fast, one peak is observed and could be captured by one global reaction. This zone is characterized by a high heating rate (Figure 5.64 right plot) and high temperature (Figure 5.65 right plot) which could reach more than  $400 \text{ K/min}$ . The water evaporation front is also overlaid with the pyrolysis zone which is not the case at  $20 \text{ kW/m}^2$  where the water evaporation front is quicker than the pyrolysis front and then is established far from the pyrolysis front (Figure 5.63 left plot).

## 5.7 Conclusion

Chapter 5 permits to conduct a comprehensive pyrolysis model validation including parameters prediction based on the Controlled Atmosphere Cone Calorimeter experiments. Relevant numerical analyses are conducted at different time and length scales for different pyrolysis scenarios. With a sample holder of thick thermal insulated silicate, the heat convection coefficient at the sides and the bottom surface is estimated to be not important. The heat convection coefficient of the top surface is well predicted

by inverse analysis to change from 3 to 5 W/m<sup>2</sup>/K for the 2D model, while it is estimated to be 0 to 3 W/m<sup>2</sup>/K for the 1D model with less accuracy. The thermal conductivity and specific heat capacity of wood and char are predicted by inverse analysis concerning the experimental conditions, and their physical meaning is verified. The moisture evaporation process of wet wood under an exposition to a heat flux of 5 kW/m<sup>2</sup> is analyzed. Good fitness is achieved concerning the mass loss, mass loss rate, and the temperature evolution at three locations through the thickness of the sample. Evaporation front is curved with different levels, with an increase of time and space evolution which is influenced by the side effect imposed by silicate heat conduction in the 2D model. The evaporation front is thin at top locations and changes to be thick when moving toward the bottom which is influenced by water endothermic reaction and heating rate decrease. Based on the analysis of temperature evolution of wet and dry wood, the water can delay the temperature evolution through the thickness, and the bottom location is the most influenced. However, the final temperatures of different locations are not influenced by water.

Based on the observation of water influence, wet and dry wood pyrolysis processes are analyzed by 1D and 2D modeling at an incident heat flux of 20 kW/m<sup>2</sup> and 50 kW/m<sup>2</sup>. The heating rate is specified as 10 K/min for wet wood pyrolysis at 20 kW/m<sup>2</sup>, and a heating rate of approximately 50 K/min is estimated at 50 kW/m<sup>2</sup>. Compared with wet wood pyrolysis, dry wood experiences a rapid heating process with an intensified reaction rate and higher temperature evolution. The temperature evolution involves different levels of the plateau, especially for the bottom locations at low heat flux. Concerning the model validation, the 2D model can predict better concerning the mass loss, mass loss rate, and temperature evolution compared with the 1D model. The model can be validated with more accuracy at lower heat flux (20 kW/m<sup>2</sup>) compared with the cases at higher heat flux (50 kW/m<sup>2</sup>). Similarly, the experimental char front is validated for the wet wood pyrolysis at 20 kW/m<sup>2</sup> and 50 kW/m<sup>2</sup> at the different characteristic time and better prediction can be observed at lower heat flux.

Numerical analysis is conducted with detail concerning the influence of water and heating process on the global and local scalars. The water can delay the mass loss process, but a fixed mass fraction of char residue is present for wet and dry wood. The reaction rate of water evaporation is globally higher initially than those of other reactions (hemicellulose, cellulose, and lignin) at  $20 \text{ kW/m}^2$ , while for the case of  $50 \text{ kW/m}^2$ , the water reaction rate is lower than the reaction rates of other components. The difference concerning the mass loss rate between dry and wet wood pyrolysis cases is more predominant at lower heat flux. The water can provide lower temperature evolution for wet wood, but the final temperature stays constant compared with the case of dry wood pyrolysis. More significant temperature differences between wet and dry wood pyrolysis can be found for the bottom location compared with that at the top or middle locations. The evaporation and pyrolysis front propagation at the different characteristic time are studied. The evaporation front is relatively thin through the whole process and it can interact in a physical way with the pyrolysis process. However, this evaporation front can change to become very thick when moving down to the cooler bottom space, and it is far from the pyrolysis front and couldn't interact with this pyrolysis process at lower heat flux.

Up to now, the wood pyrolysis has been thoroughly studied at the particle and this cone calorimeter scale. Different levels of prediction accuracy are achieved and many kinds of scalars involved are analyzed at different time and length scales. Thus, the next chapter will explore the pyrolysis process of the synthetic carbon/epoxy composite which behaves differently from wood in some aspects.

## Chapter 6

# Multi-scale application of the model to carbon/epoxy composite pyrolysis

Chapters 4 and 5 have concerned the application of the PATO model to the thermal decomposition of wood material, firstly at the TGA scale and secondly at the cone calorimeter scale. The results obtained have permitted to evaluate the availability of the model to represent the pyrolysis of wood samples. Due to these encouraging results, the model has been applied to a second material, a carbon fiber/epoxy resin composite. The same approach is used, firstly at the particle scale (TGA) and then at the small scale (Cone Calorimeter). The results obtained are presented in this Chapter.

The carbon/epoxy composite samples in this study are from the FIRECOMP project [194]. They are composed of T700S carbon fibers (a widely used fiber in composite structures for aircraft, ship, and civil infrastructure) in an epoxy matrix [15]. The volumetric fiber ratio is about 58 vol% and the density is approximately 1360 kg/m<sup>3</sup>. The samples can be considered as quasi flat because the maximum deviation from flatness is less than 0.15 mm across a length of 300 mm. As the fiber orientation in composite materials has an influence, a quasi-isotropic sequence has been studied (12°-90°-45°).

## 6.1 TGA experiments and model validation

The TGA experiment process regarding carbon/epoxy composite is similar to those conducted for wood, under inert atmosphere purging with nitrogen at a flow rate of 50-100 mL/min. The main difficulty is the sample preparation containing the carbon fiber reinforcement which needs to employ relevant equipment to prepare. Then, the samples are cut in powder accounting for approximately 12 mg from different locations to ensure the uniformity of results which contain epoxy resin and carbon fiber. Before the test, the samples are dried under 400 K for 48 h to eliminate the water. However, the carbon epoxy composite is not sensitive to water which is neglected in this work [8].

Similar to the wood TGA experiments, the TGA runs under two heating rates are conducted and linked correspondingly to the bench-scale heating rates during cone calorimeter experiments at 20 kW/m<sup>2</sup> and 50 kW/m<sup>2</sup>, presented in the following part. The heating rates are predicted by the temperature evolution at three thermocouple locations through the thickness of the sample. Because different heating rates at observed depending on the three locations, the heating rates at middle locations are specified approximately to be the representative one reflecting the sample heating behavior through the sample thickness. The heating rates at the middle locations are shown in Figure 6.1 under 20 kW/m<sup>2</sup> and Figure 6.2 with 50 kW/m<sup>2</sup>. It is apparent to observe that the heating rate is quite non-linear across the experiment. After calculating the integral of heating rates versus time, the heating rates here are specified to be “apparent” and “average” values of approximately 20 K/min and 50 K/min for corresponding heat fluxes, and relatively low heating rates (no more than 50 K/min) in TGA manipulation is considered to ensure the test accuracy.

For epoxy resin thermal decomposition under an inert atmosphere (without carbon fiber decomposition in this study), the kinetics proposed in the literature are one-global step or consecutive multistep reaction mechanism (mainly two steps) [46]. However, the model PATO used in this study currently couldn't implement this kind of consecutive reaction mechanism. Two apparent distinctive reaction peaks over the temperature range occur in relevant DSC experiments [46] which primarily represent at least two

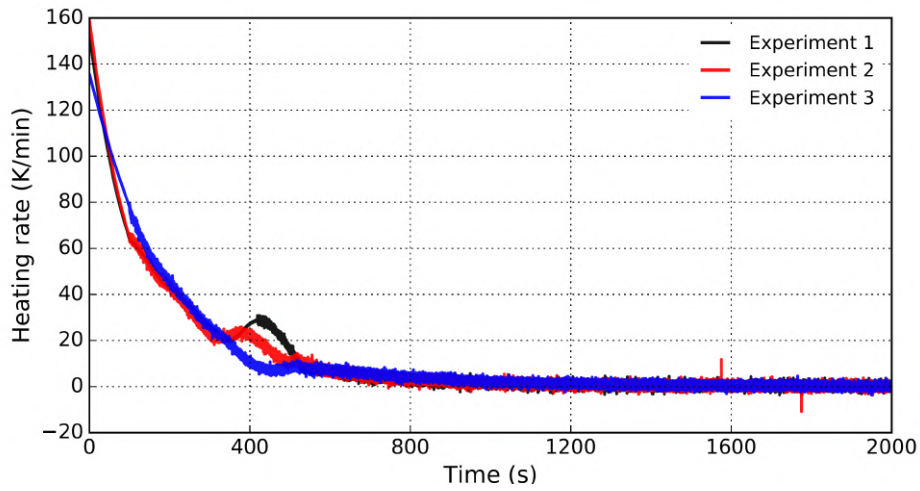


Fig. 6.1 Experimental heating rate evolution at middle locations during cone calorimeter tests under  $20 \text{ kW/m}^2$

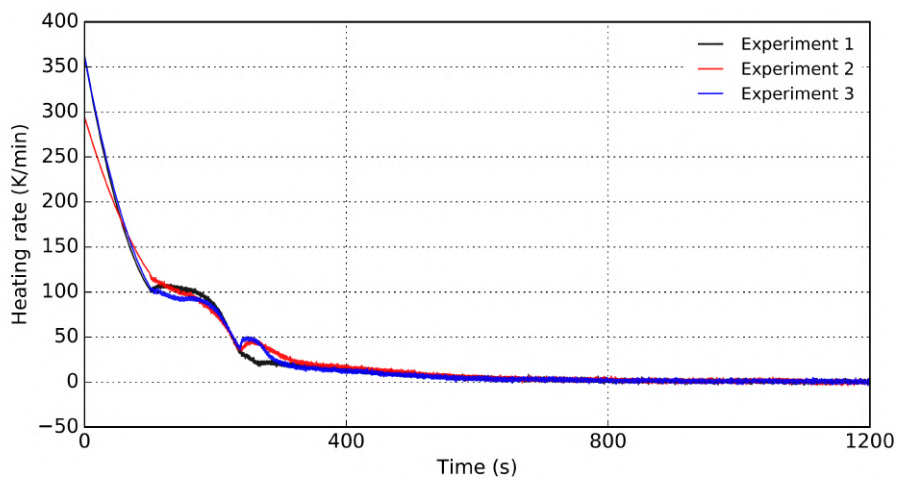


Fig. 6.2 Experimental heating rate evolution at middle locations during cone calorimeter tests under  $50 \text{ kW/m}^2$

reactions involved. Then, a one-step global reaction scheme cannot be assumed due to its less accuracy to fit the experimental curves [46]. Thus, in this study, an epoxy resin reaction with the two-parallel reaction scheme is implemented to explore the thermal decomposition behavior although the consecutive reaction scheme is mostly used in the literature [46, 10].

Up to now, a two parallel reaction mechanism is chosen, however, the relevant kinetics information is not available from the literature. Then, the kinetic parameters employed in this work are based on the previous study concerning the aforementioned Firecomp project which employed a consecutive mechanism of two reactions mechanism [194]. The kinetic parameters for each reaction in the consecutive mechanism are extracted to be the kinetic parameters of the two parallel reactions scheme studied, respectively. The stoichiometric values for each parallel reaction are estimated to reflect the mass residue history in the TGA experiment. Thus, the kinetic parameters are analyzed regarding two parallel reactions scheme to validate if it is applicable to fit the experimental data at both heating rates.

The independent parallel reaction scheme used is similar to the one performed for wood, however, some differences could display. For wood, each one of the 3 main components (reactants) involves one reaction. Here, the two parallel reaction concerns the same reactant, the epoxy resin, at different temperature ranges. This independent two parallel reaction scheme regarding epoxy resin can be illustrated as following, where F1 and F2 denote the stoichiometric value for the two reactions. The relevant parameters obtained previously in the project Firecomp are extracted for capturing the carbon/epoxy composite pyrolysis behavior.

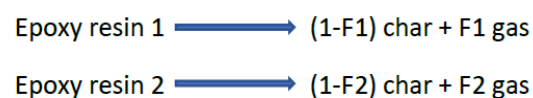


Fig. 6.3 Two parallel reactions scheme of epoxy resin thermal decomposition

Based on this, the fitting process is implemented to compare the experimental mass loss and mass loss rate curves. Figure 6.4 and Figure 6.5 show the TGA mass

loss between the simulated and experimental results at a heating rate of 20 K/min and 50 K/min, respectively. The experimental results presented are the average ones concerning three tests for each one.

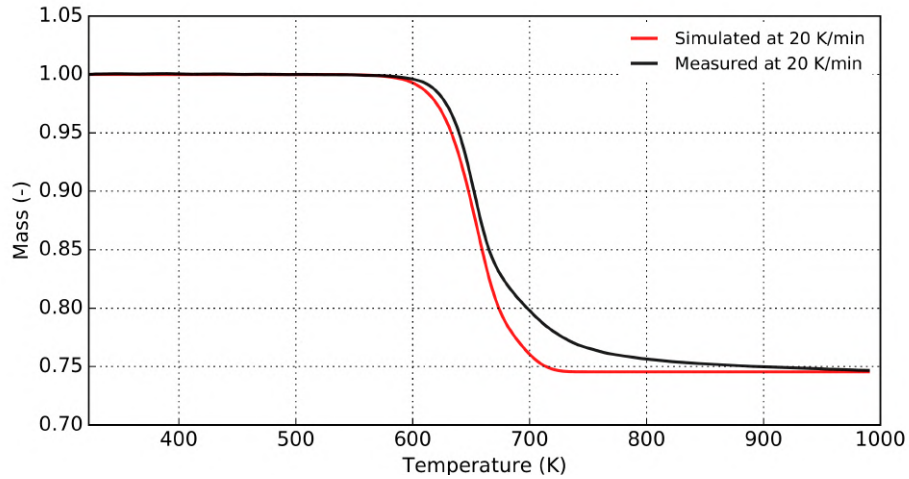


Fig. 6.4 Comparison for the measured and simulated mass loss under an inert atmosphere at 20 K/min in TGA

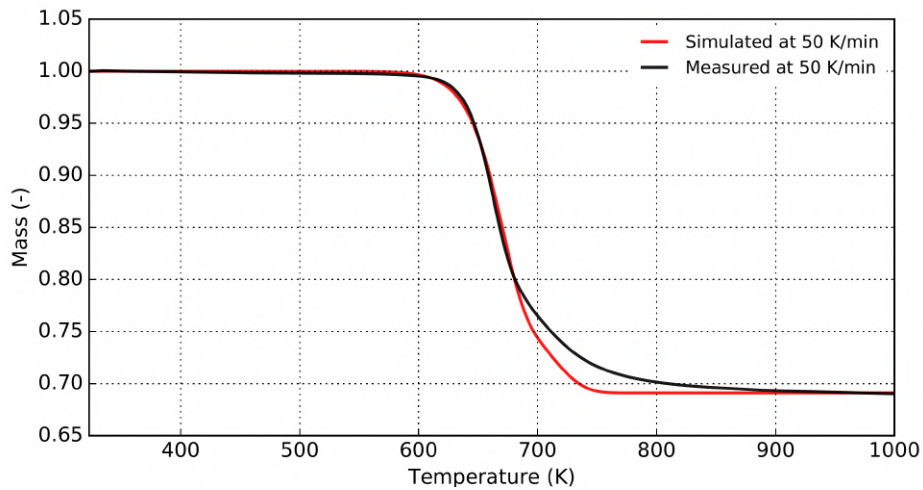


Fig. 6.5 Comparison for the measured and simulated mass loss under an inert atmosphere at 50 K/min in TGA

According to the experimental curves, it occurs a plateau after the termination of the thermal decomposition which involves the total mass loss fraction account for approximately 25% and 30% respectively for the two heating rates. This is in accordance with the value reported in [52] with a mass fraction loss of 28 wt%, and [30]

with mass consumption of 25 wt%. The experimental char yield mass fraction in this work also agrees with the general observation which involves less char residue at high heating rates [37].

Observing the two figures, good fitness occurs concerning the char residue between experimental and simulated one. The stoichiometric coefficients for the two reactions are determined by the final experimental residue mass fraction of each reaction and the assumption of no pyrolysis of carbon fiber is made. Indeed, as reported in [52], the carbon fibers could only decompose under air at relatively high temperatures, about 950-1250 K. Thus, under an inert atmosphere, the mass loss rate curve symbolizes the epoxy resin thermal decomposition without the participation of carbon fiber decomposition. The remaining mass is formed of non-decomposed resin, carbon fibers, and char, which is consistent with the observation of [108]. Thus, the stoichiometric numbers for reaction 1 and reaction 2 under 20 K/min are 0.47 and 0.25, respectively, while at the heating rate of 50 K/min, the corresponding values account for 0.59 and 0.32, respectively.

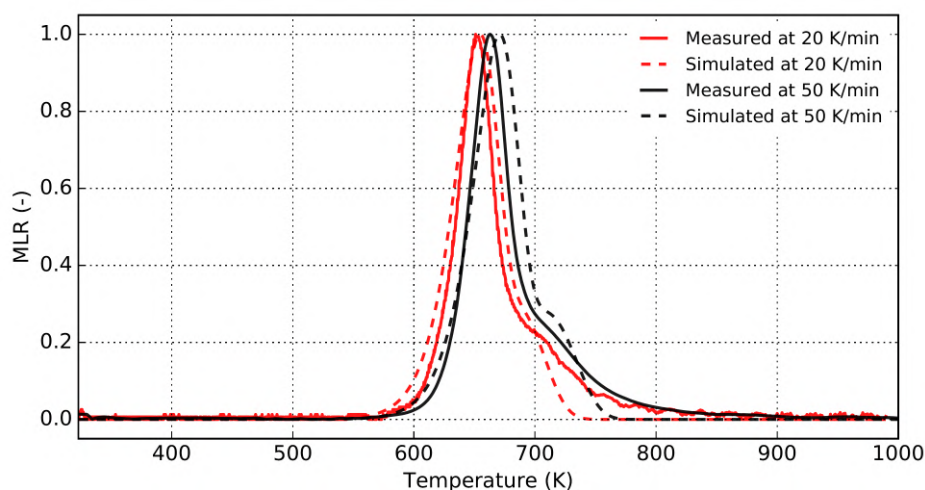


Fig. 6.6 Comparison for measured and simulated mass loss rate under an inert atmosphere at 50 K/min in TGA

Figure 6.6 plots the comparison of mass loss rate regarding optimized and experimental results at 20 K/min and 50 K/min. The observed temperature range for epoxy thermal decomposition concerning the two heating rates behaves similarly ranging

from the onset temperature of approximately 550 K to the termination temperature of approximately 900 K. The peak temperature is approximately within the range of 650-660 K for both heating rates, consistent with the results as reported in some studies [52].

Observing Figure 6.6, the kinetic parameters extracted predicted well the experimental curves, good fitness is achieved especially at 20 K/min, with exception of some levels of deviation for the tail part. The heating rate of 50 K/min involves moderate discrepancy compared with the one of 20 K/min, which is shifted to a lower temperature. This is likely to be caused by the experimental thermal gradient caused by the carbon fibers at higher heating rates, which tend to accelerate the pyrolysis reaction at a lower temperature range, due to its high thermal conductivity along the longitudinal direction. The same behavior is also observed for the kinetic parameters which are validated to fit the experimental curve at a higher heating rate with some discrepancies [21]. However, this deviation is within the range of uncertainties. As shown in some studies, the fitting result could be relatively acceptable when the char residue and the peak magnitude of the mass loss rate are within 3% and 8% [82]. Thus, it is believed that the kinetic parameters could reflect the pyrolysis reaction behavior for the different heating processes.

To conclude, when observing the fitness of experiments and the predictions obtained with the assigned mechanism and kinetic parameters, the results are reasonably in good agreement. For both heating rates, the peak magnitude and the range of temperature fit relatively well the experimental curves. This implies that the real kinetic reaction behavior at different heating conditions is captured and could be manifested by employing this set of kinetic parameters to couple with the heat and mass transfer process at a larger scale.

## 6.2 Cone calorimeter experiments and model validation

This part concentrates on the pyrolysis behavior of carbon/epoxy composite at a larger scale, using the cone calorimeter apparatus. The experiments are conducted in order to validate the model by using mass loss history and temperature profile at different locations through the thickness of the samples.

### 6.2.1 Experimental protocol

To conduct the Controlled Atmosphere Cone Calorimeter (CACC) experiments, the samples are cut in a parallelepiped of  $100 \times 100 \text{ mm}^2$  and a thickness of 5 mm. This is different from a cylindrical wood specimen since it is not possible to obtain a cylinder sample of carbon/epoxy composite. The carbon/epoxy composite samples are placed in the sample holder involving silicate thermal insulation material and the precise mass calibration over time is captured. The temperature measurement of the carbon/epoxy composite sample is similar to that of wood except for the thermocouples setup. The thermocouples are attached to the top location, middle location, and bottom location due to the small thickness of 5 mm of the samples. They are denoted  $T_{top}$ ,  $T_{middle}$  and  $T_{bottom}$ . The illustration of carbon/epoxy composite with the thermocouple locations is shown in Figure 6.7. The temperature measurements are repeated three times under the irradiant heat flux of  $20 \text{ kW/m}^2$  and  $50 \text{ kW/m}^2$ . Considering the sensitivity of mass balance imposed by thermocouples, the experimental manipulations of mass loss and thermocouple temperature measurements are separated.

At the cone calorimeter scale, heat and mass transfer have to be represented by the model. It is then necessary to determine the physical and thermal properties required.

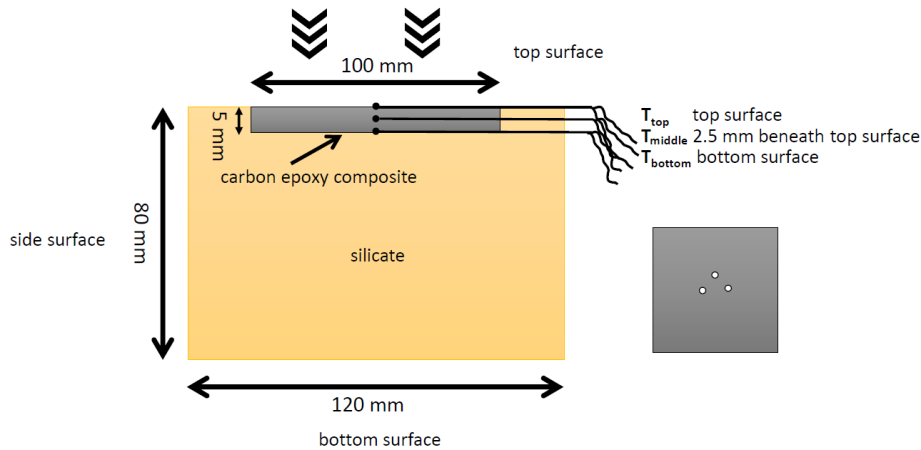


Fig. 6.7 Schematic of experimental preparation of carbon/epoxy composite pyrolysis in cone calorimeter apparatus

## 6.2.2 Determination of the thermophysical parameters

Due to the observed serious delamination of carbon/epoxy composite during the cone calorimeter experiments and the complexity to conduct the corresponding experiments to obtain the thermal parameters, an inverse analysis is not conducted for this part. Indeed, classically, the relevant inverse analysis for predicting the carbon/epoxy composite thermal properties is realized according to the back surface temperature profile [21]. Many uncertainties, especially for char thermal parameters, can involve the serious presence of delamination cracks. The anisotropic thermal properties across different directions are hard to determine, especially at a temperature of more than 473 K as demonstrated in [46]. Due to those reasons, in this study, the thermal parameters are obtained from earlier laboratory experimental data and relevant papers [15, 195]. As noted in [21, 45, 46], the carbon/epoxy composite involves larger thermal conductivity for in-plane direction than that for through-thickness direction. Thus, in accordance with [45, 46], 5 times difference is taken for the in-plane direction compared with that of through-thickness direction.

As noted in [120], an average value of the absorptivity of carbon epoxy composite is approximately 0.9 and similar results are also reported [10]. This value of 0.9 is chosen in this work due to the rough surface of the carbon/epoxy composite employed.

The emissivity of char residue employed in this work is estimated as 0.9, based on [21]. The permeability adopted in this study comes from [8], the values are  $2.42 \times 10^{-17} \text{ m}^2$  for virgin and  $2.83 \times 10^{-10} \text{ m}^2$  for char. For char properties, as noted in [101], the residue of carbon/epoxy composite accounts for the carbon fibers with the presence of epoxy resin char.

During the pyrolysis process of carbon epoxy composite, it is assumed that the entire volume of the sample remains constant, so it is not affected by the thermal decomposition. The carbon/epoxy composite decomposes with the presence of approximately 25 wt% of mass loss and subsequent apparent density decreases as noted in [196]. The declining density of epoxy resin, i.e. mass fraction decrease, corresponds to the volume fraction decrease which increases the material porosity and the carbon fiber density and volume fraction are assumed to be constant.

To assess the accuracy of these extracted thermal parameters, the main thermal conductivity and specific heat capacity of virgin carbon/epoxy composite and corresponding char properties are presented in the following figures by comparing with those reported.

Figure 6.8 and Figure 6.9 plot the specific heat capacity of carbon/epoxy composite and char from literature and in this study. It can be observed that the values in this work are within the uncertainties of the ones reported in the literature. Regarding the laminate structure of carbon/epoxy composite, the thermal conductivity at in-plane direction is much larger than that for through-thickness direction (Figure 6.10 and Figure 6.11). In this work, this value is specified with 5 times larger as described earlier. The thermal properties of carbon/epoxy composite are quite dependent on carbon fiber intrinsic properties and the epoxy resin matrix. Indeed, the thermal conductivity of carbon fiber is much higher than that of epoxy resin, and the longitudinal thermal conductivity of carbon fiber is found to be  $10.2 \text{ W/m/K}$  while the radial one is just  $1.256 \text{ W/m/K}$  [15]. As noted in [15], the specific heat capacity for epoxy resin is approximately two times larger than that of carbon fiber. Thus, the carbon fiber volume fraction contributes to the composite thermal conductivity while the specific

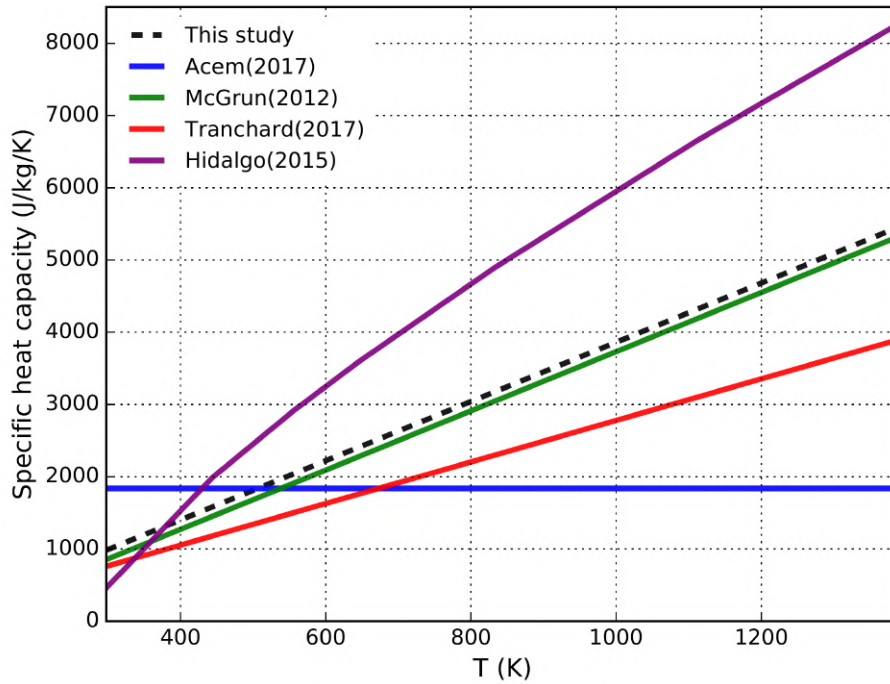


Fig. 6.8 Specific heat capacity of carbon/epoxy composite from literature and in this study. (Acem(2017) [120], McGrun(2012) [9], Tranchar(2017) [46], Hidalgo(2015) [101])

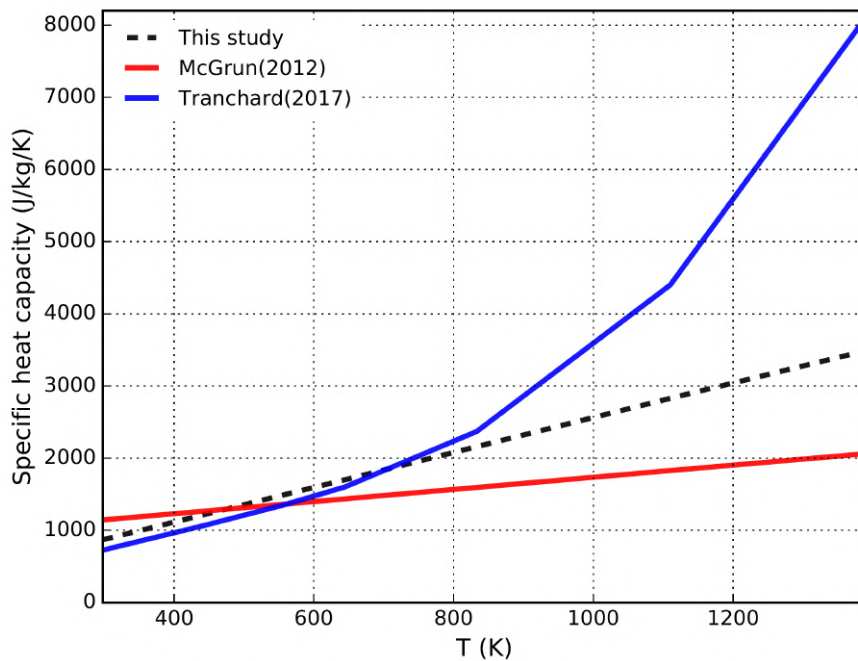


Fig. 6.9 Specific heat capacity of carbon/epoxy composite char from literature and in this study. (McGrun(2012) [9], Tranchar(2017) [46])

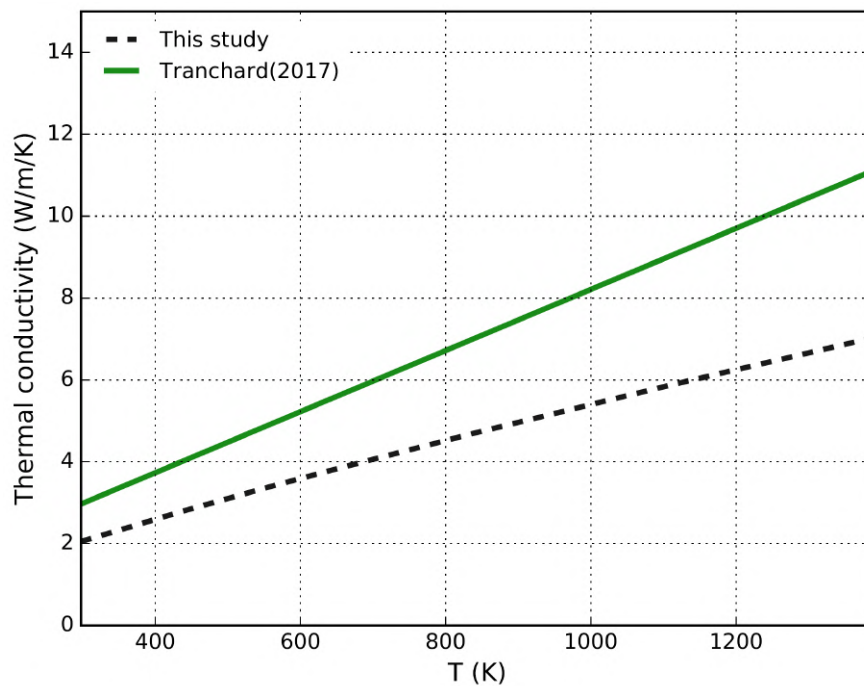


Fig. 6.10 Thermal conductivity at the in-plane direction of carbon/epoxy composite from literature and in this study. (Tranchar(2017) [46])

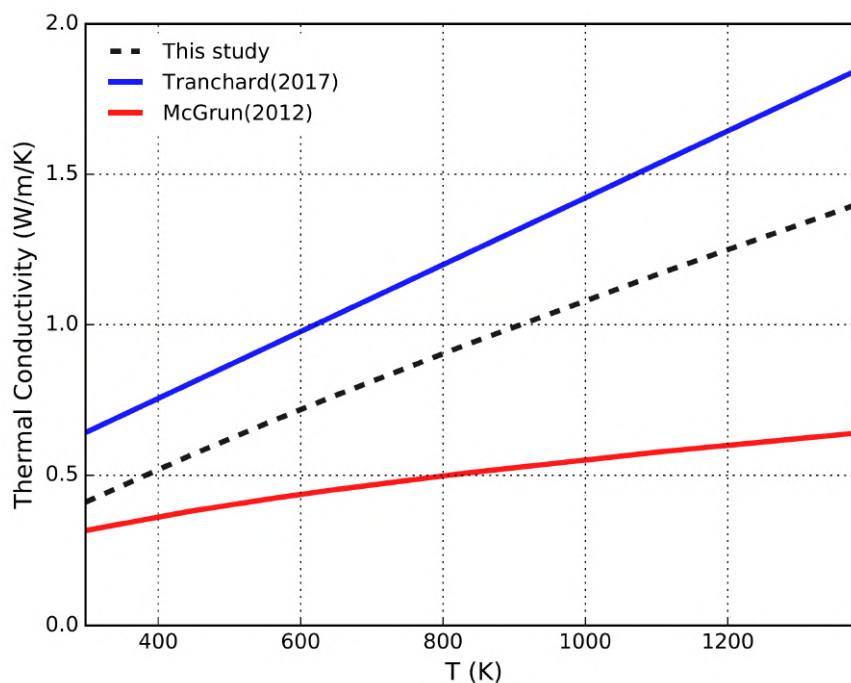


Fig. 6.11 Thermal conductivity at the through-thickness direction of carbon/epoxy composite from literature and in this study. (Tranchar(2017) [46], (McGrun(2012) [9])

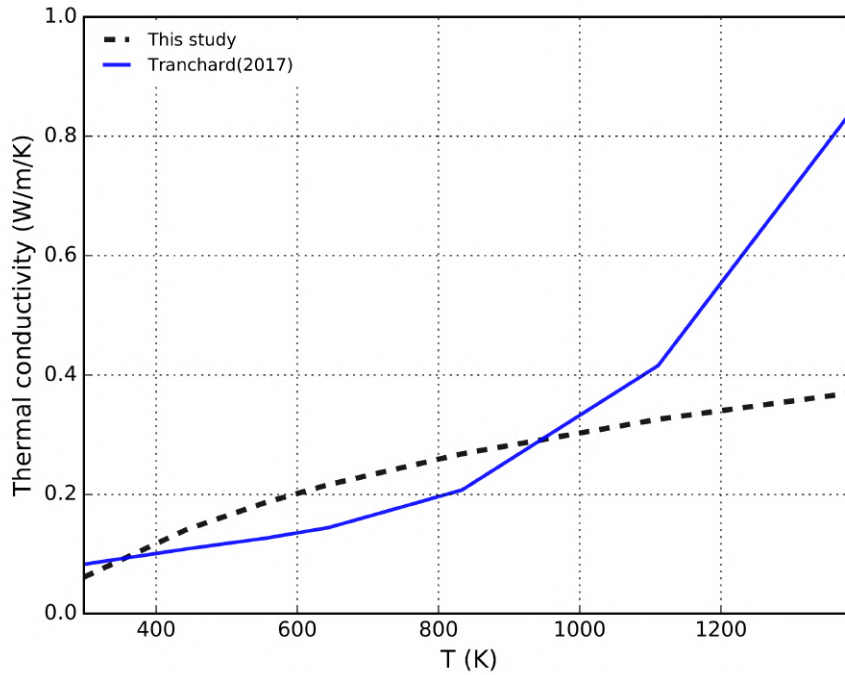


Fig. 6.12 Thermal conductivity of carbon/epoxy composite char from literature and in this study. (Tranchard(2017) [46])

heat capacity dominates the composite heat capacity, as demonstrated in [197]. For char thermal conductivity, relatively large uncertainties are presented when observing Figure 6.12. This is due to the serious delamination cracks of the composite during the pyrolysis process. Indeed, the char properties with expansion or without expansion can involve an apparent difference in thermal conductivity [46]. As noted in [21], the expansion of char residue calibration due to the delamination of carbon/epoxy composite involves an order of two compared to the virgin state, i.e., from 3.2 mm to 6.4 mm.

### 6.2.3 Experimental and numerical prediction analysis

Some studies assumed that virgin carbon epoxy composite is homogeneous accounting for isotropic properties such as [21, 9]. Thus, the 1D modeling work is first conducted in this study. However, the carbon/epoxy composite accounts for primarily anisotropic laminate as discussed above. To testify the anisotropic properties influence

which involves different values across different directions of carbon/epoxy composite, 3D modeling work is also realized for comparison.

The thermal decomposition experiments of carbon/epoxy composite are done in the cone calorimeter under the incident heat flux of  $20 \text{ kW/m}^2$  and  $50 \text{ kW/m}^2$ . The comparison of measured and predicted mass loss, mass loss rate at  $20 \text{ kW/m}^2$  with 1D and 3D model are shown in Figure 6.13 and Figure 6.14, respectively.

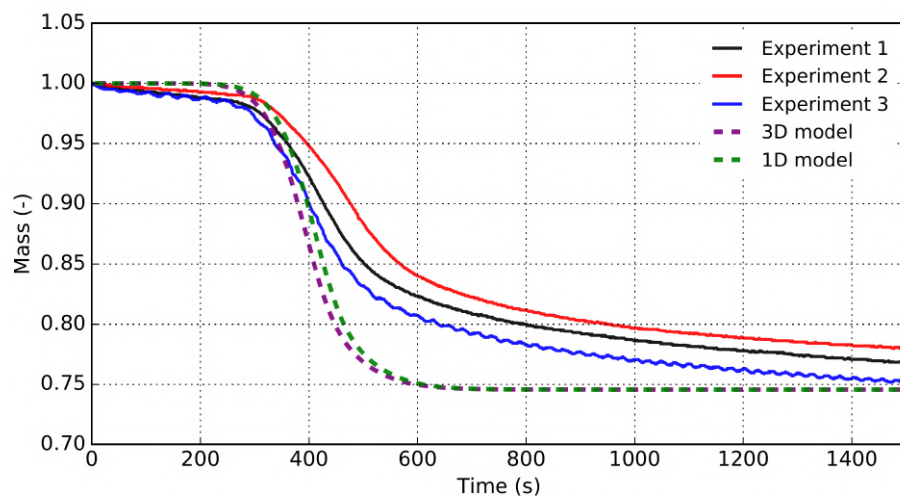


Fig. 6.13 Experimental and prediction of mass loss of carbon/epoxy composite pyrolysis at  $20 \text{ kW/m}^2$  with 1D and 3D model

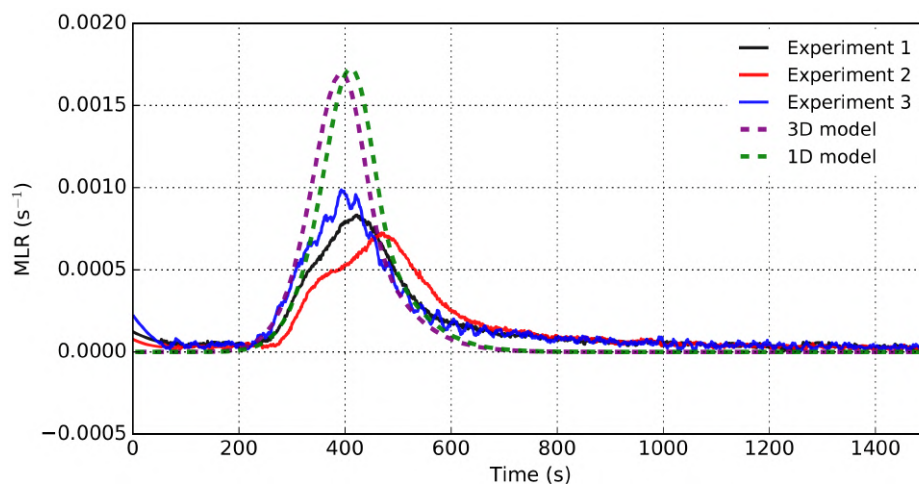


Fig. 6.14 Experimental and prediction of mass loss rate of carbon/epoxy composite pyrolysis at  $20 \text{ kW/m}^2$  with 1D and 3D model

Observing the experimental data, the pyrolysis of carbon/epoxy composite at cone calorimeter scale doesn't appear the second peak of mass loss rate which is mainly due to the thin thickness of the sample, as noted in [32]. It can be observed that the mass loss rate and the temperature prediction under 1D and 3D involve a similar variation trend which demonstrates that the isotropic assumption does not affect the simulation of thermal decomposition of carbon/epoxy composite. The carbon fibers are distributed uniformly within the resin matrix and the thermal conductivity along the fiber is much higher than that across the fiber direction, as mentioned above. Thus, the variation of heat dissipation through the thickness can be expected to be very low compared to the one for the horizontal cross-section direction (parallel to the top surface). It is reasonably correct to suppose that the temperature distribution is uniform for the horizontal cross-section direction. This is illustrated by different studies [10] which show that the thermal conductivity can be 15 times larger for the in-plane direction than those at the through-thickness direction. This justifies why the results difference between 1D and 3D can be negligible and the threshold temperature for 1D and 3D at which the pyrolysis starts to take place present nearly no difference.

The averaged residue mass fraction of carbon/epoxy composite accounts for approximately 75 wt%, which is consistent with [195]. It is observed that reasonable agreement is achieved for the normalized mass loss and corresponding mass loss rate, especially regarding the final char residue mass fraction and the duration range of mass loss rate peak. The occurrence and the termination of the pyrolysis process are captured with precision. However, the predicted magnitude of the mass loss rate peak deviates with relatively large error compared with the experiment data. The detailed analysis is addressed in the following part.

When comparing the mass loss and mass loss rate between the measured and the predicted ones, it shows perfect agreement from the onset up to 300 s. It demonstrates the validity and accuracy of this model at the initial pyrolysis stage. However, during the experimental peak temperature range, between 300 s to 700 s, the prediction involves a notable increment compared with peak magnitude. This discrepancy is

likely to be caused by the delamination cracks which induce some air layer limiting the thermal transport. Thus, the numerical mass loss rate can be higher. Another reason could be the char density non-uniformity employed at different heat fluxes with the carbonaceous structure of different levels. The density and porosity at different heat fluxes could influence the heat and mass transfer, which could contribute to the majority of discrepancy and the char in this work denotes the fully decomposed ones. As noted, the char properties are also dominated by the fiber orientation, volume fraction, and epoxy resin volume fraction which could provide some uncertainties to lead to this discrepancy. The presence of a low magnitude of experimental mass loss rate also tends to be caused by the migration of volatile gases downward to the bottom surface which can delay the mass loss process as noted in [20]. Indeed, the delamination is observed to increase the permeability of material which takes place at the bottom sites of carbon/epoxy composite. Thus, the pyrolysis gas could migrate to the bottom parts of the material to delay the mass loss. The uncertain heat of thermal decomposition could be a factor that determines the magnitude and duration of the mass loss rate peak. Indeed, some studies found that epoxy resin thermal decomposition could involve both exothermic and endothermic reactions [46], which makes the heat of decomposition quite uncertain. When the absolute value of endothermic heat of pyrolysis decreases, the mass loss rate curve is expected to occur with shorter peak duration and larger peak magnitude as well as steeper temperature variation trend.

The comparison of measured and predicted temperature profiles at the top, middle, and bottom location for 1D and 3D models at  $20 \text{ kW/m}^2$  are shown in Figure 6.15, Figure 6.16, and Figure 6.17, respectively. Overall good agreement is achieved when comparing the temperature evolution between experiments and predictions at the three locations. The temperature measured for the first experiment at the top location occurs serious drop after 700 K due to the experimental surface swelling leading to the thermocouple separation. It is observed that from the onset to approximately 500 s, the model under-predicts the top surface and middle temperatures by about 20 K, while back surface temperature involves good fitness with experimental data. This is

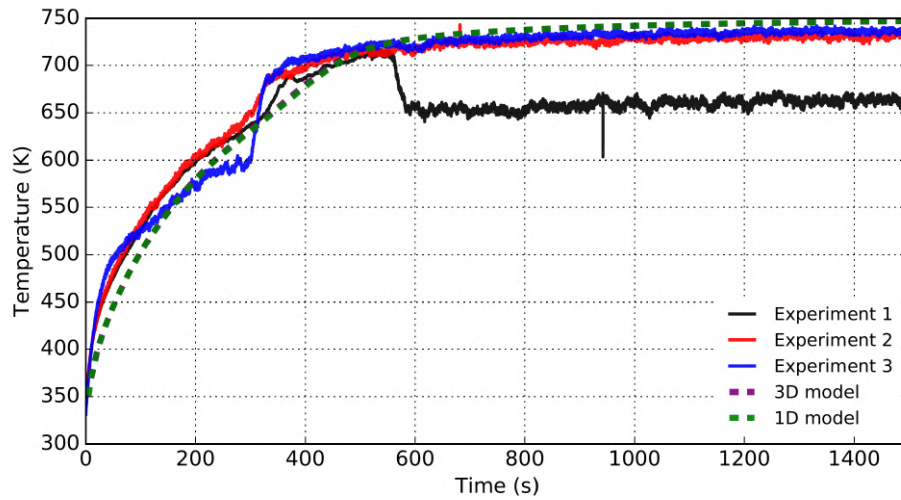


Fig. 6.15 Experimental and prediction of temperature evolutions of carbon/epoxy composite pyrolysis at  $20 \text{ kW/m}^2$  with 1D and 3D model (Top location)

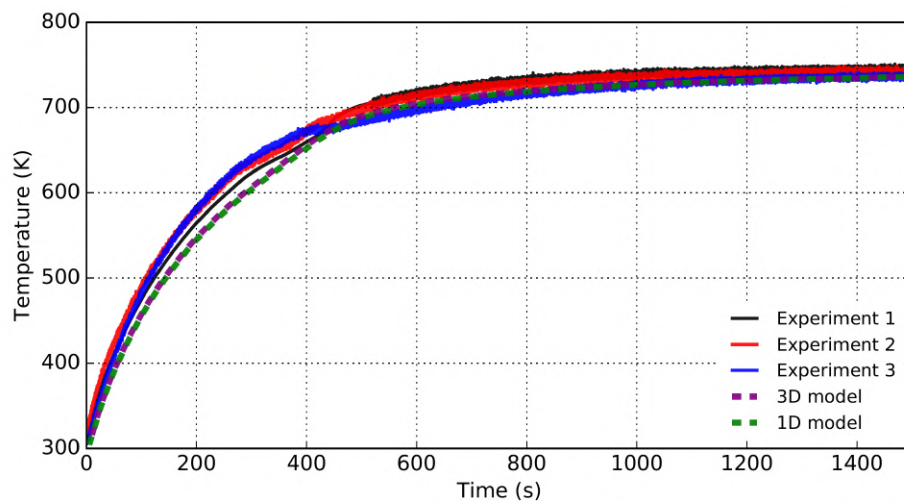


Fig. 6.16 Experimental and prediction of temperature evolutions of carbon/epoxy composite pyrolysis at  $20 \text{ kW/m}^2$  with 1D and 3D model (Middle location)

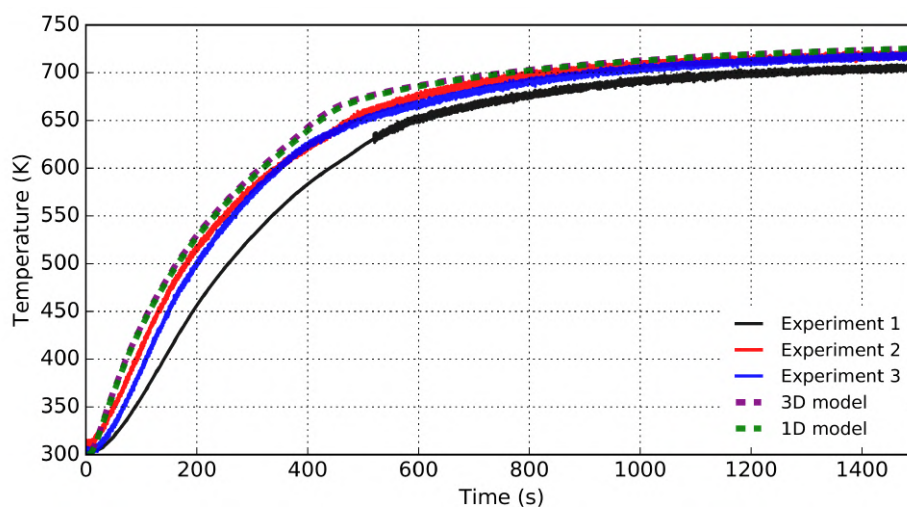


Fig. 6.17 Experimental and prediction of temperature evolutions of carbon/epoxy composite pyrolysis at  $20 \text{ kW/m}^2$  with 1D and 3D model (Bottom location)

likely to be the consequence of large uncertainty at the top surface measurement as noted in [90].

The delamination cracks could limit the heat dissipation to the bottom surface accompanied by the reduction of effective thermal conductivity. Indeed, the carbon/epoxy composite could undergo thermal delamination and swell, which change the top surface condition and absorb more heat from the cone heater, thus the temperature increase significantly. At  $20 \text{ kW/m}^2$ , the moderate temperature deviation especially at the surface location is also attributed to the shift of thermocouple position accompanying the serious top surface expansion, although the level of delamination cracks for this sample at this level of heat flux is not important. Due to the highly fragile and developing char surface structure, the exposure to the irradiant heat flux involves much uncertainty in addition to the higher thermal gradients caused by the delamination cracks. At the final stage, the temperature prediction for the top surface and middle location is highly improved compared with the experimental data. The temperature of the bottom surface is in good agreement with the experimental one due to the balance of larger heat absorption of the top surface and the decrease of thermal conductivity. Indeed, the surface heat increase is induced by swelling which decreases the distance between the irradiant heater and top surface, while thermal conductivity decrease is

caused by the delamination air layer which plays a role in the thermal barrier due to the low thermal conductivity of air. To conclude this part, it is believed that a reasonable degree of accuracy is achieved especially for temperature prediction at 20 kW/m<sup>2</sup> except for the peak magnitude of mass loss rate.

The comparison of measured and prediction concerning mass loss and mass loss rate for carbon/epoxy composite under 1D and 3D at 50 kW/m<sup>2</sup> are shown in Figure 6.18 and Figure 6.19, respectively.

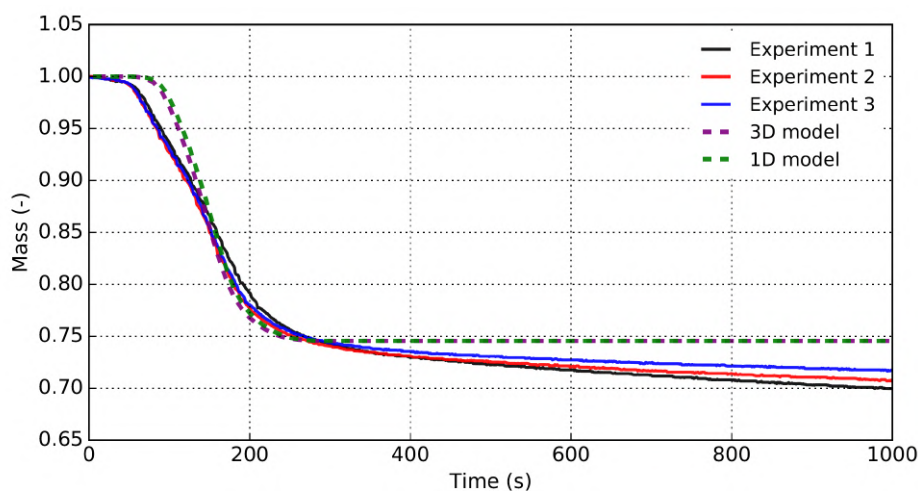


Fig. 6.18 Experimental and prediction of mass loss of carbon/epoxy composite pyrolysis at 50 kW/m<sup>2</sup> with 1D and 3D model

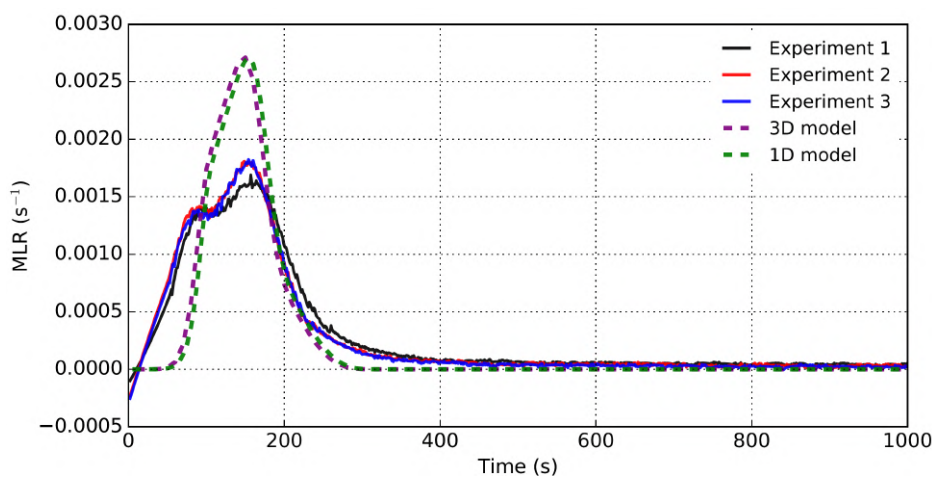


Fig. 6.19 Experimental and prediction of mass loss rate of carbon/epoxy composite pyrolysis at 50 kW/m<sup>2</sup> with 1D and 3D model

The comparison of measured and prediction concerning temperature evolution for carbon/epoxy composite under 1D and 3D at  $50 \text{ kW/m}^2$  are showed in Figure 6.20 to Figure 6.21, respectively. Figure 6.20 plots the temperature profile at the middle location, and Figure 6.21 plots the temperature profile at the bottom location. The temperature evolution of the surface location is not presented here due to the experimental appearance of significant separation between thermocouples and material surface, thus we failed to capture the temperature data at this location. Indeed, the thermocouple at the top surface shifts to the upper sites due to swelling, and the predicted temperatures are much lower than the experimental ones.

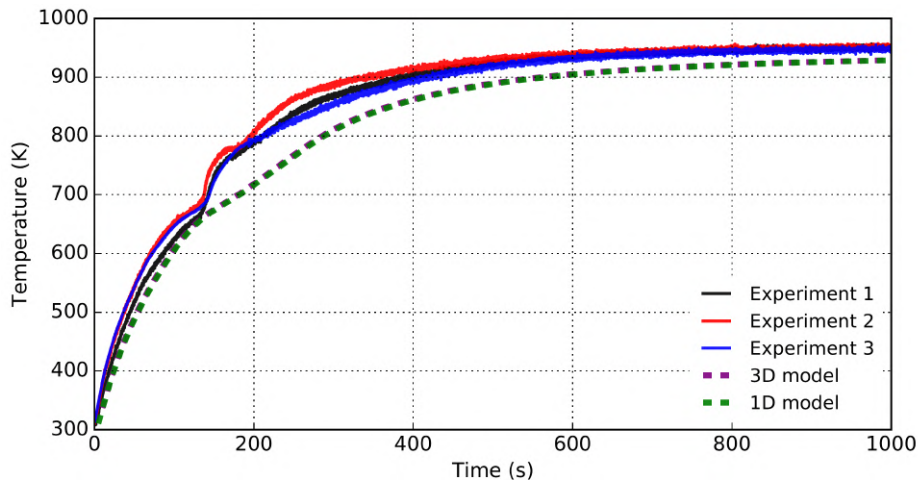


Fig. 6.20 Experimental and prediction of temperature evolution of carbon/epoxy composite pyrolysis at  $50 \text{ kW/m}^2$  with 1D and 3D model (Middle location)

Observing the numerical 1D and 3D modeling at  $50 \text{ kW/m}^2$ , the results are within good similarities. Similar to the observations formulated at  $20 \text{ kW/m}^2$ , the non-isotropic thermal conductivity consideration has a little effect on the pyrolysis results, as found in [21].

Comparing the experimental mass loss profile at  $50 \text{ kW/m}^2$  with the one at  $20 \text{ kW/m}^2$ , the residue mass fraction is approximately 70 wt% under  $50 \text{ kW/m}^2$ , lower than the one at  $20 \text{ kW/m}^2$  which is about 75 wt%. The time to reach the mass loss rate peak is approximately 150 s and it is well represented by the model. However, the peak magnitude is over-predicted. The mass loss rate profile at  $50 \text{ kW/m}^2$  involves a

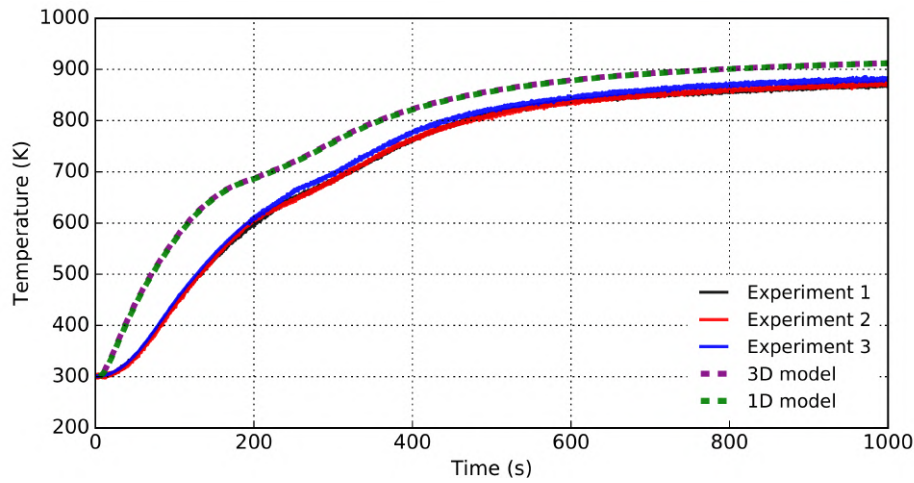


Fig. 6.21 Experimental and prediction of temperature evolution of carbon/epoxy composite pyrolysis at  $50 \text{ kW/m}^2$  with 1D and 3D model (Bottom location)

sharp drop-off which is not observed at  $20 \text{ kW/m}^2$ . Indeed, at approximately 160 s, the experimental temperature at the middle location involves an apparent discontinuity at approximately 650 K, which is also observed in [10]. It should be caused by the abrupt presence of serious delamination cracks due to the gas pressure accumulation among the carbon fiber plies. Figure 6.18 demonstrates that the top surface temperature evolution failed to be captured, due to the strong swelling at the surface. These delamination cracks are accompanied by a relatively thick air layer formation which immediately decreases some amount of thermal transport to the bottom sites of the material and the temperature could experience a drop. With the duration of heating up, the materials accumulate sufficient heat and the temperature continuously rises to attain its maximal value. This observation of significant change demonstrates that the sample tends to experience single or several serious thermal delamination cracks although many small cracks could take place which has a slight influence on the overall mass loss and temperature variations. Overall, the model predicted well the onset and termination of the mass loss rate except for the reaction peak magnitude. As evaluated in [10], the acceptance criterion is defined for the deviation of approximately 10% between the experimental and the modeling of mass loss rate peak magnitude.

Thus the model has the potential to predict the experimental data with quantitative accuracy provided that some main uncertainties can be manipulated well.

Some different predictions of temperature evolution at the top, middle, and bottom surface are observed under the heat flux of 20 kW/m<sup>2</sup> and 50 kW/m<sup>2</sup>. At 20 kW/m<sup>2</sup>, the top surface of the material could take place moderate swelling with smaller delamination cracks, as also displayed in the literature review [30]. While the thermocouple at the middle location is nearly fixed, the experimental data are also relatively higher than the predicted ones. At the bottom location, a good agreement between predictions and experiments is observed. It is believed to be the compromise effect between the thermal barrier formed by the air layer and more heat absorption by swelling as discussed earlier.

At 50 kW/m<sup>2</sup>, the top surface can undergo serious swelling with strong delamination cracks which influence the temperature evolution. For the temperature at the middle location, a similar compromise effect takes place which yields relatively better agreement, especially at the initial pyrolysis stage. For the temperature of the bottom location, it is poorly predicted due to the large cracks of the thermal barrier leading to much lower experimental temperature.

It can be concluded that serious delamination occurs at different locations through the thickness in the cases of 20 kW/m<sup>2</sup> and 50 kW/m<sup>2</sup>. Regarding this study, serious delamination occurs between the top and middle locations at 20 kW/m<sup>2</sup>. While for 50 kW/m<sup>2</sup>, this serious delamination occurs between middle and bottom locations.

To conclude this part, a similar prediction level is observed at 20 kW/m<sup>2</sup> and 50 kW/m<sup>2</sup>. Except for the larger discrepancies of mass loss rate peak magnitude prediction, the prediction at lower heat flux seems to be more accurate when targeting the temperature evolution.

## 6.3 Conclusion

This chapter has been dedicated to the modeling of thermal decomposition of a resin epoxy/carbon fibers composite, firstly at TGA scale and secondly at cone calorimeter scale. A two parallel mechanism of thermal decomposition has been employed and the associated kinetic parameters have been validated at the TGA scale by comparison with the experimental data. The physical and the thermal properties required for the modeling of thermal decomposition at the cone calorimeter scale has been determined from different literature sources. The evaluation of the model to represent the thermal decomposition of the carbon/epoxy composite has been done addressing the mass loss, the mass loss rate, and the temperature profiles into the thickness of the composite samples. The comparison of the experimental and the numerical data shows that the model tends to over-predict, whatever the heat flux studied, the kinetic of mass loss and the mass loss rate. This is mainly attributed to the phenomenon of delamination, cracking, char formation, etc. that the model does not permit to represent. Concerning the temperature evolutions, the accordance between the model and the experiments is relatively good.



# Chapter 7

## Sensitivity analysis

Up to now, wood and carbon/epoxy composite pyrolysis behavior under TGA and Cone Calorimeter scales are conducted by modeling with PATO. In the previous parts, different levels of discrepancies can be identified in experimental and model data. Indeed, many input parameters are involved during this modeling study, they can be collected as chemical, physical, or other parameters. As noted in [104], the more input parameters are used in the model, the higher uncertainties can be observed. In order to test how these parameters are linked to the pyrolysis behavior and which ones are more uncertain, this part of the manuscript is dedicated to a sensitivity analysis in order to explore their effects. As noted in [118], the sensitivity analysis could give some knowledge about how parameters influence the results. For example, during the pyrolysis process, different parameters can play different roles in the results. Thus, in the future, we can focus on those parameters which have to be determined properly by numerical or experimental ways such that it can allow to diminish the model uncertainties caused by input parameters and to improve the model prediction efficiency.

The bench-scale cone calorimeter simulation couples both processes of kinetics and heat and mass transfers for pyrolysis modeling. Thus, the cone calorimeter simulations allow identifying the role of each parameter inside a single pyrolysis model. Moreover, with this scale, each parameter's contribution to the overall pyrolysis behavior can

be analyzed to have some knowledge about its contribution to the cone calorimeter simulation outputs. As noted in [10], the current pyrolysis models are mainly used in the fire community to predict the mass loss rate and the temperature evolution. In this sense, the following sensitivity analysis will focus on the mass loss rate and temperature evolution differences influenced by the corresponding parameters.

It exists two types of sensitivity analysis [198]. The first one is a local sensitivity analysis where only one parameter varies around its nominal average value (such as One-At-a-Time, OAT) [199]. The second one is a global sensitivity analysis where all parameters change simultaneously (such as Sobol sensitivity analysis) [200]. In this study, the local sensitivity analysis is performed on the pyrolysis model prediction because we want first to know the influence of each parameter independently from the others. For this sensitivity analysis, the following important input parameters are identified during our modeling work: kinetic parameters, thermodynamic parameter (the heat of thermal decomposition), convection boundary parameters, thermophysical parameters of virgin and char, and water content.

A similar sensitivity analysis can be found in [118] which focused on the mass loss rate and surface temperature. As we have shown in earlier chapters, the uncertainty of parameters presents different levels of influence to the temperature evolution at different locations through the thickness. Thus, we need to better understand the nature and the complexity of these parameters influences (inputs) to enhance the result precision (outputs: MLR, temperature...). Moreover, this analysis is performed with different heat fluxes. Indeed, as shown in earlier chapters, different heat fluxes involve different levels of chemical reaction, heat transfer, and mass transfer. By consequences, the corresponding parameters can also be of different levels of importance as a function of the heat fluxes.

The first initiative is to decide the type of material to conduct the pyrolysis modeling work. As shown in earlier chapters, wood and carbon/epoxy pyrolysis are studied. However, wood shows more complex pyrolysis behaviors and this can be observed concerning the shape of mass loss rate and temperature profile. In order to

deeply analyze the coupling of the thermal and chemical part under a more complex application scenario, wood is chosen in this study to conduct the sensitivity analysis on the more complex material (see Chapter 4). However, the variation of simultaneous reaction of the three components is excluded from this first sensitivity analysis, due to its complexity. Since cellulose constitutes the majority of the mass fraction (approximately 40 wt%) of wood by approximately two times larger than those of cellulose and lignin, in a first approach, we assume the assumption that cellulose contributes to the maximum part of overall wood pyrolysis reaction rate (see Chapter 4). Thus, we focus on the cellulose reaction kinetics in order to estimate the factors influencing the wood pyrolysis.

Another point is about the model resolution technique used to study the sensitivity analysis (dimensional model). The common practice is using 1D model to analyze the sensitivity of the results to different chemical or thermophysical parameters such as presented in [118]. Two reasons can be given, firstly the previous observation in Chapter 5 shows quite a similar trend of the pyrolysis process captured under 1D and 2D simulations. Secondly, in this study, the sample holder (thermally insulated silicate) is relatively thick, the back surface temperature is the ambient one, the side convection effect is moderate and could be neglected (see Chapter 5). Thus, 1D simulation cases are conducted for this sensitivity analysis. Furthermore, this kind of simulation presents the advantage of a low computational cost while involving relatively good prediction accuracy.

The second initiative for conducting a sensitivity analysis is to choose the parameters variation range. In fact, the results are dependent on these ranges and their roles can be more or less important on the outputs and the sensitivity analysis results [201]. It is hard to determine the variation criteria concerning the range for each parameter, these parameters involve their intrinsic properties which show different levels of uncertainty. Thus, in this work, the choice can be very versatile and flexible for different parameters with different ranges. For sure, sensitivity analysis is highly dependent on the parameter range used. The more we increase the range of variations and the more the sensitivity value obtained increases.

Finally, we use the OAT method to analyze the sensitivity of all pyrolysis model parameters. This method highlights rapidly the consequences of a parameter variation (input) on the output data (for example, the mass loss rate and temperature evolution). In this study, the consequences of the parameter variations are identified by graphical lecture. Different levels of variation range are selected in order to correctly capture some differences to study the influence of these parameters on the final pyrolysis results.

## 7.1 Kinetic and thermodynamic parameters influence

When conducting sensitivity analysis concerning kinetic parameters [32, 74], the upper values are usually increased by a factor of 2 based on the average value concerning the reaction order, and correspondingly, the lower value is decreased by a factor of 2. While for activation energy, based on the average value, the upper value and lower value are increased by approximately +10% and -10%, respectively. And for the pre-exponential factor, based on the average value, it could be increased by a factor of 10 for the upper value, and can be decreased by a factor of 10 for the lower value. The average values concerning kinetic parameters at two heat fluxes, i.e., 20 kW/m<sup>2</sup> and 50 kW/m<sup>2</sup>, are based on the model optimization values employed in this (see Chapter 4).

Concerning the heat of thermal decomposition, the reported values for softwood pyrolysis are changing approximately based on  $-1 \times 10^5$  J/kg (endothermic) [56, 192, 75, 110]. Indeed, the heat of decomposition can vary a lot due to different types of wood and the variation range is quite large. Concerning the sensitivity analysis of this parameter, based on the average value, the upper and lower values are changed by a factor of 2 [32]. Based on the average value employed in this study ( $-1 \times 10^5$  J/kg), two values are specified for the lower and upper value to define the range: from  $-2 \times 10^5$  to  $-5 \times 10^4$  J/kg.

The corresponding variation range concerning the parameters studied are listed in Table 7.1, where A is the pre-exponential factor, E is the activation energy, and n is

Table 7.1 The variation range of kinetic and thermodynamic parameters for the sensitivity analysis

Parameters	Units	Lower values	Average values	Upper values
E (20 kW/m <sup>2</sup> )	J/mol	$2.26 \times 10^5$	$2.51 \times 10^5$	$2.76 \times 10^5$
A (20 kW/m <sup>2</sup> )	/s	$9.47 \times 10^{17}$	$9.47 \times 10^{18}$	$9.47 \times 10^{19}$
n (20 kW/m <sup>2</sup> )	-	0.5	1.0	2.0
E (50 kW/m <sup>2</sup> )	J/mol	$2.25 \times 10^5$	$2.50 \times 10^5$	$2.75 \times 10^5$
A (50 kW/m <sup>2</sup> )	/s	$3.2 \times 10^{18}$	$3.2 \times 10^{19}$	$3.2 \times 10^{20}$
n (50 kW/m <sup>2</sup> )	-	0.9	1.8	3.6
Heat of decomposition	J/kg	$-2 \times 10^5$	$-1 \times 10^5$	$-5 \times 10^4$

the reaction order. These values are used in the next part concerning the sensitivity analysis of the kinetic parameters.

### 7.1.1 Activation energy influence

Figure 7.1 and Figure 7.2 present the mass loss rate and temperature evolution by the influence of activation energy at 20 kW/m<sup>2</sup> and 50 kW/m<sup>2</sup>, respectively. The values used for E are exposed in Table 7.1.

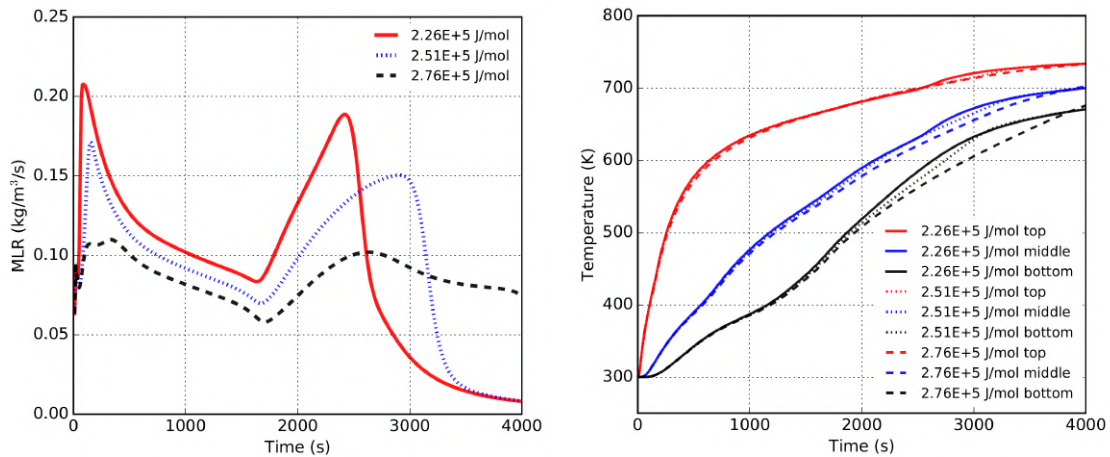


Fig. 7.1 Influence of activation energy on the mass loss rate and temperature evolution at heat flux of 20 kW/m<sup>2</sup>

It can be observed that the activation energy parameter can impose a serious effect on the mass loss rate evolution during the whole pyrolysis process at different heat flux. Lower activation energy can lead to a higher peak magnitude of mass loss rate and

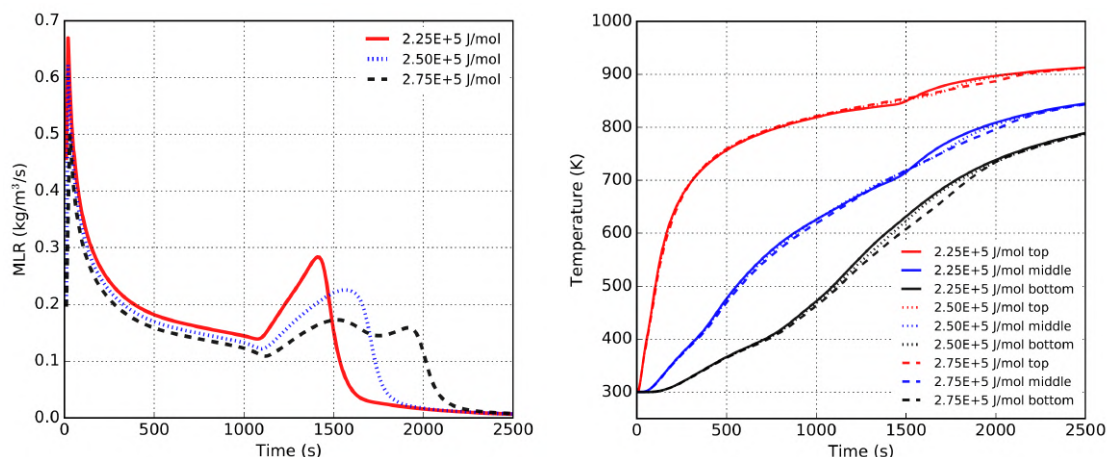


Fig. 7.2 Influence of activation energy on the mass loss rate and temperature evolution at heat flux of  $50 \text{ kW/m}^2$

reduce the time to attain a peak. This influence is more intense at  $20 \text{ kW/m}^2$  than at  $50 \text{ kW/m}^2$ . However, the temperature evolution displays not significant difference with different activation energy values at both heat fluxes. This influence can take place only in the strong chemical reaction stage and the temperature can be the same as soon as the pyrolysis reaction complete which can be seen clearly at the tail stage at  $50 \text{ kW/m}^2$ .

Activation energy can symbolize the pyrolysis reaction intensity. Consequently, this parameter is sensitive when the pyrolysis process is controlled by kinetics at lower heat flux, as demonstrated in Chapter 5. However, at a higher heat flux, the pyrolysis process is mostly controlled by heat and mass transfers. Then, the pyrolysis process can present an infinitely fast reaction, especially at the material surface at the onset stage due to the high heating rate process. As viewed in the wood or carbon/epoxy part, the surface location at this onset stage involves more than approximately  $100 \text{ K/min}$ . Thus, within the same level of activation energy variation, a more prominent difference of mass loss rate can be observed at lower heat flux. At the top surface location of material, the heating rate is much higher than in the interior sites, and the temperature at the top surface is influenced seriously by the heating process, while

the bottom surface location could experience strong coupling between heat and kinetic process.

To conclude this part, the mass loss rate is quite sensitive to the activation energy during the whole pyrolysis process and this influence is stronger at lower heat flux. Whereas the temperature evolution is slightly sensitive to the activation energy only during the second peak of mass loss rate where stronger chemical reactions take place. As described earlier in Chapter 4, before attaining the peak of reaction rate, the process is controlled by the heating process, while after this peak, the reaction is controlled by the remaining mass fraction. Thus, due to the remaining mass is of a large fraction to involve the reaction by the feedback from the thermal insulating material. While for other pyrolysis stages, the temperature is insensitive to the activation energy.

### 7.1.2 Pre-exponential factor influence

Figure 7.3 and Figure 7.4 present the mass loss rate and temperature evolution by the influence of the pre-exponential factor at  $20 \text{ kW/m}^2$  and  $50 \text{ kW/m}^2$ , respectively. The values used for  $A$  are exposed in Table 7.1.

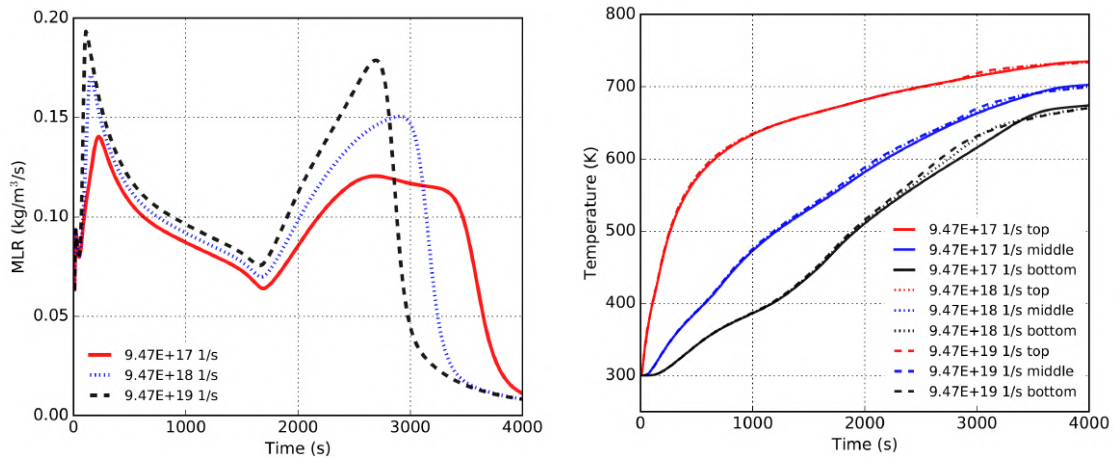


Fig. 7.3 Influence of pre-exponential factor on the mass loss rate and temperature evolution at heat flux of  $20 \text{ kW/m}^2$

Similarly to the activation energy, the pre-exponential factor represents the pyrolysis reaction activity and larger values can provide a stronger reaction [32]. It can be

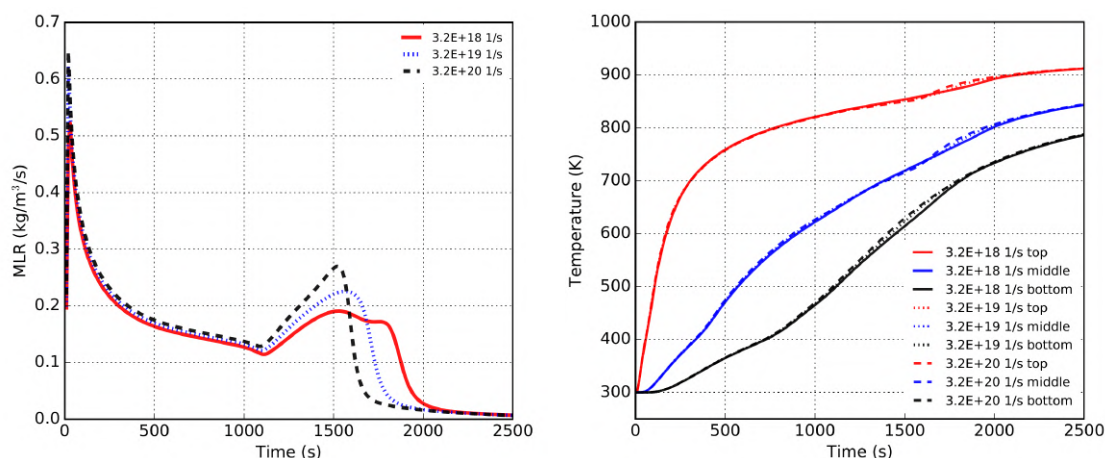


Fig. 7.4 Influence of pre-exponential factor on the mass loss rate and temperature evolution at heat flux of  $50 \text{ kW/m}^2$

observed that significant differences occur for both mass loss rate peaks at different pre-exponential factors. A higher pre-exponential factor can lead to a larger mass loss rate and reduce the time to react. This variation trend is similar to the case of activation energy influence, i.e., much stronger differences occur in the case of  $20 \text{ kW/m}^2$ . Despite the pre-exponential factor variation, the temperature evolution at  $20 \text{ kW/m}^2$  and  $50 \text{ kW/m}^2$  display quite good similarity with the exception of the short duration of the second peak at  $20 \text{ kW/m}^2$  where a minor difference occurs. It can be observed comparing the case of activation energy influence, nearly identical influence on the mass loss rate and temperature evolution can be found concerning larger activation energy and smaller activation energy. However, the variation range of the pre-exponential factor is larger compared with that of activation energy in order to lead to the same levels of the difference of pyrolysis results. Indeed, under the same variation degree with activation energy, we have found that pre-exponential factor can be insensitive to the pyrolysis results.

To conclude this part, the pyrolysis process at lower heat flux is relatively more sensitive to pre-exponential factor compared with that at higher heat flux. And the influence of pre-exponential factor and activation energy is similar while in opposite direction.

### 7.1.3 Reaction order influence

Figure 7.5 and Figure 7.6 present the mass loss rate and temperature evolution by the influence of reaction order at  $20 \text{ kW/m}^2$  and  $50 \text{ kW/m}^2$ , respectively. The values used for  $n$  are exposed in Table 7.1.

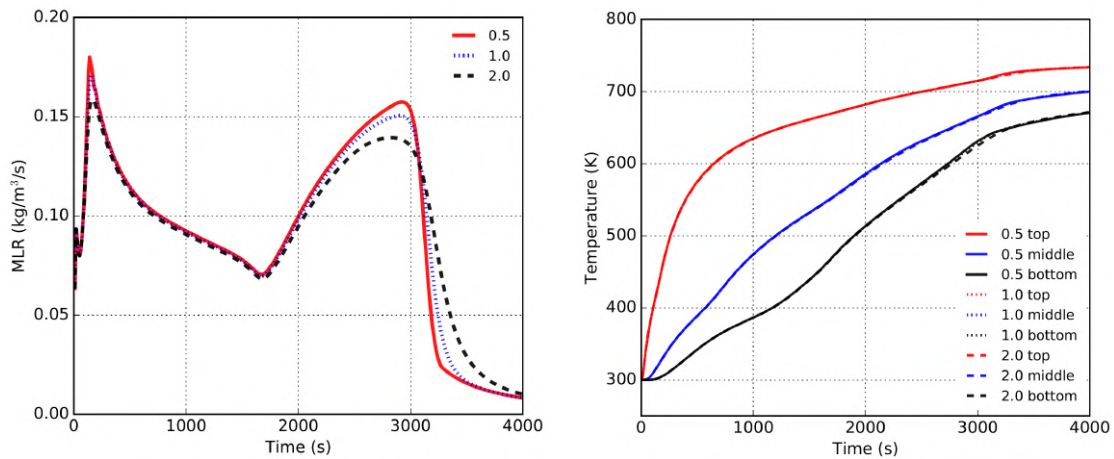


Fig. 7.5 Influence of reaction order on the mass loss rate and temperature evolution at heat flux of  $20 \text{ kW/m}^2$

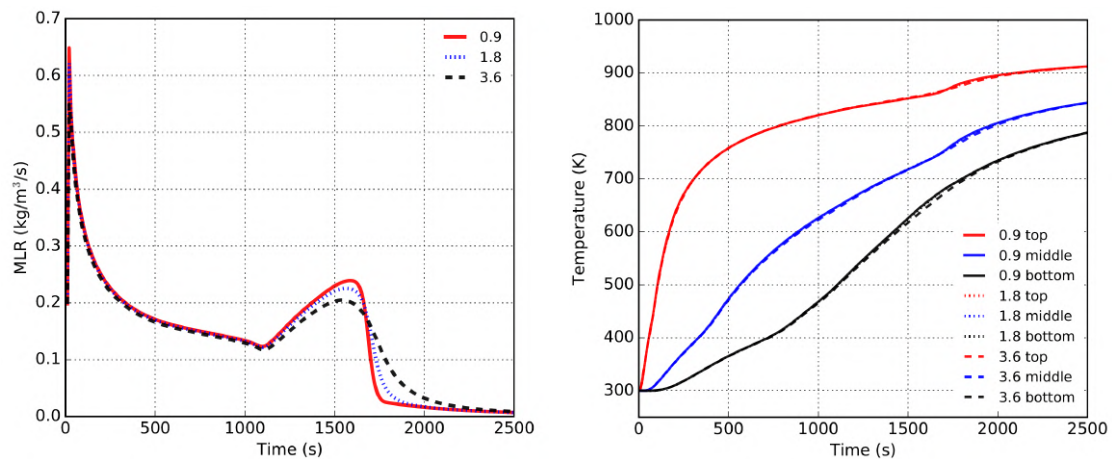


Fig. 7.6 Influence of reaction order on the mass loss rate and temperature evolution at heat flux of  $50 \text{ kW/m}^2$

It can be observed that the reaction order influences the mass loss rate only during the peaks and mainly during the second peak. Indeed, a smaller reaction order can lead to a higher reaction rate and shorter duration of reaction when focusing on the presence

of steeper evolution trend for the second peak. While for temperature evolution, no apparent difference is observed under different heat flux. All these observations are coherent to those found in earlier activation energy and pre-exponential factor influence analysis. Indeed, for different heat fluxes, these three kinetic parameters play an important role in the pyrolysis reaction rate whereas they have a limited effect on the temperature in the condensed phase. Neglecting the effect of the range, it seems in this preliminary study, that the activation energy can have the most important effect on the pyrolysis reaction. Correspondingly, the pre-exponential factor's influence is lower than the activation energy and the least importance can be given by the reaction order.

To conclude concerning the kinetics parameters ( $A$ ,  $E$ ,  $n$ ) influence, they should be responsible to involve chemical reaction part in the pyrolysis process. Then, if the kinetic is highly influential, these three parameters should be predicted precisely and correctly. For example, we have demonstrated that the heating rate can influence the kinetics with a “non-linear” form even during the relatively small different heating process at the TGA scale. At a larger scale with a high heating process, the kinetics difference is believed to be higher and the correct chemical kinetics can't be obtained. This is still a challenge and more focus should be paid in the future. However, if our studies rely on the fire pyrolysis engineering field to predict the temperature profile inside the condensed phase, then the kinetic parameters can be neglected. This last conclusion should be paid attention. Indeed in this study, the pyrolysis process is linked to the heat transfer process in the model used through the enthalpy of decomposition and then the convection and diffusion process of gas released through the pores of the solid. Here the sensitivity analysis has been made with a quite low “endothermic” enthalpy of decomposition. For reactions with a higher “endothermic” enthalpy of decomposition, the change of chemistry (through kinetic parameters) could have more influence on temperatures.

### 7.1.4 The heat of thermal decomposition influence

Due to the uncertainty of heat of thermal decomposition, the sensitivity study to this parameter is performed. Figure 7.7 and Figure 7.8 plot the mass loss rate and temperature evolution by the influence of heat of thermal decomposition at 20 kW/m<sup>2</sup> and 50 kW/m<sup>2</sup>. The values used for the heat of decomposition are exposed in Table 7.1.

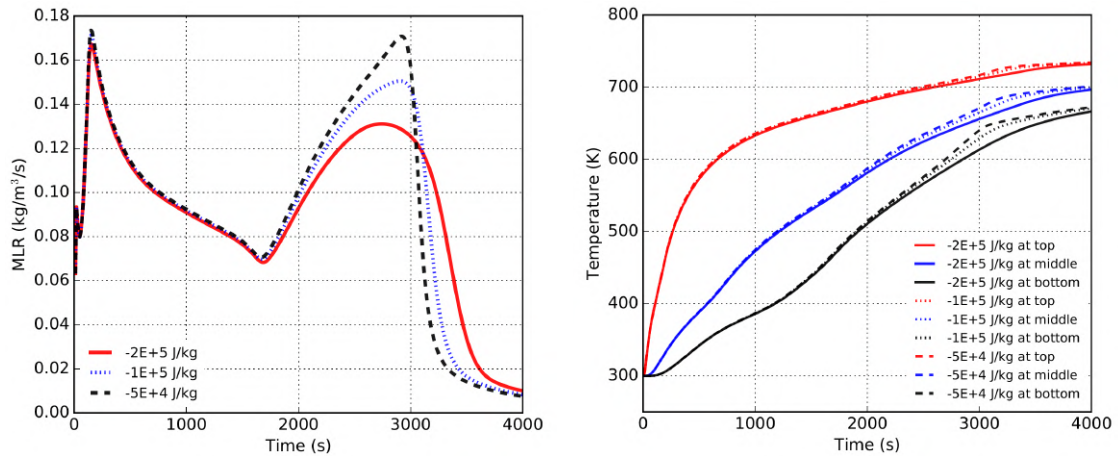


Fig. 7.7 Influence of decomposition heat factor on the mass loss rate and temperature evolution at heat flux of 20 kW/m<sup>2</sup>

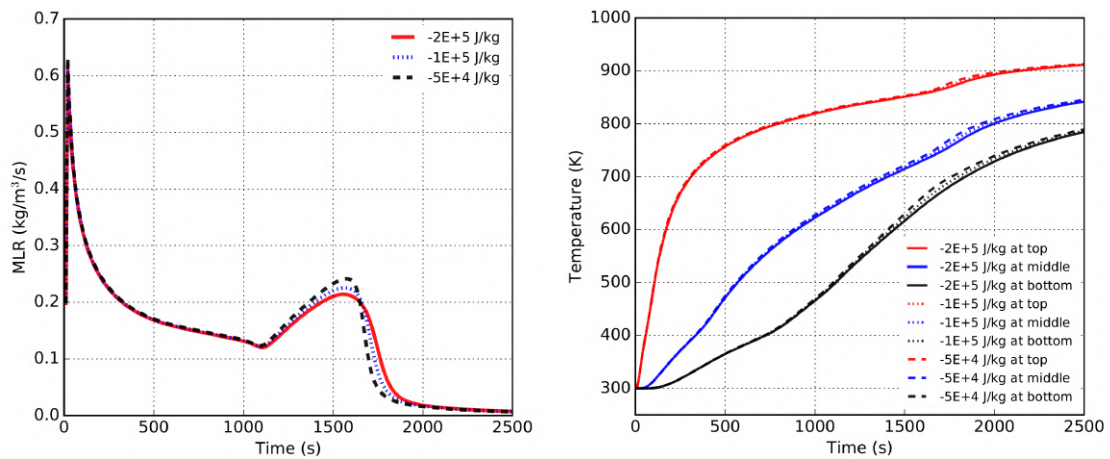


Fig. 7.8 Influence of decomposition heat factor on the mass loss rate and temperature evolution at heat flux of 50 kW/m<sup>2</sup>

It can be observed that the heat of thermal decomposition can involve a significant effect on the second peak of mass loss rate magnitude and its duration at both heat

fluxes. Higher intensity of mass loss rate and shorter duration of the second peak can present with lower energy absorption. The first peak of mass loss rate presents quite good similarities under different values of decomposition heat. This phenomenon can be explained by infinitely fast reactions occurring with a high heating rate and high temperature at the wood surface. This can also explain that more apparent influence can be found for the second peak of the reaction rate at  $20 \text{ kW/m}^2$  compared with the one at  $50 \text{ kW/m}^2$ , due to higher temperature distribution at higher heat flux to start the chemical reaction easily.

Again, no significant difference occurs by different heat of thermal decomposition. This can also be testified by a very good superposition for the first reaction peak at a high heat flux of  $50 \text{ kW/m}^2$ . Indeed, at the initial stage, the chemical reaction only occurs at the material surface. The pyrolysis process is limited by the heating process due to the fact that small heat is accumulated in a deep location and then, the heat is not sufficient to permit the pyrolysis reaction which means that the heat of decomposition has no influence. Conversely, in this study compared with a lower heat flux of  $20 \text{ kW/m}^2$ , the higher heat flux of  $50 \text{ kW/m}^2$  could lead to pyrolysis reaction of short time length. Thus, the effect of the heat of thermal decomposition on the initial pyrolysis stage can be neglected in this study. This can also explain the different evolution trends of temperature evolution at different in-depth locations. On the contrary, during the second peak of mass loss rate, the heating rate is smaller while a large amount of heat is accumulated by heat conduction along with the heat feedback of silicate thermal insulation. Strong pyrolysis reaction occurs due to a large mass fraction of remaining virgin material. Indeed, at this stage, the remaining mass can be a leading factor to contribute to the large second reaction peak. Therefore, the pyrolysis process is limited by chemical reaction and different heats of decomposition can give many serious differences at this location (near the material bottom surface) on the mass loss rate evolution and the corresponding temperature evolution. When comparing the different levels of influence on the reaction rate at different heat fluxes, similar observations can be obtained with a more serious impact on the temperature evolution

at lower heat flux. Indeed, the heat of decomposition represents the correlation of reaction and heat, more serious reaction means more heat is absorbed as a heat sink. Thus, the temperature is lower, this can be seen at approximately 3000 s concerning temperature evolution especially at 20 kW/m<sup>2</sup> in Figure 7.7.

To conclude this part, the pyrolysis stage at the second peak of the mass loss rate is highly sensitive to the heat of thermal decomposition. However, the pyrolysis stage prior to the second peak is insensitive to the heat of decomposition. Temperature evolution is slightly sensitive to the heat of decomposition only at the duration of the second peak, where strong reactions take place. The influence on the bottom location is more serious compared with the location of the top and middle. The pyrolysis case at lower heat flux is more sensitive to the heat of decomposition, while at higher heat flux, the influence is moderate. It can demonstrate that when conducting relevant pyrolysis studies, much more attention should be paid if they involve low-temperature environment.

## 7.2 Thermal and physical parameters influence

Thermal and physical parameters can reflect the heat and mass transfer behavior during the pyrolysis process. These parameters are mainly including virgin thermal conductivity (virgin  $\mathbf{k}$ ), char thermal conductivity (char  $\mathbf{k}$ ), virgin specific heat capacity (virgin  $c_p$ ), char specific heat capacity (char  $c_p$ ), virgin permeability (virgin  $\mathbf{K}$ ), char permeability (char  $\mathbf{K}$ ), emissivity ( $\varepsilon$ ), and absorptivity ( $\alpha$ ). The emissivity and absorptivity are assumed to be identical in this study.

The variation range of thermophysical parameters is mainly selected by the common practice used in the literature. For example, it is reported that some thermophysical parameters could vary by approximately 10% such as thermal conductivity and specific heat capacity [32, 74]. This variation value can also be found in [128, 126] due to the different uncertainty levels of related parameters and the variation range of 10% is commonly used for these studies. Thus, for specific heat capacity and thermal

conductivity, their values will be changed approximately in this study by minus or plus 10% of average nominal values to conduct the sensitivity analysis. Indeed, the thermophysical parameters are highly dependent on temperature, they can involve large differences concerning thermal conductivity and specific heat capacity [101].

The emissivity is the material surface properties representing the capacity of surface heat radiation to the ambient atmosphere. During the pyrolysis experiment, it is observed that the material surface can be relatively slow or fast to form a char layer. Indeed, at a low heating rate, the char formation process is quite slow. Thus, the virgin emissivity can have some influence due to it needs some time to convert to char. However, when under a high heating rate, the surface instantaneously presents a char layer, thus, the virgin emissivity can be reasonably neglected. For the two heat flux employed in this study, it is observed that even at the location of 4mm beneath the top surface of the material, the heating rate can attain more than approximately 150 K/min for both heat flux. Thus, the virgin emissivity can only have little influence just during the very short onset time. Furthermore, after this stage, all the emissivity is determined totally by char properties through the rest pyrolysis process in case of no in-depth radiation absorption reaching the virgin layer under the char layer. In this study, only the char properties are used. For the char emissivity, some reported values concern 0.88 [98] and 0.9 [55]. However, due to the uncertain properties, as discussed in the literature review [80, 81], a larger variation range is given, from 0.8 to 1.0.

For wood permeability, the reported values are  $7.5 \times 10^{-13} \text{ m}^2$  [98] and  $1.0 \times 10^{-14} \text{ m}^2$  [55]. Consequently, the variation range in this study is changing from  $1.0 \times 10^{-13} \text{ m}^2$  to  $1.0 \times 10^{-15} \text{ m}^2$  to increase a little more or less. For char permeability, the corresponding literature values are approximately with  $1.0 \times 10^{-11} \text{ m}^2$  [98, 55]. Similar with wood permeability, they are changed from  $1.0 \times 10^{-12} \text{ m}^2$  to  $1.0 \times 10^{-10} \text{ m}^2$ .

The corresponding thermal and physical parameters are collected in Table 7.2.

Table 7.2 The variation range of thermal and physical parameters for the sensitivity analysis

Parameters	Units	Lower values	Average values	Upper values
virgin $k$	W/m/K	90% $\times$ predicted	predicted	110% $\times$ predicted
char $k$	W/m/K	90% $\times$ predicted	predicted	110% $\times$ predicted
virgin $c_p$	J/kg/K	90% $\times$ predicted	predicted	110% $\times$ predicted
char $c_p$	J/kg/K	90% $\times$ predicted	predicted	110% $\times$ predicted
virgin $K$	m <sup>2</sup>	$1.0\times 10^{-15}$	$1.0\times 10^{-14}$	$1.0\times 10^{-13}$
char $K$	m <sup>2</sup>	$1.0\times 10^{-12}$	$1.0\times 10^{-11}$	$1.0\times 10^{-10}$
char $\varepsilon$	-	0.8	0.9	1.0

### 7.2.1 Virgin thermal conductivity influence

In this part, the sensitivity study to the virgin thermal conductivity is performed. Three sets of values are employed: lower value (90% of the average value), average value, and upper value (110% of the average value). Figure 7.9 and Figure 7.10 plot the mass loss rate and temperature evolution by the influence of virgin thermal conductivity at 20 kW/m<sup>2</sup> and 50 kW/m<sup>2</sup>.

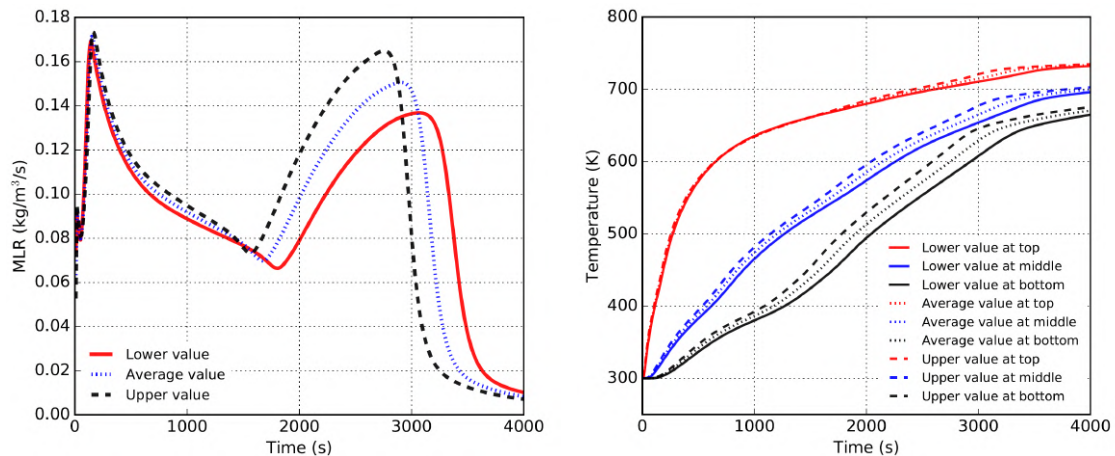


Fig. 7.9 Influence of virgin thermal conductivity on the mass loss rate and temperature evolution at heat flux of 20 kW/m<sup>2</sup>

When observing these figures, at both heat flux, the virgin thermal conductivity influences only the second peak of the mass loss rate. The onset and intermediate stage of pyrolysis reaction rate present relatively quite good similarities for each conductivity values. Then, higher virgin thermal conductivity can lead to a stronger reaction rate

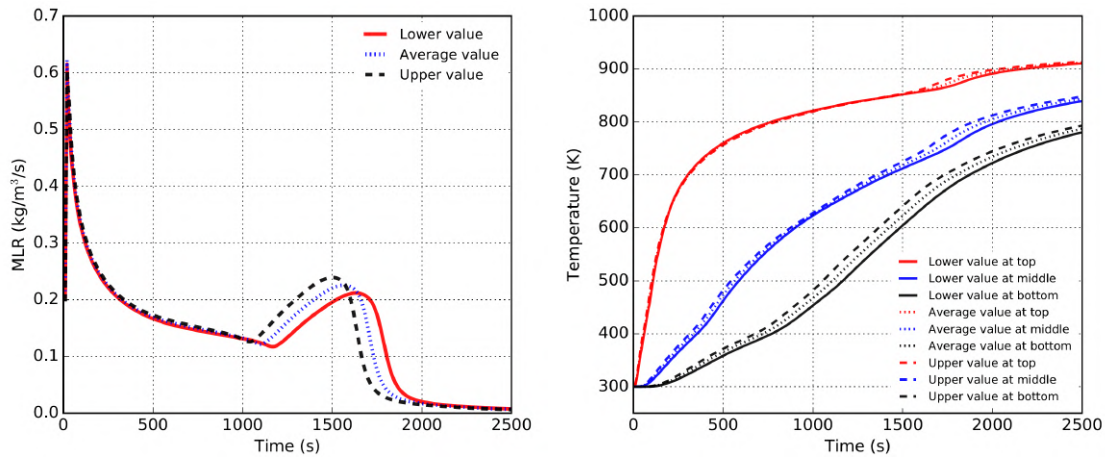


Fig. 7.10 Influence of virgin thermal conductivity on the mass loss rate and temperature evolution at heat flux of  $50 \text{ kW/m}^2$

and a shorter time to attain and finish the second peak. The temperature curves evolution shows the virgin thermal conductivity can influence the temperature evolution during the whole pyrolysis stage. Indeed, higher virgin thermal conductivity can lead to higher temperature profile and this influence is more predominant at the intermediate stage (from 1000 s to 3000 s at heat flux of  $20 \text{ kW/m}^2$ ). The bottom location gives the most differences under different virgin thermal conductivity. Comparing the difference of reaction rate and temperature evolution given by the different virgin thermal conductivity, higher influences occur for the lower heat flux of  $20 \text{ kW/m}^2$ .

Indeed, after the onset stage of the pyrolysis process, at the material surface, higher values of virgin thermal conductivity increase the amount of heat conducted in the depth of the solid. Thus, the pyrolysis zone can present higher intensity of reaction rate and higher temperature distribution. Similar to the influence of virgin thermal conductivity on the first peak of reaction rate, this influence on the temperature evolution at the top surface is also quite slight. Indeed, due to the high thermal diffusivity at the surface location, the effect of virgin thermal conductivity can be quite small. While for the bottom location, more heat is absorbed with higher virgin thermal conductivity and its difference leads to apparent different temperature evolution. This also explains the dominant role that the virgin thermal conductivity plays at lower heat flux.

To conclude this part, the mass loss rate and temperature evolutions show high sensitivity to the virgin thermal conductivity at lower and higher heat flux. For chemical reactions, the onset and intermediate stages of pyrolysis processes are not sensitive to the virgin thermal conductivity. However, during the pyrolysis stage of the second reaction rate peak, it exists strong correlations with the virgin thermal conductivity. The temperature at the bottom surface location is more sensitive to the virgin thermal conductivity than those on the top surface or middle location. Thus, it can be demonstrated that the virgin thermal conductivity is not important to study the material ignition behavior, even though this work doesn't account for the flame or oxidation.

### 7.2.2 Char thermal conductivity influence

For the sensitivity analysis of the char thermal conductivity, three sets of values are employed: lower value (90% of the average value), average value, and upper value (110% of the average value). Figure 7.11 and Figure 7.12 plot the mass loss rate and temperature evolution by the influence of char thermal conductivity at  $20 \text{ kW/m}^2$  and  $50 \text{ kW/m}^2$ .

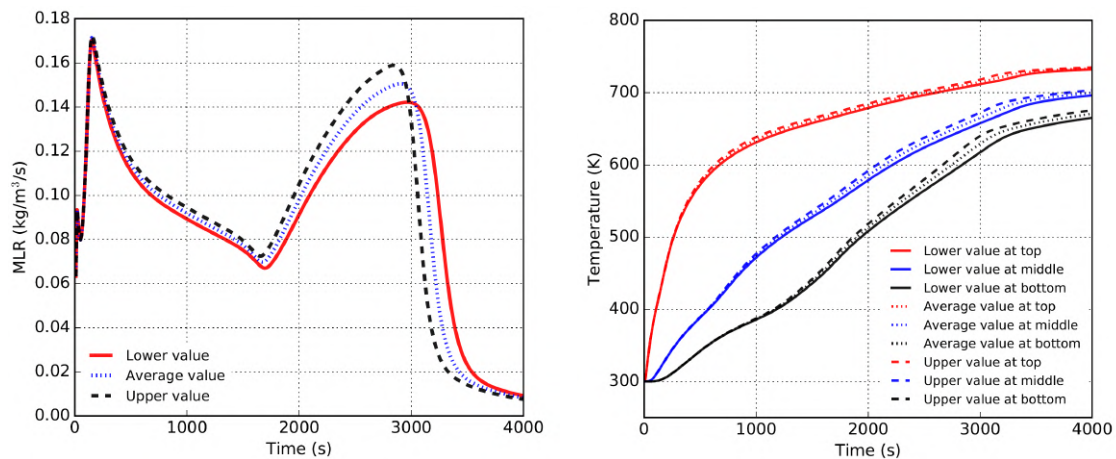


Fig. 7.11 Influence of char thermal conductivity on the mass loss rate and temperature evolution at heat flux of  $20 \text{ kW/m}^2$

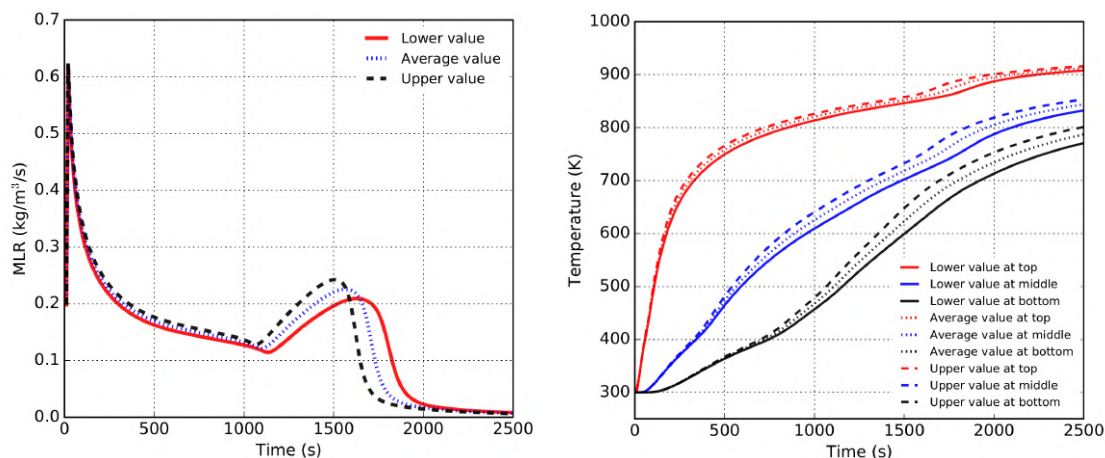


Fig. 7.12 Influence of char thermal conductivity on the mass loss rate and temperature evolution at heat flux of  $50 \text{ kW/m}^2$

Overall, similar influence concerning char and virgin thermal conductivity are observed on the mass loss rate and temperature evolution at lower and high heat flux. Due to the delay of the formation process from virgin to char, the influence of the char thermal conductivity on the initial stage can be ignored. It is shown for the first reaction peak for both heat flux. Indeed, the reaction at the surface needs some time to convert virgin to char. As virgin conductivity and density are higher than char ones, at this stage, the heat dissipation by the virgin material is the most important part. After the surface is completely converted to char, the difference of heat transportation inside the solid is dominated by char thermal conductivity, with small heat absorption involving small specific heat capacity. During the stage of the second peak of reaction rate, with a thick char layer at the surface, the temperature evolutions especially at the bottom location are more sensitive to the char thermal conductivity. This is due to the fact that the heat transported to the bottom through the char layer is controlled mostly by char thermal conductivity. It can be observed that the temperature evolution is more sensitive at higher heat flux when more heat is transferred, given the same difference of char thermal conductivity, especially for the temperature at the bottom location. Indeed for the experimental char residue mass fraction, at  $20 \text{ kW/m}^2$  it can account for approximately 30% while this value at  $50 \text{ kW/m}^2$  is approximately 20%.

The char density at higher heat flux is lower, less heat is dissipated, this can explain a more apparent difference of temperature.

To conclude, the pyrolysis process is quite sensitive to the char thermal conductivity, which is consistent with work [81]. Some similarities for virgin and char stage influence on the pyrolysis process can be present.

### 7.2.3 Virgin and char specific heat capacity influence

For the sensitivity analysis of the virgin and char specific heat capacity, three sets of values are employed: lower value (90% of the average value), average value, and upper value (110% of the average value). The influence of virgin specific heat capacity influence on mass loss rate and temperature evolution at 20 kW/m<sup>2</sup> and 50 kW/m<sup>2</sup> are shown in Figure 7.13 and Figure 7.14. Correspondingly, the char specific heat capacity influences are presented in Figure 7.15 and Figure 7.16.

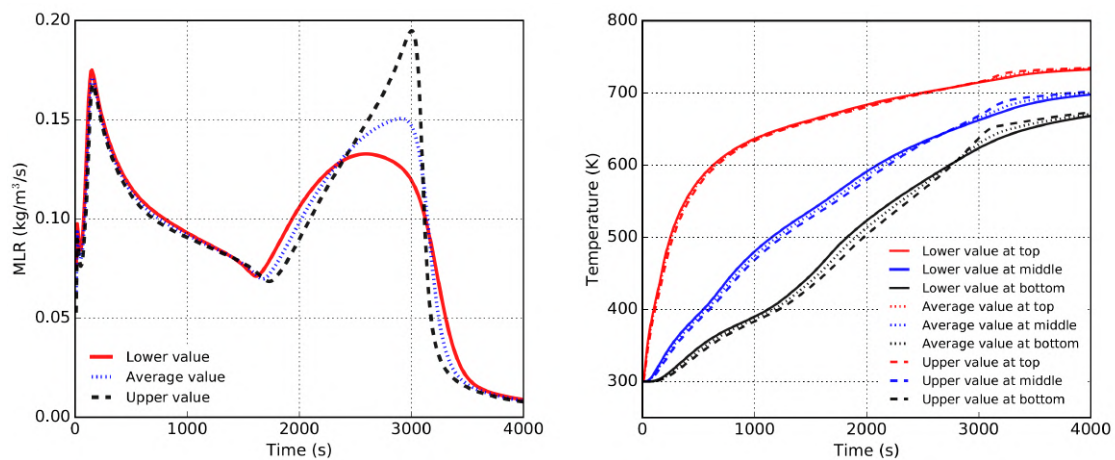


Fig. 7.13 Influence of virgin specific heat capacity on the mass loss rate and temperature evolution at heat flux of 20 kW/m<sup>2</sup>

It can be observed from these figures, before the occurrence of the second reaction peak of pyrolysis, relatively good similarities of mass loss rate under different virgin and char specific heat capacities. However, opposite influences are found concerning the stage on the second peak of the reaction rate. Indeed, for both virgin and char specific heat capacities, more predominant influence can be observed at the bottom

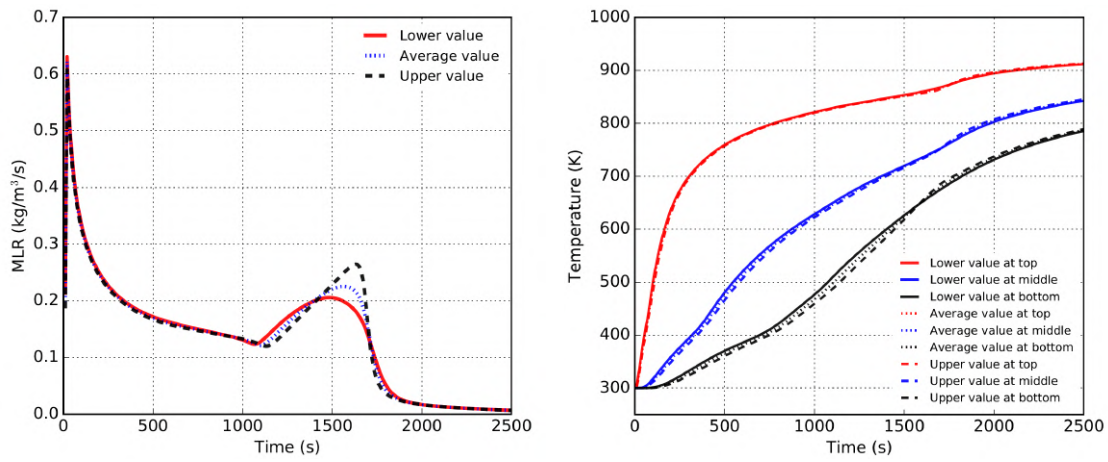


Fig. 7.14 Influence of virgin specific heat capacity on the mass loss rate and temperature evolution at heat flux of  $50 \text{ kW/m}^2$

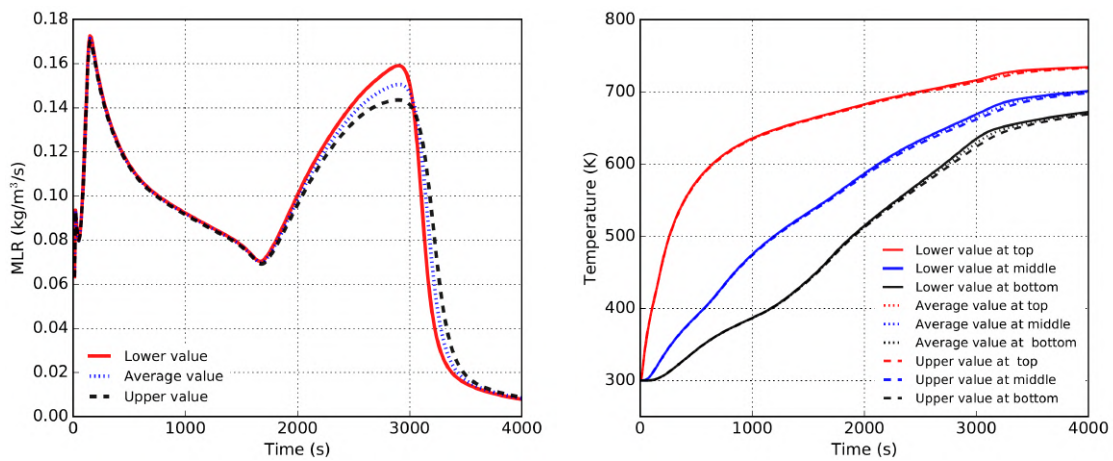


Fig. 7.15 Influence of char specific heat capacity on the mass loss rate and temperature evolution at heat flux of  $20 \text{ kW/m}^2$

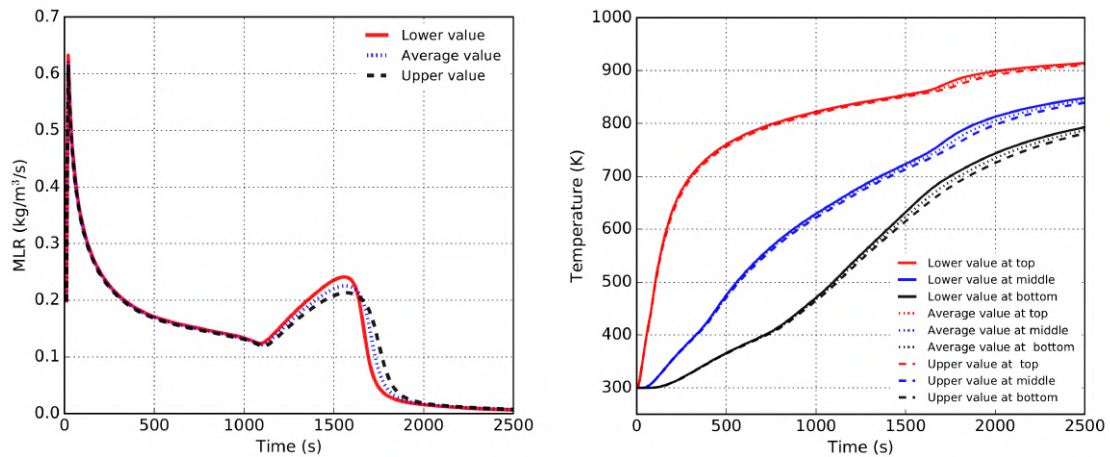


Fig. 7.16 Influence of char specific heat capacity on the mass loss rate and temperature evolution at heat flux of  $50 \text{ kW/m}^2$

location. Larger virgin specific heat capacity can lead to steeper and higher magnitude of the second peak of mass loss rate. While larger char specific heat capacity can induce smoother and lower magnitude of the second peak of mass loss rate. Regarding the temperature evolution which shows a slight difference with different values of virgin and char specific heat capacity, the virgin specific heat capacity tends to dominate the initial and intermediate stages, while the char specific heat capacity can affect more at the final stage.

Specific heat capacity displays the energy storage capacity during the energy transfer process and higher specific heat capacity can induce less energy transfer in the depth of the solid. However, at the onset stage of pyrolysis, the material surface heating rate is very high, enough energy can be absorbed very quickly and no difference tends to occur under different specific heat capacities. Therefore, the mass loss rate and temperature evolution involve negligible change under different specific heat capacities at this initial stage for both virgin and char specific heat capacities.

Lower specific heat capacity of char can speed up the heating process due to its smaller heat storage property and a larger amount of heat transfer to the interior sites. It can involve a stronger pyrolysis reaction at the interior sites with a steeper evolution trend and a higher magnitude of mass loss rate during the second peak. Conversely, during this same pyrolysis stage of the second peak of mass loss rate, the higher specific

heat capacity of virgin induce more heat absorption to storage. It can delay the time to attain the maximum reaction rate, with a a slow-moving trend of reaction rate variation. Then, the reaction rate quickly drops due to the fact that it has experienced a long reaction time and a small fraction of the remaining mass to react. Furthermore, this effect is less apparent at higher heat flux, which could be explained that enough heat can be given for virgin wood to absorb at higher heat flux and this process of heat absorption for higher heat flux situation is less important.

To conclude this part, the mass loss rate is sensitive to the virgin and char specific heat capacities during the second peak of the reaction rate and their influences are opposite. The temperature evolution at the initial pyrolysis stage is more sensitive to virgin specific heat capacity, while it is more sensitive to char specific heat capacity at the initial stage.

#### 7.2.4 Virgin and char permeability influence

For the sensitivity analysis of the virgin and char permeability, three sets of values are employed for virgin permeability:  $1.0 \times 10^{-15} \text{ m}^2$ ,  $1.0 \times 10^{-14} \text{ m}^2$ , and  $1.0 \times 10^{-13} \text{ m}^2$ , and three represents char permeability:  $1.0 \times 10^{-12} \text{ m}^2$ ,  $1.0 \times 10^{-11} \text{ m}^2$ , and  $1.0 \times 10^{-10} \text{ m}^2$ . The virgin permeability influence on the mass loss rate and the temperature evolution at  $20 \text{ kW/m}^2$  and  $50 \text{ kW/m}^2$  are shown in Figure 7.17 and Figure 7.18. Correspondingly, the char permeability influence is presented in Figure 7.19 and Figure 7.20.

The permeability influences the porous pressure and gas mass transfer according to Darcy's law. Thus, the mass loss profile can involve some variations under different permeability values. Three different virgin permeability values are investigated and quite good similarities are observed for the mass loss rate and the temperature evolution at different heat fluxes. The mass loss rate and the temperature evolution sensitivity to permeability can be negligible, in accordance with [36, 116]. This is reasonable because the pyrolysis gases only migrate to the top char surface after the occurrence of pyrolysis. Consequently, the virgin permeability has nearly no effect on mass loss rate

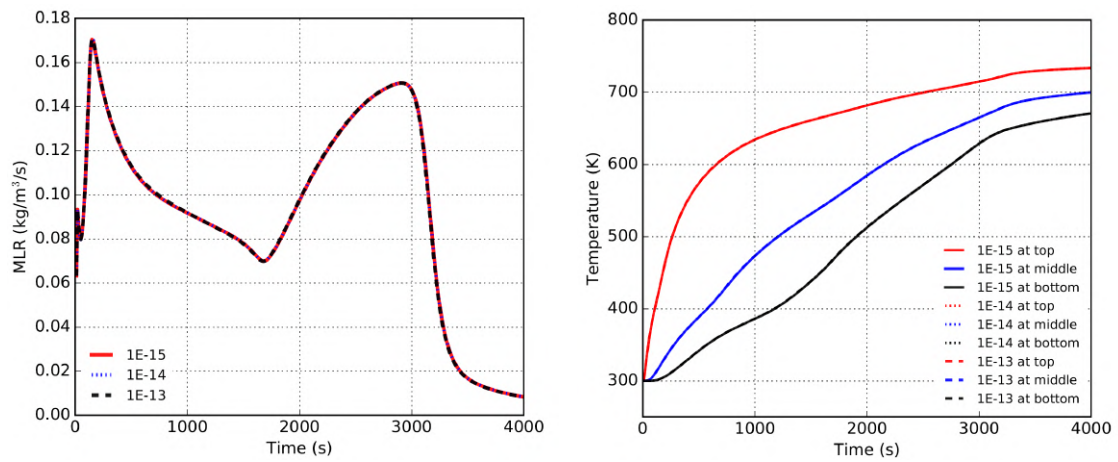


Fig. 7.17 Influence of virgin permeability on the mass loss rate and temperature evolution at heat flux of  $20 \text{ kW/m}^2$

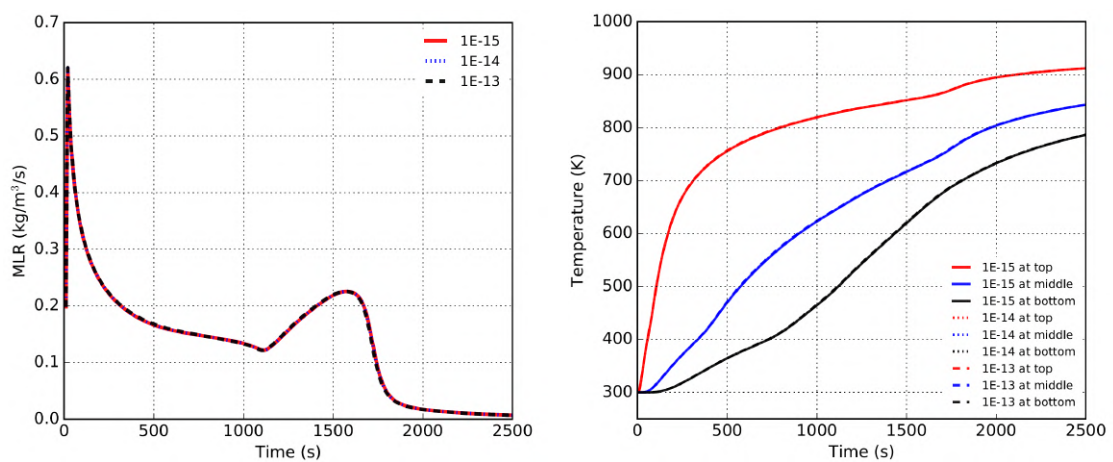


Fig. 7.18 Influence of virgin permeability on the mass loss rate and temperature evolution at heat flux of  $50 \text{ kW/m}^2$

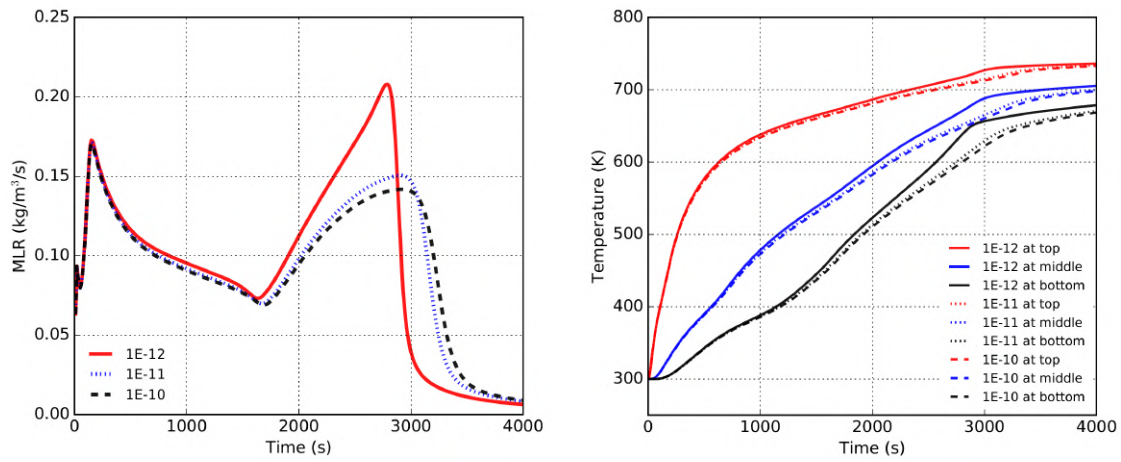


Fig. 7.19 Influence of char permeability on the mass loss rate and temperature evolution at heat flux of  $20 \text{ kW/m}^2$

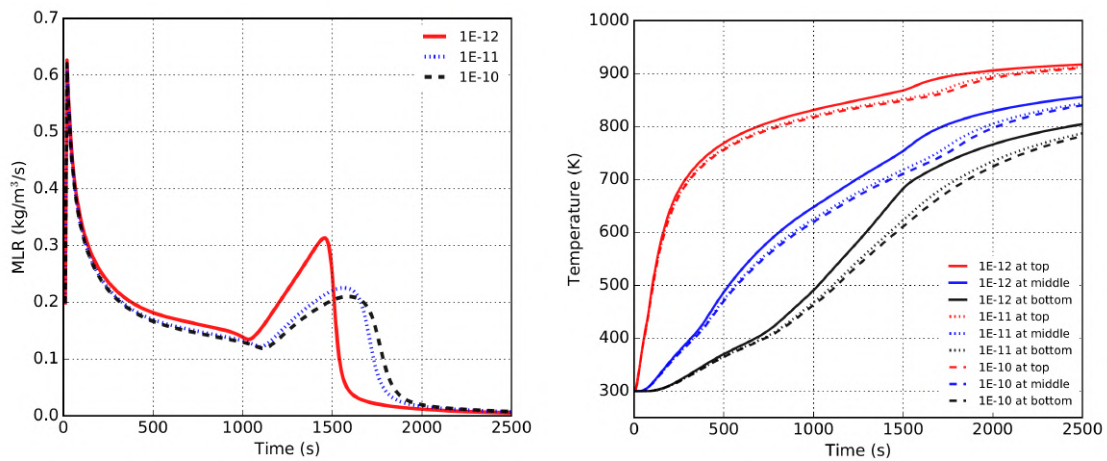


Fig. 7.20 Influence of char permeability on the mass loss rate and temperature evolution at heat flux of  $50 \text{ kW/m}^2$

and temperature evolution. However, the char permeability induces quite a serious difference for both mass loss rate and temperature evolution especially at the pyrolysis stage of the second peak of mass loss rate. Lower char permeability could lead to a higher magnitude of second mass loss rate with the presence of a steeper variation trend and a shorter time to reach the peak. Finally, the bottom location experiences a more serious difference compared with that of the top and middle locations.

During the pyrolysis process which transforms virgin solid to char, the gases are produced and migrate to the top surface of the material depending on permeability. At the initial stage, the pyrolysis occurs at the top surface of the material, the gas migration duration is very quick due to the short length scale and relatively larger char permeability. The effect of the char permeability variations is limited and no apparent difference of pyrolysis results can be observed. However, during the time of the second peak of mass loss rate, a smaller char permeability of given values can increase the pressure, and the pressure becomes more important at the bottom locations. The velocity could decrease which tend to induce less heat convection involving higher values of second peak of mass loss rate.

To conclude, the pyrolysis mass loss rate and temperature evolution are not sensitive to the virgin permeability. The mass loss rate and temperature evolution are more sensitive to char permeability at higher heat flux especially during the stage of the second peak of mass loss rate. The temperature of the bottom location is more sensitive to the char permeability compared with that of top and middle location. This could be one of the causes that the model doesn't capture very well temperatures and the end of the pyrolysis process. Indeed, especially for  $50 \text{ kW/m}^2$  as mentioned, serious cracks in the char structure have been observed and the in-depth radiation has not taken into account into the model. The char "apparent" permeability should change drastically due to their cracks, while in the model, the char permeability is keeping constant despite the char structure change.

### 7.2.5 Char emissivity influence

For the sensitivity analysis of the char emissivity, three values are employed: 0.8, 0.9, and 1.0. The influence of char emissivity influence on mass loss rate and temperature evolution at  $20 \text{ kW/m}^2$  and  $50 \text{ kW/m}^2$  are shown in Figure 7.21 and Figure 7.22.

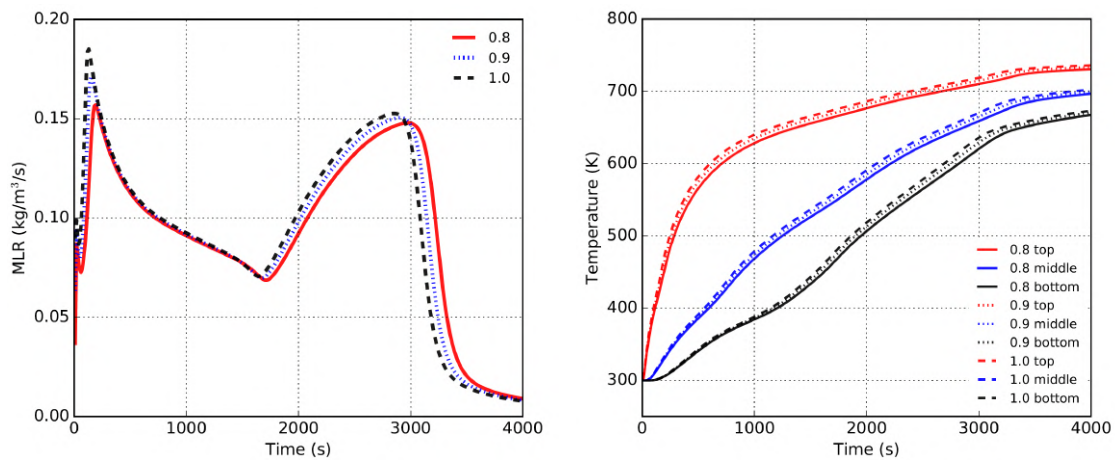


Fig. 7.21 Influence of char emissivity on the mass loss rate and temperature evolution at heat flux of  $20 \text{ kW/m}^2$

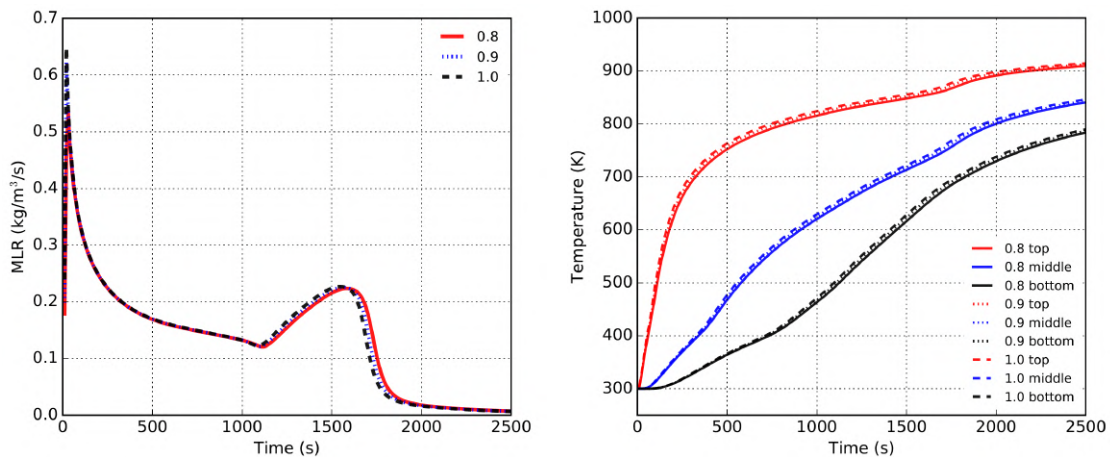


Fig. 7.22 Influence of char emissivity on the mass loss rate and temperature evolution at heat flux of  $50 \text{ kW/m}^2$

Figure 7.21 shows that lower char emissivity can lead to smaller mass loss rate magnitude, a longer time to the first and second reaction peak as well as smaller

temperature profile at lower heat flux. However, good similarities are observed at higher heat flux with respect to mass loss rate and temperature evolution with different values of char emissivity. Indeed, the char emissivity and absorptivity dominate the outer heating transport to the inner sites. At lower heat flux with low emissivity, the amount of absorbed heat is smaller while emitting relatively a large amount of energy. Thus, the mass loss rate and temperature value are smaller. Under higher heat flux, some compensation approximations can occur which can lead to smaller heat absorption as well as a smaller amount of heat emitted with smaller char emissivity and absorptivity, and no apparent difference occurs. To conclude, the char emissivity is a more important factor to the pyrolysis cases at lower heat flux.

### 7.3 Boundary parameters influence

As discussed earlier, the 1D simulation is chosen and only the heat convection coefficient of the material top surface is considered. The variation of these boundary condition parameters is in accordance with our experimental results regarding the inverse analysis with Aluminum heat conduction shown in Chapter 5. Different convective parameters at the top surface are used to fit its temperature evolution curve. The variation range is based on these parameters uncertainty, specifically in our experimental configuration. These values can be more or less correct to predict the heating of Aluminum, thus a large variation level is not considered. Three values of 0, 3 and 5 W/m<sup>2</sup>/K are tested, it is estimated that 3 W/m<sup>2</sup>/K is the best one to represent the experimental curve.

The influence of heat convection coefficient  $h_{top}$  on the mass loss rate and the temperature evolution at 20 kW/m<sup>2</sup> and 50 kW/m<sup>2</sup> are shown in Figure 7.23 and Figure 7.24, respectively. Under different values of  $h_{top}$ , the mass loss rate and temperature evolution at 50 kW/m<sup>2</sup> show a slight difference. For the case at 20 kW/m<sup>2</sup>, the  $h_{top}$  can influence both the first peak and the second peaks of the mass loss rate. Smaller values can lead to a higher magnitude of the first and the second peaks as well as reducing

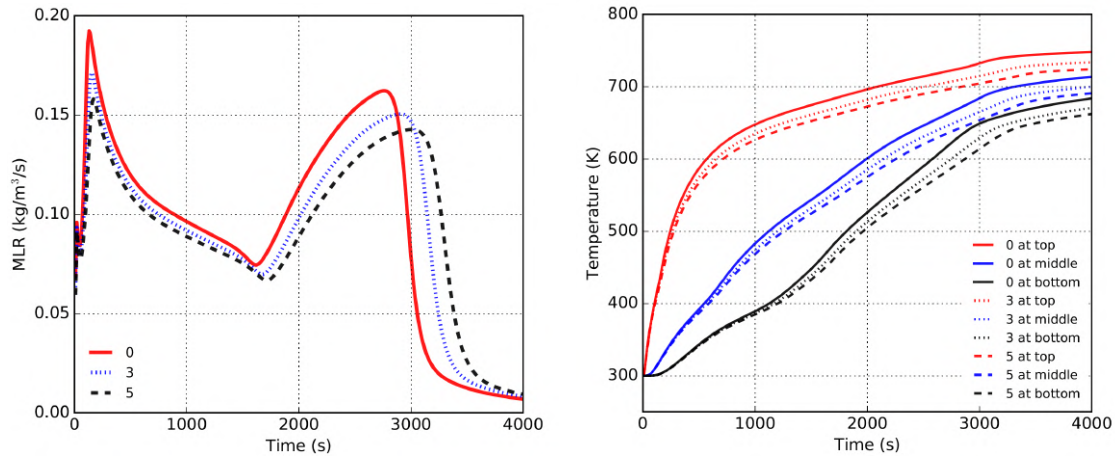


Fig. 7.23 Influence of heat convection on the mass loss rate and temperature evolution at heat flux of  $20 \text{ kW/m}^2$

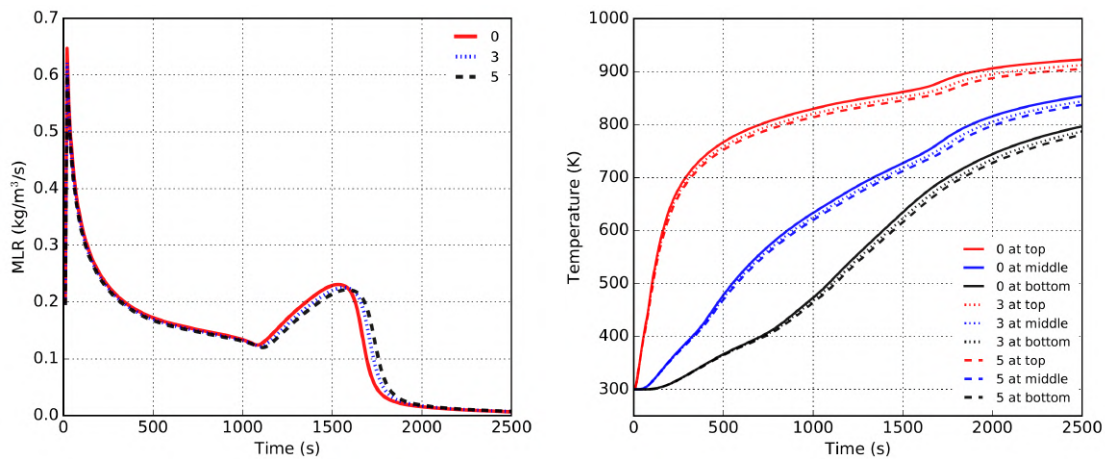


Fig. 7.24 Influence of heat convection on the mass loss rate and temperature evolution at heat flux of  $50 \text{ kW/m}^2$

the time to the second peak. The temperature at the start in different locations shows good similarities under different values of  $h_{top}$ , while at the next pyrolysis stages, the temperature at different locations presents some differences. These differences seem to be homogeneous for the three locations.

Indeed, with a lower ambient temperature, the convective heat loss at the top surface can influence a part of the heat that is not conducted inside the condensed phase. At higher heat flux, the top surface absorbs more heat, thus the convective heat loss under different convection coefficients are small compared with those absorbed largely under high heat flux. However, for lower heat flux, this portion of convective heat loss can account for a large amount of heat absorbed at this lower heat flux. It can show more serious influence on the lower heat flux, while it has slight influence on higher heat flux. To conclude, the mass loss rate and temperature evolution are sensitive to the  $h_{top}$  at lower heat flux while they are insensitive at higher heat flux. In real fire when flame occurs, the heat convection at the surface of the solid still a challenge for modeling. Indeed, to capture such phenomenon correctly very fine mesh is needed or a specific well-defined model applicable with a coarse mesh. The sensitivity of convection on pyrolysis process point out in this study demonstrate that we should make effort to develop an appropriate model to capture the convection process especially at ignition or extinction time where this process should be dominant as demonstrate here because of strong impact when heat fluxes involves are low.

## 7.4 Water content influence

This part is focused on the moisture content uncertainty. The reason why we study unreliable water content in wood is that water plays an important role in pyrolysis, as we have already discussed concerning the pyrolysis of wet wood and dry wood in Chapter 6. However, the way the water content influence under different heating scenarios is not clear. The following part will study the wood pyrolysis behavior containing different water content.

For wood water content in Fir wood, the variation values are based on our water evaporation experiments. As shown in Chapter 5, the moisture content is estimated with an average of 10% and the experimental final water release is approximately from 8% to 12%. Thus, these three values will be used.

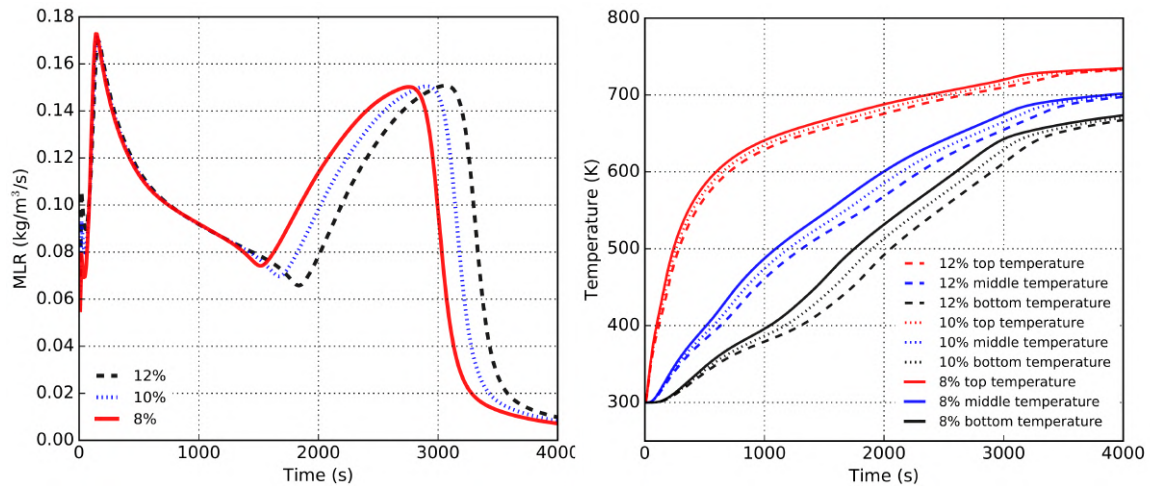


Fig. 7.25 Influence of water content on the mass loss rate and temperature evolution at heat flux of  $20 \text{ kW/m}^2$

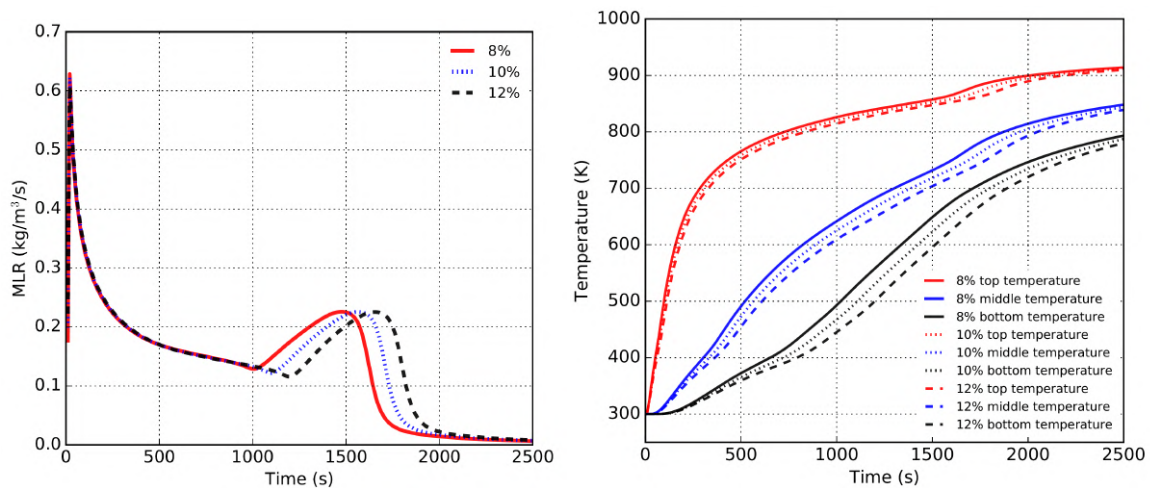


Fig. 7.26 Influence of water content on the mass loss rate and temperature evolution at heat flux of  $50 \text{ kW/m}^2$

The influence of water content on the mass loss rate and temperature evolution at  $20 \text{ kW/m}^2$  and  $20 \text{ kW/m}^2$  are shown in Figure 7.25 and Figure 7.26, respectively. At  $20 \text{ kW/m}^2$ , the water reaction peak occurs and a smaller water mass fraction can

lead to smaller intensity of this water reaction peak. For the two heat fluxes, the first pyrolysis mass loss rate peak involves relatively good similarities with different water mass fractions. At both lower and higher heat flux, lower water mass fraction in wood can lead to a shorter time to the second peak as well as a higher magnitude of mass loss rate. Consequently, water content plays a significant role in the temperature evolution during the whole pyrolysis process. Furthermore, a smaller water fraction can induce higher temperature profiles and the more serious effects occur at the bottom location.

Water evaporation is an endothermic reaction. On the top material surface and at the initial stage of pyrolysis, the water evaporation process is infinitely fast and the temperature is very high. Consequently, the influence of the endothermic reaction is limited at this place. However, after this initial pyrolysis stage, the heating rate inside the material is smaller and the temperature is lower. Thus, the water evaporation endothermic reaction effects are predominant in the pyrolysis reaction. To conclude, the mass loss rate especially at the second peak of pyrolysis reaction is sensitive to the water fraction. The temperature evolution is sensitive to the water fraction through the whole pyrolysis process.

## 7.5 Conclusion

To conclude, many unreliable parameters are involved in pyrolysis modeling implementation. As we have shown in the previous chapters, these parameters are highly coupled into the overall pyrolysis behavior. Again, these unreliable parameters can affect differently, at different time or length scales, the pyrolysis process. This part permits to explore the influence of these parameters and give us more knowledge about how and which parameters can have more effect on the pyrolysis results, such as mass loss rate or temperature evolutions. The kinetic parameters are more important to chemical reaction prediction while for temperature prediction they are not sensitive. The mass loss rate is highly sensitive to the heat of decomposition. Both mass loss rate and temperature evolution are sensitive to virgin and char thermal conductivity.

For virgin and char specific heat capacity, they are more important at lower heat flux. The mass loss rate and temperature evolution are sensitive to char permeability and insensitive to virgin permeability. The water content can be more important to the material surface at the initial time thus for the material ignition study, this water effect should be noticed. Again, the water content can influence the temperature evolution through the whole pyrolysis process for different heat flux, but this influence on the top surface at high heat flux can be negligible.

In the future, this water content should be put much emphasis, especially when conducting some experiments at low heating environment. Similar to water content, the char emissivity is more important in a lower heating environment and much attention should be paid to determine this value. Char thermal conductivity is more important than char specific heat capacity, but the char is quite uncertain and fragile with a highly changing properties evolution. This is still a challenge to capture this aspect and future studies should be given. Boundary heat convective coefficient is more important in the low heating environment, however, these values are usually estimated dependent on experimental conditions. In the future, this part should be highly experimentally or numerically solved in order to know the correct heating loss circumstance at the ambient environment.

# Chapter 8

## Conclusion and perspective

### 8.1 Conclusion

Natural or synthetic composite materials are used widely in different applications. However, they are involved with high fire risks. Then, one actual large challenge is to improve their fire safety properties, consisting of fire resistance and reaction to fire. When considering the action of these materials during a fire, the thermal decomposition step is very important and has to be understood and described with specific attention. Indeed, a solid has a huge influence on the ignition, fire growth, flame characteristics and propagation, extinction, etc. In this sense, many studies are conducted in past years in the fire safety research community in order to develop performant models of pyrolysis. These studies associate experimental and numerical investigations at different scales.

In this context, the present thesis aims to study the pyrolysis of two different composite materials in order to better understand the thermal decomposition process and to give data required for the PATO model development and validation. The first material is wood while the second one is carbon fiber/epoxy resin composite. Wood is chosen because it is a kind of isotropic composite material while carbon/epoxy is chosen because it is a kind of non-isotropic material. To study the whole pyrolysis process, the up-scaling method is used to first study the aspects separately in a detailed

scale (kinetic, heat and mass transfer, porosity, etc.), and secondly, these aspects are coupled on a larger scale to study the interactions. Then, during this work, two scales are used: the particle scale TGA (thermally thin) and bench-scale cone calorimeter scale (thermally thick). Furthermore, to validate the model more accurately in a first approach and to avoid the uncertainties due to poorly controlled boundary conditions (formed by flame or oxidation), the experimental manipulations are conducted under an inert atmosphere for both scales.

The comprehensive pyrolysis model PATO is dealing with heat and mass transfers into porous media and involves chemical reactions. It contains different solid phases and one single gas phase. The different components within composite materials are separated which involve their own intrinsic chemical and physical properties. The local thermal equilibrium is considered between the gas volatiles and solid phase, and they are implemented based on the volume averaging method. Different numbers of parallel reactions are defined for each component and they are finally integrated to implement the overall material pyrolysis behavior. This developed 3D model describes the gas transport within the pores of materials at the Darcy scale. Thermal conductivity is formulated in a tensor form allowing the definition of heat transfer in three directions of the domain. The radiation boundary conditions concerning fire scenarios are added to the model, and it is expected to be an alternative applicable comprehensive pyrolysis model to provide potential prediction accuracy when evaluating the current pyrolysis models in the fire safety community.

The thermal decomposition of wood has been studied using a TGA apparatus. From the evolution of the mass loss and the mass loss rate curves, two mechanisms (one-step and multi-step parallel reactions) of thermal decomposition have been proposed to assess their predictability. The kinetic parameters are predicted to implement the chemical reactions by modeling fitting method with TGA experiment which is described with the Arrhenius-type equation through different time scales. The multi-step parallel reaction scheme fits quite well the mass loss and the MLR, while the one-step global reaction scheme doesn't capture well the MLR peak value and the temperature range

at which the pyrolysis reaction occurs. It seems to approve that the kinetics are not predicted qualitatively well with the one-step global reaction scheme compared with the parallel one. However, from a macroscopic view, targeting experimental and numerical mass loss profile, the one-step global mechanism succeeds to represent the overall pyrolysis trend, such mechanism could be applicable to describe the pyrolysis process when a fire is fully developed.

To analyze the assumption of no presence of heat and mass gradient in the sample during the TGA experiment, a 0D (zero-gradient model) and 2D axis-symmetry (gradient model) simulations have been compared. For both simulations, no significant difference has been identified. The influence of the heating rate on the pyrolysis process has been analyzed. It is demonstrated that only the peak of reaction rate shifts to a higher temperature range when the heating rate increases. We conclude that for a mass fraction of the virgin wood material more than 50 wt%, the kinetic process is governed by the heating process. When it comes to less than 50 wt% of virgin mass fraction, the remaining mass becomes the limited parameter on the overall reaction process. The heating process can interact with the global pyrolysis process and each reaction is not affected in the same way by the heating process. Only the cellulose thermal decomposition reaction seems to be affected by the heating rate, while the reactions of hemicellulose and lignin are not affected. Moreover, the lignin decomposition can produce the largest mass fraction of char residue at the end of the pyrolysis process, and this char residue doesn't change with heating rate. However, the heating process changes the mass fraction of char residue given by the cellulose and hemicellulose reactions. As the heating process plays an important role in the thermal decomposition, 2D simulations have been conducted to analyze the possible thermal gradients into the solid in TGA configuration at 50 K/min. It is demonstrated that heat and mass transfer interact with pyrolysis reactions in TGA when the global heating rate is high. These interactions need to be correctly captured by the model to describe correctly the overall pyrolysis process.

In order to explore the pyrolysis behavior at different thermal conditions, a bench-scale cone calorimeter under a controlled atmosphere with nitrogen has been introduced accompanied by a silicate sample holder for thermal insulation. The numerical models are implemented to study the pyrolysis processes at different time and length scales under 1D and 2D. The sensitivity of mesh size and time steps on numerical results are verified, it has been demonstrated that the heat transfer process is far less sensitive to mesh size and time steps compared with the chemistry process. The convective heat coefficients are extracted by inverse analysis with pure heat conduction of Aluminum and a set of heat convection coefficients are assigned for model prediction. The thermal parameters of wood are obtained based on dry wood pure heat conduction experiments. The thermophysical properties, i.e., specific heat capacity and thermal conductivity of wood, are estimated similarly by inverse analysis. To verify if the char matrix and the associated thermal parameters are or not highly dependent on heat flux conducted, an inverse analysis to obtain char thermal parameters is conducted with the char pure heat conduction. The experiments for temperature evolution are found to be predicted with accuracy under  $20 \text{ kW/m}^2$ . When subjected to the high heat flux of  $50 \text{ kW/m}^2$ , the experiments can involve serious scatter compared with prediction and they are quite unreliable compared with reality, and they are not appropriate to predict the pyrolysis process under  $50 \text{ kW/m}^2$ . It is demonstrated that in-depth radiation is a key process under  $50 \text{ kW/m}^2$ , and the char conductivity extracted is an “apparent” value. We conclude that the char data from the inverse analysis under lower heat flux is preferable.

The 1D and 2D models are matching up quite well for the top locations and the difference is increased for the bottom temperature. It is pointed out that the role of insulating silicate material is very important which can give a better prediction of mass loss and temperature profile by the 2D model, and this “side effect” tends to be increased in the slow heating process. It is demonstrated that water evaporation involves a relatively slow rate for the bottom location and the water could prolong the pyrolysis severely. It is found that the final char yield fraction and temperature concerning wet

wood and dry wood pyrolysis behave similarly and no apparent differences are involved. Then, the water only tends to delay the pyrolysis process and the corresponding reaction peak or temperature rise is then influenced. It is demonstrated that the difference of MLR between dry and wet cases is enhanced at low heat flux and the temperature difference between dry and wet wood increases with the thickness. For low heat flux, the reaction rate and the pyrolysis advancement are slow with a thick pyrolysis layer accompanied by a smaller temperature gradient. While for high heat flux, it is involved with a thin pyrolysis layer with a high-temperature gradient. Globally, the predicted char depth matches reasonably well the experiment at  $20 \text{ kW/m}^2$  while it is over-predicted at  $50 \text{ kW/m}^2$  except for the initial stage of pyrolysis

Similar to wood experimental manipulation, the modeling of thermal decomposition of the carbon/epoxy composite is conducted firstly at the TGA scale and secondly at the cone calorimeter scale. A parallel mechanism of thermal decomposition has been employed and the associated kinetic parameters have been validated at the TGA scale by comparison with the experimental data. The experimental char yield mass fraction in this work contributes to the general observation which involves less char residue at a high heating rate. The kinetic parameters extracted could reflect the pyrolysis reaction behavior for the different heating processes. The evaluation of the model to represent the thermal decomposition of the carbon/epoxy composite is conducted addressing the mass loss, the mass loss rate, and the temperature profiles at different locations. The occurrence and the termination of the pyrolysis process are captured well by the model, but the magnitude of the mass loss rate peak is over-predicted compared with the experiment for both heat fluxes. The prediction at lower heat flux seems to be better when targeting the temperature evolution and the delamination and cracking are responsible for these discrepancies. It is demonstrated that serious delamination occurs at different locations through the thickness of the composite under different heat fluxes. In order to explore the non-isotropic thermal conductivity of carbon/epoxy composite, the values are tackled by tensor changing along with different directions under 3D. 1D and 3D modeling are compared, the mass loss and temperature account

for nearly the same variation trend which concludes that the isotropic assumption can be appropriate regarding the simulation of thermal decomposition of carbon/epoxy composite.

Many input parameters are involved during this modeling study. The more input parameters are used in the model, the higher uncertainties can be observed. Thus, a sensitivity analysis is conducted to explore how these parameters are linked to the pyrolysis behavior and which ones are more uncertain. The OAT method is employed to analyze the sensitivity of relevant pyrolysis model parameters, they are including kinetics, the heat of decomposition, thermal, and physical parameters. To point out the different key parameters involved and to investigate their role in these interactions, sensitivity analysis of the mass loss rate and temperature evolution at different locations is conducted. It is found that the mass loss rate is quite sensitive to the kinetic parameters (activation energy, pre-exponential factor, and reaction order), and this influence is stronger at lower heat flux, while the temperature evolution is slightly sensitive to the activation energy. A similar influence is observed with the heat of thermal decomposition compared with those kinetic parameters, and the bottom location is more influenced. Similar influences are found concerning virgin and char thermal conductivity, and their influence on the bottom location is more serious. Virgin and char specific heat capacity has some influence on different pyrolysis stages. It is found that the char emissivity is more important in a lower heating environment and much attention should be paid to determine this value. The virgin permeability has no influence can be concluded, while char permeability could pose some effect especially at high heat flux environment and bottom location. Heat convection coefficient is found more important at lower heat flux. The temperature evolution is quite sensitive to the water content through the whole pyrolysis process, and it can be more important to the material surface at the initial time, thus, for the material ignition study, this water effect should be noticed.

Finally, the results obtained show that the PATO model involves good capabilities to provide a relatively accurate prediction for the pyrolysis behavior of different

composite materials under different heating environment. The present work gives new insights when manipulating numerical studies for pyrolysis especially coupling the complexity of physical phenomenon in fire scenarios.

## 8.2 Perspective

In this work, the released gas during the pyrolysis process is tabulated with Nitrogen, the volatile gas reactions concerned are neglected, and the energy is mainly from heat conduction and pyrolysis in the condensed phase. Thus in the future, more complicated options should be adopted such as equilibrium elemental conservation and finite species conservation to capture the evolution of the specific pyrolysis gases composition and corresponding element/species transfer. Moreover, this study focused on an anaerobic environment concerning the chemical and thermophysical process, thus the kinetics and thermophysical process under a realistic air environment should be continuously described, which needs to consider oxidation and flame. And the capability of the model prediction needs to be evaluated under more detailed boundary conditions. In such case, based on a bench-scale in this study, a larger scale experiment and corresponding modeling study should be performed.

Due to the fact that the thermal conductivity of carbon/epoxy composite along the fibers is much higher than in other directions, thus, it is reasonably correct to suppose that the temperature distribution is uniform for the horizontal cross-section direction. In this study, the top surface is parallel to the cone heater which is assumed as a 1D experimental configuration, However, when the sample is subjected to irradiant heat flux at different directions in a real fire scenario, it is expected to behave quite differently regarding the non-isotropic thermal conductivity. This behavior influence on relevant modeling studies concerning different boundary configurations can be explored.

As demonstrated, the char thermal conductivity is more important than char specific heat capacity, but the char is quite uncertain and fragile with highly changing properties during pyrolysis reaction. This is still a challenge to capture this aspect and

future studies should be given more concentration. As shown, at high heat fluxes, the char heat conduction is dominated by in-depth radiation due to large cracks presence, thus the in-depth radiation factor should be included in the modeling study. The boundary heat convective coefficient is more important in the low heating environment, however, these values are usually estimated with less accuracy. In the future, this part should be highly experimentally or numerically solved to know the accurate heating loss circumstance in the ambient environment.

The local thermal equilibrium between the solid and gas phase is assumed in the present work with no heat exchange between gas in the pore and the solid. For example, the water evaporation process which involves a highly endothermic reaction, and local thermal equilibrium cannot be correct and this assumption could be developed to be more realistic for a non-local thermal equilibrium case in the future.

This work doesn't take into account the shrinkage, swelling, cracks, and delamination during the pyrolysis process. The physical structure change could lead to serious influences on the pyrolysis results. Thus, the modeling of the physical structure change implementation is still challenging work. One of the most complicated numerical manipulations concerning shrinkage and swelling to account for the physical structure change would be inherited to the model and some validation work is expected to be conducted.

In this work, the parallel reaction scheme is employed. As found in this study, one of the most important drawbacks of a parallel reaction mechanism is that it doesn't take into account the heating rate into the chemical reaction when the heating condition is a key parameter on the pyrolysis process, and it fails to predict the final residual mass fraction making this mechanism inconsistent in terms of mass conservation. It has been shown that it is especially applicable for conditions when the reaction is slow compared to the heat transfer process because slow reactions are very sensitive to kinetic parameters. The highest heating rates are involved at the beginning of the pyrolysis process as well as the highest gradient of heating rates. During this beginning stage, the pyrolysis gases are released governing the ignition process when

---

the thermal decomposition is involved in air. Then, to capture correctly ignition process, the pyrolysis model should describe correctly those first stages when heating and gradients are high. As a perspective of this study, the heating process should be taken into account carefully in the chemical mechanism, with competitive and consecutive reactions. Such mechanisms would allow defining some prior reactions pathway in function of the heating process.

Finally, the condensed phase pyrolysis model is expected to be coupled with the gas phase flame model to predict the real fire behaviors in the air atmosphere.



# References

- [1] Chittaranjan Deo and SK Acharya. Effect of moisture absorption on mechanical properties of chopped natural fiber reinforced epoxy composite. *Journal of reinforced plastics and composites*, 29(16):2513–2521, 2010.
- [2] Shurong Wang, Gongxin Dai, Haiping Yang, and Zhongyang Luo. Lignocellulosic biomass pyrolysis mechanism: a state-of-the-art review. *Progress in Energy and Combustion Science*, 62:33–86, 2017.
- [3] Yanming Ding, Ofodike A Ezekoye, Shouxiang Lu, and Changjian Wang. Thermal degradation of beech wood with thermogravimetry/fourier transform infrared analysis. *Energy Conversion and Management*, 120:370–377, 2016.
- [4] Izabella Vermesi, Matthew J DiDomizio, Franz Richter, Elizabeth J Weckman, and Guillermo Rein. Pyrolysis and spontaneous ignition of wood under transient irradiation: Experiments and a-priori predictions. *Fire safety journal*, 91:218–225, 2017.
- [5] N Grange, K Chetehouna, N Gascoin, A Coppalle, I Reynaud, and S Senave. One-dimensional pyrolysis of carbon based composite materials using firefoam. *Fire Safety Journal*, 97:66–75, 2018.
- [6] Robert Clive Easby. *Fire behaviour of pultruded composites*. PhD thesis, Newcastle University, 2007.
- [7] Maxime Villière, Damien Lecointe, Vincent Sobotka, Nicolas Boyard, and Didier Delaunay. Experimental determination and modeling of thermal conductivity tensor of carbon/epoxy composite. *Composites Part A: Applied Science and Manufacturing*, 46:60–68, 2013.
- [8] Matthew T McGurn. *Numerical Modeling and Simulation of Flame Spread Over Charring Materials*. PhD thesis, State University of New York at Buffalo, 2013.
- [9] Matthew T McGurn, Paul E DesJardin, and Amanda B Dodd. Numerical simulation of expansion and charring of carbon-epoxy laminates in fire environments. *International Journal of Heat and Mass Transfer*, 55(1-3):272–281, 2012.
- [10] Mark McKinnon. *A generalized methodology to characterize composite materials for pyrolysis models*. PhD thesis, 2016.
- [11] Anna Matala et al. *Methods and applications of pyrolysis modelling for polymeric materials*. VTT Technical Research Centre of Finland, 2013.

- 
- [12] Isaac T Leventon, Kevin T Korver, and Stanislav I Stoliarov. A generalized model of flame to surface heat feedback for laminar wall flames. *Combustion and Flame*, 179:338–353, 2017.
- [13] Deborah DL Chung and Deborah Chung. *Carbon fiber composites*. Elsevier, 2012.
- [14] N Burger, A Laachachi, M Ferriol, M Lutz, V Toniazzo, and D Ruch. Review of thermal conductivity in composites: mechanisms, parameters and theory. *Progress in Polymer Science*, 61:1–28, 2016.
- [15] Kai Dong, Kui Liu, Qian Zhang, Bohong Gu, and Baozhong Sun. Experimental and numerical analyses on the thermal conductive behaviors of carbon fiber/epoxy plain woven composites. *International Journal of Heat and Mass Transfer*, 102:501–517, 2016.
- [16] Yue Liu, Bernd Zwingmann, and Mike Schlaich. Carbon fiber reinforced polymer for cable structures—a review. *Polymers*, 7(10):2078–2099, 2015.
- [17] Duy Quang Dao, Thomas Rogaume, Jocelyn Luche, Frank Richard, Lucas Bustamante Valencia, and Sindonie Ruban. Thermal degradation of epoxy resin/carbon fiber composites: Influence of carbon fiber fraction on the fire reaction properties and on the gaseous species release. *Fire and Materials*, 40(1):27–47, 2016.
- [18] Ziqing Yu. *Thermal and mechanical responses of fiber reinforced polymer composites under one-sided fire exposure*. PhD thesis, 2012.
- [19] Tian Tian and Kevin D Cole. Anisotropic thermal conductivity measurement of carbon-fiber/epoxy composite materials. *International Journal of Heat and Mass Transfer*, 55(23-24):6530–6537, 2012.
- [20] Pauline Tranchard, Fabienne Samyn, Sophie Duquesne, Matthieu Thomas, Bruno Estèbe, Jean-Luc Montès, and Serge Bourbigot. Fire behaviour of carbon fibre epoxy composite for aircraft: Novel test bench and experimental study. *Journal of Fire Sciences*, 33(3):247–266, 2015.
- [21] Mark B McKinnon, Yan Ding, Stanislav I Stoliarov, Sean Crowley, and Richard E Lyon. Pyrolysis model for a carbon fiber/epoxy structural aerospace composite. *Journal of Fire Sciences*, 35(1):36–61, 2017.
- [22] Talal Fateh, Jianping Zhang, Michael Delichatsios, and T Rogaume. Experimental investigation and numerical modelling of the fire performance for epoxy resin carbon fibre composites of variable thicknesses. *Fire and Materials*, 41(4):307–322, 2017.
- [23] Zhi Zhang, Changjian Wang, Gai Huang, Haoran Liu, Shenlin Yang, and Aifeng Zhang. Thermal degradation behaviors and reaction mechanism of carbon fibre-epoxy composite from hydrogen tank by tg-ftir. *Journal of hazardous materials*, 357:73–80, 2018.

- [24] Huichang Niu and Naian Liu. Thermal decomposition of pine branch: Unified kinetic model on pyrolytic reactions in pyrolysis and combustion. *Fuel*, 160:339–345, 2015.
- [25] Talal Fateh, Franck Richard, Thomas Rogaume, and Paul Joseph. Experimental and modelling studies on the kinetics and mechanisms of thermal degradation of polymethyl methacrylate in nitrogen and air. *Journal of Analytical and Applied Pyrolysis*, 120:423–433, 2016.
- [26] Andrea Frangi and MARIO Fontana. Fire performance of timber structures under natural fire conditions. *Fire Safety Science*, 8:279–290, 2005.
- [27] K Grigoriou and AP Mouritz. Comparative assessment of the fire structural performance of carbon-epoxy composite and aluminium alloy used in aerospace structures. *Materials & Design*, 108:699–706, 2016.
- [28] Serge Bourbigot and Sophie Duquesne. Fire retardant polymers: recent developments and opportunities. *Journal of Materials Chemistry*, 17(22):2283–2300, 2007.
- [29] AP Mouritz, S Feih, E Kandare, Z Mathys, AG Gibson, PE Des Jardin, SW Case, and BY Lattimer. Review of fire structural modelling of polymer composites. *Composites Part A: Applied Science and Manufacturing*, 40(12):1800–1814, 2009.
- [30] MA Maaroufi, Y Carpier, Benoît Vieille, L Gilles, A Coppalle, and Fabrice Barbe. Post-fire compressive behaviour of carbon fibers woven-ply polyphenylene sulfide laminates for aeronautical applications. *Composites Part B: Engineering*, 119:101–113, 2017.
- [31] Long Shi, Michael Yit Lin Chew, Xuanya Liu, Xudong Cheng, Bo Wang, and Guomin Zhang. An experimental and numerical study on fire behaviors of charring materials frequently used in buildings. *Energy and Buildings*, 138:140–153, 2017.
- [32] Chris Lautenberger. *A Generalized Pyrolysis Model for Combustible Solids*. PhD thesis, 2007.
- [33] Jing Li, Junhui Gong, and Stanislav I Stoliarov. Development of pyrolysis models for charring polymers. *Polymer Degradation and Stability*, 115:138–152, 2015.
- [34] Jose Manuel Sañes Iborra. Pyrolysis modelling. new test cases for fds fire simulator. B.S. thesis, Universitat Politècnica de Catalunya, 2015.
- [35] Kathrin Grewolls. *Probabilistic Modelling of Sensitivity in Fire Simulations*. PhD thesis, University of Central Lancashire, 2013.
- [36] Stanislav I Stoliarov, Sean Crowley, Richard N Walters, and Richard E Lyon. Prediction of the burning rates of charring polymers. *Combustion and Flame*, 157(11):2024–2034, 2010.
- [37] Andrés Anca-Couce. Reaction mechanisms and multi-scale modelling of lignocellulosic biomass pyrolysis. *Progress in Energy and Combustion Science*, 53:41–79, 2016.

- [38] Michele Corbetta, Alessio Frassoldati, Hayat Bennadji, Krystle Smith, Michelle J Serapiglia, Guillaume Gauthier, Thierry Melkior, Eliseo Ranzi, and Elizabeth M Fisher. Pyrolysis of centimeter-scale woody biomass particles: kinetic modeling and experimental validation. *Energy & fuels*, 28(6):3884–3898, 2014.
- [39] K Kwiatkowski, PJ Zuk, K Bajer, and M Dudyński. Biomass gasification solver based on openfoam. *Computer Physics Communications*, pages 1–29, 2013.
- [40] Xiao-Min Wang, Li-Song Zhang, Chi Yang, Na Liu, and Wen-Long Cheng. Estimation of temperature-dependent thermal conductivity and specific heat capacity for charring ablators. *International Journal of Heat and Mass Transfer*, 129:894–902, 2019.
- [41] Jun Koyanagi, Kenta Shinba, Yasuhiro Fukuda, Kenichi Hirai, Akiko Nakazato, Akinori Yoshimura, Takuya Aoki, and Yasuo Kogo. A numerical simulation of delamination caused by internal gas pressure for mid-density cfrp. *Composites Part A: Applied Science and Manufacturing*, 115:255–263, 2018.
- [42] Chris Lautenberger and Carlos Fernandez-Pello. Generalized pyrolysis model for combustible solids. *Fire Safety Journal*, 44(6):819–839, 2009.
- [43] Stanislav I Stoliarov, Isaac T Leventon, and Richard E Lyon. Two-dimensional model of burning for pyrolyzable solids. *Fire and Materials*, 38(3):391–408, 2014.
- [44] K McGrattan, R McDermott, S Hostikka, J Floyd, and M Vanella. *Fire Dynamics Simulator Technical Reference Guide Volume 1: Mathematical Model*. US Department of Commerce, National Institute of Standards and Technology, 2019.
- [45] Valentin Biasi. *Modélisation thermique de la dégradation d’un matériau composite soumis au feu*. PhD thesis, 2014.
- [46] Pauline Tranchard, Fabienne Samyn, Sophie Duquesne, Bruno Estèbe, and Serge Bourbigot. Modelling behaviour of a carbon epoxy composite exposed to fire: Part i—characterisation of thermophysical properties. *Materials*, 10(5):494, 2017.
- [47] George M Lloyd, A Razani, and Kwang J Kim. Formulation and numerical solution of non-local thermal equilibrium equations for multiple gas/solid porous metal hydride reactors. *Journal of Heat Transfer*, 123(3):520–526, 2001.
- [48] CT Sun and Rajesh S Vaidya. Prediction of composite properties from a representative volume element. *Composites science and Technology*, 56(2):171–179, 1996.
- [49] Toufik Kanit, Samuel Forest, Isabelle Galliet, Valérie Mounoury, and Dominique Jeulin. Determination of the size of the representative volume element for random composites: statistical and numerical approach. *International Journal of Solids and Structures*, 40(13-14):3647–3679, 2003.
- [50] Swantje Bargmann, Benjamin Klusemann, Jürgen Markmann, Jan Eike Schnabel, Konrad Schneider, Celal Soyarslan, and Jana Wilmers. Generation of 3d representative volume elements for heterogeneous materials: A review. *Progress in Materials Science*, 96:322–384, 2018.

- [51] Kai-Yuan Li, Xinyan Huang, Charles Fleischmann, Guillermo Rein, and Jie Ji. Pyrolysis of medium-density fiberboard: optimized search for kinetics scheme and parameters via a genetic algorithm driven by Kissinger's method. *Energy & Fuels*, 28(9):6130–6139, 2014.
- [52] Haoran Liu, Changjian Wang, Bing Chen, and Zhi Zhang. A further study of pyrolysis of carbon fibre-epoxy composite from hydrogen tank: Search optimization for kinetic parameters via a shuffled complex evolution. *Journal of Hazardous Materials*, 374:20–25, 2019.
- [53] Chris Lautenberger, Guillermo Rein, and Carlos Fernandez-Pello. The application of a genetic algorithm to estimate material properties for fire modeling from bench-scale fire test data. *Fire Safety Journal*, 41(3):204–214, 2006.
- [54] R Carvel, T Steinhaus, G Rein, and JL Torero. Determination of the flammability properties of polymeric materials: A novel method. *Polymer Degradation and Stability*, 96(3):314–319, 2011.
- [55] Morten G Grønli and Morten C Melaaen. Mathematical model for wood pyrolysis comparison of experimental measurements with model predictions. *Energy & Fuels*, 14(4):791–800, 2000.
- [56] Andrés Anca-Couce, Nico Zobel, Anka Berger, and Frank Behrendt. Smouldering of pine wood: Kinetics and reaction heats. *Combustion and Flame*, 159(4):1708–1719, 2012.
- [57] Mehran Jalili, Andres Anca-Couce, and Nico Zobel. On the uncertainty of a mathematical model for drying of a wood particle. *Energy & Fuels*, 27(11):6705–6717, 2013.
- [58] Inge Haberle, Øyvind Skreiberg, Joanna Łazar, and Nils Erland L Haugen. Numerical models for thermochemical degradation of thermally thick woody biomass, and their application in domestic wood heating appliances and grate furnaces. *Progress in Energy and Combustion Science*, 63:204–252, 2017.
- [59] Murlidhar Gupta, Jin Yang, and Christian Roy. Specific heat and thermal conductivity of softwood bark and softwood char particles. *Fuel*, 82(8):919–927, 2003.
- [60] Franz Richter, Arvind Atreya, Panagiotis Kotsovinos, and Guillermo Rein. The effect of chemical composition on the charring of wood across scales. *Proceedings of the Combustion Institute*, 37(3):4053–4061, 2019.
- [61] Colomba Di Blasi. Modeling chemical and physical processes of wood and biomass pyrolysis. *Progress in Energy and Combustion Science*, 34(1):47–90, 2008.
- [62] Morten Gunnar Grønli. *A theoretical and experimental study of the thermal degradation of biomass*. PhD thesis, Norwegian University of Science and Technology Trondheim, Norway, 1996.
- [63] Martin Kaltschmitt and Wolfgang Streicher. Energie aus Biomasse. In *Regenerative Energien in Österreich*, pages 339–532. Springer, 2009.

- [64] J Ratte, Frederic Marias, Jean Vaxelaire, and Philippe Bernada. Mathematical modelling of slow pyrolysis of a particle of treated wood waste. *Journal of hazardous materials*, 170(2-3):1023–1040, 2009.
- [65] Won Chan Park, Arvind Atreya, and Howard R Baum. Experimental and theoretical investigation of heat and mass transfer processes during wood pyrolysis. *Combustion and Flame*, 157(3):481–494, 2010.
- [66] Won Chan Park. *A Study of Pyrolysis of Charring Materials and its Application to Fire Safety and Biomass Utilization*. PhD thesis, 2008.
- [67] Michel Bellais. *Modelling of the pyrolysis of large wood particles*. PhD thesis, KTH-Royal Institute of Technology, 2007.
- [68] Long Shi and Michael Yit Lin Chew. A review of fire processes modeling of combustible materials under external heat flux. *Fuel*, 106:30–50, 2013.
- [69] Richard Chippendale. *Modelling of the thermal chemical damage caused to carbon fibre composites*. PhD thesis, University of Southampton, 2013.
- [70] Laurent Pouliot Laforte and Louis Laberge Lebel. Thermal analysis and degradation of properties in carbon fiber/epoxy laminate riveting at high temperatures. *Polymer Testing*, 67:205–212, 2018.
- [71] D Quang Dao, J Luche, F Richard, T Rogaume, C Bourhy-Weber, and S Ruban. Determination of characteristic parameters for the thermal decomposition of epoxy resin/carbon fibre composites in cone calorimeter. *International journal of hydrogen energy*, 38(19):8167–8178, 2013.
- [72] Tian Tian. *Anisotropic thermal property measurement of carbon-fiber/epoxy composite materials*. PhD thesis, The University of Nebraska-Lincoln, 2011.
- [73] Kamila Salasinska, Mateusz Barczewski, Monika Borucka, Rafał L Górny, Paweł Kozikowski, Maciej Celiński, and Agnieszka Gajek. Thermal stability, fire and smoke behaviour of epoxy composites modified with plant waste fillers. *Polymers*, 11(8):1234, 2019.
- [74] SHI LONG. *Pyrolysis and Combustion Processes of Combustible Materials under External Heat Flux*. PhD thesis, 2014.
- [75] Won Chan Park, Arvind Atreya, and Howard R Baum. Determination of pyrolysis temperature for charring materials. *Proceedings of the combustion Institute*, 32(2):2471–2479, 2009.
- [76] Mark B McKinnon, Stanislav I Stoliarov, and Artur Witkowski. Development of a pyrolysis model for corrugated cardboard. *Combustion and Flame*, 160(11):2595–2607, 2013.
- [77] Ashish Davinderkumar Vinayak. Mathematical modeling & simulation of pyrolysis & flame spread in openfoam. Master’s thesis, Bergische Universität Wuppertal, 2017.

- [78] N Grange, P Tadini, K Chetehouna, N Gascoin, I Reynaud, and S Senave. Determination of thermophysical properties for carbon-reinforced polymer-based composites up to 1000° c. *Thermochimica Acta*, 659:157–165, 2018.
- [79] John R Howell, M Pinar Menguc, and Robert Siegel. *Thermal Radiation Heat Transfer*. CRC Press, 2015.
- [80] Adrian P Mouritz and Arthur Geoff Gibson. *Fire properties of polymer composite materials*, volume 143. Springer Science & Business Media, 2007.
- [81] Himanshu Goyal and Perrine Pepiot. On the validation of a one-dimensional biomass pyrolysis model using uncertainty quantification. *ACS Sustainable Chemistry & Engineering*, 6(9):12153–12165, 2018.
- [82] Joshua D Swann, Yan Ding, and Stanislav I Stoliarov. Characterization of pyrolysis and combustion of rigid poly (vinyl chloride) using two-dimensional modeling. *International Journal of Heat and Mass Transfer*, 132:347–361, 2019.
- [83] Mathew John Hagge. *A numerical model for biomass pyrolysis*. PhD thesis, Iowa State University, 2005.
- [84] Damien M Marquis and Eric Guillaume. Modelling reaction-to-fire of polymer-based composite laminate. In *Nanocomposites with Unique Properties and Applications in Medicine and Industry*. IntechOpen, 2011.
- [85] Daniel Neves, Henrik Thunman, Arlindo Matos, Luís Tarelho, and Alberto Gómez-Barea. Characterization and prediction of biomass pyrolysis products. *Progress in Energy and Combustion Science*, 37(5):611–630, 2011.
- [86] Giancarlo Gentile, Paulo Eduardo Amaral Debiagi, Alberto Cuoci, Alessio Frassoldati, Eliseo Ranzi, and Tiziano Faravelli. A computational framework for the pyrolysis of anisotropic biomass particles. *Chemical Engineering Journal*, 321:458–473, 2017.
- [87] A Yu Snegirev, VA Talalov, VV Stepanov, and JN Harris. A new model to predict pyrolysis, ignition and burning of flammable materials in fire tests. *Fire safety journal*, 59:132–150, 2013.
- [88] NK Kim, S Dutta, and D Bhattacharyya. A review of flammability of natural fibre reinforced polymeric composites. *Composites Science and Technology*, 162:64–78, 2018.
- [89] Gillian Leplat, Cédric Huchette, and Valentin Biasi. Thermal and damage analysis of laser-induced decomposition within carbon/epoxy composite laminates. *Journal of Fire Sciences*, 34(5):361–384, 2016.
- [90] K Grigoriou and AP Mouritz. Influence of ply stacking pattern on the structural properties of quasi-isotropic carbon-epoxy laminates in fire. *Composites Part A: Applied Science and Manufacturing*, 99:113–120, 2017.

- [91] Zohreh Ghorbani, Robert Webster, Mariano Lázaro, and Arnaud Trouvé. Limitations in the predictive capability of pyrolysis models based on a calibrated semi-empirical approach. *Fire safety journal*, 61:274–288, 2013.
- [92] Behdad Moghtaderi. The state-of-the-art in pyrolysis modelling of lignocellulosic solid fuels. *Fire and Materials: An International Journal*, 30(1):1–34, 2006.
- [93] MJ Spearpoint and JG Quintiere. Predicting the burning of wood using an integral model. *Combustion and Flame*, 123(3):308–325, 2000.
- [94] Nicolas Bal. *Uncertainty and complexity in pyrolysis modelling*. PhD thesis, The University of Edinburgh, 2012.
- [95] Abhishek Bhargava, Patrick Van Hees, and Berit Andersson. Pyrolysis modeling of pvc and pmma using a distributed reactivity model. *Polymer Degradation and Stability*, 129:199–211, 2016.
- [96] Yan Ding, Joshua D Swann, Qi Sun, Stanislav I Stoliarov, and Roland H Kraemer. Development of a pyrolysis model for glass fiber reinforced polyamide 66 blended with red phosphorus: Relationship between flammability behavior and material composition. *Composites Part B: Engineering*, 176:107263, 2019.
- [97] Franz Richter and Guillermo Rein. Pyrolysis kinetics and multi-objective inverse modelling of cellulose at the microscale. *Fire Safety Journal*, 91:191–199, 2017.
- [98] Victor Pozzobon, Sylvain Salvador, Jean Jacques Bézian, Mouna El-Hafi, Yannick Le Maout, and Gilles Flamant. Radiative pyrolysis of wet wood under intermediate heat flux: Experiments and modelling. *Fuel Processing Technology*, 128:319–330, 2014.
- [99] CHRIS Lautenberger and AC Fernandez-Pello. Optimization algorithms for material pyrolysis property estimation. *Fire Safety Science*, 10:751–764, 2011.
- [100] Nicolas Bal and Guillermo Rein. On the effect of inverse modelling and compensation effects in computational pyrolysis for fire scenarios. *Fire safety journal*, 72:68–76, 2015.
- [101] JP Hidalgo, P Pironi, RM Hadden, and S Welch. A framework for evaluating the thermal behaviour of carbon fibre composite materials. In *Proceedings of the 2nd IAFSS European symposium of fire safety science*, pages 195–200, 2015.
- [102] Ariza Sharikin Abu Bakar. *Characterization of fire properties for coupled pyrolysis and combustion simulation and their optimised use*. PhD thesis, Victoria University, 2015.
- [103] Ramin Mehrabian, Robert Scharler, and Ingwald Obernberger. Effects of pyrolysis conditions on the heating rate in biomass particles and applicability of tga kinetic parameters in particle thermal conversion modelling. *Fuel*, 93:567–575, 2012.
- [104] E Kim and N Dembsey. Parameter estimation for comprehensive pyrolysis modeling: guidance and critical observations. *Fire Technology*, 51(2):443–477, 2015.

- [105] Imtiaz Ali, Salman Raza Naqvi, and Ali Bahadar. Kinetic analysis of botryococcus braunii pyrolysis using model-free and model fitting methods. *Fuel*, 214:369–380, 2018.
- [106] Quang-Vu Bach and Wei-Hsin Chen. Pyrolysis characteristics and kinetics of microalgae via thermogravimetric analysis (tga): A state-of-the-art review. *Bioresource technology*, 246:88–100, 2017.
- [107] Michael Ewart Brown. *Introduction to thermal analysis: techniques and applications*, volume 1. Springer Science & Business Media, 2001.
- [108] Pauline Tranchard, Sophie Duquesne, Fabienne Samyn, Bruno Estebe, and Serge Bourbigot. Kinetic analysis of the thermal decomposition of a carbon fibre-reinforced epoxy resin laminate. *Journal of Analytical and Applied Pyrolysis*, 126:14–21, 2017.
- [109] Ariza Sharikin Abu Bakar. *Characterization of fire properties for coupled pyrolysis and combustion simulation and their optimised use*. PhD thesis, Victoria University, 2015.
- [110] Yousef Haseli. *Modeling combustion of single biomass particle*. PhD thesis, 2012.
- [111] Yanming Ding, Ofodike A Ezekoye, Jiaqing Zhang, Changjian Wang, and Shouxiang Lu. The effect of chemical reaction kinetic parameters on the bench-scale pyrolysis of lignocellulosic biomass. *Fuel*, 232:147–153, 2018.
- [112] James G Quintiere, Richard N Walters, and Sean Crowley. Flammability properties of aircraft carbon-fiber structural composite. Technical report, 2007.
- [113] Hsiang-Cheng Kung. A mathematical model of wood pyrolysis. *Combustion and flame*, 18(2):185–195, 1972.
- [114] Henderson. A model for the thermal response of polymer composite materials with experimental verification. *Journal of composite materials*, 19(6):579–595, 1985.
- [115] Naadia Nawaz. Modelling and experimental analysis of aerospace composites in fire. Master’s thesis, 2011.
- [116] Chris Lautenberger and Carlos Fernandez-Pello. A model for the oxidative pyrolysis of wood. *Combustion and Flame*, 156(8):1503–1513, 2009.
- [117] Marcos Chaos, Mohammed M Khan, Niveditha Krishnamoorthy, John L de Ris, and Sergey B Dorofeev. Evaluation of optimization schemes and determination of solid fuel properties for cfd fire models using bench-scale pyrolysis tests. *Proceedings of the Combustion Institute*, 33(2):2599–2606, 2011.
- [118] Marcos Chaos. Application of sensitivity analyses to condensed-phase pyrolysis modeling. *Fire safety journal*, 61:254–264, 2013.
- [119] Junhui Gong, Yixuan Chen, Juncheng Jiang, Lizhong Yang, and Jing Li. A numerical study of thermal degradation of polymers: Surface and in-depth absorption. *Applied Thermal Engineering*, 106:1366–1379, 2016.

- [120] Zoubir Acem, Damien Brissinger, Anthony Collin, Gilles Parent, Pascal Boulet, Thi Hay Yen Quach, Benjamin Batiot, Franck Richard, and Thomas Rogaume. Surface temperature of carbon composite samples during thermal degradation. *International Journal of Thermal Sciences*, 112:427–438, 2017.
- [121] Talal Fateh, T Rogaume, and F Richard. Multi-scale modeling of the thermal decomposition of fire retardant plywood. *Fire safety journal*, 64:36–47, 2014.
- [122] S Stoliarov and R Lyon. Thermo-kinetic model of burning for pyrolyzing materials. *Fire Safety Science*, 9:1141–1152, 2008.
- [123] <https://code.google.com/archive/p/firefoam-dev/>. Firefoam.
- [124] Yan Ding, Kyungok Kwon, Stanislav I Stoliarov, and Roland H Kraemer. Development of a semi-global reaction mechanism for thermal decomposition of a polymer containing reactive flame retardant. *Proceedings of the Combustion Institute*, 37(3):4247–4255, 2019.
- [125] Yan Ding, Stanislav I Stoliarov, and Roland H Kraemer. Pyrolysis model development for a polymeric material containing multiple flame retardants: Relationship between heat release rate and material composition. *Combustion and Flame*, 202:43–57, 2019.
- [126] Stanislav I Stoliarov, Sean Crowley, Richard E Lyon, and Gregory T Linteris. Prediction of the burning rates of non-charring polymers. *Combustion and Flame*, 156(5):1068–1083, 2009.
- [127] Chris Lautenberger. Gpyro3d: A three dimensional generalized pyrolysis model. *Fire Safety Science*, 11:193–207, 2014.
- [128] Florian Kempel, Bernhard Schartel, Gregory T Linteris, Stanislav I Stoliarov, Richard E Lyon, Richard N Walters, and Anja Hofmann. Prediction of the mass loss rate of polymer materials: Impact of residue formation. *Combustion and Flame*, 159(9):2974–2984, 2012.
- [129] Artur Witkowski, Bertrand Girardin, Michael Försth, Fiona Hewitt, Gaëlle Fontaine, Sophie Duquesne, Serge Bourbigot, and T Richard Hull. Development of an anaerobic pyrolysis model for fire retardant cable sheathing materials. *Polymer degradation and stability*, 113:208–217, 2015.
- [130] Jing Li. *A MULTISCALE APPROACH TO PARAMETERIZATION OF BURNING MODELS FOR POLYMERIC MATERIALS*. PhD thesis, 2014.
- [131] Bernhard Peters and Christian Bruch. Drying and pyrolysis of wood particles: experiments and simulation. *Journal of analytical and applied pyrolysis*, 70(2):233–250, 2003.
- [132] Jing Li and Stanislav I Stoliarov. Measurement of kinetics and thermodynamics of the thermal degradation for charring polymers. *Polymer degradation and stability*, 106:2–15, 2014.

- [133] KY Li, DSW Pau, YN Hou, and J Ji. Modeling pyrolysis of charring materials: determining kinetic properties and heat of pyrolysis of medium density fiberboard. *Industrial & Engineering Chemistry Research*, 53(1):141–149, 2014.
- [134] Stanislav I Stoliarov and Jing Li. Parameterization and validation of pyrolysis models for polymeric materials. *Fire Technology*, 52(1):79–91, 2016.
- [135] Jing Li and Stanislav I Stoliarov. Measurement of kinetics and thermodynamics of the thermal degradation for non-charring polymers. *Combustion and Flame*, 160(7):1287–1297, 2013.
- [136] Özge Çepelioğullar, Hanzade Haykırı-Açma, and Serdar Yaman. Kinetic modelling of rdf pyrolysis: Model-fitting and model-free approaches. *Waste management*, 48:275–284, 2016.
- [137] Ruiyu Chen, Xiaokang Xu, Yang Zhang, Siuming Lo, and Shouxiang Lu. Kinetic study on pyrolysis of waste phenolic fibre-reinforced plastic. *Applied Thermal Engineering*, 136:484–491, 2018.
- [138] ISO 5660-1: 2002. Reaction-to-fire tests—heat release, smoke production and mass loss rate—part 1: Heat release rate (cone calorimeter method), 2002.
- [139] 2058 ASTM, E. Standard test methods for measurement of synthetic polymer material flammability using a fire propagation apparatus (fpa). astm international, west conshohocken, pa, 2013, doi: 10.1520/e2058-13.
- [140] Qingfeng Xu, Lingzhu Chen, Kent A Harries, Fuwen Zhang, Qiong Liu, and Jinghui Feng. Combustion and charring properties of five common constructional wood species from cone calorimeter tests. *Construction and Building Materials*, 96:416–427, 2015.
- [141] Romain Meinier, Rodolphe Sonnier, Pascal Zavaleta, Sylvain Suard, and Laurent Ferry. Fire behavior of halogen-free flame retardant electrical cables with the cone calorimeter. *Journal of hazardous materials*, 342:306–316, 2018.
- [142] Pietro Di Modica. *Modelling fire behaviour of composite materials*. PhD thesis, Newcastle University, 2016.
- [143] Xuan Liu. Design and analysis of new gasification apparatus based on the standard cone calorimeter. Master’s thesis, 2012.
- [144] JEJ Staggs. Convection heat transfer in the cone calorimeter. *Fire Safety Journal*, 44(4):469–474, 2009.
- [145] Yeqing Wang, Timothy K Risch, and Joseph H Koo. Assessment of a one-dimensional finite element charring ablation material response model for phenolic-impregnated carbon ablator. *Aerospace Science and Technology*, 91:301–309, 2019.
- [146] Vincent Blay and Luis F Bobadilla. Numerical study of the accuracy of temperature measurement by thermocouples in small-scale reactors. *Chemical Engineering Research and Design*, 131:545–556, 2018.

- [147] Zhengping Zou, Weiping Yang, Weihao Zhang, Xiaokui Wang, and Jian Zhao. Numerical modeling of steady state errors for shielded thermocouples based on conjugate heat transfer analysis. *International Journal of Heat and Mass Transfer*, 119:624–639, 2018.
- [148] Xue Chen, Xin-Lin Xia, Chuang Sun, and Yang Li. Numerical analysis on the transient measurement of gas temperature in porous material using thermocouples at high temperatures. *International Journal of Heat and Mass Transfer*, 91:1060–1068, 2015.
- [149] Chenghang Zheng, Leming Cheng, Alexei Saveliev, Zhongyang Luo, and Kefa Cen. Gas and solid phase temperature measurements of porous media combustion. *Proceedings of the Combustion Institute*, 33(2):3301–3308, 2011.
- [150] Thomas Steinhaus. *Determination of intrinsic material flammability properties from material tests assisted by numerical modelling*. PhD thesis, The University of Edinburgh, 2010.
- [151] Pedro Reszka. *In-depth temperature profiles in pyrolyzing wood*. PhD thesis, The University of Edinburgh, 2008.
- [152] Lucie Hasalová, Jiří Ira, and Milan Jahoda. Practical observations on the use of shuffled complex evolution (sce) algorithm for kinetic parameters estimation in pyrolysis modeling. *Fire safety journal*, 80:71–82, 2016.
- [153] Jing Li, Junhui Gong, and Stanislav I Stoliarov. Gasification experiments for pyrolysis model parameterization and validation. *International Journal of Heat and Mass Transfer*, 77:738–744, 2014.
- [154] J Lachaud, JB Scoggins, TE Magin, MG Meyer, and NN Mansour. A generic local thermal equilibrium model for porous reactive materials submitted to high temperatures. *International Journal of Heat and Mass Transfer*, 108:1406–1417, 2017.
- [155] James B Scoggins, Vincent Leroy, Georgios Bellas-Chatzigeorgis, Bruno Dias, and Thierry E Magin. Mutation++: Multicomponent thermodynamic and transport properties for ionized gases in c++. *arXiv preprint arXiv:2002.01783*, 2020.
- [156] Stephen Whitaker. *The method of volume averaging*, volume 13. Springer Science & Business Media, 1999.
- [157] Jie Chen, Shuyu Sun, and Xiaoping Wang. Homogenization of two-phase fluid flow in porous media via volume averaging. *Journal of Computational and Applied Mathematics*, 353:265–282, 2019.
- [158] John M Dinwoodie. *Timber: its nature and behaviour*. CRC Press, 2000.
- [159] Benoit Gentilleau. *Modélisation et validation expérimentale du comportement thermomécanique de multicouches polymère-composite bobine*. PhD thesis, Chasseneuil-du-Poitou, Ecole nationale supérieure de mécanique et d . . . , 2012.

- [160] Jean Lachaud, Tom van Eekelen, James B Scoggins, Thierry E Magin, and Nagi N Mansour. Detailed chemical equilibrium model for porous ablative materials. *International Journal of Heat and Mass Transfer*, 90:1034–1045, 2015.
- [161] Jeremie BE Meurisse, Jean Lachaud, Francesco Panerai, Chun Tang, and Nagi N Mansour. Multidimensional material response simulations of a full-scale tiled ablative heatshield. *Aerospace Science and Technology*, 76:497–511, 2018.
- [162] TALAL Fateh, FRANCK Richard, and THOMAS Rogaume. Modeling of the pyrolysis of plywood exposed to heat fluxes under cone calorimeter. *Fire Safety Science*, 11:208–221, 2014.
- [163] James Quintiere. *Fundamentals of Fire Phenomena*. Wiley, 2006.
- [164] Brian M Adams, Mohamed S Ebeida, Michael S Eldred, Gianluca Geraci, John D Jakeman, Kathryn A Maupin, Jason A Monschke, J Adam Stephens, Laura P Swiler, Dena M Vigil, et al. Dakota, a multilevel parallel object-oriented framework for design optimization, parameter estimation, uncertainty quantification, and sensitivity analysis: Version 6.7 user’s manual. 2014.
- [165] Esther Kim, N Dembsey, and S Shivkumar. Evaluating effects of applying different kinetic models to pyrolysis modeling of fiberglass-reinforced polymer composites. *Fire and Materials*, 39(2):153–173, 2015.
- [166] R Lyon, NATALLIA Safronava, and EZGI Oztekin. A simple method for determining kinetic parameters for materials in fire models. *Fire Safety Science*, 10:765–777, 2011.
- [167] Marcin Wojdyr. Fityk: a general-purpose peak fitting program. *Journal of Applied Crystallography*, 43(5-1):1126–1128, 2010.
- [168] David E Goldenberg. *Genetic algorithms in search, optimization and machine learning*. Addison Wesley, Reading: MA, 1989.
- [169] Zbigniew Michalewicz. *Genetic algorithms+ data structures= evolution programs*. Springer Science & Business Media, 2013.
- [170] Kaiyuan Li, Dennis SW Pau, Jinhui Wang, and Jie Ji. Modelling pyrolysis of charring materials: determining flame heat flux using bench-scale experiments of medium density fibreboard (mdf). *Chemical engineering science*, 123:39–48, 2015.
- [171] ASM International Handbook Committee et al. *ASM Handbook, Volume 15-Casting*. ASM International., 2008.
- [172] Joshua D Swann, Yan Ding, Mark B McKinnon, and Stanislav I Stoliarov. Controlled atmosphere pyrolysis apparatus ii (capa ii): A new tool for analysis of pyrolysis of charring and intumescent polymers. *Fire Safety Journal*, 91:130–139, 2017.

- [173] U Sand, J Sandberg, J Larfeldt, and R Bel Fdhila. Numerical prediction of the transport and pyrolysis in the interior and surrounding of dry and wet wood log. *Applied Energy*, 85(12):1208–1224, 2008.
- [174] VILLE Hankalin, TUUKKA Ahonen, and RISTO Raiko. On thermal properties of a pyrolysing wood particle. *Finnish-Swedish Flame Days*, 16, 2009.
- [175] Richard S Miller and J Bellan. A generalized biomass pyrolysis model based on superimposed cellulose, hemicellulose and lignin kinetics. *Combustion science and technology*, 126(1-6):97–137, 1997.
- [176] Hong Lu, Elvin Ip, Justin Scott, Paul Foster, Mark Vickers, and Larry L Baxter. Effects of particle shape and size on devolatilization of biomass particle. *Fuel*, 89(5):1156–1168, 2010.
- [177] Andrés Anca-Couce and Robert Scharler. Modelling heat of reaction in biomass pyrolysis with detailed reaction schemes. *Fuel*, 206:572–579, 2017.
- [178] CA Koufopoulos, N Papayannakos, G Maschio, and A Lucchesi. Modelling of the pyrolysis of biomass particles. studies on kinetics, thermal and heat transfer effects. *The Canadian journal of chemical engineering*, 69(4):907–915, 1991.
- [179] Toshiro Harada, Toshimitsu Hata, and Shigehisa Ishihara. Thermal constants of wood during the heating process measured with the laser flash method. *Journal of Wood Science*, 44(6):425–431, 1998.
- [180] BV Babu and AS Chaurasia. Pyrolysis of biomass: improved models for simultaneous kinetics and transport of heat, mass and momentum. *Energy conversion and Management*, 45(9-10):1297–1327, 2004.
- [181] Julien Blondeau and Hervé Jeanmart. Biomass pyrolysis at high temperatures: Prediction of gaseous species yields from an anisotropic particle. *Biomass and bioenergy*, 41:107–121, 2012.
- [182] Lee J Curtis and Dennis J Miller. Transport model with radiative heat transfer for rapid cellulose pyrolysis. *Industrial & engineering chemistry research*, 27(10):1775–1783, 1988.
- [183] Forest Products Laboratory (US). *Wood handbook: Wood as an engineering material*. The Laboratory, 1999.
- [184] DL Pyle and CA Zaror. Heat transfer and kinetics in the low temperature pyrolysis of solids. *Chemical engineering science*, 39(1):147–158, 1983.
- [185] Bertil Fredlund. *A model for heat and mass transfer in timber structures during fire*. PhD thesis, 1988.
- [186] KW Ragland, DJ Aerts, and AJ Baker. Properties of wood for combustion analysis. *Bioresource technology*, 37(2):161–168, 1991.
- [187] RKK Yuen, GH Yeoh, G de Vahl Davis, and E Leonardi. Modelling the pyrolysis of wet wood—i. three-dimensional formulation and analysis. *International journal of heat and mass transfer*, 50(21-22):4371–4386, 2007.

- [188] Amit Kumar Biswas and Kentaro Umeki. Simplification of devolatilization models for thermally-thick particles: Differences between wood logs and pellets. *Chemical Engineering Journal*, 274:181–191, 2015.
- [189] Christian Bruch, Bernhard Peters, and Thomas Nussbaumer. Modelling wood combustion under fixed bed conditions. *Fuel*, 82(6):729–738, 2003.
- [190] Mollie Rose Semmes. *A Model for Non-Oxidative and Oxidative Pyrolysis of Corrugated Cardboard*. PhD thesis, 2013.
- [191] Yanming Ding, Changjian Wang, and Shouxiang Lu. Modeling the pyrolysis of wet wood using firefoam. *Energy conversion and management*, 98:500–506, 2015.
- [192] Johannes Rath, MG Wolfinger, Gerhard Steiner, Gernot Krammer, Federica Barontini, and Valerio Cozzani. Heat of wood pyrolysis. *Fuel*, 82(1):81–91, 2003.
- [193] Abhishek Sharma, Vishnu Pareek, and Dongke Zhang. Biomass pyrolysis—a review of modelling, process parameters and catalytic studies. *Renewable and Sustainable Energy Reviews*, 50:1081–1096, 2015.
- [194] <http://www.firecomp.info/>. Firecomp project.
- [195] Aixi Zhou. *Stiffness and strength of fiber reinforced polymer composite bridge deck systems*. PhD thesis, Virginia Tech, 2002.
- [196] Pauline Tranchard. High temperature-dependent thermal properties of a carbon-fiber epoxy composite. 2018.
- [197] Georgios Kalogiannakis, Danny Van Hemelrijck, and Guy Van Assche. Measurements of thermal properties of carbon/epoxy and glass/epoxy using modulated temperature differential scanning calorimetry. *Journal of composite materials*, 38(2):163–175, 2004.
- [198] Ning Tian. *A general thermal thickness model and a heating rate related ignition criterion for combustible solids*. PhD thesis, The University of North Carolina at Charlotte, 2013.
- [199] Jiri Nossent, Pieter Elsen, and Willy Bauwens. Sobol’sensitivity analysis of a complex environmental model. *Environmental Modelling & Software*, 26(12):1515–1525, 2011.
- [200] Meng Xu, Jin Yang, and Ziyou Gao. Using one-at-a-time sensitivity analysis designs for genetic algorithm solving continuous network design problems. In *2009 International Joint Conference on Computational Sciences and Optimization*, volume 2, pages 114–118. IEEE, 2009.
- [201] Andrea Saltelli, Stefano Tarantola, Francesca Campolongo, and Marco Ratto. *Sensitivity analysis in practice: a guide to assessing scientific models*, volume 1. Wiley Online Library, 2004.



# Appendix A

## Summary in French for each chapter/Résumé en français pour chaque chapitre

### A.1 Chapitre 1: Introduction

Il existe deux grands ensembles de matériaux composites, à savoir les fibres naturelles et les fibres artificielles. Le bois, qui est une sorte de matériau de la biomasse, représente les composites de fibres naturelles les plus couramment utilisés, qui comprennent principalement de l'hémicellulose, de la cellulose et de la lignine. Les matériaux composites synthétiques, qui sont une combinaison de certains sous-composants dans différents processus de manipulation, ont le potentiel d'être l'un des matériaux les plus influents utilisés en raison de leur champ d'application différent à grande échelle dans l'industrie. Les composites en fibre de carbone représentent l'un des composites en fibres artificielles largement utilisés.

Cependant, les matériaux composites naturels ou synthétiques possèdent un potentiel relativement élevé de provoquer un incendie qui pourrait produire une grande quantité de gaz et de fumée toxiques. Dans l'industrie à haute pression, les composites carbone/époxy sont largement utilisés pour les réservoirs de stockage d'hydrogène et

peuvent provoquer des incendies et des explosions catastrophiques lorsque le composite carbone/époxy est endommagé par la chaleur externe ou des sources mécaniques. Des études de pyrolyse du bois et de sécurité incendie devraient également être menées en permanence dans les feux de forêt ainsi que dans les domaines connexes tels que le traitement thermique du bois et les incendies de bâtiments en bois. En bref, tous ces matériaux composites présentent un risque d'incendie élevé et les processus thermo-physiques et chimiques fondamentaux doivent être largement étudiés.

Il existe deux principaux domaines de recherche concernant le feu composite, l'un implique une étude expérimentale ou théorique fondamentale pour la prédiction et la prévention des tendances d'inflammabilité des matériaux telles que la recherche sur les produits ignifuges. Cela concerne la réaction au feu. L'autre se concentre sur la résistance au feu et concerne l'étude de l'intégrité de la structure du feu comme dans les infrastructures ou l'industrie du transport. En effet, du fait de l'influence du feu sur la structure composite ainsi que des accidents graves, les études de la structure incendie sont en partie menées en ce qui concerne la réponse du matériau à l'échauffement du feu et le temps d'exposition. Pour conclure, de nombreux événements d'incendies catastrophiques et tendances aux risques impliquent le composite carbone/époxy et le bois dans notre vie quotidienne ou dans des domaines industriels connexes.

Le phénomène fondamental de l'incendie est la pyrolyse, alors sa modélisation est un moyen efficace d'évaluer les comportements. L'étude de modélisation de la pyrolyse est une partie importante en tant qu'approche supplémentaire du travail expérimental et de la mise en œuvre détaillée du phénomène de pyrolyse pour prédire la croissance du feu. Le modèle de pyrolyse a été largement utilisé pour obtenir et optimiser le comportement au feu des matériaux, en particulier pour les nouveaux matériaux qui sont assez compliqués et avancés. En outre, pour les essais de pyrolyse sont complexes et coûteux, une étude de modélisation de la pyrolyse a été largement réalisée pour prédire la réponse thermique et chimique des matériaux tels que le profil de perte de masse et l'évolution de la température pour prédire progressivement le processus d'allumage.

Pour de nombreux modèles de pyrolyse, le matériau composite est généralement considéré comme une nouvelle structure homogène, qui implique des propriétés thermiques et physiques individuelles constituées de différents composants. La conductivité thermique du matériau vierge et du charbon, qui sont des propriétés cruciales pendant le processus de pyrolyse, est normalement traitée comme des valeurs constantes dans différentes directions, bien qu'elle se comporte bien différemment en réalité. Le changement de structure de la matrice pendant le processus de pyrolyse est toujours un défi dans la modélisation. En effet, cela pourrait affecter de manière significative le paramètre apparent calculé. Les milieux poreux sont également traités la plupart du temps à «l'échelle de Darcy» en utilisant le concept de «volume équivalent représentatif» (REV) pour définir les propriétés apparentes à partir des propriétés locales en utilisant des techniques de mise à l'échelle. Mais, lorsque la structure du milieu poreux change dans le temps et dans l'espace pendant le processus de pyrolyse, les techniques de mise à l'échelle peuvent être difficiles à obtenir. En plus des paramètres thermo-physiques, les paramètres cinétiques sont généralement traités comme des valeurs généralisées sous différentes vitesses de chauffage TGA, ce qui est acceptable en raison de la plage relativement petite de vitesses de chauffage, compte tenu de l'influence du retard thermique sous des vitesses de chauffage élevées. Cependant, il pourrait se comporter différemment sous différentes vitesses de chauffage en raison de la complexité de la cinétique multiple et de chevauchement des différents composants. De nombreuses études ont été réalisées pour explorer le comportement de pyrolyse des matériaux composites, telles que les expériences TGA pour la détermination de mécanismes cinétiques et le calorimètre à cône utilisé pour capturer le processus de transfert de chaleur et de masse 1D. Cependant, de nombreuses expériences de calorimètre à cône sont menées sous atmosphère ambiante pour étudier le comportement de combustion et des études limitées sont trouvées dans des conditions anaérobies. C'est souvent le bon choix lors de l'examen du scénario d'incendie pratique, mais cela pourrait entraîner beaucoup d'incertitude lors de la validation du modèle de pyrolyse en raison de la perturbation de la flamme et de l'oxydation du charbon. Ainsi, il est crucial d'éliminer

ces incertitudes connexes pour maximiser la précision de la prédiction pour la validation du modèle de pyrolyse. De plus, très peu d'études de modélisation prennent en compte la condition aux limites de la surface latérale et inférieure, une hypothèse d'adiabatique ou impénétrable est généralement effectuée.

Le but de recherche du présent travail est de développer un modèle de pyrolyse complet traitant des transferts de chaleur et de masse dans des milieux poreux ainsi que des réactions chimiques impliquées en même temps. Le bois et le matériau composite carbone/époxy sont choisis pour développer un modèle 3D incluant des paramètres physiques non isotropes. Les paramètres de prévision d'incendie les plus importants sont concentrés, y compris le front de pyrolyse, le profil de perte de masse et la distribution de la température à différents endroits en profondeur. Les trois processus, y compris la chaleur, le transfert de masse et les réactions chimiques, sont mis en œuvre sur différentes échelles de temps et de longueur, qui comprennent principalement des essais au calorimètre à cône à atmosphère contrôlée et à l'échelle du milligramme. Les différentes vitesses de chauffage utilisées dans le test TGA sont extraites des expériences de calorimètre à cône correspondant pour approcher le comportement de chauffage réel. Les paramètres thermiques et aux limites sont assez incertains concernant les différentes configurations de test. Par conséquent, la concentration est effectuée pour obtenir les propriétés du matériau exactement utilisées dans cette étude. Dans différents scénarios d'incendie, ces processus pourraient interagir plus ou moins fortement ensemble. Un accent est mis sur cela pour mettre en évidence les différents paramètres clés impliqués et étudier leur rôle dans ces interactions.

Ce travail se concentre sur la validation du modèle de pyrolyse et les travaux connexes tels que l'estimation des propriétés et des paramètres. Un nouveau modèle complet de pyrolyse traitant des transferts de chaleur et de masse à travers un milieu poreux ainsi que des réactions chimiques est développé et proposé. Comme mentionné ci-dessus, le processus de transfert de chaleur, de transfert de masse et de décomposition thermique chimique pourrait interagir sur de nombreuses échelles de temps et de longueur. La modélisation de la pyrolyse dans cette étude n'implique pas la combustion

en phase gazeuse et l'oxydation du charbon qui contient beaucoup de perturbations dans la limite. Les processus thermo-physiques et chimiques sont concentrés dans la phase condensée. Pour caractériser correctement chaque processus et les valider avec soin, ils sont étudiés un par un à des échelles différentes dans le temps et dans l'espace. Après avoir capturé correctement chacun d'eux par le modèle numérique, le travail se concentre sur les interactions entre eux. Certains régimes sont identifiés lorsque l'un des processus régit toute la partie pyrolyse. Dans un tel cas, les paramètres clés régissant la pyrolyse globale sont identifiés et analysés par des techniques de sensibilité.

En ce qui concerne la théorie thermiquement mince, l'expérience TGA à l'échelle du milligramme et la méthode d'ajustement du modèle utilisées pour obtenir les paramètres cinétiques exactes (c'est-à-dire l'énergie d'activation, le facteur pré-exponentiel, l'ordre de réaction) et la fraction massique finale du charbon sous différentes vitesses de chauffage. Des expériences de calorimètre à cône à atmosphère contrôlée (CACC) sont menées pour obtenir le taux de perte de masse et l'évolution du gradient de température à différents endroits. Les propriétés thermo-physiques inconnues telles que la capacité thermique spécifique, la conductivité thermique et les coefficients de convection thermique aux limites sont prédites à l'aide d'une méthode de modélisation inverse. Enfin, les différentes analyses de sensibilité des paramètres sont effectuées pour caractériser l'incertitude du modèle. Différentes conditions de chauffage sont étudiées pour faire varier l'intensité et les interactions entre ces processus afin d'étudier le rôle de chaque processus. Des modélisations ont été menées sur les deux matériaux en 1D et 2D.

## A.2 Chapitre 2: Revue de la littérature

Ce chapitre fournit un contexte complet pour l'étude de modélisation de la pyrolyse. Premièrement, les matériaux de carbonisation poreux cibles sont axés sur le bois et le composite carbone/époxy dans cette étude. Leurs propriétés chimiques et physiques fondamentales sont évaluées, en particulier les différents composants à

l'intérieur des matériaux. Les similitudes et les différences sont discutées, le bois peut être considéré comme isotrope tandis que le composite carbone/époxy implique des propriétés anisotropes compte tenu des différences de conductivité thermique dans différentes directions.

Les processus de pyrolyse de ces deux matériaux dans le scénario d'incendie sont décrits sous les aspects chimiques, de chaleur et de transfert de masse ainsi que sous les aspects de changement de structure physique. Les similitudes de la formation de la couche de charbon ont un effet important sur le processus de pyrolyse, tandis que le retrait du bois et la délamination des composites carbone/époxy font que ces deux matériaux se pyrolyse avec une grande différence. Différents types de modèles de pyrolyse sont évalués, des modèles de pyrolyse simples aux modèles complets. L'accent est mis sur le modèle complet de pyrolyse, qui se couple principalement aux réactions chimiques, à la chaleur et au transfert de masse. Les modèles élémentaires concernant ces trois parties sont formulés mathématiquement et utilisent principalement l'équation d'Arrhenius et la loi de Darcy. Ensuite, les modèles de pyrolyse développés dans la communauté des incendies sont décrits brièvement, leurs avantages et leurs inefficacités sont évalués.

Le processus de validation du modèle de pyrolyse implique la comparaison de la prédiction du modèle avec les données expérimentales. Des tests TGA à l'échelle du milligramme et des tests de calorimètre à cône expérimental à l'échelle du banc sont introduits et décrits lors de l'examen de différentes échelles de longueur caractéristique sous la théorie thermiquement mince et thermiquement épaisse. Différents paramètres d'entrée pour mettre en œuvre le modèle de pyrolyse sont discutés, et ils sont principalement collectés avec des paramètres chimiques et thermo-physiques. Les propriétés cinétiques sont spécifiées pour contrôler la réaction de pyrolyse tandis que les propriétés thermo-physiques déterminent le processus de transfert de chaleur et de masse. Les paramètres cinétiques sont principalement estimés par des expériences TGA en s'ajustant aux profils de perte de masse correspondants basés sur la modélisation de la pyrolyse. La méthode d'analyse inverse d'ajustement de courbe est généralement

utilisée pour caractériser les propriétés thermo-physiques en complément de la méthode expérimentale.

Sur la base de la description du processus de modélisation de la pyrolyse susmentionnée avec différents aspects, le chapitre suivant présentera un nouveau modèle de pyrolyse PATO pour surmonter certaines inefficacités des modèles de pyrolyse actuels dans la communauté des incendies. Ce modèle implique l'hypothèse de la théorie de la moyenne des volumes, et les équations de conservation pertinentes contenant la conductivité thermique et le tenseur de perméabilité sont décrites. Il peut être mis en œuvre avec des conditions aux limites de convection flexibles sur différentes surfaces. En utilisant ce modèle, les paramètres cinétiques, les paramètres thermo-physiques et les paramètres des conditions aux limites sont également collectés avec un certain niveau de précision. Ils sont estimés avec différentes options de simulation à hériter comme paramètres d'entrée pour enfin valider ce modèle de pyrolyse.

### **A.3 Chapitre 3: Description du solveur PATO**

Le présent chapitre a permis de présenter le modèle PATO utilisé dans cette étude, la théorie détaillée de la moyenne volumique est décrite et les équations de conservation correspondantes sont fournies ainsi que les expressions des propriétés des matériaux connexes. Différents mécanismes de réaction cinétique concernant la pyrolyse du bois et des composites carbone/époxy sont expliqués. Les méthodes numériques et les conditions aux limites à différentes surfaces de matériaux utilisées dans cette étude sont présentées pour mettre en œuvre les simulations qui incluent principalement des simulations de TGA, de conduction thermique pure et de calorimètre à cône. Enfin, certaines hypothèses du modèle et les options de simulation correspondantes sont données.

La boîte à outils d'analyse des matériaux poreux (PATO) basée sur OpenFOAM est un solveur numérique open-source (GNU GPL) publié par la NASA pour analyser le processus de transfert de chaleur et de masse des matériaux poreux réactifs, par

exemple, le comportement de pyrolyse des matériaux carbonisés. Ce solveur résout les équations aux dérivées partielles par la méthode des volumes finis. PATO intègre également Mutation++ en tant que bibliothèque tierce qui est développée par Von Karman Institute. Le Mutation++ est utilisé pour calculer les réactions chimiques à l'équilibre qui incluent la base de données pour les compositions chimiques des gaz, la thermodynamique et le transport. PATO est développé initialement pour l'ablateur de carbonisation, qui est utilisé dans le système de protection thermique pour la rentrée des véhicules aérospatiaux impliquant des conditions de chauffage aux limites rigoureuses. Cette limite explique le flux de gaz à haute enthalpie. Le gaz sous l'environnement aérothermique à haute pression et la température est contrôlée par le flux de chaleur de convection tandis que le flux de chaleur de rayonnement est moins prédominant. La couche limite est traitée comme un équilibre thermique pour la réaction chimique, le transfert de chaleur et le transfert de masse, qui traitent de l'interaction entre le gaz ambiant, le gaz de pyrolyse et la couche de charbon de surface.

Ce modèle de pyrolyse complet a été développé pour traiter les transferts de chaleur et de masse dans des milieux poreux ainsi que les réactions chimiques impliquées en même temps. Ce modèle implique différentes phases solides et une phase gazeuse unique. Différents composants des matériaux composites sont séparés et impliquent leurs propres propriétés chimiques et physiques intrinsèques. L'équilibre thermique local est considéré entre les gaz volatils et la phase solide, et ils sont mis en œuvre sur la base de la méthode de moyenne volumique. Différents nombres de schémas de réaction parallèles sont définis pour chaque composant et ils sont finalement intégrés pour mettre en œuvre l'ensemble du comportement de pyrolyse du matériau. Les simulations de différents cas de décomposition thermique permettent d'étudier les interactions entre les processus de transfert de chaleur et de masse ainsi que les réactions chimiques au sein du solide. Le modèle 3D développé décrit le transport du gaz dans les pores des matériaux à l'échelle de Darcy. La conductivité thermique est formulée sous une forme tenseur permettant la définition du transfert de chaleur dans trois directions du domaine. Les conditions aux limites de rayonnement concernant les scénarios

d'incendie sont ajoutées au modèle. Et on s'attend à ce qu'il s'agisse d'un autre modèle de pyrolyse complet applicable pour fournir une précision de prédiction potentielle lors de l'évaluation des modèles de pyrolyse actuels dans la communauté de la sécurité incendie.

Dans ce travail, le bois est traité comme un matériau composite isotrope, c'est-à-dire que le tenseur de conductivité thermique et de perméabilité est négligé, tandis que pour le composite carbone/époxy, ces valeurs ne sont pas uniformes pour différentes directions. Lorsqu'on s'attaque à des schémas de réaction parallèles indépendants pour le bois qui implique quatre composants, à savoir l'eau, l'hémicellulose, la cellulose, la lignine. Ainsi, l'eau, l'hémicellulose, la cellulose et la lignine impliquent les quatre phases solides. Pour le composite carbone/époxy, seule la résine époxy représente la réaction avec deux schémas de réaction parallèles, la réaction de la fibre de carbone et de l'eau à l'intérieur sont négligeables. Dans ce travail, on suppose que la production de pyrolyse est de l'azote pour tous les gaz libérés.

## A.4 Chapitre 4: Modélisation à l'échelle des particules de la pyrolyse du bois

Ce chapitre est dédié à la modélisation de la décomposition thermique du bois à l'échelle des particules, c'est-à-dire à l'échelle TGA (Analyse Thermogravimétrique). Des expériences ont été réalisées en utilisant l'appareil TGA sous atmosphère inerte, pour deux vitesses de chauffage: 10 K/min et 50 K/min. À partir des évolutions de la perte de masse et du taux de perte de masse, deux schémas de réaction ont été proposés: un global et un multi-parallèles. Les paramètres cinétiques inconnus ont été déterminés par le modèle DAKOTA en PATO. Les évolutions de modélisation de la perte de masse et des taux de perte de masse ont été comparées aux évolutions expérimentales afin d'analyser l'influence du schéma réactionnel. L'influence de la vitesse de chauffe sur les paramètres cinétiques est analysée. Ainsi, les paramètres cinétiques optimisés par une vitesse de chauffage sont comparés par les paramètres

cinétiques extraits d'autres vitesses de chauffage. Enfin, la modélisation 2D avec le modèle PATO permet d'explorer l'interaction des transferts de chaleur et de masse à cette échelle de particules spécifique.

Afin d'explorer l'influence de la vitesse de chauffage sur la réaction de pyrolyse, il est choisi d'extraire un ensemble de données cinétiques pour chaque condition de chauffage. Les paramètres cinétiques sont obtenus tout d'abord par une vitesse de chauffage et après leur analyse pour simuler un autre cas de vitesse de chauffage. L'influence de la vitesse de chauffage sur le processus de pyrolyse est analysée, il est démontré que la fraction de résidu massique finale semble être indépendante de la vitesse de chauffage, et le pic de vitesse de réaction se déplace vers une plage de température plus élevée lorsque la vitesse de chauffage augmente. Nous avons constaté que pour une fraction massique de matière vierge supérieure à 50% en poids, le processus cinétique est régi par l'élévation de température de l'échantillon. Lorsqu'il s'agit de moins de 50% en poids de fraction massique vierge, la masse restante devient le paramètre limité du processus de réaction global. Il est démontré que le processus de chauffage peut interagir avec le processus de pyrolyse global, et chaque réaction de décomposition thermique n'est pas affectée de la même manière par le processus de chauffage. Seule la réaction vis-à-vis de la décomposition thermique de la cellulose semble être affectée par la vitesse de chauffage en termes de plage de température de début. De plus, la vitesse de chauffage n'affecte pas la température de début de la réaction hémicellulosique. Il peut être démontré qu'une vitesse de chauffage plus élevée tend à favoriser l'intensité et la durée de la réaction hémicellulosique. Une vitesse de chauffage plus élevée semble affaiblir le processus de décomposition thermique de la cellulose avec une plus grande plage de températures de réaction lorsque la vitesse de chauffage augmente. La vitesse de chauffage affecte la cinétique de chaque réaction de différentes manières, la vitesse de chauffage n'a pratiquement aucun impact sur la décomposition thermique de la lignine. Cependant, les réactions de décomposition thermique de l'hémicellulose et de la cellulose sont affectées par le processus de chauffage.

Afin d'évaluer la prévisibilité pour différents schémas de réaction, un simple schéma de réaction global en une étape et un schéma de réaction parallèle indépendant complexe avec un modèle de réaction de nième ordre sont proposés pour décrire le comportement de décomposition thermique du matériau. On constate que pour les deux vitesses de chauffage, les deux schémas conviennent bien au processus d'évaporation de l'eau, de sorte que l'évaporation de l'eau est indépendante des schémas de réaction de pyrolyse. Pour les deux vitesses de chauffage, le schéma de réaction parallèle indépendant convient assez bien. Le schéma de réaction global en une étape ne capture pas bien la valeur de pic de MLR et la plage de température à laquelle la réaction de pyrolyse se produit. Cependant, d'un point de vue macroscopique, ciblant le profil de perte de masse expérimental et numérique, le mécanisme global en une étape réussit à représenter la tendance globale de la pyrolyse, de sorte qu'un tel mécanisme pourrait être applicable pour décrire le processus de pyrolyse lorsqu'un incendie est pleinement développé.

Des simulations 2D ont été menées pour analyser les gradients thermiques possibles dans le solide en configuration TGA à 50 K/min. Différents temps caractéristiques sont concentrés pour explorer le comportement de réaction concernant la vitesse de réaction de l'hémicellulose, de la cellulose et de la lignine. Les trois temps caractéristiques concernant: le temps de pic de vitesse de réaction, le temps avant et après ce pic, respectivement. Il est démontré que l'avancement des réactions est assez constant sur toute l'épaisseur du solide. Une plus grande différence est observée pour la réaction hémicellulosique au moment où la vitesse de réaction est maximale. On montre que la vitesse de réaction maximale globale est observée lorsque l'avancement d'une telle réaction globale est d'environ 0.5 en 0D. Cependant, pour le modèle 2D, concernant l'avancement de la réaction de chaque composant qui se comporte en fonction de l'épaisseur. Les principales différences concernent l'hémicellulose et une progression d'environ 0.41 est observée en surface et de 0.38 au centre au temps caractéristique de 349.3 s. Au temps caractéristique précédant la vitesse de réaction maximale, les réactions d'hémicellulose et de cellulose présentent des gradients de vitesse de réaction

plus élevés avec une différence d'environ 15% de la vitesse de réaction entre la surface et le centre de l'échantillon. La lignine est moins influencée par une différence de vitesse de réaction inférieure à 10%. On constate une évolution de vitesse de chauffage plus élevée qui atteint 54 K/min en comparant la réaction d'hémicellulose où les vitesses de chauffage sont encore proches de 50 K/min. Au moment où les vitesses de réaction sont maximales, nous avons observé moins de gradient de vitesse de réaction pour l'hémicellulose et la lignine. Leur vitesse de réaction à la surface et aux emplacements intermédiaires (impliquent une vitesse de réaction maximale) de l'échantillon est d'environ 5%. Cependant, cette différence de vitesse de réaction est d'environ 15% pour la cellulose accompagnée d'une différence de 2K entre la surface et le milieu de l'échantillon, et d'une vitesse de chauffage supérieure à 50 K/min (environ 56 K/min). On peut noter qu'à ces instants caractéristiques, lorsque les vitesses de réaction sont maximales, la valeur maximale de la vitesse de réaction est située au milieu de l'échantillon et différentes valeurs plus petites sont observées à la surface, démontrant que les fronts de réaction se déplacent de la surface vers le milieu de l'épaisseur de l'échantillon. Pour le temps caractéristique après le pic de vitesse de réaction (courbes vertes), on observe une tendance similaire pour les réactions de lignine et de cellulose. Alors que des gradients de vitesse de réaction plus élevés pour la réaction de cellulose, une tendance opposée pour la vitesse de réaction d'hémicellulose. Cela démontre qu'un gradient d'avancement de réaction est formé à travers l'épaisseur du solide. Avec un tel comportement discuté ci-dessus, nous pouvons conclure que les transferts de chaleur et de masse interagissent avec les réactions de pyrolyse lorsque la vitesse de chauffage globale est supérieure à 50 K/min. Ces interactions doivent être correctement capturées par le modèle pour décrire correctement le processus global de pyrolyse.

## A.5 Chapitre 5: Expériences au cône calorimètre et validation du modèle de pyrolyse du bois

En raison du lien étroit entre les processus chimiques et thermo-physiques au cours du scénario de pyrolyse par incendie réel, ce chapitre se concentre sur la pyrolyse du bois à une plus grande échelle de laboratoire, avec l'appareil calorimétrique à cône. Des expériences sont menées afin de caractériser la décomposition thermique du bois, avec à la fois des transferts de chaleur et de masse. Les paramètres convectifs aux limites et thermo-physiques sont prédits spécifiquement dans les conditions expérimentales concernant le calorimètre à cône. L'évaporation de l'humidité est ciblée, la pyrolyse du bois humide et du bois sec est étudiée numériquement à différentes échelles de temps et de longueur.

Des analyses numériques pertinentes sont menées à différentes échelles de temps et de longueur pour différents scénarios de pyrolyse. Avec un porte-échantillon en silicate épais à isolation thermique, le coefficient de convection thermique sur les côtés et sur la surface inférieure n'est pas considéré comme important. Le coefficient de convection thermique de la surface supérieure est bien prédit par analyse inverse pour passer de 3 à 5 W/m<sup>2</sup>/K pour le modèle 2D, alors qu'il est estimé à 0 à 3 W/m<sup>2</sup>/K pour le modèle 1D avec moins précision. La conductivité thermique et la capacité thermique spécifique du bois et du charbon sont prédites par analyse inverse des conditions expérimentales, et leur signification physique est vérifiée. Le processus d'évaporation de l'humidité du bois humide sous une exposition à un flux de chaleur de 5 kW/m<sup>2</sup> est analysé. Une bonne adaptation est obtenue en ce qui concerne la perte de masse, le taux de perte de masse et les évolutions de température à trois endroits dans l'épaisseur de l'échantillon. Le front d'évaporation est courbé avec différents niveaux, avec une augmentation de l'évolution dans le temps et dans l'espace qui est influencée par l'effet secondaire imposé par la conduction thermique du silicate dans le modèle 2D. Le front d'évaporation est mince aux emplacements supérieurs et devient épais lorsqu'il se déplace vers le bas, ce qui est influencé par la réaction endothermique de l'eau et la diminution de la

vitesse de chauffage. Sur la base de l'analyse de l'évolution de la température du bois humide et sec, l'eau peut retarder l'évolution de la température à travers l'épaisseur, et l'emplacement du fond est le plus influencé. Cependant, les températures finales des différents endroits ne sont pas influencées par l'eau.

Sur la base de l'observation de l'influence de l'eau, les procédés de pyrolyse du bois humide et sec sont analysés par modélisation 1D et 2D à un flux thermique incident de 20 kW/m<sup>2</sup> et 50 kW/m<sup>2</sup>. La vitesse de chauffage est spécifiée à 10 K/min pour la pyrolyse humide du bois à 20 kW/m<sup>2</sup>, et une vitesse de chauffage d'environ 50 K/min est estimée à 50 kW/m<sup>2</sup>. Comparé à la pyrolyse humide du bois, le bois sec subit un processus de chauffage rapide avec une vitesse de réaction intensifiée et une évolution de température plus élevée. L'évolution de la température implique différents niveaux du plateau, en particulier pour les emplacements inférieurs à faible flux thermique. Concernant la validation du modèle, le modèle 2D permet de mieux prédire la perte de masse, le taux de perte de masse et l'évolution de la température par rapport au modèle 1D. Le modèle peut être validé avec plus de précision à un flux thermique plus faible (20 kW/m<sup>2</sup>) par rapport aux cas à flux thermique plus élevé (50 kW/m<sup>2</sup>). De même, le front de charbon expérimental est validé pour la pyrolyse humide du bois à 20 kW/m<sup>2</sup> et 50 kW/m<sup>2</sup> aux différents temps caractéristiques et une meilleure prédiction peut être observée à un flux thermique plus faible.

Une analyse numérique est menée avec des détails concernant l'influence de l'eau et du processus de chauffage sur les scalaires globaux et locaux. L'eau peut retarder le processus de perte de masse, mais une fraction massique fixe de résidus de charbon est présente pour le bois humide et sec. La vitesse de réaction d'évaporation de l'eau est globalement plus élevée au départ que celles des autres réactions (hémicellulose, cellulose et lignine) à 20 kW/m<sup>2</sup>, tandis que pour le cas de 50 kW/m<sup>2</sup>, la vitesse de réaction de l'eau est inférieure aux vitesses de réaction de autres composants. La différence concernant le taux de perte de masse entre les cas de pyrolyse du bois sec et humide est plus prédominante à un flux thermique plus faible. L'eau peut fournir une évolution de température plus faible pour le bois humide, mais la température

finale reste constante par rapport au cas de la pyrolyse du bois sec. Des différences de température plus importantes entre la pyrolyse du bois humide et sec peuvent être trouvées pour l'emplacement inférieur par rapport à celui des emplacements supérieurs ou intermédiaires. On étudie la propagation du front d'évaporation et de pyrolyse aux différents temps caractéristiques. Le front d'évaporation est relativement mince tout au long du processus et il peut interagir de manière physique avec le processus de pyrolyse. Cependant, ce front d'évaporation peut changer pour devenir très épais en descendant vers l'espace inférieur plus frais, et il est loin du front de pyrolyse et ne pourrait pas interagir avec ce processus de pyrolyse à un flux thermique plus faible.

## **A.6 Chapitre 6: Modélisation de multi-échelle à la pyrolyse du composite carbone/époxy**

Ce chapitre a été dédié à la modélisation de la décomposition thermique d'un composite résine époxy/fibres de carbone, d'une part à l'échelle TGA et d'autre part à l'échelle d'un calorimètre conique. Un mécanisme à deux parallèles de décomposition thermique a été utilisé et les paramètres cinétiques associés ont été validés à l'échelle TGA par comparaison avec les données expérimentales. Les propriétés physiques et thermiques requises pour la modélisation de la décomposition thermique à l'échelle du calorimètre à cône ont été déterminées à partir de différentes sources de la littérature. L'évaluation du modèle pour représenter la décomposition thermique du composite carbone/époxy a été effectuée en tenant compte de la perte de masse, du taux de perte de masse et des profils de température dans l'épaisseur des échantillons composites.

Le procédé de pyrolyse composite carbone/époxy à l'échelle TGA et à l'échelle du calorimètre à cône est étudié. Selon les courbes expérimentales, il se produit un plateau après la fin de la décomposition thermique qui implique que la fraction de perte de masse totale représente respectivement environ 25% et 30% pour les deux vitesses de chauffage. La fraction massique expérimentale du rendement en charbon dans ce travail est également conforme à l'observation générale qui implique moins de

résidus de charbon à une vitesse de chauffage élevée. Les paramètres cinétiques extraits ont bien prédit les courbes expérimentales, une bonne remise en forme est obtenue notamment à 20 K/min, à l'exception de certains niveaux de déviation pour la partie queue. La vitesse de chauffage de 50 K/min implique un écart modéré par rapport à celle de 20 K/min, qui est décalée vers une température plus basse. Il est démontré que les paramètres cinétiques pourraient refléter le comportement de la réaction de pyrolyse pour différents processus de chauffage. Ces vitesses de chauffage sont liées à l'expérience du cône calorimètre avec un flux de chaleur de 20 kW/m<sup>2</sup> et 50 kW/m<sup>2</sup>.

Afin d'explorer les propriétés thermo-physiques non isotropes telles que la conductivité thermique, les valeurs sont abordées par changement de tenseur avec différentes directions sous 3D pour la pyrolyse composite carbone/époxy. Le composite carbone/époxy implique une conductivité thermique plus grande pour la direction dans le plan que celle pour la direction de l'épaisseur. Ainsi, 5 fois la différence est prise cette étude. Un travail de modélisation 1D est d'abord effectué pour témoigner de l'hypothèse que le composite de carbone époxy vierge est homogène en tenant compte des propriétés isotropes. Afin de montrer l'influence des propriétés anisotropes sur le comportement de la pyrolyse qui impliquent différentes valeurs dans différentes directions du composite carbone/époxy, des travaux de modélisation 3D sont également réalisés à titre de comparaison. En observant les données expérimentales, la pyrolyse du composite carbone/époxy à l'échelle du calorimètre à cône n'apparaît pas comme le deuxième pic du taux de perte de masse dans cette étude, On peut observer que le taux de perte de masse et la prédiction de température sous 1D et 3D impliquent des tendances de variation qui démontrent que l'hypothèse isotrope peut être applicable en ce qui concerne la simulation de la décomposition thermique du composite carbone/époxy. En fin de test en cône calorimètre, la fraction massique moyenne du résidu du composite carbone/époxy représente environ 75% en poids, On observe qu'un accord raisonnable est obtenu pour la perte de masse normalisée et le taux de perte de masse correspondant, en particulier en ce qui concerne la fraction massique finale du résidu de charbon et la plage de durée du pic du taux de perte de masse. L'occurrence et la fin du

processus de pyrolyse sont capturées avec précision. Cependant, l'amplitude prévue du pic de taux de perte de masse est déviée avec une erreur relativement importante par rapport aux données de l'expérience. Pour un flux de chaleur de 20 K/min. Lorsque l'on compare la perte de masse et le taux de perte de masse entre les valeurs mesurées et les prédites, il montre une concordance parfaite du début jusqu'à 300 s. Il démontre la validité et la précision de ce modèle au stade initial de la pyrolyse. Il est observé que du début à environ 500 s, le modèle sous-prédit la surface supérieure et les températures moyennes d'environ 20 K, tandis que la température de la surface arrière implique une bonne adaptation avec les données expérimentales. La température de la surface inférieure est en bon accord avec celle expérimentale. on pense qu'un degré raisonnable de précision est obtenu en particulier pour la prédiction de température à 20 kW/m<sup>2</sup> à l'exception de l'amplitude de crête du taux de perte de masse. On peut conclure qu'un délaminage grave se produit à différents endroits à travers l'épaisseur dans les cas de 20 kW/m<sup>2</sup> et 50 kW/m<sup>2</sup>. Concernant cette étude, le délaminage grave se produit entre les emplacements supérieurs et intermédiaires à 20 kW/m<sup>2</sup>. Alors que pour 50 kW/m<sup>2</sup>, cette délamination grave se produit entre les emplacements du milieu et du bas. Pour conclure cette partie, un niveau de prédiction similaire est observé à 20 kW/m<sup>2</sup> et 50 kW/m<sup>2</sup>. À l'exception des écarts plus importants de la prédiction de l'amplitude du pic du taux de perte de masse, la prédiction à un flux thermique plus faible semble être plus précise lorsque l'on cible l'évolution de la température.

## A.7 Chapitre 7: Analyse de sensibilité

Plus la quantité des paramètres d'entrée du modèle est importante, plus les incertitudes sont élevées. Afin de tester comment ces paramètres sont liés au comportement de pyrolyse et lesquels sont les plus incertains, le chapitre 7 est consacré à une analyse de sensibilité afin d'explorer leurs effets. L'analyse de sensibilité pourrait donner des informations sur la manière dont les paramètres influencent les résultats. Par exemple, pendant le processus de pyrolyse, différents paramètres peuvent jouer des

rôles différents sur les résultats. Ainsi, à l'avenir, nous pourrions nous concentrer sur les paramètres qui doivent être déterminés correctement par des moyens numériques ou expérimentaux de manière à permettre de diminuer les incertitudes du modèle causées par les paramètres d'entrée et d'améliorer l'efficacité de la prédiction du modèle.

Pour conclure, de nombreux paramètres non fiables sont impliqués pour la mise en œuvre de la modélisation de la pyrolyse. Les paramètres cinétiques sont plus importants pour la prédiction des réactions chimiques alors que pour la prédiction de la température, ils ne sont pas sensibles. Le taux de perte de masse est très sensible à la chaleur de décomposition. Le taux de perte de masse et l'évolution de la température sont sensibles à la conductivité thermique vierge et carbonisée. Pour la capacité thermique spécifique de la vierge et du charbon, elles sont plus importantes à un flux thermique plus faible. Le taux de perte de masse et l'évolution de la température sont sensibles à la perméabilité au charbon et insensibles à la perméabilité vierge. La teneur en eau peut être plus importante pour la surface du matériau au moment initial, donc pour l'étude d'inflammation du matériau, cet effet de l'eau doit être remarqué. Là encore, la teneur en eau peut influencer l'évolution de la température tout au long du processus de pyrolyse pour différents flux de chaleur, mais cette influence sur la surface supérieure à un flux de chaleur élevé peut être négligeable.

À l'avenir, cette teneur en eau devrait être mise beaucoup plus en évidence, en particulier lors de la réalisation d'une expérience dans un environnement à faible chauffage. De même avec la teneur en eau, l'émissivité du charbon est plus importante dans un environnement de chauffage inférieur et une grande attention doit être accordée pour déterminer cette valeur. La conductivité thermique du charbon est plus importante que la capacité thermique spécifique du charbon, mais le charbon est assez incertain et fragile avec une évolution des propriétés très changeante. Il est toujours difficile de saisir cet aspect et des études futures devraient être données. Le coefficient de convection de la chaleur limite est plus important dans un environnement à faible chauffage, cependant, ces valeurs sont généralement estimées en fonction des conditions expérimentales. À l'avenir, cette partie du travail devrait être résolue de manière

hautement expérimentale ou numérique afin de connaître les circonstances correctes de perte de chaleur dans l'environnement ambiant.

## A.8 Chapitre 8: Conclusion et perspective

Dans ce contexte, la présente thèse vise à étudier la pyrolyse de deux matériaux composites différents afin de mieux comprendre le processus de décomposition thermique et de fournir les données nécessaires au développement et à la validation du modèle PATO. Le premier matériau est le bois tandis que le second est un composite fibre de carbone/résine époxy. Le bois est choisi car il s'agit d'une sorte de matériau composite isotrope tandis que le carbone/époxy est choisi car il s'agit d'une sorte de matériau non isotrope. Pour étudier l'ensemble du processus de pyrolyse, la méthode multi-échelle a été choisie qui consiste à étudier les aspects séparément à une échelle détaillée (cinétique, transfert de chaleur et de masse, porosité, etc.), et deuxièmement, ces aspects sont couplés à plus grande échelle pour étudier les interactions. Ensuite, au cours de ce travail, deux échelles sont utilisées: l'échelle de la matière TGA (thermiquement mince) et l'échelle du cône calorimètre (thermiquement épaisse). De plus, pour valider plus précisément le modèle dans une première approche et éviter les incertitudes dues à des conditions aux limites mal contrôlées (formées par flamme ou oxydation), les manipulations expérimentales sont conduites sous atmosphère inerte pour les deux échelles.

La décomposition thermique du bois a été étudiée à l'aide d'un appareil TGA. A partir de l'évolution des courbes de perte de masse et de taux de perte de masse, deux mécanismes (réactions parallèles à une étape et à plusieurs étapes) de décomposition thermique ont été proposés. Les paramètres cinétiques devraient mettre en œuvre les réactions chimiques en modélisant la méthode d'ajustement avec l'expérience TGA qui est décrite avec l'équation de type Arrhenius à travers différentes échelles de temps. Le schéma de réaction parallèle en plusieurs étapes modélise bien la perte de masse et la vitesse de perte de masse MLR, tandis que le schéma de réaction global en une étape

ne capture pas bien la valeur du pic du MLR et la plage de températures à laquelle la réaction de pyrolyse se produit. Pour analyser l'hypothèse d'absence de chaleur et de gradient de masse dans l'échantillon lors de l'expérience TGA, des simulations 0D (modèle à gradient nul) et 2D à symétrie d'axe (modèle à gradient) ont été comparées. Pour les deux simulations, aucune différence significative n'a été identifiée. L'influence de la vitesse de chauffage sur le processus de pyrolyse a été analysée. Il est démontré que seul le pic de vitesse de réaction passe dans une plage de températures plus élevée lorsque la vitesse de chauffage augmente. Le processus de chauffage peut interagir avec le processus de pyrolyse global et chaque réaction n'est pas affectée de la même manière par le processus de chauffage. Le processus de chauffage jouant un rôle important dans la décomposition thermique, des simulations 2D ont été menées pour analyser les gradients thermiques possibles dans le solide en configuration TGA à 50 K/min. Il est démontré que le transfert de chaleur et de masse interagit avec les réactions de pyrolyse dans TGA lorsque la vitesse de chauffage globale est élevée. Ces interactions doivent être correctement capturées par le modèle pour décrire correctement le processus global de pyrolyse.

Afin d'explorer le comportement de la pyrolyse dans différentes conditions thermiques, des tests en cône calorimètre sous atmosphère contrôlée sous l'azote ont été réalisés avec un porte-échantillon en silicate pour l'isolation thermique. Les modèles numériques sont mis en œuvre pour étudier les processus de pyrolyse à différentes échelles de temps et de longueur sous 1D et 2D. Les coefficients de chaleur convective sont extraits par analyse inverse avec conduction thermique pure de l'aluminium et un ensemble de coefficients de convection thermique est attribué pour la prédiction du modèle. Les paramètres thermiques du bois et du charbon sont obtenus sur la base d'expériences de conduction thermique pure. Les modèles 1D et 2D correspondent assez bien pour les emplacements supérieurs et la différence est augmentée pour la température inférieure. On précise que le rôle du matériau silicate isolant est très important ce qui peut donner une meilleure prédiction de la perte de masse et du profil de température par le modèle 2D, et cet «effet secondaire» a tendance à être augmenté

dans le processus de chauffage lent. On constate que la fraction et la température de rendement final du charbon concernant le bois humide et la pyrolyse du bois sec se comportent de la même manière et aucune différence apparente n'est impliquée. Ensuite, l'eau a seulement tendance à retarder le processus de pyrolyse et le pic de réaction ou l'élévation de température correspondant est alors influencé. Il est démontré que la différence de MLR entre les caisses sèches et humides est augmentée à faible flux thermique et que la différence de température entre le bois sec et humide augmente avec l'épaisseur. Pour un faible flux thermique, la vitesse de réaction et l'avancement de la pyrolyse sont lents avec une couche de pyrolyse épaisse accompagnée d'un gradient de température plus petit. Alors que pour un flux thermique élevé, il s'agit d'une fine couche de pyrolyse à gradient de température élevée. Pour la modélisation de la décomposition thermique du composite carbone/époxy est réalisée d'une part à l'échelle TGA et d'autre part à l'échelle du cône calorimètre. Un mécanisme parallèle de décomposition thermique a été utilisé et les paramètres cinétiques associés ont été validés à l'échelle TGA par comparaison avec les données expérimentales. La fraction massique expérimentale du rendement en charbon dans ce travail contribue à l'observation générale qui implique moins de résidus de charbon à une vitesse de chauffage élevée. Les paramètres cinétiques extraits pourraient refléter le comportement de la réaction de pyrolyse pour les différents processus de chauffage. L'évaluation du modèle pour représenter la décomposition thermique du composite carbone/époxy est menée en tenant compte de la perte de masse, du taux de perte de masse et des profils de température à différents endroits. L'occurrence et la fin du processus de pyrolyse sont bien capturées par le modèle, mais l'ampleur du pic du taux de perte de masse est surestimée par rapport à l'expérience pour les deux flux de chaleur. Il est démontré qu'une délamination grave se produit à différents endroits à travers l'épaisseur du composite sous différents flux de chaleur. Afin d'explorer la conductivité thermique non isotrope du composite carbone/époxy, les valeurs sont abordées par changement de tenseur avec différentes directions sous 3D. Les modélisations 1D et 3D sont comparées, la perte de masse et la température expliquent à peu près la même

tendance de variation qui conclut que l'hypothèse isotrope peut être appropriée en ce qui concerne la simulation de la décomposition thermique du composite carbone/époxy.

Pour l'étude de sensibilité, on constate que le taux de perte de masse est assez sensible aux paramètres cinétiques (énergie d'activation, facteur pré-exponentiel et ordre de réaction), et cette influence est plus forte à flux thermique plus faible, alors que l'évolution de la température est légèrement sensible à l'énergie d'activation. Une influence similaire est observée avec la chaleur de décomposition thermique par rapport à ces paramètres cinétiques, et l'emplacement du fond est plus influencé. Des influences similaires sont trouvées concernant la conductivité thermique vierge et carbonisée, et leur influence sur l'emplacement du fond est plus grave. La capacité thermique spécifique de la vierge et du charbon a une certaine influence sur les différentes étapes de pyrolyse. On constate que l'émissivité du charbon est plus importante dans un environnement de chauffage plus faible et qu'une grande attention doit être accordée pour déterminer cette valeur. La perméabilité vierge n'a aucune influence peut être conclue, tandis que la perméabilité au charbon pourrait avoir un certain effet, en particulier dans un environnement à flux thermique élevé et à l'emplacement du fond. Le coefficient de convection thermique est plus important lorsque le flux thermique est plus faible. L'évolution de la température est assez sensible à la teneur en eau tout au long du processus de pyrolyse, et elle peut être plus importante pour la surface du matériau au moment initial, ainsi, pour l'étude d'inflammation du matériau, cet effet de l'eau doit être remarqué.

Enfin, les résultats obtenus montrent que le modèle PATO implique de bonnes capacités pour fournir une prédiction relativement précise du comportement de pyrolyse de différents matériaux composites sous différents environnements de chauffage. Le présent travail donne de nouvelles perspectives lors de la manipulation d'études numériques pour la pyrolyse couplant en particulier la complexité des phénomènes physiques dans les scénarios d'incendie.